Fall 10-1-2021

Three-wave Mixing in Superconducting Circuits: Stabilizing Cats with SNAILs

Nicholas Frattini

Yale University Graduate School of Arts and Sciences, nick.frattini@gmail.com

Abstract

Three-wave Mixing in Superconducting Circuits:

Stabilizing Cats with SNAILs

Nicholas E. Frattini

2021

Three-wave mixing, by which a photon splits into two correlated photons and vice versa, is a powerful quantum process with many applications in fundamental quantum mechanics experiments and quantum information processing. However, in superconducting circuits, the predominant form of nonlinearity provided by a Josephson junction is only of even order, and thus symmetry forbids three-wave mixing. This Kerr nonlinearity is useful in its own right for engineering quantum operations, but it is accompanied by unavoidable frequency shifts that become especially problematic as the number of interacting electromagnetic modes, and therefore frequency crowding, increases. How then can we endow superconducting devices with the necessary nonlinearity to perform three-wave mixing?

In this thesis, we introduce a simple and compact way to add three-wave-mixing capabilities to a superconducting circuit: the superconducting nonlinear inductive element (SNAIL). Additionally, we optimize these devices for quantum-coherent three-wave mixing applications. The many orders of magnitude over which circuit nonlinearities may be designed allow a rich space for different behaviors. We focus on three-wave mixing for single-mode squeezing in two distinct contexts: quantum-noise-limited parametric amplification, and protection of quantum information in a Schrödinger cat qubit. The former showcases the capability to design three-wave-mixing processes free of residual Kerr nonlinearity; the latter explicitly includes Kerr nonlinearity to protect quantum information from decoherence and quickly manipulate it. Both applications indicate the importance of three-wave mixing in quantum information contexts and for the exploration of fundamental quantum effects.

Three-wave Mixing in Superconducting Circuits:

Stabilizing Cats with SNAILs

A Dissertation
Presented to the Faculty of the Graduate School
of
Yale University
in Candidacy for the Degree of
Doctor of Philosophy

by
Nicholas E. Frattini

Dissertation Director: Michel H. Devoret

December 2021

Contents

List of Figures

List of Tables

List of Symbols

Acronyms

AC	alternating current ($\omega > 0$)
BBQ	black-box quantization
cQED	circuit quantum electrodynamics
CQR	cat-quadrature readout
DC	direct current ($\omega = 0$)
FQ	Fock qubit
HEMT	high-electron-mobility transistor
JJ	Josephson junction
JPC	Josephson parametric converter
JRM	Josephson ring modulator
KC	Kerr cat
QEC	quantum error correction
QED	quantum electrodynamics
QLE	quantum Langevin equation
QND	quantum non-demolition
RF	radio-frequency
SLUG	superconducting low-inductance undulatory galvanometer
SNR	signal-to-noise ratio
SNAIL	superconducting nonlinear asymmetric inductive element
SPA	SNAIL parametric amplifier
SPAM	state preparation and measurement
SQUID	superconducting quantum interference device

Constants

h	Planck's constant
$\hbar$	reduced Planck's constant ($= h/2\pi$)
e	charge of an electron
c	speed of light
Φ_0	magnetic flux quantum ($= h/2e$)
φ_0	reduced magnetic flux quantum ($= \hbar/2e$)
k_B	Boltzmann constant

3-wave mixing with SNAILs

φ_s	superconducting phase difference across a SNAIL's small junction
E_J	Josephson tunnelling energy
L_J	Josephson inductance ($= \varphi_0^2/E_J$)
n	number of large Josephson junctions in a SNAIL
α	ratio of small and large junction tunnelling energies
Φ	externally applied magnetic flux bias
φ_{ext}	externally applied magnetic phase ($= 2\pi\Phi/\Phi_0$)
$U_S(\varphi_s)$	SNAIL potential energy
$I_S(\varphi_s)$	SNAIL current-phase relation
E_C	Coulomb charging energy associated with a capacitance C ($= e^2/2C$)
C_J	junction capacitance intrinsic to the junction's construction
C_0	capacitance to ground of each island between arrayed junctions
Ω_J	junction plasma frequency ($= \sqrt{8E_J E_C}/\hbar$)
$\varphi_{s,\text{min}}$	phase that minimizes SNAIL potential $U_S(\varphi_s)$
c_k	Taylor expansion coefficients of U_S
$\tilde{\varphi}_s$	canonical phase centered about the minimum of U_S ($= \varphi_s - \varphi_{s,\text{min}}$)
$U_{S,\text{eff}}(\tilde{\varphi}_s)$	effective Taylor-expanded SNAIL potential
M	number of SNAILs arrayed in series
L	inductance of ideal linear inductor
E_L	inductive energy associated with inductance L ($= \varphi_0^2/L$)
C	capacitance of ideal linear capacitor

L_s	effective flux-dependent linear inductance of a SNAIL ($= L_J/c_2$)
$\mathcal{L}_{M+1}$	Langrangian for circuit with $M+1$ canonical coordinates
U_{M+1}	potential energy of Lagrangian $\mathcal{L}_{M+1}$
φ	canonical branch phase across the capacitor C
$\varphi_{s,m}$	branch phase across the small junction of SNAIL m
$\mathcal{L}_2$	Langrangian for circuit with 2 canonical coordinates
U_2	potential energy of Lagrangian $\mathcal{L}_2$
x_J	junction-to-linear inductance ratio ($= L_J/L = E_L/E_J$)
$\mathcal{L}_1$	Langrangian for circuit reduced to 1 canonical coordinate
U_1	potential energy of Lagrangian $\mathcal{L}_1$
$\bar{\varphi}_{\min}$	φ that minimizes potential U_1
$\tilde{c}_k$	Taylor expansion coefficients of U_1
p	SNAIL array's inductive participation ratio ($= ML_s/(L+ML_s)$)
$\boldsymbol{\mathcal{H}_1}$	one degree of freedom Hamiltonian associated with $\mathcal{L}_1$
$\boldsymbol{N}$	Cooper pair number conjugate to φ
φ_{zpf}	zero-point fluctuations of the phase ($= (2E_C/\tilde{c}_2 E_J)^{1/4}$)
N_{zpf}	zero-point fluctuations of the Cooper pair number ($= 1/2\varphi_{\mathrm{zpf}}$)
ω_a	lab-frame oscillator frequency
g_k	nonlinear Hamiltonian term of order k ($= \tilde{c}_k E_J (\varphi_{\mathrm{zpf}})^k/\hbar k!$)
n_{crit}	critical photon number
Δ_a	Lamb shift
K	Kerr nonlinearity
K'	effective sixth-order nonlinearity

BBQ with SNAILs

C_s	shunting capacitance of a single SNAIL
Ω_s	plasma frequency of a SNAIL ($= 1/\sqrt{L_s C_s}$)
$U_{\mathrm{NL}}(\tilde{\varphi}_s)$	nonlinear part of SNAIL potential U_S
$Z_{\mathrm{NL}}[s]$	impedance environment that the nonlinearity sees
$\omega_\pm$	poles of $Z_{\mathrm{NL}}[s]$
$Z_\pm$	residues of $Z_{\mathrm{NL}}[s]$ at poles $\omega_\pm$
$L\pm$	effective inductance associated with the pole ($= Z_\pm/\omega_\pm$)
$C_\pm$	effective capacitance associated with the pole ($= 1/\omega_\pm Z_\pm$)
$\varphi_\pm$	canonical branch phase across $L_\pm$

$\mathcal{H}_2$	Hamiltonian of two mode circuit
$\varphi_{\pm,\mathrm{zpf}}$	zero-point fluctuations of the canonical branch phases
$\mathcal{H}_{\mathrm{NL}}$	nonlinear part of $\mathcal{H}_2$
$C_p,\ L_p,\ R_p$	capacitance, inductance, and resistance associated with pole p
$\omega_p,\ Z_p,\ Q_p$	frequency, impedance, and quality factor of pole p
P	total number of complex pairs of poles
Ω_{max}	high frequency cutoff
P_{max}	total number of poles with $\omega_p < \Omega_{\mathrm{max}}$
$\tilde{Z}_{\mathrm{NL}}[s]$	impedance seen by renormalized nonlinear dipole
$\tilde{U}_{\mathrm{NL}}(\tilde{\varphi}_{\mathrm{NL}})$	potential of renormalized nonlinear dipole
$\tilde{\varphi}_{\mathrm{NL}}$	branch phase across the renormalized nonlinearity
$\mathcal{L}_{P_{\mathrm{max}}}$	Lagrangian with P_{max} degrees of freedom
$\mathcal{H}_{P_{\mathrm{max}}}$	Hamiltonian with P_{max} degrees of freedom
$\boldsymbol{\varphi}_p$	canonical phase across inductor associated with pole p
$\boldsymbol{N}_p$	conjugate momentum to $\boldsymbol{\varphi}_p$
$\tilde{\mathcal{H}}_{\mathrm{NL}}$	nonlinear part of $\mathcal{H}_{P_{\mathrm{max}}}$

Quantum bits

$\boldsymbol{X}$	Pauli X operator
$\boldsymbol{Y}$	Pauli Y operator
$\boldsymbol{Z}$	Pauli Z operator
$\boldsymbol{I}$	Identity operator
$\lvert\pm X\rangle$	$\boldsymbol{X}$ eigenstates
$\lvert\pm Y\rangle$	$\boldsymbol{Y}$ eigenstates
$\lvert\pm Z\rangle$	$\boldsymbol{Z}$ eigenstates

Oscillators

$\boldsymbol{a}$	bosonic excitation annihilation operator
$\boldsymbol{a}^\dagger$	bosonic excitation creation operator
$\boldsymbol{D}(\alpha)$	displacement operator ($= e^{\alpha \boldsymbol{a}^\dagger - \alpha^* \boldsymbol{a}}$)
$\lvert n\rangle$	Fock state with n photons ($\boldsymbol{a}^\dagger \boldsymbol{a}\lvert n\rangle = n\lvert n\rangle$)
$\lvert\alpha\rangle$	coherent state with amplitude α ($\boldsymbol{a}\lvert\alpha\rangle = \alpha\lvert\alpha\rangle$)

Schrödinger cat qubit

α	stabilized coherent state amplitude
$\lvert\mathcal{C}_\alpha^\pm\rangle$	Schrödinger cat states ($= \mathcal{N}_\alpha^\pm(\lvert+\alpha\rangle \pm \lvert-\alpha\rangle)$)
$\mathcal{N}_\alpha^\pm$	cat-state normalization coefficients ($= 1/\sqrt{2(1 \pm e^{-2\lvert\alpha\rvert^2})}$)
r	ratio of normalization coefficients ($= \mathcal{N}_\alpha^+/\mathcal{N}_\alpha^-$)
$\boldsymbol{P}_\mathcal{C}$	projector onto cat-qubit Bloch sphere
$\bar{n}$	average photon number of coherent states ($= \lvert\alpha\rvert^2$)
$\bar{n}_\pm$	average photon number of even/odd cat states ($= r^{\pm2}\lvert\alpha\rvert^2$)

Cat qubit stabilization

ω_a	lab-frame resonant frequency of oscillator a
ω_p	lab-frame frequency of squeezing drive for 3-wave-mixing process ($= 2(\omega_a + \Delta)$)
$\mathcal{H}_1$	Hamiltonian to stabilize one coherent state
α_0	displacement amplitude for frame transformation
ϵ_1	single-photon or linear drive strength
Δ	drive detuning from oscillator frequency
κ_1	single-photon energy decay rate of an oscillator
$\mathcal{H}_{1c}$	non-Hermitian Hamiltonian to stabilize one coherent state
$\tilde{\Delta}$	generalized detuning ($= \Delta + i\kappa_1/2$)
$\mathcal{H}_{2c}$	non-Hermitian Hamiltonian stabilize two coherent states
ϵ_2	two-photon or squeezing drive strength
K	Kerr nonlinearity (anharmonicity of transmon $= 2K$)
κ_2	two-photon decay rate of an oscillator
$\tilde{K}$	generalized Kerr ($= K + i\kappa_2/2$)
ω_{gap}	dispersive energy gap
κ_{gap}	dissipative energy gap
$\tilde{\omega}_{\text{gap}}$	generalized energy gap ($= \omega_{\text{gap}} - i\kappa_{\text{gap}}/2$)
$\mathcal{H}_{\text{KC}}$	non-Hermitian Hamiltonian to stabilize generalized Kerr-cat qubit
ϕ_0	phase of α_0
$\tilde{\phi}_0$	phase of α_0 relative to case when $\tilde{\Delta} = 0$
$\tilde{\delta}$	reduced detuning ($= \tilde{\Delta}\tilde{K}^*/2\lvert\epsilon_2\tilde{K}\rvert$)

Kerr-cat qubit realization

T_1	amplitude damping time of the Fock qubit ($= 1/\kappa_1$)

T_2	decay time or Ramsey experiment on the Fock qubit
Ω_x	Rabi rotation rate around the X axis
Ω_Z	Rabi rotation rate around the Z axis
$\mathcal{F}_{\mathrm{map}}$	gate fidelity of the mapping operation
$T_{X(\pi/2)}$	total time duration of an $X(\pi/2)$ gate
$\mathcal{F}_{X(\pi/2)}$	gate fidelity of the $X(\pi/2)$ operation
$T_{Z(\pi/2)}$	total time duration of an $Z(\pi/2)$ gate
$\mathcal{F}_{Z(\pi/2)}$	gate fidelity of the $Z(\pi/2)$ operation
ω_b	lab-frame resonant frequency of readout oscillator b
κ_b	linewidth of readout cavity b
$\boldsymbol{b}$, $\boldsymbol{b}^\dagger$	bosonic annihilation and creation operators for oscillator b
ω_{cqr}	frequency of applied drive for CQR ($= \omega_b - \omega_p/2$)
α_{cqr}	drive amplitude with mode a resulting from CQR drive
g_{ba}	rate of weak capacitive coupling between modes b and a
Δ_{ba}	detuning between modes b and a ($= \omega_b - \omega_a$)
$\mathcal{H}_{\mathrm{cqr}}$	effective interaction Hamiltonian to implement CQR
g_{cqr}	drive-induced bilinear coupling between modes b and a
β	coherent state amplitude within mode b
τ	measurement pulse time duration
η	quantum efficiency of a qubit measurement
T_{cqr}	total time duration of CQR
$I_{\pm X}$	average in-phase quadrature readout signal for qubit preparation in $|{\pm}X\rangle$
σ	standard deviation of readout signal histogram
$\mathcal{F}$	readout fidelity of CQR
$\mathcal{Q}$	readout QNDness of CQR
n_{th}	thermal population of an oscillator coupled to a thermal bath
τ_s	decay timescale for preparation in qubit state $s = \pm X, \pm Y, \pm Z$

Kerr-cat future directions

ω_{spec}	lab-frame frequency swept for spectroscopy
τ_{cqr}	decay timescale of coherent states under repeated CQR
CNOT	controlled-not operation
$\mathcal{H}_{\mathrm{CNOT}}$	Hamiltonian to enact a CNOT between two Kerr-cat qubits

ϕ	time-dependant phase that parameterizes the time evolution of the CNOT
K_m	self-Kerr nonlinearity of mode $m = a,\, b$

Acknowledgements

Finishing a Ph.D. is by no means a solo adventure; it absolutely takes collaboration, kindness, and support from those around you. I have been lucky enough to find those things at Yale and in New Haven generally that has made this place home. In no small way, this is due to the people in the superconducting quantum information team. Michel and Rob have built a community where people generally flourish, have fun, and support each other. And I am grateful for this and every member of our community who helps make it so.

There are some people who I wish to further thank in particular. First, my advisor, Michel Devoret. Given his reputation, I had high expectations and I was not disappointed. Intelligence is a given; but the wealth of knowledge and intuition that carried into many areas of physics was truly astounding. Michel sets the example of someone who understands concepts to their core and yet always continues to question them for a deeper, more intuitive explanation. This level of intuition and ability to explain concepts without getting bogged down in mathematics is something I aspire to achieve. He is also remarkably open—both in discussion and in scientific projects. His door was always open. No idea was too small to be discussed, and the lab benefits greatly from his willingness to try something new. His excitement about physics is infectious. I am honored to have been his Ph.D. student.

The fourth floor would not exist without Rob Schoelkopf, and I am grateful for him. His strong vision for the future and his insightful questions during presentations are enough to inspire any young graduate student—me included. Also, the amount of information passed daily between Qlab and RSL is truly astounding; the teamwork propels the science forward. This is a great testament to both Rob and Michel. Steve Girvin. A theorist with an excellent appreciation for the practical as well as an extremely clear communicator. I found that I often left meetings with Steve feeling that I learned something. Finally, Shruti Puri. In no small part, Shruti herself has driven the results in this thesis. Aside from once over-torquing a clicky wrench, Shruti has been exceedingly helpful support for an experimentalist. Her insight and dedication to asking the practical questions about what limits quantum error correction are inspiring to say the least. I cannot wait to see what more is to come.

The lab would not run without Luigi Frunzio. Review a paper? Call Luigi. Having fab trouble? Call Luigi. Out of nitrogen or helium? Call Luigi. Power out in the building? Call Luigi. Interesting conversation about life? Definitely call Luigi. And this is only a few. Similarly, the administrative staff—Giselle Maillet, Theresa Evangeliste, Nuch Graves, Maria Rao—put in countless hours to make the lab run smoothly and provide a welcoming atmosphere. The same should also be said for all the events and coffee supplied by the YQI staff: Florian Carle and Racquel Miller.

Amplifier research in Qlab has a long standing history and I benefited so much from the work of many. Shyam Shankar, Katrina Sliwa, and Anirudh Narla trained me from the

beginning. Whether it was kind advice on navigating graduate school, patience with my many questions, or simply showing me sound scientific practice by example, I owe them each a debt of gratitude. Then Vlad Sivak joined the lab and I found a partner in all things SNAILs. His hard work ethic, enthusiasm, and meticulous attention to detail were infectious. His incite though is unparalleled. Most importantly though, Vlad is a pleasure to work with: quick to laugh or even draw a SNAIL cartoon to cheer you up on a rough day.

I am also indebted to the bosonic QEC team: Zaki Leghtas, Uri Vool, Steven Touzard, Shantanu Munhada, Philippe Campagne-Ibarcq, Alec Eickbusch, Akshay Koottandavida, Ioannis Tsioutsios, Alex Grimm and Rodrigo Cortiñas. Each of these individuals welcomed me onto the team and taught me the wonders of bosonic QEC in one way or another. Alex Grimm however deserves special further mention. The Kerr-cat was his baby that he shared with me, and we had fun. He taught me all things qubit measurement and pulsed experiments. More than that, his talent for translating theoretical ideas into technically sound experiments, coupled with the perseverance to see them through, is something to be admired. Joining the Kerr-cat team in the last year, Rodrigo Cortiñas has inspired me with a sharp intellect and questions probing the origins of quantum mechanics. I have enjoyed our time together and look forward to what the future holds for him.

A few more lab members deserve special thanks. Although I never touched a fermion, the quasiparticle crew—Kyle Serniak, Spencer Diamond, Valla Fatemi, and Max Hays—included me as one of their own and I am grateful to call them each friends. Kyle taught me so much about all aspects of lab: mostly importantly though, was leading by example. His willingness to help others solve problems set a high bar for good lab citizenship. A bar Spencer Diamond lives up to. Spencer is exceedingly fun to work with, quick to pick things up, and brightens the room for those around him. Valla Fatemi loves physics. Genuinely, loves it. His enthusiasm is infectious and his willingness to engage in problems that might not be his is to be admired. Max Hays is a great friend. In lab and in life. Pushing me to understand beyond the world of bosons; pushing me to try new beer. I will always value these years we have spent together at Yale, and I already feel his absence. Chris Wang has also been with me every step of the way, a steadfast friend in good times and bad. Many fridge issues would have been true problems without him. More than that though, Chris truly cares deeply for people, and that should not be undervalued. I am grateful for these years and I know we will stay in touch.

And to all of the others whom I had the chance to work with: Gijs de Lange, Evan Zalys-Geller, Ioan Pop, Mike Hatridge, Zlatko Minev, Ananda Roy, Angela Kou, Clarke Smith, Zhixin Wang, Mazyar Mirrahimi, Sumita Ghosh, Tom Connolly, Wei Dai, Andy Ding, Vidul Joshi, Pavel Kurilovich, Vlad Kurilovich, Jaya Venkatraman, Xu Xiao, Gangqiang Liu, Andrew Lingenfelter, Owen Duke, Alessandro Miano, Ben Chapman, Jacob Curtis, Stijn de Graaf, Suhas Ganjam, Vijay Jain, Lev Krayzman, Chan U Lei, Yao Lu, Aniket Maiti, Alex Read, James Teoh, Taekwan Yoon, Wolfgang Pfaff, Luke Burkhart, Philip Reinhold,

1

Introduction

Three-wave mixing, by which a photon can be split into two correlated photons and vice versa, is a powerful quantum process with many applications in fundamental quantum mechanics experiments and quantum information processing. Classical electromagnetic theory however is completely linear—green light does not spontaneously split into two different colors. Such a mixing process may only be achieved through light-matter interaction, which is the purview of quantum electrodynamics (QED). The interaction provides the nonlinearity necessary to generate three-wave mixing.

Generally, symmetry forbids third-order nonlinearity, and therefore three-wave mixing. The strongest nonlinearity is often of the fourth order—the so-called *Kerr nonlinearity*—that enables four-wave mixing, or interactions between four photons. In nonlinear optics, such Kerr nonlinearity is intrinsic to $\chi^{(3)}$ media [Boyd 2008]. In superconducting circuits, Josephson junctions provide the same, but in a purely dispersive and quantum coherent manner [Vool and Devoret 2017]. While four-wave mixing itself is useful for engineering interactions, it imparts undesired frequency shifts in response to applied power, considerably increasing the engineering complexity. Such frequency shifts become especially problematic as the number of interacting electromagnetic modes, and therefore frequency crowding, increases, putting even more stringent requirements on allowable cross-talk in state-of-the-art quantum processors [Devoret and Schoelkopf 2013].

Three-wave mixing promises an avenue to alleviate these problems. The necessary nonlinearity for mixing—the third order—is distinct from the one that often limits device performance—the fourth and even higher orders. In nonlinear optics, the crystalline structures of $\chi^{(2)}$ media have a broken spatial symmetry that allows for appreciable third-order nonlinearity. In a standard microwave mixer, the rectifying property of diodes breaks the similar symmetry, but at the consequence of added dissipation not suitable for devices operating in a quantum coherent regime. In superconducting circuits based on Josephson junctions, how do we break the same symmetry to endow our devices with third-order nonlinearity? How do we optimize these devices for quantum-coherent three-wave mixing applications? The many orders of magnitude over which circuit nonlinearities may be designed allows a rich space of different behaviors. In the context of circuit quantum electrodynamics (cQED) [Blais et al. 2004; Wallraff et al. 2004; Blais et al. 2021], we focus on three-wave mixing for single-mode squeezing in two distinct contexts: quantum-noise-limited parametric amplification, and protection of quantum information in a Schrödinger cat qubit.

a   3-wave-mixing dipoles   **b**   3-wave-mixing quadrupoles

RF-SQUID   SNAIL   JRM   flux-pumped DC-SQUID
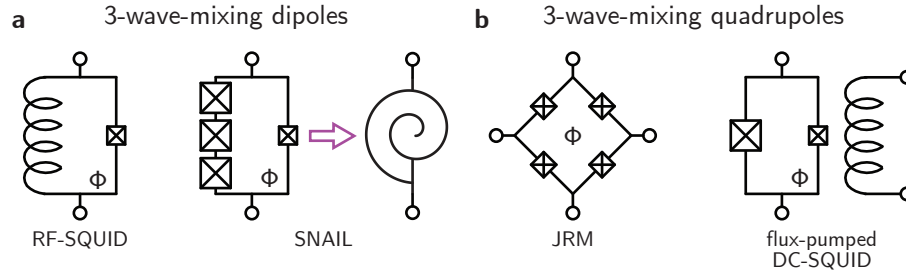
Figure 1.1 | Effective circuit elements made with Josephson junctions (crossed box circuit elements) that add third-order nonlinearity and thereby three-wave-mixing capabilities to superconducting devices. All require a DC external flux bias Φ to induce a DC circulating loop current that breaks the symmetry and enables odd orders of nonlinearity. (a) Two Josephson *dipole* elements: the RF-SQUID (superconducting quantum interference device) and the SNAIL (superconducting nonlinear asymmetric inductive element). (b) Two Josephson *quadrupole* elements: the JRM (Josephson ring modulator) and the AC flux-pumped DC-SQUID.

1.1 Three-wave mixing in superconducting circuits

The simplest way to achieve third order nonlinearity in superconducting circuits is to DC-current bias a Josephson junction, where the direction of the current flow breaks the symmetry. To limit the susceptibility to low-frequency electrical noise, such a DC-current bias may be incorporated via a DC-flux bias to a superconducting loop that contains Josephson junctions. The DC-flux induces a persistent circulating current that biases the junctions.

Fig. 1.1 depicts a set of one-loop Josephson circuits with a DC-flux bias that provide third order nonlinearity for three-wave mixing. We focus on two flavors: *dipole* elements that impose a current-phase relation between *two* nodes of a circuit, and *quadrupole* elements that impose a current-phase relation between *four* nodes of a circuit. Historically, the two depicted quadrupole elements, the Josephson Ring Modulator (JRM) [Bergeal et al. 2010a; Bergeal et al. 2010b] and AC-flux pumped DC-SQUID (superconducting quantum interference device) [Clarke and Braginski 2004; Yamamoto et al. 2008] are the most commonly used for three-wave mixing applications. Owing to their quadrupole form, they present sometimes unwieldy design constraints when combined in more complicated circuits. Moreover, they both also contain fourth-order nonlinearity and thus four-wave mixing capabilities, which may be undesirable for a given application. As we will explore in detail throughout this dissertation, the two dipoles, the RF-SQUID and the SNAIL (superconducting nonlinear inductive element), offer the opportunity to circumvent both of these properties [Zorin 2016; Frattini et al. 2017]. Note, however, that a DC-flux-biased DC-SQUID alone is equivalent to a single Josephson junction with a tunable inductance and only even orders of nonlinearity [Vool and Devoret 2017]. Thus, our nonlinearity of choice will be the SNAIL as a vehicle for engineering effective Hamiltonians for the de-

sired applications of quantum-noise-limited amplification and the protection of quantum information in a stabilized Schrödinger cat qubit.

1.2 Structure of this thesis

This thesis is arranged into three main sections: superconducting circuits with third-order nonlinearity (Chapter 2), three-wave mixing for quantum-noise-limited amplification (Chapter 3), and three-wave mixing for the manipulation and storage and a Schrödinger cat qubit (Chapters 4–6).

In order to harness the power of three-wave mixing, we must design superconducting circuits with third-order nonlinearity. Chapter 2 introduces the SNAIL—superconducting nonlinear asymmetric inductive element—that the circuit designer may substitute for the standard single Josephson junction to add third-order nonlinearity. We further derive the Hamiltonian, and with it the strengths of the third- and fourth-order nonlinearities, of simple SNAIL-based devices, as well as extend the procedure to be compatible with finite-element electromagnetic simulations. With the necessary nonlinearity in hand, we apply microwave radiation to activate three-wave-mixing processes. Chapter 3 focuses on three-wave mixing for the amplification of small—even single photon—microwave signals in the SNAIL parametric amplifier (SPA). We experimentally verify our Hamiltonian model and its dependence on physical device characteristics. We further optimize these characteristics for robustness to large input signals in a way that maintains the added noise during amplification at near the minimum required by quantum mechanics.

In the remainder of this thesis, we move to a regime where nonlinearity regulates the added energy from the squeezing drive instead of the dissipation. This regime stabilizes Schrödinger cat states, which are the basis of a quantum error correction code within a single oscillator. Chapter 4 theoretically introduces this two-legged cat code and treats the stabilization within a single oscillator via an interplay between a squeezing drive and Kerr nonlinearity—the *Kerr-cat qubit*. In Chapter 5, we present experimental results on the implementation of such a Kerr-cat qubit in a Kerr nonlinear resonator with three-wave-mixing capabilities provided by a SNAIL. Crucially, this implementation not only successfully extends the memory lifetime of quantum information with minimal hardware complexity, but is also accompanied by a fast complete set of single qubit gates as well as a quantum nondemolition (QND) measurement of the encoded information. Finally, Chapter 6 explores further improvements to the Kerr-cat qubit with an eye toward future applications as a fault-tolerant measurement apparatus or as a component in a future quantum computing architecture.

3-wave mixing with SNAILs

<div style="text-align: right; font-size: 3em;">2</div>

In this Chapter, we discuss how to pragmatically and systematically design superconducting circuits with three-wave mixing capabilities. What is the simplest way to add three-wave mixing capabilities? We propose the Superconducting Nonlinear Asymmetric Inductive eLement (SNAIL): an effective dipole for 3-wave mixing made from Josephson junctions [Frattini et al. 2017].

This chapter is entirely theoretical. We begin by introducing the SNAIL as an effective three-wave mixing dipole element in Sec. 2.1. In Sec. 2.2, we then incorporate an array of M SNAILs into a circuit with a single electromagnetic degree of freedom and derive its Hamiltonian—both linear and third- and fourth-order nonlinear terms. Sec. 2.3 focuses on the scaling of the nonlinearities with an eye toward the mixing applications in the remaining chapters. In Sec. 2.4, we explore the renormalization of Kerr nonlinearity due to the presence of high frequency degrees of freedom that experimentally we would otherwise like to ignore. We find a procedure to reliably implement a high frequency cutoff to recover the originally derived Hamiltonian of Sec. 2.2. Finally, we extend apply these principles to arbitrary SNAIL-based circuits and extend the procedure for implementing a high frequency cutoff to finite element simulations via black-box quantization [Nigg et al. 2012].

2.1 Meet the SNAIL

In quantum devices based on superconductors, Josephson junctions provide a nonlinear interaction between electromagnetic modes that is purely dispersive. Specifically, the Josephson potential reads

$$U_{JJ}(\varphi) = -E_J \cos(\varphi) \tag{2.1}$$

where φ is the superconducting phase difference across the junction, and E_J is the Josephson tunnelling energy. However, because this potential is an even function of the superconducting phase difference φ, this potential's nonlinearity is, to lowest order, of the form φ^4. This sources the so-called Kerr nonlinearity that is useful for engineering interactions between modes. It also imparts undesired frequency shifts, which become problematic as the number of interacting modes, and thus frequency crowding, increases. An alternative strategy is to use a minimal φ^3 nonlinearity for engineering the same useful interactions via 3-wave mixing, while suppressing the unwanted Kerr-induced frequency shifts.

A form of φ^3 nonlinearity has been realized with a ring of four Josephson junctions threaded by a DC magnetic flux called the Josephson ring modulator (JRM) [Bergeal et al. 2010a; Bergeal et al. 2010b]. However, the JRM is a quadrupole element—it imposes a current and phase relation between four nodes of a circuit. Would it be possible to engineer

a third-order φ^3 nonlinearity in a dipole device similar to a Josephson junction?

We answer affirmatively with the circuit in Fig. 2.1(a). Because this dispersive dipole element is asymmetric under the transformation of $\varphi \to -\varphi$, in contrast with the SQUID [Zimmerman and Silver 1966; Clarke and Braginski 2004] and the SLUG [Clarke 1966; Hover et al. 2012], we named it the Superconducting Nonlinear Asymmetric Inductive eLement (SNAIL) [Frattini et al. 2017; Zorin 2016].

The SNAIL consists of a superconducting loop of n large Josephson junctions and a single smaller junction (tunneling energies E_J and αE_J respectively), which we thread with a DC magnetic flux Φ. With a few caveats to be discussed shortly, it has the inductive energy:

$$U_S(\varphi_s) = -\alpha E_J \cos\left(\varphi_s\right) - nE_J \cos\left(\frac{\varphi_{\text{ext}} - \varphi_s}{n}\right) \tag{2.2}$$

where φ_s is the superconducting phase across the small junction, $\varphi_{\text{ext}} = 2\pi\Phi/\Phi_0$ is the reduced applied magnetic flux, and $\Phi_0 = h/2e$ is the magnetic flux quantum. The SNAIL also has a current-phase relation

$$\begin{aligned} I_S(\varphi_s) &= \frac{1}{\varphi_0} \frac{\partial U_S}{\partial \varphi_s} \\ &= \frac{E_J}{\varphi_0}\left[\alpha \sin\left(\varphi_s\right) + \sin\left(\frac{\varphi_s - \varphi_{\text{ext}}}{n}\right)\right] \end{aligned} \tag{2.3}$$

where $\varphi_0 = \Phi_0/2\pi = \hbar/2e$ is the reduced flux quantum.

With $\alpha \sim 0.8$ and $\Phi/\Phi_0 \sim 0.5$, this circuit is well known as the flux qubit [Mooij et al. 1999; Wal et al. 2000], which has a double-well potential. Here, we focus on a different parameter regime to create a potential with a single minimum, similar to the capacitively shunted flux qubit [You et al. 2007]. Moreover, we can adjust the potential to cancel the forth-order term while keeping a substantial cubic term for a particular choice of α and Φ. Such a parameter regime that achieves an asymmetric potential was previously proposed [Zapata et al. 1996] and realized [Sterck, Kleiner, and Koelle 2005] in the resistively shunted regime under the name "SQUID ratchet" intended for voltage rectification.

Returning to the validity of the potential, under what conditions does the arrangement of Josephson junctions in Fig. 2.1a act as an effective inductive element described by Eq. 2.2? First, we require the phase slip rate in the array to be sufficiently slower than the inverse of the timescales of any experiment so that phase slip dynamics can be ignored. Since the phase slip rate is proportional to $\exp(-\sqrt{E_J/E_{C_J}})$ where $E_{C_J} = e^2/2C_J$ is the Coulomb charging energy with the junction capacitance C_J [Matveev, Larkin, and Glazman 2002], we fabricate junctions with $E_J \gg E_{C_J}$. Additionally, note that Eq. 2.2 is only a function of a single degree of freedom φ despite being an $n+1$ junction circuit with only 1 loop constraint that includes an externally threaded flux Φ. This reduction is valid when the dynamics in which we are interested occur at sufficiently lower frequencies than the
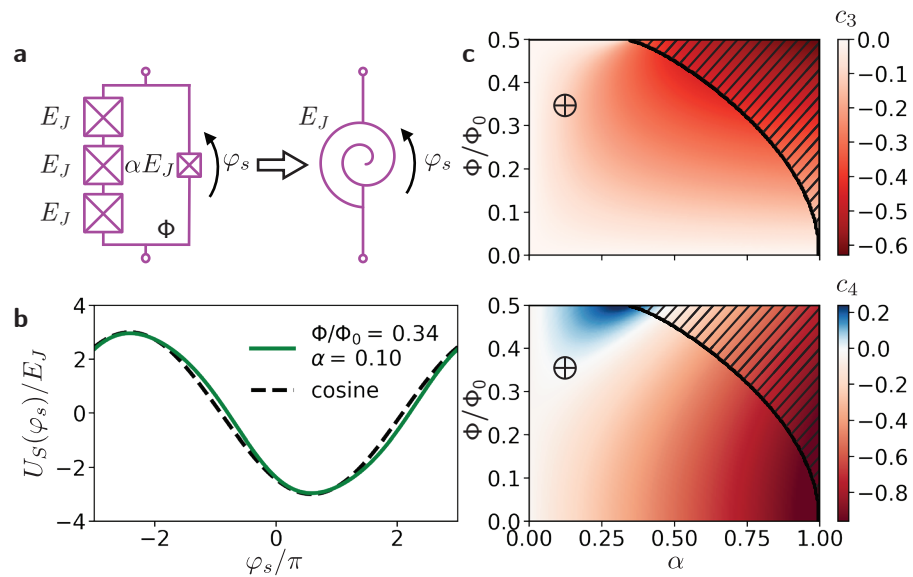
Figure 2.1 | (a) Circuit for a Superconducting Nonlinear Asymmetric Inductive eLement (SNAIL) reduced to one degree of freedom φ_s. The loop of $n = 3$ large junctions and one smaller junction (tunneling energies E_J and αE_J respectively) is threaded with an external DC magnetic flux Φ. (b) An example SNAIL potential (green) for $\alpha = 0.10$ and $\Phi/\Phi_0 = 0.34$ showcases an asymmetry about the minimum when compared to a scaled and shifted cosine (black). (c) Colormaps of the (α, Φ) parameter space for the third-order c_3 (top) and fourth-order c_4 (bottom) nonlinear potential terms. The black-hatched regions correspond to double-well potentials similar to the flux qubit that should be avoided when optimizing for a 3-wave mixing inductive dipole element. The crosses mark the set of parameters chosen for (b).

junction plasma frequency $\Omega_J = \sqrt{8E_J E_{C_J}}/\hbar$ such that these fast degrees of freedom can be integrated out. The simplest form of integration, replacing the canonical phase with its mean value as used to generate Eq. 2.2, is also only valid in the $E_J \gg E_{C_J}$ limit where phase fluctuations are small. We will examine this mode elimination procedure in more detail later in Section 2.4 in the context of predicting Kerr nonlinearity. Finally, any physical implementation of a SNAIL will have disorder in the large array junctions, parasitic inductance in the leads connecting the junctions, and parasitic capacitance to ground for each island (none drawn in Fig. 2.1a). Disorder of array junction inductance and lead inductance both induce perturbative corrections to Eq. 2.2 insofar as they are small compared to L_J. As for parasitic capacitance C_0 to ground of each island between junctions, as long as $C_0 \ll C_J/n^2$, the array of junctions will act as an effective inductive element passing a common RF current through each junction [Manucharyan 2012]. This current conservation justifies the $(\varphi_{\text{ext}} - \varphi_s)/n$ argument to each cosine for an array junction. For the remainder of this thesis, we will assume that all of the preceding conditions are realized by fabricating SNAILs in a process with $\Omega_J/2\pi \in [20, 45]$ GHz and sufficiently large junctions with $E_J \gg E_C$ and minimal parasitic inductance and capacitance.

With that admittedly extended list of conditions out of the way, we analyze the SNAIL's mixing capabilities by Taylor expanding about one of its equivalent minima φ_{min}. We denote the expansion coefficients $c_k = (1/E_J)(d^k U_S/d\varphi_s^k)|_{\varphi_s = \varphi_{s,\text{min}}}$ where $\varphi_{s,\text{min}}$ is numerically determined from the condition

$$c_1 = \alpha \sin(\varphi_{s,\text{min}}) + \sin\left(\frac{\varphi_{s,\text{min}} - \varphi_{\text{ext}}}{n}\right) = 0. \tag{2.4}$$

This condition is equivalent to insisting that $I_S(\varphi_{s,\text{min}}) = 0$; there is no DC current flowing across the entire dipole, only circulating current within it in response to the applied flux (i.e. $\sin(\varphi_{s,\text{min}}) \neq 0$ for all Φ). The result is an effective potential for $\tilde{\varphi}_s = \varphi_s - \varphi_{s,\text{min}}$:

$$U_{S,\text{eff}}(\tilde{\varphi}_s)/E_J = \frac{c_2}{2!}\tilde{\varphi}_s^2 + \frac{c_3}{3!}\tilde{\varphi}_s^3 + \frac{c_4}{4!}\tilde{\varphi}_s^4 + \cdots \tag{2.5}$$

that ceases to be $2\pi n$-periodic for any finite truncation of the series. The coefficients c_k, whose specific values depend n, α, and Φ, maintain the periodicity in external flux $c_k(\Phi) = c_k(\Phi + \Phi_0)$ as well as the symmetry $c_k(\Phi) = (-1)^k c_k(-\Phi)$.

The desire for a 3-wave mixing dipole element now translates to the requirement of nonzero c_3. Note that the case of $n = 1$, corresponding to an asymmetric DC-SQUID, always gives $c_3 = 0$ (in fact $c_k = 0$ for all odd $k > 2$) since the potential about φ_{min} is always a pure cosine ($\propto \cos(\tilde{\varphi})$) irrespective of the values of α and Φ [Vool and Devoret 2017]. Interestingly, α and Φ are not enough to break the $\tilde{\varphi}_s \to -\tilde{\varphi}_s$ symmetry in this case. Additionally, in the limit $n \gg 1$, the array behaves as a linear inductance and the potential approaches that of the fluxonium qubit/RF-SQUID [Manucharyan et al. 2009; Masluk 2012]. Replacing the array with a geometric inductance in an RF-SQUID configuration also

achieves the desired nonlinearity [Zorin 2016]. Experimentally, we choose the smallest $n \geq 2$ that is easy to fabricate, which is $n = 3$ for our fabrication processes. We specialize all further analysis in this thesis to the case $n = 3$ as depicted in Fig. 2.1a, but the results are easily extendable to different values of n.

Given $n = 3$, we are free to optimize the parameter space of (α, Φ). The top and bottom panels of Fig. 2.1c show c_3 and c_4 respectively as a function of the (α, Φ) parameter space. Focusing on the top, we want to maximize c_3 while avoiding any parameter space where the potential has multiple minima, marked by the black-hatched region, as this could cause hysteresis when sweeping Φ. This is achieved by restricting ourselves to $\alpha \leq 1/n$. When phrased in terms of inductances, this condition is identical to the standard condition to avoid hysteresis in RF-SQUIDs: the small junction inductance L_J/α must be larger than the rest of the total loop inductance, here nL_J from the array [Clarke and Braginski 2004].

In the bottom panel, we see that c_4 changes sign as a function of Φ from $c_4(\Phi = 0) < 0$ to $c_4(\Phi/\Phi_0 = 0.5) > 0$. This c_4 sign change enables the cancellation of Kerr nonlinearity in devices that contain SNAILs, as we shall examine in detail for self-Kerr nonlinearity in Section 2.2. To have robust experimental access to such Kerr-free bias points, it is convenient to choose $\alpha = 1/n^2$ so that the Φ at which $c_4 = 0$ is furtherest from $\Phi/\Phi_0 = 0.5$. As an example $U_S(\varphi_S)$ in this parameter regime, Fig. 2.1b depicts one period of the potential where the asymmetry about $\varphi_{s,\text{min}}$ is clearly visible when compared to a shifted cosine.

In these parameter regimes, SNAILs may be added to superconducting circuits wherever the circuit designer desires $\tilde{\varphi}_s^3$ and/or $\tilde{\varphi}_s^4$ nonlinearity. So long as there is no DC current bias across the SNAIL (including via another flux-biased DC-connected superconducting loop) in which case $\varphi_{s,\text{min}}$ would need to be recalculated, the internal dynamics of the SNAIL may be abstracted away leaving an effective dipole element. This continues the longstanding trend in superconducting circuits of distilling complex microscopic phenomena down to their electromagnetic responses. The microscopic dynamics of Andreev reflection can often be summarized by the Josephson relations for standard Josephson tunnel junctions; the SNAIL (like the SQUID before it) takes this abstraction one step further for a combination of junctions. The primary result is one of ease and intuition in designing more complex circuits for different applications: breaking selection rules in artificial atoms [Vool et al. 2018], engineering clean mixing processes for parametric amplification [Frattini et al. 2017; Frattini et al. 2018; Sivak et al. 2019; Sivak et al. 2020], or protecting quantum information from common sources of decoherence [Grimm et al. 2020].

2.2 The simplest case: 1 nonlinear mode

Given that the SNAIL can be treated as an effective inductive dipole element, we may ask how the electromagnetic environment in which SNAILs are embedded results in electromagnetic degrees of freedom with nonlinearity. In this section, we take a richly parameter-

ized circuit model with a single degree of freedom involving several SNAILs and derive its Hamiltonian in the absence of dissipation and incident microwave radiation. This circuit models well the lowest frequency degree of freedom in both the amplifier [Frattini et al. 2018; Sivak et al. 2019] and qubit [Grimm et al. 2020] experiments discussed in this thesis. The explicit analytic dependence of the Hamiltonian on circuit parameters will inform design decisions. Moreover, we shall see in Section 2.4 how higher frequency degrees of freedom can be eliminated in more complicated circuits to reveal a single low-frequency degree of freedom well-modelled by this same circuit.

2.2.1 Reducing the Lagrangian to one coordinate

Depicted in Fig. 2.2a, the circuit consists of a series array of M SNAILs in series with an ideal inductor with inductance L, and an ideal capacitor with capacitance C. The goal of this section is to derive the Lagrangian for this single degree of freedom circuit. We assume identical SNAILs each with $n = 3$ large junctions (each of inductance L_J), a single small junction (inductance L_J/α), and a DC flux bias Φ. As we saw, the set of flux-dependent coefficients $c_k = c_k(\Phi)$ along with L_J completely characterize each SNAIL. For instance, linear inductance of each SNAIL is $L_s(\Phi) = L_J/c_2(\Phi)$.

Following standard definitions and procedures [Vool and Devoret 2017], we begin by defining the generalized branch phase[1] across each element: φ_C for the capacitor, φ_L for the inductor, and $\varphi_{s,m}$ for the small junction of SNAIL m (where m ranges from 1 to M). With foresight, we define another phase

$$\varphi = \varphi_L + \sum_{m=1}^{M} \varphi_{s,m} \tag{2.6}$$

that represents the total phase across the inductive portion of the circuit defined through the small junction of each SNAIL. We emphasize that this choice is one of convenience for the form of future equations, but it has the eventual virtue of leaving the kinetic energy quadratic and relegating all nonlinearity to the potential energy.

Furthermore, we invoke Kirchhoff's voltage law around the loop, which constrains

$$\dot{\varphi}_C = \dot{\varphi}_L + \sum_{m=1}^{M} \dot{\varphi}_{s,m}$$
$$= \dot{\varphi} \tag{2.7}$$

with the overdot denoting total time derivative. Note that the integral of this constraint still has the freedom of an offset constant that we will use to insist that there is no DC current flowing through the capacitor.

---

[1]Recall the branch phase is the branch flux rescaled by $\varphi_0 = \hbar/2e$, which itself is the time integral of the voltage across a branch.

With these definitions, we write the Lagrangian of this system with $M + 1$ generalized coordinates

$$\mathcal{L}_{M+1} = \frac{C\varphi_0^2}{2}\dot{\varphi}^2 - U_{M+1}(\varphi, \varphi_{s,1}, \cdots, \varphi_{s,M}) \qquad (2.8)$$

$$U_{M+1}(\varphi, \varphi_{s,1}, \cdots, \varphi_{s,M}) = \frac{1}{2}E_L\left(\varphi - \sum_{m=1}^{M}\varphi_{s,m}\right)^2 + \sum_{m=1}^{M}U_S(\varphi_{s,m}) \qquad (2.9)$$

where $E_L = \varphi_0^2/L$, and $\varphi_{s,m}$ and φ are now generalized coordinates as defined above.

The kinetic energy of $\mathcal{L}_{M+1}$ only depends on a single generalized coordinate through $\dot{\varphi}$. Note, this is simply a fact in this lumped-element model; we *choose* not to draw capacitors across each SNAIL and promise only to consider dynamics at frequencies low enough for this lumped-element approximation to hold (see Section 2.4 for more detail on the validity of excluding these capacitors). We clearly have more generalized coordinates than the one φ that we need and we must choose constraints to eliminate the other M. Luckily, there are M Euler-Lagrange equations of motion that do *not* depend on $\dot{\varphi}$, specifically

$$0 = -\frac{\partial\mathcal{L}_{M+1}}{\partial\varphi_{s,m}} \qquad (2.10)$$

$$= \frac{\partial U_{M+1}}{\partial\varphi_{s,m}}$$

$$= -E_L\left(\varphi - \sum_{m=1}^{M}\varphi_{s,m}\right) + \frac{dU_S}{d\varphi_{s,m}}$$

and may therefore easily enforce those constraints. A particularly convenient way to proceed is the difference between equation m and $m + 1$ to recover

$$\frac{dU_S}{d\varphi_{s,m}} = \frac{dU_S}{d\varphi_{s,m+1}}, \qquad (2.11)$$

which is precisely current conservation

$$I_S(\varphi_{s,m}) = I_S(\varphi_{s,m+1}) \qquad (2.12)$$

at each node in between SNAILs. We have in essence derived Kirchhoff's current law from the Euler-Lagrange equations, ensuring there are no corrections due the presence of non-linearity.

Solving Eq. 2.12 enforces $\varphi_{s,m} = \varphi_{s,m+1}$ since we assumed identical SNAILs with identical current-phase relations. Note perturbative disorder in SNAIL parameters would perturbatively change this statement. With this reduction, we are left with the reduced La-
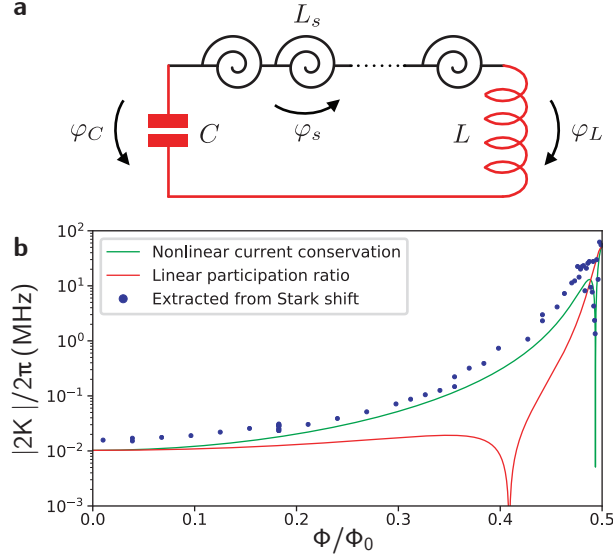
Figure 2.2 | (a) A single degree of freedom, lumped element circuit model for a series array of M identical SNAILs–each with a phase drop φ_s across its small junction, a DC-flux bias Φ, and an effective inductance at this flux bias L_s–in series with an ideal inductor (inductance L, phase drop φ_L) and a capacitor (capacitance C, phase drop φ_C). (b) Magnitude of self-Kerr or anharmonicity $2K$ measured via Stark shift on a low participation ratio p device with $M = 1$ SNAIL (device A from Table 3.1), together with theoretical predictions: green includes current conservation Eq. 2.16 to renormalize the potential, red is the purely participation ratio-based approach in which $K \propto c_4$.

grangian

$$\mathcal{L}_2 = \frac{C\varphi_0^2}{2}\dot{\varphi}^2 - U_2(\varphi, \varphi_s) \tag{2.13}$$

$$U_2(\varphi, \varphi_s) = \frac{1}{2}E_L\left(\varphi - M\varphi_s\right)^2 + MU_S(\varphi_s) \tag{2.14}$$

where $\varphi_s = \varphi_{s,m}$ to drop the subscript since all m are equivalent. At this point, the *entire* array of SNAILs is treated as an effective dipole element in its own right with total potential energy $MU_S(\varphi_s)$ and total phase drop across it[2] of $M\varphi_s$.

We still however have not finished; φ_s is not an independent variable, as it does not have its own kinetic energy. Therefore, prior to quantization, we follow the same procedure to enforce the current conservation between the SNAIL array and the inductor: minimize the

---

[2]The path for this total phase drop of $M\varphi_s$ is defined through each of the small junctions.

potential $U_2(\varphi, \varphi_s)$ as a function of φ_s. The resulting equation

$$0 = \frac{\partial U_2}{\partial \varphi_s}$$

$$= M E_L (M\varphi_s - \varphi) + M \frac{dU_S}{d\varphi_s} \tag{2.15}$$

$$0 = x_J (M\varphi_s - \varphi) + \alpha \sin(\varphi_s) + \sin\left(\frac{\varphi_s - \varphi_{\text{ext}}}{n}\right) \tag{2.16}$$

implicitly determines the SNAIL phase $\varphi_s[\varphi]$ as a function of the mode generalized coordinate φ, where in the last line we have rescaled introducing junction-to-linear inductance ratio $x_J = L_J/L = E_L/E_J$ and used Eq. 2.2.

The Lagrangian can now be written in terms of a single degree of freedom φ

$$\mathcal{L}_1 = \frac{C\varphi_0^2}{2}\dot\varphi^2 - U_1(\varphi) \tag{2.17}$$

$$U_1(\varphi) = \frac{1}{2}E_L \left(\varphi - M\varphi_s[\varphi]\right)^2 + MU_S(\varphi_s[\varphi]) \tag{2.18}$$

where again the function $\varphi_s[\varphi]$ is determined from Eq. 2.16. Note that this potential now treats the *entire* SNAIL array *and* the linear inductor together as a single effective dipole element. Although Eq. 2.16 originates from the *linear* current conservation of Kirchhoff's current law, it results in a manifestly *nonlinear* constraint equation in terms of phases; $\varphi_s[\varphi]$ is clearly nonlinear. Thus, the potential energy of the nominally linear inductor will actually contribute to the *nonlinearity* of $U_1(\varphi)$ as we shall now explore in detail.

2.2.2 Taylor expanding the potential

To elucidate our new effective dipole element's mixing capabilities, in the regime of small phase fluctuations we can again Taylor expand the renormalized potential $U_1(\varphi)$ about its minimum $\bar\varphi_{\text{min}}$, resulting in the coefficients $\tilde{c}_k = (1/E_J)(d^k U_1/d\varphi^k)|_{\varphi=\bar\varphi_{\text{min}}}$, where $\bar\varphi_{\text{min}}$ is determined from the condition $\tilde{c}_1 = 0$. Using current conservation Eq. 2.16 to simplify $\tilde{c}_1$,

we can write the first six Taylor coefficients as

$$\tilde{c}_1 = x_J \left(\bar{\varphi}_{\min} - M \varphi_s[\bar{\varphi}_{\min}] \right) \tag{2.19}$$

$$\tilde{c}_2 = x_J \left(1 - M \frac{d\varphi_s}{d\varphi}[\bar{\varphi}_{\min}] \right) \tag{2.20}$$

$$\tilde{c}_3 = -M x_J \frac{d^2\varphi_s}{d\varphi^2}[\bar{\varphi}_{\min}] \tag{2.21}$$

$$\tilde{c}_4 = -M x_J \frac{d^3\varphi_s}{d\varphi^3}[\bar{\varphi}_{\min}] \tag{2.22}$$

$$\tilde{c}_5 = -M x_J \frac{d^4\varphi_s}{d\varphi^4}[\bar{\varphi}_{\min}] \tag{2.23}$$

$$\tilde{c}_6 = -M x_J \frac{d^5\varphi_s}{d\varphi^5}[\bar{\varphi}_{\min}] \tag{2.24}$$

The derivatives of the implicit function $\varphi_s[\varphi]$ can be found by differentiating Eq. 2.16 from current conservation. For example,

$$\frac{d\varphi_s}{d\varphi} = \left(M + \frac{1}{E_L} \frac{d^2 U_S}{d\varphi_s^2} \right)^{-1} \tag{2.25}$$

$$= \frac{x_J}{\alpha \cos(\varphi_s) + (1/n) \cos[(\varphi_s - \varphi_{\text{ext}})/n] + M x_J}$$

$$\frac{d^2\varphi_s}{d\varphi^2} = \frac{-1}{E_L} \frac{d^3 U_S}{d\varphi_s^3} \left(\frac{d\varphi_s}{d\varphi} \right)^3 \tag{2.26}$$

$$\frac{d^3\varphi_s}{d\varphi^3} = \frac{-1}{E_L} \left[\frac{d^4 U_S}{d\varphi_s^4} \left(\frac{d\varphi_s}{d\varphi} \right)^4 - \frac{3}{E_L} \left(\frac{d^3 U_S}{d\varphi_s^3} \right)^2 \left(\frac{d\varphi_s}{d\varphi} \right)^5 \right] \tag{2.27}$$

Additionally, we can show from the current conservation Eq. 2.16 that the presence of the series linear inductor does not change the location of each SNAIL's potential minimum. Mathematically, this means $\varphi_s[\bar{\varphi}_{\min}] = \varphi_{s,\min}$ (defined Eq. 2.4) and solving $\tilde{c}_1 = 0$ we find $\bar{\varphi}_{\min} = M \varphi_{s,\min}$. Intuitively, the linear inductor is not a DC current source nor is it part of a DC-connected superconducting loop, so the solution to zero the current through each SNAIL $I_S(\varphi_{s,\min}) = 0$ is undisturbed by addition of the linear inductor in series. Therefore, we can express the Taylor coefficients $\tilde{c}_k$ for the renormalized potential $U_1(\varphi)$ in terms of

the bare c_k introduced earlier a single SNAIL potential $U_S(\varphi_s)$ (see Eqs. 2.2 and 2.5):

$$\tilde{c}_2 = \frac{p}{M} c_2 \tag{2.28}$$

$$\tilde{c}_3 = \frac{p^3}{M^2} c_3 \tag{2.29}$$

$$\tilde{c}_4 = \frac{p^4}{M^3} \left[c_4 - \frac{3c_3^2}{c_2 + Mx_J} \right]$$

$$= \frac{p^4}{M^3} \left[c_4 - \frac{3c_3^2}{c_2}(1-p) \right] \tag{2.30}$$

$$\tilde{c}_5 = \frac{p^5}{M^4} \left[c_5 - \frac{10c_4c_3}{c_2}(1-p) + \frac{15c_3^3}{c_2^2}(1-p)^2 \right] \tag{2.31}$$

$$\tilde{c}_6 = \frac{p^6}{M^5} \left[c_6 - \frac{10c_4^2 + 15c_5c_3}{c_2}(1-p) + \frac{105c_4c_3^2}{c_2^2}(1-p)^2 - \frac{105c_3^4}{c_2^3}(1-p)^3 \right] \tag{2.32}$$

where we have defined the SNAIL array's inductive participation ratio:

$$p = \frac{ML_s}{L + ML_s} = \frac{Mx_J}{c_2 + Mx_J} \tag{2.33}$$

which is inherently flux-dependent since $c_2 = c_2(\Phi)$ or equivalently $L_s = L_s(\Phi) = L_J/c_2$.

Note that $1 - p = L/(L + ML_s)$ is the proportion of the total inductance that comes from the *linear* inductor, and we have made no assumptions on its magnitude. Similarly, all SNAIL coefficients $|c_k/c_2| \sim \mathcal{O}(1)$ (except for interference effects at special values of applied flux Φ). Thus, all terms in the above $\tilde{c}_k$ coefficients are equally important; none are *a priori* small compared to others.

To insist on the importance of this, consider the case of a single Josephson junction with a linear inductance in series. For our parameters, this implies setting $M = 1$ and $(c_2, c_3, c_4, c_5, c_6, \cdots) = (1, 0, -1, 0, 1, \cdots)$ in accordance with $-E_J \cos(\varphi_s)$ potential. The renormalized coefficients for $U_1(\varphi)$ in this case would be

$$\tilde{c}_2 = p \tag{2.34}$$

$$\tilde{c}_3 = 0$$

$$\tilde{c}_4 = -p^4$$

$$\tilde{c}_5 = 0$$

$$\tilde{c}_6 = p^6 \left[1 - 10(1-p) \right]$$

implying that if $p < 0.9$ then the sixth order term has the *opposite sign* from what is naïvely expected from the cosine expansion. As such, when examining a device's nonlinearity, it is important to consider the renormalization of the potential due to the presence of a linear

inductance in series with Josephson mixing elements.

2.2.3 Quantization

Now that we understand the structure of our potential and its nonlinearity, we perform a Legendre transformation on $\mathcal{L}_1$ and canonically quantize to get the Hamiltonian

$$\mathcal{H}_1 = 4E_C \boldsymbol{N}^2 + U_1(\boldsymbol{\varphi}) \tag{2.35}$$

$$U_1(\boldsymbol{\varphi}) = \frac{1}{2}E_L \left(\boldsymbol{\varphi} - M\varphi_s[\boldsymbol{\varphi}]\right)^2 + MU_S(\varphi_s[\boldsymbol{\varphi}]) \tag{2.36}$$

where Eq. 2.16 defines $\varphi_s[\varphi]$, $E_C = e^2/2C$ is the charging energy, $\boldsymbol{N}$ is the conjugate momentum of position-like variable φ and counts the charge (in units of Cooper pairs $2e$) across the capacitance[3]. The phase φ and Cooper pair number $\boldsymbol{N}$ are equivalently conjugate in the quantum sense:

$$[\boldsymbol{\varphi}, \boldsymbol{N}] = i. \tag{2.37}$$

Note we have ignored and will continue to ignore the effects of offset charges throughout this thesis, but some comments are warranted. The potential $U_1(\varphi)$ is *not* periodic so, within the standpoint that the periodicity of the potential restricts the eigenspectrum of φ and $\boldsymbol{N}$ [Devoret 2021], the eigenspectrum of $\boldsymbol{N}$ should be continuous. When $L = 0$ (a short replaces the inductor), the potential acquires the symmetry $U_1(\varphi) = U_1(\varphi + 2\pi nM)$ and thus an associated offset charge[4]. As such, this case is quite amenable to numerical diagonalization in the charge basis. As in the transmon qubit, which corresponds to $M = 1$ and $n = 1$, the eigenspectrum will become exponentially insensitive to offset charge in the $E_J/E_C \to \infty$ limit [Koch et al. 2007]. In the finite but vanishing limit of inductance $L \to 0$, although the potential is strictly not periodic, we expect the eigenspectrum and associated matrix elements to mimic the physics of the $L = 0$ case; this is the dual of a similar result for adding a large inductance $L \to \infty$ in parallel with a transmon qubit [Koch et al. 2009]. Finally, we could also consider the effect of offset charges on every island between junctions within each SNAIL and similarly on every island between SNAILs. Again, the effect of these offset charges is suppressed in arrays of junctions under the same $E_J \gg E_{C_J}$ condition ensuring a small phase-slip rate [Matveev, Larkin, and Glazman 2002]. We henceforth assume the above conditions are satisfied and ignore offset charges.

Expanding the above Hamiltonian Eq. 2.35 about $\bar{\varphi}_{\min}$, we find

$$\mathcal{H}_1 = 4E_C \boldsymbol{N}^2 + E_J \left(\frac{\tilde{c}_2}{2!}\tilde{\varphi}^2 + \frac{\tilde{c}_3}{3!}\tilde{\varphi}^3 + \frac{\tilde{c}_4}{4!}\tilde{\varphi}^4 + \cdots \right) \tag{2.38}$$

where $\tilde{\varphi} = \varphi - \bar{\varphi}_{\min}$ describes phase fluctuations about the potential minimum and still satisfies $[\tilde{\varphi}, \boldsymbol{N}] = i$. For more convenience, we introduce the standard bosonic creation and

---

[3]Explicitly, $\boldsymbol{N} = (1/\hbar)(\partial \mathcal{L}_1/\partial \dot{\varphi}) = (\hbar/8E_C)\dot{\varphi}$

[4]Following from $U_S(\varphi_s) = U_S(\varphi_S + 2\pi n)$ and that $\varphi_s[\varphi] = \varphi/M$ when $L = 0$.

annihilation operators $a^\dagger$ and a with commutation relation $\left[a, a^\dagger\right] = 1$ that diagonalize the quadratic part of the Hamiltonian in the excitation number basis. They relate to the canonical phase via $\tilde{\varphi} = \varphi_{\mathrm{zpf}}(a + a^\dagger)$, where the zero-point fluctuations of the phase is

$$\varphi_{\mathrm{zpf}} = \left(\frac{2E_C}{\tilde{c}_2 E_J}\right)^{1/4}$$

$$= \left(\frac{1}{8(\hbar/4e^2)^2}\frac{L + ML_s}{C}\right)^{1/4} \tag{2.39}$$

and $\tilde{c}_2 = pc_2/M$ as in Eq. 2.28. The canonical momentum $N = iN_{\mathrm{zpf}}(a^\dagger - a)$ has zero-point fluctuations $N_{\mathrm{zpf}} = 1/2\varphi_{\mathrm{zpf}}$.

With these definitions, the Hamiltonian after this second quantization can be written

$$\boxed{\mathcal{H}_1/\hbar = \omega_a a^\dagger a + g_3(a + a^\dagger)^3 + g_4(a + a^\dagger)^4 + \cdots} \tag{2.40}$$

where the oscillator's frequency is

$$\omega_a = \frac{1}{\hbar}\sqrt{8\tilde{c}_2 E_J E_C} = \frac{1}{\sqrt{C(L + ML_s)}} \tag{2.41}$$

and the nonlinear parameters are

$$\hbar g_k = \frac{\tilde{c}_k}{k!}E_J\left(\varphi_{\mathrm{zpf}}\right)^k \tag{2.42}$$

that set the mixing capabilities of this degree of freedom. This Hamiltonian and the dependence of its parameters on physical device characteristics are the central result of this section. It distills the dynamics down to a few parameters and serves as the starting point for the application of microwave radiation for three-wave mixing applications, specifically for parametric amplification in Chapter 3 and the stabilization of quantum information in Chapters 4–6.

Examining the nonlinearities more closely, since a device's frequency ω_a is often a convenient design parameter, we rewrite Eq. 2.39

$$\varphi_{\mathrm{zpf}} = \sqrt{\frac{4E_C}{\hbar\omega_a}}$$

$$= \sqrt{\frac{\hbar\omega_a}{2\tilde{c}_2 E_J}} \tag{2.43}$$

using Eq. 2.41 to eliminate the dependence on the inductive or capacitive energies respec-

tively. Rewriting the nonlinearity in turn as

$$\hbar g_k = \frac{1}{k!} \frac{\tilde{c}_k}{\tilde{c}_2} \frac{\hbar \omega_a}{2} \left(\varphi_{\text{zpf}} \right)^{k-2} \tag{2.44}$$

$$= \frac{1}{k!} \frac{\tilde{c}_k}{\tilde{c}_2} \frac{\hbar \omega_a}{2} \left(\frac{4E_C}{\hbar \omega_a} \right)^{k/2-1}$$

we have an intuitive expression with which to work for the purpose of designing nonlinearity. For a given mode frequency and designed capacitance, together implying a fixed total inductance $ML_s + L$ of our effective SNAILs-and-linear inductive mixing element, the coefficients $\tilde{c}_k / \tilde{c}_2 \propto p^{k-1} / M^{k-2}$ scale the strength of all the nonlinearities g_k. Specifically for future comparison, we write the third-

$$\boxed{\hbar g_3 = \frac{1}{6} \frac{p^2}{M} \frac{c_3}{c_2} \sqrt{E_C \hbar \omega_a}} \tag{2.45}$$

and fourth-order nonlinearities

$$\boxed{\hbar g_4 = \frac{1}{12} \frac{p^3}{M^2} \left[c_4 - \frac{3c_3^2}{c_2} (1-p) \right] \frac{1}{c_2} E_C} \tag{2.46}$$

using Eqs. 2.29- 2.30 to write in terms of single-SNAIL coefficients c_2, c_3, and c_4.

To explicitly reveal the perturbative structure, we pull out this p and M dependence of $\tilde{c}_k$ to find

$$\hbar g_k = \frac{p}{k!} \left(\frac{\tilde{c}_k}{\tilde{c}_2} \frac{M^{k-2}}{p^{k-1}} \right) \frac{\hbar \omega_a}{2} \left(\frac{p}{M} \varphi_{\text{zpf}} \right)^{k-2} \tag{2.47}$$

$$\propto \frac{p}{k!} \left(\mathcal{O}(c_k / c_2) \right) \frac{\hbar \omega_a}{2} \left(\frac{p}{M} \varphi_{\text{zpf}} \right)^{k-2}$$

where in the last line we use $\mathcal{O}(c_k / c_2)$ to indicate the $\mathcal{O}(1)$ combination of single-SNAIL parameters $c_{j \leq k}$ and powers of $1 - p$ as visible in the square brackets of Eqs. 2.28- 2.32. This rewriting makes evident that, as long as $p\varphi_{\text{zpf}} / M << 1$, we can hope to truncate the series expansion and still model the relevant dynamics.

Any truncation however will always break down at a critical number of photons n_{crit} within the mode, which we crudely estimate by comparing successive terms from Eq. 2.40 while making the substitution a, $a^\dagger \rightarrow \sqrt{n_{\text{crit}}}$. Comparing the fourth and sixth order terms,

we calculate

$$n_{\text{crit}} = 15 \left(\frac{\tilde{c}_4}{\tilde{c}_6} \frac{p^2}{M^2} \right) \frac{M^2}{p^2} \frac{1}{\varphi_{\text{zpf}}^2} \tag{2.48}$$

$$\propto 15 \left(\mathcal{O}(c_4/c_6) \right) \frac{M^2}{p^2} \frac{1}{\varphi_{\text{zpf}}^2}$$

where we have again an $\mathcal{O}(1)$ prefactor. Similar results with larger prefactors are obtained for comparing higher order terms; a π^2 prefactor is obtained when asking how many photons puts π phase across a single SNAIL. Although crude, n_{crit} shows that the range of validity of a truncated Hamiltonian Eq. 2.40 is inextricably linked to our small parameter $p\varphi_{\text{zpf}}/M$.

Given the hierarchy of parameters $g_k \ll \omega_a$, we perform perturbation theory in the small parameter $p\varphi_{\text{zpf}}/M$ and organize the results for the eigenstates and eigenenergies as an effective Hamiltonian

$$\mathcal{H}_{1,\text{eff}}/\hbar = (\omega_a + \Delta_a)\boldsymbol{a}^\dagger\boldsymbol{a} + K\boldsymbol{a}^{\dagger 2}\boldsymbol{a}^2 + K'\boldsymbol{a}^{\dagger 3}\boldsymbol{a}^3 + \cdots \tag{2.49}$$

with the first three parameters

$$\Delta_a = 12g_4 - \frac{60g_3^2}{\omega_a} + \left[90g_6 - \frac{1100g_3g_5}{\omega_a} - \frac{288g_4^2}{\omega_a} + \frac{6768g_3^2g_4}{\omega_a^2} - \frac{10320g_3^4}{\omega_a^3} \right] \tag{2.50}$$

$$K = 6g_4 - \frac{30g_3^2}{\omega_a} + \left[90g_6 - \frac{1260g_3g_5}{\omega_a} - \frac{306g_4^2}{\omega_a} + \frac{8100g_3^2g_4}{\omega_a^2} - \frac{12690g_3^4}{\omega_a^3} \right] \tag{2.51}$$

$$K' = 20g_6 - \frac{280g_3g_5}{\omega_a} - \frac{68g_4^2}{\omega_a} + \frac{1800g_3^2g_4}{\omega_a^2} - \frac{2820g_3^4}{\omega_a^3} \tag{2.52}$$

solved with corrections $\mathcal{O}(\omega_a(p\varphi_{\text{zpf}}/M)^6)$, whose eigenstates are Fock states satisfying $\boldsymbol{a}^\dagger\boldsymbol{a}\ket{n} = n\ket{n}$ just like a harmonic oscillator. Note the higher order corrections were programmatically generated and may be carried out to arbitrary order—even in the presence of strong microwave drives [Venkatraman et al. 2021]. The Lamb shift Δ_a is fundamentally quantum in nature, resulting from normal ordering higher order terms; classical perturbation theory, or even a finite-element electromagnetic solver, would always result in $\Delta_a = 0$.

The Kerr nonlinearity, often written in terms of the anharmonicity $= 2K$ of a weakly anharmonic oscillator like a transmon (anharmonicity $2\hbar K = -E_C$) [Koch et al. 2007], deserves special scrutiny. We first rewrite the leading order contribution

$$\boxed{2\hbar K = \frac{p^3}{M^2} \left[c_4 - \frac{3c_3^2}{c_2}(1-p) - \frac{5}{3}\frac{c_3^2}{c_2}p \right] \frac{1}{c_2}E_C + \mathcal{O}(\omega_a(p\varphi_{\text{zpf}}/M)^4)} \tag{2.53}$$

by substituting g_3 and g_4 with Eqs. 2.45–2.46. This represents the central result of this sec-

tion, and we will systematically compare this predication to multiple devices in Chapter 3. While the values themselves may be renormalized in the presence of strong microwave drives [Sivak et al. 2019; Venkatraman et al. 2021], the undriven—or at least weakly driven for measurement—values correspond well with the given expression.

We would like to stress that the calculation of the Kerr nonlinearity here differs significantly from previous calculations in three-wave-mixing amplifiers, such as JPCs [Schackert 2013; Flurin 2015; Liu et al. 2017]. Previous calculations considered first the linearized circuit, in which the total phase drop φ splits between the nonlinear circuit elements and the linear inductor in proportion to their respective participation ratios[5] p and $1 - p$. Then they assumed that the nonlinearity is diluted by the corresponding power of the participation ratio, in which case we would have $g_k \propto p^{k-1} c_k$. As we can see from Eqs. 2.45 and Eqs. 2.46 or even Eqs.2.29-2.32, this approach yields the correct values for the lowest order of cubic nonlinearity, but fails to predict higher-order nonlinearities, such as g_4 and therefore the anharmonicity $2K$ correctly.

This discrepancy arises because the linear participation ratio-based approach does not properly account for the linear current conservation, Eq. 2.16, between the SNAIL array and the inductor to the necessary order in φ. This effect leads to a renormalization of g_4 due to c_3 evident in Eq. 2.46. One can see that in the limit of small participation ratio $p \to 0$ the additional contribution is equal to $-3c_3^2/c_2$, which does not contain any small parameters relative to c_4. This significantly shifts the Kerr-free point in flux and modifies the whole Kerr nonlinearity profile. The comparison of data taken on a low-participation-ratio device[6] with predictions of both approaches is shown in Fig. 2.2b. At $\Phi/\Phi_0 = 0$ and $\Phi/\Phi_0 = 0.5$ where symmetry forbids odd order nonlinearity, the predictions agree; yet, at certain fluxes, the predictions different by several orders of magnitude.

Moreover, apart from this renormalization effect, there is a trivial second-order perturbation theory correction to energy levels due to the g_3 term in the Hamiltonian, which affects the anharmonicity $2K$ (see last term in Eq. 2.53). Note that both g_4 and this correction scale identically with E_C. This perturbative correction is insignificant in the limit of small participation ratio. On the other hand, in the limit $p \to 1$, the renormalization effect due to the linear inductance becomes irrelevant and the perturbative contribution becomes important instead.

In the case where symmetry forbids odd order terms, a similar story occurs; the leading order g_4 is correct, but the linear participation ratio method fails to predict the sixth order nonlinearity g_6 and therefore K' and corrections to K correctly. Specifically, consider a single DC-SQUID circuit with some linear inductance in series. In this case, $c_k = 0$ and

---

[5]Explicitly in our notation, the equivalent approximation would be assuming $\varphi_s[\varphi] = p\varphi/M$

[6]Specifically, device A from Table 3.1.

thus $g_k = 0$ for all odd k. The lowest even orders are:

$$\hbar g_4 = \frac{1}{12} \frac{p^3}{M^2} \frac{c_4}{c_2} E_C \tag{2.54}$$

$$\hbar g_6 = \frac{1}{30} \frac{p^5}{M^4} \left[c_6 - \frac{10 c_4^2}{c_2}(1-p) \right] \frac{1}{c_2} \left(\frac{E_C}{\hbar \omega_a} \right)^2 \tag{2.55}$$

leaving the leading contribution to the effective sixth order shift

$$\hbar K' = 20 \frac{p^5}{M^4} \left[c_6 - \frac{10 c_4^2}{c_2}(1-p) - \frac{17}{8} \frac{c_4^2}{c_2} p \right] \frac{1}{c_2} \left(\frac{E_C}{\hbar \omega_a} \right)^2 \tag{2.56}$$

$$= 20 \frac{p^5}{M^4} \left[1 - 10(1-p) - \frac{17}{8} p \right] \left(\frac{E_C}{\hbar \omega_a} \right)^2 \tag{2.57}$$

where in the last line we used $c_4/c_2 = -1$ and $c_6/c_2 = 1$ for a DC-SQUID with purely cosine potential. These expressions make clear that even in standard transmon circuits, not only is careful consideration of series linear inductance important, but that cascaded lower order processes (e. g. $\propto c_4^2/c_2$) often dominate the higher order nonlinearity. It is for this reason that controllable higher order processes in superconducting circuits have thusfar been realized in a Raman-assisted manner [Mundhada et al. 2017; Mundhada et al. 2019].

In summary of what we achieved this section, we derived the Hamiltonian Eq. 2.35 for a circuit containing an array of M SNAILs in series with an inductor and capacitor (Fig. 2.2). We expanded this Hamiltonian in terms of the small parameter $p\varphi_{\mathrm{zpf}}/M$ to find the Hamiltonian Eq. 2.40 of a weakly anharmonic oscillator with nonlinearities g_k (Eqs. 2.45- 2.46). These nonlinearities, as well as their effect on the oscillator's eigenenergies (parameterized by Δ_a, K, K'), depend to leading order on the coefficients of a renormalized potential Eqs. 2.28–2.32. This renormalization effect results from linear current conservation between the SNAIL array and the linear inductor Eq. 2.16 enforcing $\varphi_s[\varphi]$ to be a nonlinear function. Counterintuitively, the importance of this renormalization scales with the proportion of *linear* inductance $1-p$ in the system rendering it important for many superconducting devices, especially parametric amplifiers.

2.3 Arrays of SNAILs

Postponing further discussion of the renormalization of Kerr for Sec. 2.4, we first focus on the dependence of the effective Kerr nonlinearity (Eq. 2.53) on the number of SNAILs M arrayed in series. The inclusion of the number Josephson dipoles in series opens up regimes of Kerr nonlinearity that are otherwise impossible to achieve simply by scaling the critical current of a single junction. A primary example would be arrays of Josephson junctions to implement a superinductance [Masluk et al. 2012; Manucharyan 2012]. Also, as we
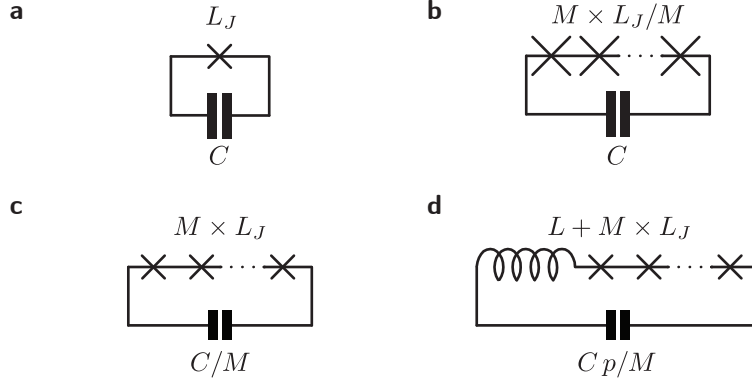
Figure 2.3 | Josephson junction circuits all with the the same operating frequency but with different Kerr nonlinearities. (a) A single junction with inductance L_J shunted by a capacitance C. (b) Arraying M junctions in series each with inductance L_J/M. (c) Arraying M junctions each with inductance L_J and shunting capacitance C/M adjusted to keep the operating frequency constant. (d) Arraying M junctions each with inductance L_J in series with geometric inductance L; shunting capacitance Cp/M where $p = ML_J/(L + ML_J)$ is the array's inductive participation ratio.

shall discuss in detail in Chapter 3, the Kerr nonlinearity often determines a parametric amplifier's power-handling performance. As such, arrays of Josephson junctions have been used since the early days of amplifiers [Castellanos-Beltran et al. 2008], suggested for the improvement of power handling [Eichler and Wallraff 2014], and then implemented for the same [Eichler et al. 2014; Frattini et al. 2018; Planat et al. 2019; Sivak et al. 2020]. Finally, the model of an array of Josephson junctions captures well the linear and nonlinearity characteristics of devices made from kinetic inductive materials like granular aluminum [Maleeva et al. 2018] or even the investigation of phase slips in a superconducting devices [Matveev, Larkin, and Glazman 2002; Pop et al. 2010].

To focus the discussion on a design perspective, consider the set of circuits in Fig. 2.3 corresponding to different design choices. The circuit parameters have been chosen to fix the operating frequency at $\omega_a = 1/\sqrt{CL_J}$, and different design choices will result in different nonlinearities. The single-junction circuit Fig. 2.3a has anharmonicity $2\hbar K = -E_C$, given by Eq. 2.53 with appropriate substitution of parameters[7]. The maximum number of allowed photons $n_{\rm crit} \propto 1/\varphi_{\rm zpf}^2 = \hbar\omega_a/E_C = 2E_J/\hbar\omega_a$, as per Eq. 2.48 scales with the critical current. In fact, the linear inductance, Kerr nonlinearity, and maximum photon number are all locked together in this circuit by the structure of the cosine potential; choosing the frequency therefore leaves only one parameter, say the junction critical current, to set all of the nonlinearity.

Introducing an array of Josephson junctions decouples the linear inductance from the nonlinearity. For the most efficient dilution of the nonlinearity, consider circuit Fig. 2.3b

---

[7]Concretely, $c_k = 0$ for odd k and $c_k = (-1)^{k/2+1}$ for even k; $p = 1$ and $M = 1$.

where we replace the junction with M junctions each with M times larger critical current (inductance L_J/M) [Eichler and Wallraff 2014]. In this case, the canonical mode phase splits equally among the junctions resulting, to leading order, in an anharmonicity

$$2\hbar K = -12\frac{ME_J}{4!}\sum_{m=1}^{M}\left(\frac{\varphi_{\mathrm{zpf}}}{M}\right)^4$$

$$= -\frac{1}{M^2}E_C. \tag{2.58}$$

Importantly, in this approach to arraying, the resonant frequency and the impedance both remain independent of M. The critical photon number $n_{\mathrm{crit}} \propto M^2/\varphi_{\mathrm{zpf}}^2$ matches the scaling of the M^2 reduction in Kerr, indicating all orders of nonlinearity are still locked together. While the dilution of nonlinearity in this case appears quite efficient $\propto 1/M^2$, in practice this approach quickly runs into fabrication limitations. For example, in a fabrication process with a fixed critical current density, reducing the junction inductance to L_J/M requires an M times larger area junction. The finite size of the junctions and the leads connecting them will contribute linear inductance appreciable compared to L_J/M that can no longer be ignored.

A more realistic practical approach is to array fixed-E_J junctions (inductance L_J assumed larger than any parasitic geometric inductance) as depicted in Fig. 2.3c. In this case the total mode inductance grows $\propto M$, and therefore the capacitance must be adjusted $\propto 1/M$ to keep the frequency constant. This leads to $\propto M$ increase in the mode impedance and a corresponding $\propto \sqrt{M}$ increase in φ_{zpf}. This significantly alters the array's ability to dilute the Kerr nonlinearity:

$$2\hbar K = -12\frac{E_J}{4!}\sum_{m=1}^{M}\left(\frac{\varphi_{\mathrm{zpf}}}{M}\right)^4$$

$$= -\frac{1}{M}E_C \tag{2.59}$$

with the critical photon number $n_{\mathrm{crit}} \propto M^2/\varphi_{\mathrm{zpf}}^2 = 2ME_J/\hbar\omega_a$ again mirroring the Kerr nonlinearity. Interestingly, the nonlinearity all scales with ME_J, exactly as it would in the single junction circuit Fig. 2.3a with an M times larger junction and compensating capacitance ($L_J \to L_J/M$ and $C \to MC$). For a given mode frequency, the nonlinearity is *completely* agnostic to whether the inductance comes in the series form of an array, or the parallel form via more parallel conduction channels within a single junction[8]. The only difference between these two cases is the mode's impedance. This impacts the ease with which the desired capacitance can be realized while adding minimal linear inductance, as well as the engineering of couplings to other circuits. This equivalence explains the apparent confusion that state-of-the-art amplifiers based on single (or two) junction circuits [Mutus et

---

[8]Recall that the Ambegaokar-Baratoff relation for E_J sums over many parallel conduction channels.

al. 2014; Roy et al. 2015] often have similar power-handling capabilities to those based on arrays [Eichler et al. 2014; Frattini et al. 2018; Planat et al. 2019; Sivak et al. 2019; Sivak et al. 2020]. The only difference is in the fabrication constraints: arrays relax the constraint for large capacitors in single-junction circuits while requiring a stable fabrication process for M junctions at a time.

Finally, in Fig. 2.3d, we include the linear inductance L in series with the array. The anharmonicity

$$2\hbar K = -12 \frac{E_J}{4!} \sum_{m=1}^{M} \left(p \frac{\varphi_{\text{zpf}}}{M} \right)^4$$

$$= -\frac{p^2}{M} E_C \tag{2.60}$$

in this case resembles the previous case with an additional p^2 factor. The critical photon number $n_{\text{crit}} \propto M^2/p^2\varphi_{\text{zpf}}^2 = 2ME_J/p\hbar\omega_a$ however now has a lightly different scaling $\propto M/p$. When $p \ll 1$ implying linear inductance is appreciable, which is common in amplifiers like the JPC [Bergeal et al. 2010a; Bergeal et al. 2010b; Schackert 2013; Flurin 2015], $p \approx ML_J/L$ drastically changing the apparent scaling of Kerr to $2\hbar K \approx -ME_C(L_J/L)^2 \propto M$ and $n_{\text{crit}} \propto 2E_J/\hbar\omega_a \times L/L_J$. The Kerr nonlinearity *increases* with M because there is M times more of the perturbative amount of nonlinearity, but the critical photon number is completely independent of M. These considerations lead us to choose designs with $p \to 1$ to have the ability to put the largest possible number of photons for a given amount of nonlinearity.

Overall, these simple scaling arguments demonstrate that larger array size M is not strictly equivalent to smaller Kerr nonlinearity. Rather, arraying is another design tool for weakly anharmonic circuits that enables access to regimes of Kerr nonlinearity that are otherwise inaccessible due to other fabrication or design constraints. Moreover, in the large M limit, the lumped element approximation surely breaks down and we should consider a transmission line model. The scaling of Kerr nonlinearity with number of junctions still remains weak $\propto 1/M$ in this regime for the mode at the desired operating frequency [Sivak et al. 2020]. As such, fabrication constraints will lower bound the Kerr nonlinearities achievable in high participation ratio $p \to 1$ devices made of Al-AlO$_x$-Al. Lower nonlinearities may be designed with kinetic inductive materials, such as granular aluminum [Maleeva et al. 2018] or NbTiN [Vissers et al. 2016; Parker et al. 2021].

2.4 Renormalization of Kerr

In the single degree of freedom model of Sec. 2.2, we saw how the renormalization of the SNAIL potential due to current conservation with the linear inductor in series was crucial to the prediction of g_4 and thus effective Kerr nonlinearity K. We can also explain the physics

of this nontrivial contribution to g_4 in Eq. 2.46 from a different perspective. This correction is nothing but a renormalization of the potential due to high-frequency degrees of freedom that are inevitably present in the system (for example, the plasma mode associated with each junction). Such modes cannot be directly probed by low-energy experiments, but their effect is evident in measurable quantities such as the anharmonicity $2K$.

To demonstrate this point, consider the circuit in Fig. 2.4a that includes a capacitance C_s shunting the SNAIL (we set $M = 1$ for simplicity). This is the simplest addition of a high-frequency mode: the SNAIL plasma mode with frequency $\Omega_s = 1/\sqrt{L_sC_s}$ much larger than our desired operating frequency $\omega_a = 1/\sqrt{C(L + L_s)}$ (Eq. 2.41).

In this system, in contrast with the Lagrangian Eq. 2.13 in Sec. 2.2, the variable φ_s becomes a real quantum-mechanical coordinate with its own conjugate momentum. Therefore, it should be quantized on equal footing with φ.[9] However, since $\Omega_s \gg \omega_a$, this fast degree of freedom can be integrated out using the Born-Oppenheimer method or more sophisticated quantum field theory techniques [Altland and Simons 2010]. After such an integration, we will show that the effective Kerr nonlinearity K of the low-frequency mode coincides with Eq. 2.53 and does *not* depend on the precise value of Ω_s in the limit $\Omega_s \gg \omega_a$ and $\varphi_{\mathrm{zpf}} \ll 1$; thus, validating the relevance of the single mode circuit.

To this end, we first derive the Hamiltonian of the two-mode circuit Fig. 2.4a. While we could start from the Lagrangian Eq. 2.13 with additional term $C_s\varphi_0^2\dot{\varphi}_s/2$, perform the Legendre transformation and then diagonalize the quadratic part, we will take a different approach sometimes referred to as *black-box qauntization* (BBQ) [Nigg et al. 2012]. This approach adds important intuition about considering dipole mixing elements as nonlinear scatterers in an otherwise linear electromagnetic environment, and generalizes nicely to finite element simulations as we will discuss in more detail in Sec. 2.5.

Following the BBQ approach, as shown in Fig. 2.4b we separate out the linear inductance L_s from the nonlinear part, effectively partitioning the SNAIL into two elements in parallel: one linear with potential energy $c_2 E_J \tilde{\varphi}_s^2/2$, and the other nonlinear with potential energy

$$U_{\mathrm{NL}}(\tilde{\varphi}_s) = U_S(\tilde{\varphi}_s + \varphi_{s,\mathrm{min}}) - \frac{c_2}{2} E_J \tilde{\varphi}_s^2 \tag{2.61}$$

with an added constraint of zero applied flux in the newly formed loop enforcing the same phase drop $\tilde{\varphi}_s$ across both elements[10]. We then compute the impedance $Z_{\mathrm{NL}}[s]$ that the nonlinearity sees[11] and express the result with a partial fraction decomposition:

$$Z_{\mathrm{NL}}[s] = sL_s\frac{\omega_+^2\omega_-^2}{\omega_+^2 - \omega_-^2}\left[\frac{1 - \omega_-^2 LC}{s^2 + \omega_-^2} - \frac{1 - \omega_+^2 LC}{s^2 + \omega_+^2}\right] \tag{2.62}$$

---

[9]Defined $\varphi = \varphi_L + \varphi_s$ consistently with Sec. 2.2.

[10]We could alternatively use φ_s, later minimize the potential and shift all coordinates accordingly.

[11]s is the standard Laplace transform variable where the substitution $s = j\omega$ recovers the Fourier transform.
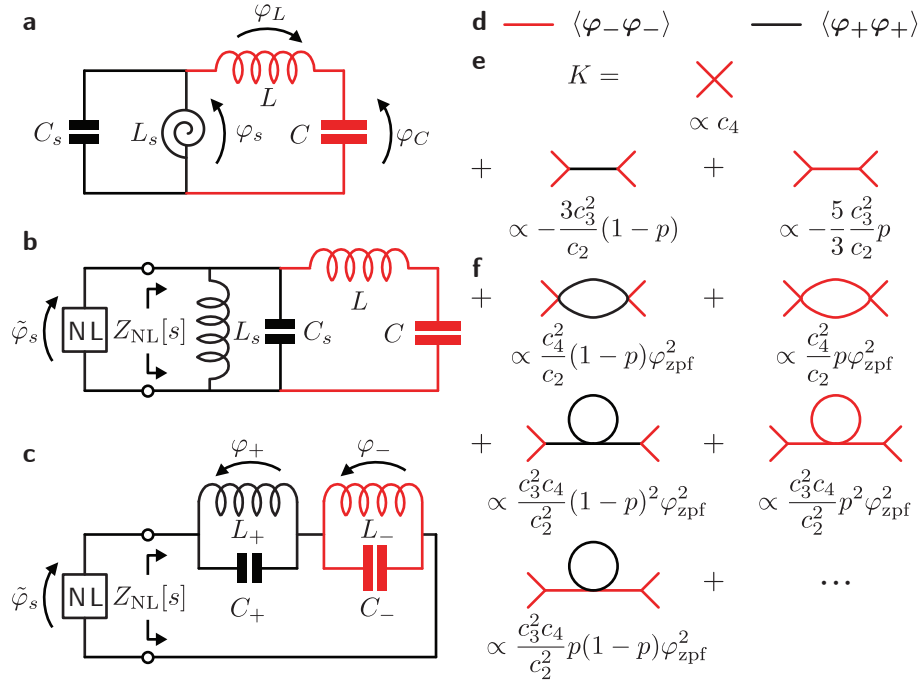
Figure 2.4 | (a) Two degree of freedom circuit with a SNAIL-mode gauge-coupled to a linear LC oscillator. The SNAIL-mode has a capacitance C_s across a SNAIL with phase drop φ_s across its small junction and an effective inductance L_s. (b) Decomposition of (a) into an impedance $Z_{\mathrm{NL}}[s]$ seen by the nonlinearity (NL) of the effective dipole element with phase drop $\tilde{\varphi}_s = \varphi_s - \varphi_{s,\mathrm{min}}$. (c) Rewriting circuit (b) using a Foster decomposition of $Z_{\mathrm{NL}}[s]$ in terms of canonical branch phases $\varphi_\pm$ across inductors $L_\pm$ and associated capacitors $C_\pm$. (d) Definitions for elements of Feynman diagrams used to eliminate the high-frequency SNAIL mode. Red (black) represent propagator for low- (high-) frequency modes with canonical coordinate φ_- (φ_+). (e) Diagrammatic series to calculate effective self-Kerr nonlinearity K low-frequency (red) mode. Each diagram corresponds to a term in Eq. 2.53 where third- (fourth-) order interaction vertices are weighted by c_3 (c_4) from the SNAIL potential. (f) Example higher-order one loop diagrams each suppressed by φ_{zpf}^2.

where we identify two pairs of poles $j\omega_\pm$ and $-j\omega_\pm$ at frequencies

$$
\begin{aligned}
\omega_\pm^2 &= \frac{L + L_s}{2LL_sC_s} + \frac{1}{2LC} \pm \sqrt{\left(\frac{L + L_s}{2LL_sC_s} + \frac{1}{2LC}\right)^2 - \frac{1}{LL_sCC_s}} \\
&= \frac{\Omega_s^2}{2(1 - p)}\left(1 + \frac{\omega_a^2}{\Omega_s^2}\right)\left[1 \pm \sqrt{1 - 4(1 - p)\frac{\omega_a^2/\Omega_s^2}{(1 + \omega_a^2/\Omega_s^2)^2}}\right]
\end{aligned}
\tag{2.63}
$$

with $p = L_s/(L + L_s)$ and simplifying with the convenient relationship $1 - p = LC\omega_a^2$. When $\Omega_s \gg \omega_a$, both reduce to

$$
\omega_- \approx \omega_a = 1/\sqrt{C(L + L_s)}
\tag{2.64}
$$

$$
\omega_+ \approx \frac{\Omega_s}{\sqrt{1 - p}} = \left(C_s\frac{L_sL}{L + L_s}\right)^{-1/2}
\tag{2.65}
$$

up to corrections $\mathcal{O}(\omega_a/\Omega_s)$.

The form of Eq. 2.62 corresponds to the Foster decomposition of the impedance as depicted in Fig. 2.4c, which contains two degrees of freedom with frequencies $\omega_\pm = 1/\sqrt{L_\pm C_\pm}$. Note that the low-frequency pole at ω_- corresponds precisely to the single mode in the previous calculation of Sec. 2.2. By inspection of Eq. 2.62 or equivalently calculating the residue for each pole, the respective characteristic impedances as seen by the nonlinearity are

$$
\begin{aligned}
Z_- &= L_s\omega_-\left[\frac{1 - (\omega_-/\omega_a)^2(1 - p)}{1 - (\omega_-/\omega_+)^2}\right] \\
&\approx pL_s\omega_- = p^2\sqrt{\frac{L + L_s}{C}}
\end{aligned}
\tag{2.66}
$$

$$
\begin{aligned}
Z_+ &= L_s\omega_+\left(\frac{\omega_-}{\omega_a}\right)^2\left[\frac{1 - p - (\omega_a/\omega_+)^2}{1 - (\omega_-/\omega_+)^2}\right] \\
&\approx (1 - p)L_s\omega_+ = p(1 - p)\frac{\omega_+}{\omega_a}\sqrt{\frac{L + L_s}{C}}
\end{aligned}
\tag{2.67}
$$

with $Z_\pm = \sqrt{L_\pm/C_\pm}$. The impedances and frequencies can be equivalently be rewritten as

effective inductances (via $Z_\pm = L_\pm \omega_\pm$)

$$L_- = L_s \left[\frac{1 - (\omega_-/\omega_a)^2 (1-p)}{1 - (\omega_-/\omega_+)^2} \right]$$

$$\approx p L_s = p^2 (L + L_s) \tag{2.68}$$

$$L_+ = L_s \left(\frac{\omega_-}{\omega_a} \right)^2 \left[\frac{1 - p - (\omega_a/\omega_+)^2}{1 - (\omega_-/\omega_+)^2} \right]$$

$$\approx (1-p) L_s = \frac{L L_s}{L + L_s} = p(1-p)(L + L_s) \tag{2.69}$$

and capacitances

$$C_- = C \left(\frac{\omega_a}{\omega_-} \right)^2 \frac{1}{p} \left[\frac{1 - (\omega_-/\omega_+)^2}{1 - (\omega_-/\omega_a)^2 (1-p)} \right]$$

$$\approx \frac{1}{p^2} C \tag{2.70}$$

$$C_+ = C_s \left(\frac{\Omega_s}{\omega_+} \right)^2 \left(\frac{\omega_a}{\omega_-} \right)^2 \left[\frac{1 - (\omega_-/\omega_+)^2}{1 - p - (\omega_a/\omega_+)^2} \right]$$

$$\approx C_s \tag{2.71}$$

via $Z_\pm = 1/C_\pm \omega_\pm$, where throughout the approximations assume $\Omega_s \gg \omega_a$.

We define the new canonical coordinates for each degree of freedom to the branch phase across each inductor $\varphi_\pm$. In these coordinates the Hamiltonian of the circuit Fig. 2.4 is

$$\mathcal{H}_2 = \sum_{\sigma=\pm} 4 E_{C_\sigma} \mathbf{N}_\sigma^2 + \frac{1}{2} E_{L_\sigma} \boldsymbol{\varphi}_\sigma^2 + U_{\text{NL}}(\boldsymbol{\varphi}_+ + \boldsymbol{\varphi}_-) \tag{2.72}$$

where we have used the loop containing the nonlinearity and the two linear inductors to enforce $\tilde{\varphi}_s = \varphi_+ + \varphi_-$. These canonical phases have respective fluctuations as seen by the nonlinearity

$$\varphi_{-,\text{zpf}} = \sqrt{p} \sqrt{\frac{1 - (\omega_-/\omega_a)^2 (1-p)}{1 - (\omega_-/\omega_+)^2}} \, \varphi_{\text{zpf}}$$

$$\approx p \varphi_{\text{zpf}} \tag{2.73}$$

$$\varphi_{+,\text{zpf}} = \sqrt{p \frac{\omega_+}{\omega_a}} \left(\frac{\omega_-}{\omega_a} \right) \sqrt{\frac{1 - p - (\omega_a/\omega_+)^2}{1 - (\omega_-/\omega_+)^2}} \, \varphi_{\text{zpf}}$$

$$\approx \sqrt{p(1-p) \frac{\omega_+}{\omega_a}} \, \varphi_{\text{zpf}} \tag{2.74}$$

where we have used Eq. 2.39 to write in terms of φ_{zpf} from the 1-mode problem of Sec. 2.2.

We emphasize that as of yet no assumptions have been made about φ_{zpf}; we have merely

made a linear canonical transformation from φ and φ_s to $\varphi_\pm$. This new basis, which diagonalizes the quadratic part of the Hamiltonian, is often preferable for numerical diagonalization, especially in inductively shunted circuits [Smith et al. 2016].

As before, we introduce standard bosonic creation and annihilation operators but now for two modes defined $\boldsymbol{\varphi}_- = \varphi_{-,\mathrm{zpf}}(\boldsymbol{a} + \boldsymbol{a}^\dagger)$ and $\boldsymbol{\varphi}_+ = \varphi_{+,\mathrm{zpf}}(\boldsymbol{s} + \boldsymbol{s}^\dagger)$ with commutators $\left[\boldsymbol{a}, \boldsymbol{a}^\dagger\right] = 1$ and $\left[\boldsymbol{s}, \boldsymbol{s}^\dagger\right] = 1$. Substituting into Eq. 2.72, we find

$$\mathcal{H}_2 = \hbar\omega_- \boldsymbol{a}^\dagger\boldsymbol{a} + \hbar\omega_+ \boldsymbol{s}^\dagger\boldsymbol{s} + \mathcal{H}_{\mathrm{NL}} \tag{2.75}$$

$$\mathcal{H}_{\mathrm{NL}} = \frac{c_3}{3!} E_J (\varphi_{-,\mathrm{zpf}}(\boldsymbol{a} + \boldsymbol{a}^\dagger) + \varphi_{+,\mathrm{zpf}}(\boldsymbol{s} + \boldsymbol{s}^\dagger))^3$$
$$+ \frac{c_4}{4!} E_J (\varphi_{-,\mathrm{zpf}}(\boldsymbol{a} + \boldsymbol{a}^\dagger) + \varphi_{+,\mathrm{zpf}}(\boldsymbol{s} + \boldsymbol{s}^\dagger))^4 + \cdots \tag{2.76}$$

where truncation of the series requires $\varphi_{-,\mathrm{zpf}} \ll 1$ and $\varphi_{+,\mathrm{zpf}} \ll 1$.

Under this condition, we can again perform perturbation theory and write the leading Kerr corrections to the eigenenergies with the effective Hamiltonian

$$\mathcal{H}_{\mathrm{NL,eff}} = K_{aa} \boldsymbol{a}^{\dagger 2}\boldsymbol{a}^2 + K_{as} \boldsymbol{a}^\dagger \boldsymbol{a}\boldsymbol{s}^\dagger\boldsymbol{s} + K_{ss} \boldsymbol{s}^{\dagger 2}\boldsymbol{s}^2 + \cdots \tag{2.77}$$

where K_{aa}, K_{as} and K_{ss} are the effective self- and cross-Kerr. Under the further assumption that $\left\langle \boldsymbol{s}^\dagger\boldsymbol{s}\right\rangle = 0$ in our experiments, which is valid if Ω_s is sufficiently large and the environment sufficiently cold, the only relevant nonlinearity is the self-Kerr K_{aa}. Remarkably, $K_{aa} = K$ from Eq. 2.53 of the single mode circuit in Sec. 2.2, which the leading order contribution is again

$$2\hbar K_{aa} = \frac{p^3}{c_2}\left[c_4 - \frac{3c_3^2}{c_2}(1-p) - \frac{5}{3}\frac{c_3^2}{c_2}p\right] E_C \tag{2.78}$$

assuming $\Omega_s \gg \omega_a$ while $\varphi_{-,\mathrm{zpf}} \ll 1$ and $\varphi_{+,\mathrm{zpf}} \ll 1$.

Instead of painstakingly reproducing the perturbation theory calculation to confirm all the numerical factors, we can gain more intuition about the contributions to Kerr nonlinearity by considering Feynman diagrams. In the diagrammatic language, the Kerr nonlinearity of the the low-frequency mode can be represented as the fourth-order self-interaction vertex. The example diagrams that contribute to the renormalization of this vertex are depicted in Figs. 2.4e and 2.4f.

The first diagram in Fig. 2.4e comes directly from the quartic term in the potential energy of the SNAIL element and is therefore proportional to the corresponding Taylor coefficient c_4. Including only this diagram results in $K_{aa} \propto c_4$, which is equivalent to the linear participation ratio-based approach discussed previously in Sec. 2.2.

The interesting and nontrivial correction to K comes from the high-energy SNAIL mode, and is represented by the second diagram in Fig. 2.4e. This term is equivalent to the sec-

ond term in Eqs. 2.53 and 2.78, and it does not depend on Ω_s as long as the requirement $\Omega_s \gg \omega_a$ is satisfied. In the single-mode calculation, this contribution arose from imposing current conservation Eq. 2.16 to the appropriate order of nonlinearity. In the two-mode case, it arises from a second order perturbation theory correction when considering the term $(a + a^\dagger)^2 (s + s^\dagger)$ as the perturbation. The correction to K_{aa} from this term is

$$\left(\frac{3c_3}{3!}E_J\right)^2 \frac{\left(\varphi_{-,\text{zpf}}^2 \varphi_{+,\text{zpf}}\right)^2}{2\hbar\omega_- + \hbar\omega_+} \approx 6c_3^2 \frac{E_J}{4!}\frac{E_J}{\hbar\omega_+}p^5(1-p)\frac{\omega_+}{\omega_a}\varphi_{\text{zpf}}^6$$
$$= \frac{3c_3^2}{c_2}\frac{E_J}{4!}p^4(1-p)\varphi_{\text{zpf}}^4 \tag{2.79}$$

where the approximation assumes $\Omega_s \gg \omega_a$ using Eqs. 2.73-2.74. In this limit, the correction indeed does not depend on Ω_s. This is *precisely* the renormalization of the SNAIL potential by the linear inductor as seen in $\tilde{c}_4$ Eq. 2.30; and in diagrammatic language it originates from a Wick contraction over the high-frequency degree of freedom (black line in associated diagram of Fig. 2.4e).

The last diagram in Fig. 2.4e depicts two cascaded c_3 self-interactions of the low-frequency mode. This is equivalent to the trivial second-order perturbation theory correction when considering $(a + a^\dagger)^3$ as the perturbation as calculated previously to generate the last term of K (Eq. 2.53). As such, this correction only depends on $\varphi_{-,\text{zpf}}$ in the two-mode calculation.

In principle, there are other contributions to the renormalization of the fourth-order self-interaction vertex. Some example one-loop processes are shown in Fig. 2.4f. However, such diagrammatic corrections are suppressed by a factor $\propto (\varphi_{\text{zpf}})^{2l}$ where l is the number of loops. We can further categorize these corrections: ones that include Wick contractions over the high frequency (black) degree of freedom, and ones that do not. The ones that do not will only contain red lines in the diagrams and thus only depend on $\varphi_{-,\text{zpf}}$; they will therefore be contained in the higher order corrections from the single-mode calculation visible in Eq. 2.51. The ones that do however will not necessarily be accounted for in the single mode calculation and so to ignore them we insist $\varphi_{+,\text{zpf}} \ll 1$. In practice, this condition is readily satisfied by fabricating junctions with $E_J \gg E_{C_J}$. Note it is fundamentally difficult to achieve the opposite regime of large phase fluctuations [Masluk et al. 2012; Smith et al. 2020].

Finally, comparing the two electrical circuits in Figs. 2.2a and 2.4a, we see that the single-mode circuit in Fig. 2.2a corresponds to taking the limit $C_s \to 0$ for the one in Fig. 2.4a. Rigorously taking this limit would lead to large quantum fluctuations of the phase φ_+, and the diagrammatic series would diverge. To ensure convergence, C_s still has to be large enough to satisfy $\varphi_{+,\text{zpf}} \ll 1$. In this case, classical elimination of the fast degree of freedom φ_+ associated with the SNAIL plasma mode via current conservation Eq. 2.16 is justified insofar as the predictions of Kerr nonlinearity agree to leading order. If this is

not the case, we may have to resort to more QFT-oriented approaches that have recently been used to predict cross-Kerr nonlinearities [Kurilovich et al. 2021] and two-photon dissipation [Cottet, Leghtas, and Kontos 2020] in more mesoscopic systems where effective Hamiltonians are often difficult to define.

Understanding these effects is important because the general approach for designing circuit QED systems relies on pushing spurious modes up in frequency and then neglecting their influence by arguing that the detuning to these modes is large. We have shown in this chapter that the presence of these modes can influence low-energy observables, particularly the Kerr nonlinearity, and they must be accounted for either by means of full current conservation, or equivalently by integrating out the high-energy modes.

2.5 Black-box quantization with SNAILs

In the preceding sections 2.2 and 2.4, we derived the Hamiltonian for two particular lumped element circuits that include SNAILs as effective Josephson dipole elements. We further saw how the low-energy dynamics of the latter two-mode circuit could be approximated sufficiently by the former one-mode circuit. This theme is ubiquitous in superconducting circuits, and really physics generally. Given a lumped element circuit, we can solve it, by brute force numerical methods if necessary. Clearly, this method quickly becomes intractable for more than a handful of degrees of freedom. The relevant question then is to ask for the *simplest* lumped element circuit that captures the dynamics at the energy scales in which we are interested.

Moreover, physical circuits have physical geometries and the translation of those to parameters of a lumped element circuit, or even which lumped element circuit to write down, is not *a priori* obvious. Physicists and electrical engineers alike start with intuition and then often resort to finite element methods to simulate classically the electromagnetic response of a given linear network via the scattering, impedance, or admittance matrices. This response can then be decomposed via a myriad of circuit synthesis methods commonly employed for engineering microwave filters and impedance matching networks [Pozar 2012]. The engineer then combines these networks with the current-voltage relationship of a lumped nonlinearity of choice (such as diodes or transistors) to design and optimize the performance of, for instance, a mixer or an amplifier. The goal in superconducting circuits is much the same: to design the desired response, be it for storage, manipulation, or amplification of quantum information. So the methods should be similar.

Working purely with response functions can become cumbersome and devoid of intuition, so we often wish to derive and manipulate Hamiltonians for our relatively lossless circuits. From these quantized Hamiltonians, the relevant response functions corresponding to different experiments or algorithms can then be derived or often intuited[12]. We want

---

[12]Deriving such effective Hamiltonians is not always possible (e. g. for dynamics at energy scales larger

to derive these Hamiltonians utilizing the full power of classical electromagnetic solvers. Enter *black-box quantization* (BBQ) [Nigg et al. 2012].

BBQ at its heart solves exactly this problem: given a Josephson dipole element with a linear environment characterized by the numerically simulated impedance $Z[s]$, what is the Hamiltonian? Simulating the impedance $Z[s]$ over the desired frequency range can be numerically tedious. Another form of BBQ based on energy participation ratios extracted from eigenmode simulations[13] can significantly speed up the design process [Minev et al. 2021]. These and related methods [Wallquist, Shumeiko, and Wendin 2006; Bourassa et al. 2012] have been successfully used throughout cQED to predict the self- and cross-Kerr nonlinearities of transmon-and-resonator systems, with a bit more care necessary in inductively shunted circuits especially when phase fluctuations are not small [Smith et al. 2016]. The catch: care must also be taken when predicting higher-than-leading order nonlinearity even when phase fluctuations are small. This is the manifestation of the renormalization effect of the preceding examples in Secs. 2.2 and 2.4. The goal of this section is to minimally extend a BBQ-based simulation and circuit quantization procedure to include this renormalization effect.

2.5.1 Foster decomposition of the environment

To this end, consider the circuit depicted in Fig. 2.5a that consists of a SNAIL with shunting capacitance C_s coupled to a linear electromagnetic environment characterized by the impedance $Z[s]$. While we specify the discussion to a single SNAIL for concreteness, the treatment here generalizes to arbitrary lumped inductive dipole elements, including arrays of such. As in Sec. 2.4, we separate the SNAIL into its linear and nonlinear parts (see Fig. 2.5b). The nonlinear part has the potential energy $U_{\mathrm{NL}}(\tilde{\varphi}_s)$ (Eq. 2.61) with $\tilde{\varphi}_s = \varphi_s - \varphi_{s,\mathrm{min}}$. The condition $\tilde{\varphi}_s = 0$ minimizes the potential of the full circuit unless the environment $Z[s]$ resembles a short circuit at DC (mathematically, $\lim_{\omega \to 0} Z[j\omega] = 0$). This is unlikely given large-area DC-connected loops should generally be avoided to reduce susceptibility to flux noise, and small-area loops can usually be incorporated into the definition of the Josephson dipole (as we have already done with the SNAIL)[14].

As guaranteed by Foster's theorem, we next synthesize the impedance seen by the nonlinearity $Z_{\mathrm{NL}}[s]$ into the equivalent circuit of a series combination of parallel LCR oscilla-

---

than the superconducting gap). In such cases, the response is the only physically meaningful quantity to calculate and we must do so for each specific experimental measurement sequence.

[13]Eigenmode simulations here refers to solvers meant for relatively lossless systems that return a list of complex frequencies corresponding to the poles of $Z[s]$ instead of simulating the impedance or scattering matrix directly at a set of frequencies and employing interpolation techniques.

[14]If it is important to have a DC-connected $Z[s]$ in this manner, we can always later enforce the loop constraint, find the global potential minimum, and shift all the the canonical coordinates. We avoid this here for simplicity.
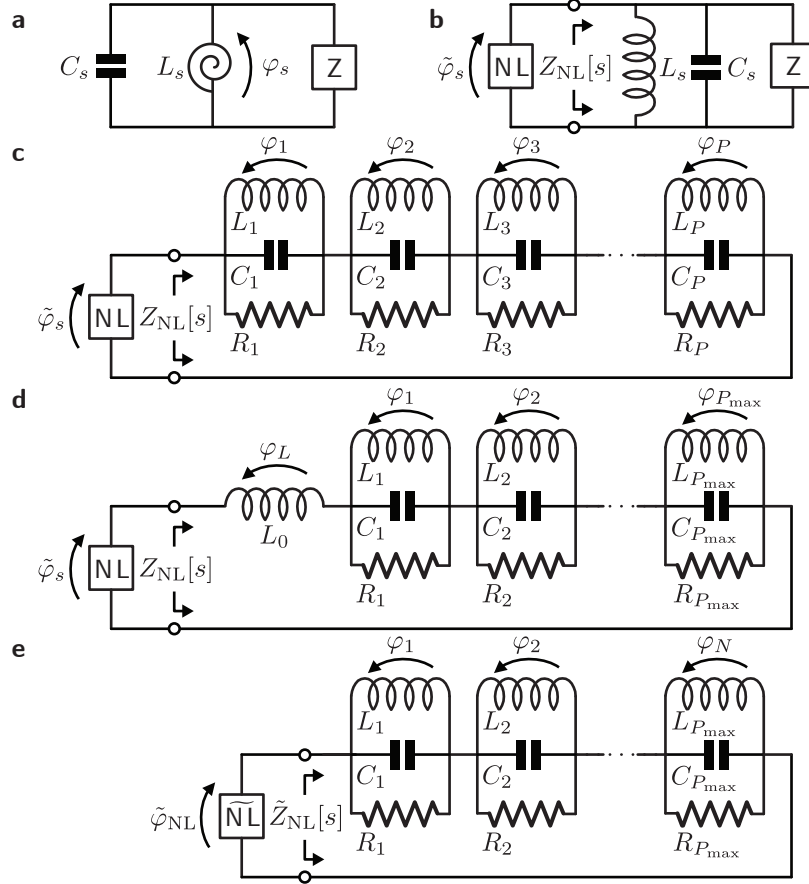
Figure 2.5 | (a) SNAIL-mode with capacitance C_s and effective inductance L_s coupled to a linear circuit characterized entirely by its linear electromagnetic response, the impedance $Z[s]$. (b) Decomposition of (a) into an impedance $Z_{\mathrm{NL}}[s]$ seen by the nonlinearity of the effective dipole element with phase drop $\tilde{\varphi}_s = \varphi_s - \varphi_{s,\mathrm{min}}$. (c) Exact P-degree-of-freedom Foster synthesis of $Z_{\mathrm{NL}}[s]$ in terms of canonical branch phase φ_p across inductor L_p along with capacitor C_p associated with each pole p. (d) Approximation of (c) after imposing a high frequency cutoff Ω_{max}. There are $P_{\mathrm{max}} < P$ degrees of freedom, each with frequency $\omega_p < \Omega_{\mathrm{max}}$. All high frequency modes are summarized by the effective inductance L_0 with associated branch phase φ_L. (e) After incorporating L_0 in the nonlinearity, the now renormalized nonlinearity sees impedance $\tilde{Z}_{\mathrm{NL}}[s] = Z_{\mathrm{NL}}[s] - sL_0$.

tors shown in Fig. 2.5. Explicitly,

$$Z_{\mathrm{NL}}[s] = \sum_{p=1}^{P} \left(sC_p + \frac{1}{sL_p} + \frac{1}{R_p} \right)^{-1}$$

$$= \sum_{p=1}^{P} Z_p \frac{s/\omega_p}{(s/\omega_p)^2 + s/\omega_p Q_p + 1} \tag{2.80}$$

where in the second line we have rewritten in terms of the resonance frequency $\omega_p = 1/\sqrt{L_p C_p}$, the characteristic impedance $Z_p = \sqrt{L_p/C_p}$ and the quality factor $Q_p = R_p/Z_p$ for each complex pair of poles $s, s^* = \omega_p(-1/2Q_p \pm j\sqrt{1 - 1/4Q_p^2}) \approx \pm j\omega_p$ (approximation corresponds to $Q_p \gg 1$). The summation runs over every pair of poles p up to the total number of P modes in the physical environment. Using the loop through the nonlinearity and each inductor with branch phase φ_p to constrain

$$\tilde{\varphi}_s = \sum_{p=0}^{P} \varphi_p, \tag{2.81}$$

we are free to quantize per the standard recipe and write the full Hamiltonian with P degrees of freedom.

2.5.2 Incorporating a high frequency cutoff

Unfortunately, the resultant Hamiltonian would be rather cumbersome since P is a large (possibly infinite) number of modes. Moreover, any finite element electromagnetic simulation will always require an upper frequency cutoff; it is intractable to simulate $Z_{\mathrm{NL}}[s]$ at all frequencies. As such, we must build this high frequency cutoff (call it Ω_{max}) into our quantization procedure, but with *care* since we know high-energy modes can alter low-energy observables as seen in Sec. 2.4.

We first organize our P degrees of freedom into the $P_{\mathrm{max}} < P$ of them that we wish to appear in our final Hamiltonian, each with $\omega_p < \Omega_{\mathrm{max}}$. For the remaining $P - P_{\mathrm{max}}$ degrees of freedom, we summarize their impedance at low frequencies as $sL_p/(1 + L_p s/R_p) \approx sL_p$, where the approximation implies $R_p \gg L_p\Omega_{\mathrm{max}}$ or the high quality factor limit[15]. After implementing this cutoff,

$$Z_{\mathrm{NL}}[s] = sL_0 + \sum_{p=1}^{P_{\mathrm{max}}} Z_p \frac{s/\omega_p}{(s/\omega_p)^2 + s/\omega_p Q_p + 1} \tag{2.82}$$

---

[15]Effectively, this throws away $P - P_{\mathrm{max}}$ poles on the real axis, each at $s = -R_p/L_p$, which play an inconsequential role in the dynamics in this limit.

corresponding to Fig. 2.5d where

$$L_0 = \sum_{p=P_{\text{max}}+1}^{P} L_p \tag{2.83}$$

$$= L_s - \sum_{p=1}^{P_{\text{max}}} L_p \tag{2.84}$$

summarizes the total series inductance seen by the nonlinearity due to now-ignored high-frequency degrees of freedom. In the second line, we have used $\lim_{\omega \to 0}(Z_{\text{NL}}[j\omega]/j\omega) = \sum_{p=1}^{P} L_p = L_s$ corresponding to the case in absence of a galvanic short through $Z[s]$.

Defining φ_L as the branch flux across the inductor L_0, we notice the parallel to the single-mode problem of Sec. 2.2; there exists an inductance L_0 in series with the nonlinearity from an effective inductive dipole element that does not have its own capacitance and thus is not an independent degree of freedom. In fact, setting $P_{\text{max}} = 1$ would *exactly* correspond to the similar Foster decomposition of the circuit in Fig. 2.2a with the entire SNAIL array as the effective nonlinear dipole [16]. Thus, we expect that the nonlinearity in this case must be renormalized by the presence of L_0.

To this end, we define a new renormalized nonlinear dipole, depicted in Fig. 2.5e, that sees the impedance

$$\tilde{Z}_{\text{NL}}[s] = Z_{\text{NL}}[s] - sL_0 \tag{2.85}$$

and has potential energy

$$\tilde{U}_{\text{NL}}(\tilde{\varphi}_{\text{NL}}, \varphi_s) = \frac{1}{2}E_{L_0}(\tilde{\varphi}_{\text{NL}} - \tilde{\varphi}_s)^2 + U_{\text{NL}}(\tilde{\varphi}_s) \tag{2.86}$$

where $\tilde{\varphi}_{\text{NL}} = \tilde{\varphi}_s - \varphi_L$ is the branch phase across the renormalized nonlinearity, and $\tilde{\varphi}_s$ remains to be eliminated. We eliminate $\tilde{\varphi}_s$ via current conservation at the node between L_0 and the nonlinearity. The resulting equation

$$0 = \frac{\partial \tilde{U}_{\text{NL}}}{\partial \tilde{\varphi}_s}$$

$$= E_{L_0}(\tilde{\varphi}_s - \tilde{\varphi}_{\text{NL}}) + \frac{dU_{\text{NL}}}{d\tilde{\varphi}_s} \tag{2.87}$$

implicitly determines the phase drop across our original nonlinearity $\tilde{\varphi}_s[\tilde{\varphi}_{\text{NL}}]$ as a function of the branch phase across the renormalized dipole, in exact accordance with Eq. 2.16.

Upon using this constraint to eliminate $\tilde{\varphi}_s$, the resultant Lagrangian with P_{max} degrees

---

[16]Taking the limit $C_s \to 0$ of $Z_{\text{NL}}[s]$ (Eq. 2.62) from the two-mode calculation recovers this one-mode Foster decomposition.

of freedom is

$$\mathcal{L}_{P_{\max}} = \sum_{p=1}^{P_{\max}} \left(\frac{C_p \varphi_0^2}{2} \dot{\varphi}_p{}^2 - \frac{1}{2} E_{L_p} \varphi_p^2 \right) - \tilde{U}_{\mathrm{NL}}(\tilde{\varphi}_{\mathrm{NL}}) \tag{2.88}$$

$$\tilde{U}_{\mathrm{NL}}(\tilde{\varphi}_{\mathrm{NL}}) = \frac{1}{2} E_{L_0} \left(\tilde{\varphi}_{\mathrm{NL}} - \tilde{\varphi}_s[\tilde{\varphi}_{\mathrm{NL}}] \right)^2 + U_{\mathrm{NL}}(\tilde{\varphi}_s[\tilde{\varphi}_{\mathrm{NL}}]) \tag{2.89}$$

with the understanding that $\tilde{\varphi}_{\mathrm{NL}}$ itself is eliminated by the loop constraint

$$\tilde{\varphi}_{\mathrm{NL}} = \sum_{p=1}^{P_{\max}} \varphi_p. \tag{2.90}$$

2.5.3 Renormalizing the nonlinearity

Before quantization, we consider our new renormalized nonlinearity. We might be concerned at first glance that $\tilde{U}_{\mathrm{NL}}(\tilde{\varphi}_{\mathrm{NL}})$ has quadratic terms, which would then linearly couple our $P_{\max}$ degrees of freedom; in fact, it does not. Upon reflection, intuitively this makes sense given we already performed a pole decomposition of $Z_{\mathrm{NL}}[s]$, so each mode's coordinate φ_p should be linearly uncoupled. Mathematically, inspecting the current conservation Eq. 2.87, we see $\tilde{\varphi}_s[\tilde{\varphi}_{\mathrm{NL}}] = \tilde{\varphi}_{\mathrm{NL}} + \mathcal{O}(\tilde{\varphi}_{\mathrm{NL}}^2)$ and thus $\tilde{U}_{\mathrm{NL}}(\tilde{\varphi}_{\mathrm{NL}}) = 0 + \mathcal{O}(\tilde{\varphi}_{\mathrm{NL}}^3)$, given we already removed the quadratic part of our original nonlinearity $U_{\mathrm{NL}}(\tilde{\varphi}_s)$.

To further inspect the nonlinearity in the regime of small phase fluctuations, we Taylor expand the full potential about its global minimum, which we have conveniently arranged to be $\varphi_1 = \cdots = \varphi_p = \cdots = \varphi_{P_{\max}} = 0$. Noticing that all of the higher-than-quadratic potential terms are only a function of the combination of coordinates given by $\tilde{\varphi}_{\mathrm{NL}}$ Eq. 2.90, we expand along this direction since partial derivatives along all others will vanish at higher than order two. The resulting coefficients for the Taylor expansion of the full potential along this direction are equivalent to $\tilde{c}_k = (1/E_J)(d^k \tilde{U}_{\mathrm{NL}}/d\tilde{\varphi}_{\mathrm{NL}}^k)|_{\tilde{\varphi}_{\mathrm{NL}}=0}$ for orders $k > 2$. The first four are:

$$\tilde{c}_3 = -x_J \frac{d^2 \tilde{\varphi}_s}{d\tilde{\varphi}_{\mathrm{NL}}^2}[0] \tag{2.91}$$

$$\tilde{c}_4 = -x_J \frac{d^3 \tilde{\varphi}_s}{d\tilde{\varphi}_{\mathrm{NL}}^3}[0] \tag{2.92}$$

$$\tilde{c}_5 = -x_J \frac{d^4 \tilde{\varphi}_s}{d\tilde{\varphi}_{\mathrm{NL}}^4}[0] \tag{2.93}$$

$$\tilde{c}_6 = -x_J \frac{d^5 \tilde{\varphi}_s}{d\tilde{\varphi}_{\mathrm{NL}}^5}[0] \tag{2.94}$$

redefining $x_J = L_J/L_0$ in direct analogy with Eqs. 2.19- 2.24. Again, the derivatives of the implicit function $\tilde{\varphi}_s[\tilde{\varphi}_{\mathrm{NL}}]$ can be found by differentiating the current conservation Eq. 2.87,

for example

$$\frac{d\tilde{\varphi}_s}{d\tilde{\varphi}_{\mathrm{NL}}} = \left(1 + \frac{1}{E_{L_0}}\frac{d^2 U_{\mathrm{NL}}}{d\tilde{\varphi}_s^2}\right)^{-1}. \tag{2.95}$$

Defining the analogous participation ratio $p = L_s/(L_s + L_0)$ for the SNAIL nonlinearity's participation in the renormalized nonlinearity, we can express the Taylor coefficients $\tilde{c}_k$ for the renormalized potential in terms of the bare c_k of the single SNAIL potential:

$$\tilde{c}_3 = c_3 \tag{2.96}$$

$$\tilde{c}_4 = c_4 - 3c_3^2\frac{E_J}{E_{L_0}}$$

$$= c_4 - \frac{3c_3^2}{c_2}(1-p) \tag{2.97}$$

$$\tilde{c}_5 = c_5 - \frac{10c_4c_3}{c_2}(1-p) + \frac{15c_3^3}{c_2^2}(1-p)^2 \tag{2.98}$$

$$\tilde{c}_6 = c_6 - \frac{10c_4^2 + 15c_5c_3}{c_2}(1-p) + \frac{105c_4c_3^2}{c_2^2}(1-p)^2 - \frac{105c_3^4}{c_2^3}(1-p)^3 \tag{2.99}$$

in agreement[17] with Eqs. 2.29- 2.32. Again, we emphasize there are no *a priori* small parameters in these coefficients, especially when one of the modes with frequency above Ω_{max} that we eliminated participates highly in the SNAIL, for instance the SNAIL plasma mode of Sec. 2.4.

2.5.4 Quantization

Now that we understand the structure of our potential and its nonlinearity, we perform a Legendre transformation on $\mathcal{L}_{P_{\mathrm{max}}}$ Eq. 2.88, and canonically quantize to get the Hamiltonian

$$\mathcal{H}_{P_{\mathrm{max}}} = \sum_{p=1}^{P_{\mathrm{max}}}\left(4E_C\boldsymbol{N}_{\boldsymbol{p}}^2 + \frac{1}{2}E_{L_p}\boldsymbol{\varphi}_{\boldsymbol{p}}^2\right) + \tilde{U}_{\mathrm{NL}}\left(\sum_{p=1}^{P_{\mathrm{max}}}\boldsymbol{\varphi}_{\boldsymbol{p}}\right) \tag{2.100}$$

where $\left[\boldsymbol{\varphi}_{\boldsymbol{p}}, \boldsymbol{N}_{\boldsymbol{q}}\right] = i\delta_{p,q}$, and Eq. 2.89 defines $\tilde{U}_{\mathrm{NL}}(\sum_{p=1}^{P_{\mathrm{max}}}\boldsymbol{\varphi}_{\boldsymbol{p}})$. Without further approximation, this Hamiltonian may now be numerically diagonalized, a more tractable task with $P_{\mathrm{max}} < P$ degrees of freedom.

We may also introduce standard bosonic creation and annihilation operators, defined by $\boldsymbol{\varphi}_{\boldsymbol{p}} = \varphi_{p,\mathrm{zpf}}(\boldsymbol{a}_{\boldsymbol{p}} + \boldsymbol{a}_{\boldsymbol{p}}^\dagger)$ and $\left[\boldsymbol{a}_{\boldsymbol{p}}, \boldsymbol{a}_{\boldsymbol{q}}^\dagger\right] = \delta_{p,q}$, where $\varphi_{p,\mathrm{zpf}} = (2E_{C_p}/E_{L_p})^{1/4}$ is the zero point fluctuations of the phase for mode p as seen by the renormalized nonlinearity. The

---

[17]The apparent difference in the p^k dependence has be absorbed into the definition of the zero point fluctuations for each mode; now the zero point fluctuations are those that the effective renormalized dipole sees, whereas previously we wrote the fluctuations the SNAIL array sees.

Hamiltonian in term of these operators is

$$\mathcal{H}_{P_{\max}} = \sum_{p=1}^{P_{\max}} \omega_p a_p^\dagger a_p + \tilde{\mathcal{H}}_{\mathrm{NL}} \tag{2.101}$$

$$\tilde{\mathcal{H}}_{\mathrm{NL}} = \frac{\tilde{c}_3}{3!} E_J \left(\sum_{p=1}^{P_{\max}} \varphi_{p,\mathrm{zpf}}(a_p + a_p^\dagger) \right)^3$$

$$+ \frac{\tilde{c}_4}{4!} E_J \left(\sum_{p=1}^{P_{\max}} \varphi_{p,\mathrm{zpf}}(a_p + a_p^\dagger) \right)^4 + \cdots \tag{2.102}$$

with $\tilde{c}_k$ given by Eqs. 2.96–2.99 and truncation requiring $\varphi_{p,\mathrm{zpf}} \ll 1$. Further approximations, such as the dispersive approximation, and perturbation theory may now be applied in a similar manner to the derivation of effective self- and cross-Kerr nonlinearity in Sec. 2.4, while remembering that cascaded third-order processes $\propto \tilde{c}_3^2$ tend to be the same magnitude as the fourth-order one $\propto \tilde{c}_4$.

Hamiltonian Eq. 2.101 constitutes the major result of this section. It governs the dynamics of $P_{\max}$ degrees of freedom, each with frequency below the imposed cutoff $\Omega_{\max}$, and includes the renormalization of the nonlinearity due to modes above $\Omega_{\max}$; all of this in terms of parameters extricable from classical electromagnetic simulations restricted to below $\Omega_{\max}$. To further clarify how to extract these parameters, consider the decomposition of $Z_{\mathrm{NL}}[s]$ depicted in Fig. 2.5d. The parameters of the finite frequency poles (L_p, C_p, R_p) may be extracted from near-resonance $\sim \omega_p$ simulations either through scattering simulations directly or eigenmode simulations, all below $\Omega_{\max}$ as standard [Nigg et al. 2012; Minev et al. 2021]. The inductance L_0 for renormalization is encoded on the low-frequency slope of $Z_{\mathrm{NL}}[s]$: mathematically, $\lim_{\omega \to 0}(Z_{\mathrm{NL}}[j\omega]/j\omega) = L_0 + \sum_{p=1}^{P_{\max}} L_p$. Given that $L_s = L_0 + \sum_{p=1}^{P_{\max}} L_p$ in the absence of a galvanic short across the SNAIL, L_0 may also be extracted from eigenmode simulations as the difference between the total imposed lumped inductance L_s and the sum of the extracted inductance from each pole L_p.

The extension of this procedure to the case of circuits with multiple Josephson dipole elements follows directly from previous works [Nigg et al. 2012; Minev et al. 2021]. Each inductive nonlinearity get its own port and the impedance $Z_{\mathrm{NL}}[s]$ generalizes to the familiar impedance matrix [Pozar 2012]. The poles of each diagonal element of the impedance matrix are the same. Thus, ω_p and Q_p are consistent across the circuit synthesis as seen from each port. The characteristic impedances Z_p, and consequently phase fluctuations $\varphi_{p,\mathrm{zpf}}$, depend however on the port. Similarly, the series inductance L_0 depends on the port. As such, the nonlinearity associated with each Josephson dipole element must be renormalized independently. The relative weight and sign with which each eigenmode participates in each renormalized dipole is then encoded in $\varphi_{p,\mathrm{zpf}}$ in the standard way[18].

---

[18]Specifically, for each dipole, $\varphi_{p,\mathrm{zpf}} = \pm(2E_{C_p}/E_{L_p})^{1/4}$ where the sign indicates the relative orientation

In this way, we have updated the BBQ quantization procedure to include the renormalization of the nonlinearity due to an imposed high-frequency cutoff. It is worth revisiting the approximations we have made. The primary approximation in BBQ generally is ignoring offset charges and phase slips. We further assumed the SNAIL acts as a lumped dipole element with no internal degrees of freedom, at least below the cutoff frequency Ω_{max}. Finally, the renormalization procedure for the nonlinearity assumes $\varphi_{p,\mathrm{zpf}} \ll 1$ for all modes $p > P_{\mathrm{max}}$ in the same way as we saw in Sec. 2.4. Within these approximations however, we insist that the Hamiltonian $\mathcal{H}_{P_{\mathrm{max}}}$ of Eq. 2.100 captures the dynamics for arbitrary phase fluctuations for modes below the cutoff. Only truncation of $\tilde{\mathcal{H}}_{\mathrm{NL}}$ in Eq. 2.102 requires the further assumption that $\varphi_{p,\mathrm{zpf}} \ll 1$ for all modes. Thus, we have a general framework for deriving and designing the low-energy Hamiltonian of circuits with arbitrary lumped Josephson dipole elements. The remainder of this thesis is dedicated to optimizing these circuits and the radiation we apply to them for quantum information applications.

---

of the mode's current through the nonlinearity, aligned or anti-aligned with a chosen convention.

3

Quantum-limited parametric amplification

To control a quantum system, we require measurements that are faster than the rate at which it loses the information in which we are interested. Often, as in the dispersive read-out of superconducting qubits [Blais et al. 2004], the measurement apparatus translates the desired information into distinguishing one emitted coherent state from another. Photon loss will inevitably increase the noise, so we need to amplify the signal before this happens to protect the signal-to-noise ratio (SNR) from future photon loss. During this amplification process, the SNR generally degrades and quantum mechanics bounds the minimum possible degradation. Reaching this quantum-noise limit places a difficult requirement on the first amplifier of a precision microwave measurement chain, often accomplished with parametric amplifiers based on Josephson junctions. This chapter focuses on the requirements for the first amplifier and how a new parametric amplifier based on SNAILs, the SNAIL parametric amplifier (SPA), realizes them. We will show that the inclusion of SNAILs as the three-wave-mixing nonlinearity of choice enables device performance impossible with other forms of nonlinearity based on DC-SQUIDS: namely, Kerr-free three-wave mixing. The mechanisms and optimizations explored here for parametric amplification are readily applicable to other quantum information processing applications, including the stabilization of Schrödinger cat states as in Chapter 4.

3.1 Requirements for first amplifier

Quantum-noise-limited Josephson parametric amplifiers [Vijay, Devoret, and Siddiqi 2009; Aumentado 2020] are a key component in many precision microwave measurement setups, such as for the readout of superconducting qubits [Johnson et al. 2012; Risté et al. 2012; Hatridge et al. 2013; Jeffrey et al. 2014; Walter et al. 2017], the high-sensitivity detection of electron spin resonance [Bienfait et al. 2016; Bienfait et al. 2017], and the search for axions [Brubaker et al. 2017; Backes et al. 2021]. As the first component of a microwave amplification chain, the main desired specifications for a linear Josephson amplifier are:

1. **Low added noise**: The noise added by the amplifier should be no larger than the minimum imposed by quantum mechanics [Caves 1982; Caves et al. 2012].

2. **High gain**: The amplifier power gain G should be large enough to overwhelm the noise temperature of the following amplification chain (in practice, at least 20 dB).

3. **Large bandwidth**: The amplifier gain should be constant over a bandwidth that is large enough for the desired application.

4. **Large dynamic range**: The output signal amplitude should be linearly proportional to the input signal amplitude over a wide enough power range. The lower limit of this power range should be defined by the quantum noise ideally setting the signal-to-noise ratio of the desired measurement.

5. **Unidirectionality**: The amplifier should, ideally, amplify signals incident from the system being probed and isolate the signal source from spurious noise that propagates back from subsequent devices in the amplification chain.

6. **Ease of operation**: The energy necessary for amplification should be delivered to the amplifier in a simple and robust manner without requiring precise tuning.

7. **Robustness of construction**: The amplifier circuit should not require too delicate tolerances.

Among these requirements, near-quantum-limited added noise is paramount in the aforementioned applications where signal power cannot be further increased for either fundamental or technical reasons. Taking the dispersive readout of superconducting qubits as an example, ideally the readout SNR scales linearly with the readout power [Blais et al. 2004]; however, in practice, higher order nonlinearities reduce readout fidelity at higher powers [Sank et al. 2016], spurring exploration of alternative readout strategies [Campagne-Ibarcq et al. 2016; Eddins et al. 2018; Touzard et al. 2019; Dassonneville et al. 2020]. As such, no compromise should be made that reduces amplifier noise performance. Moreover, the requirement for high gain with low added noise makes less stringent the noise temperature required by the second stage amplifier to maintain quantum-limited performance of the entire measurement chain.

The bandwidth of Josephson parametric amplifiers is not large compared to the limit set Bode-Fano criterion [Pozar 2012]. Thus far, it is often just large enough for single qubit readout, but the center frequency is *in situ* tunable to align with the readout cavity, partially making up for the lack of bandwidth. Impedance-matching structures have been employed to increase the bandwidth for Josephson reflection amplifiers [Mutus et al. 2014; Roy et al. 2015], which may be understood in terms of traditional microwave filter theory [Getsinger 1963; Matthaei, Young, and Jones 1980; Naaman et al. 2019].

Large dynamic range is a particularly important requirement for scaling up superconducting qubit setups to larger size systems as multiplexing becomes necessary to reduce the total number of output lines. The dynamic range characterizes the input power range over which the amplifier behaves as a linear device for a single-tone or multitone input. For quantum-limited amplifiers, the lower limit on dynamic range is set fundamentally by quantum mechanics, so improving dynamic range corresponds to increasing the upper limit. The upper limit is controlled by two distinct but closely related nonidealities in the large-signal amplifier response. The first nonideality is the phenomenon of amplifier saturation, also called *gain compression*. This limits the maximum output power that can be

produced by the device for an arbitrary input signal. The second nonideality, which we explore in this thesis, is the phenomenon of *intermodulation distortion* (IMD) for multitone inputs, where the amplifier produces spurious tones on its output in addition to the desired amplified copies of the input tones. Together, these two nonidealities limit the signal powers that can be processed by the amplifier and thus are a problem for faster or higher-power qubit readout as well as for the readout of multiple qubits [Jeffrey et al. 2014].

The unidirectionality requirement is often enforced by a pair of ferrite-based microwave circulators together with sufficient isolation to protect the quantum system of interest from amplified noise propagating from the rest of the measurement chain. These ferrite circulators limit the achievable noise performance and there is active work on replacing them with superconducting counterparts [Naaman et al. 2016; Chapman et al. 2017]. Furthermore, directional amplifiers based on the interference of multiple parametric processes hope to replace reflection amplifiers [Abdo et al. 2013a; Sliwa et al. 2015; Lecocq et al. 2017; Lecocq et al. 2021], and admit an intuitive graph-based description [Ranzani and Aumentado 2015] that comes from a more general quantum theory of nonreciprocity [Metelmann and Clerk 2014; Metelmann and Clerk 2015]. Travelling wave parametric amplifiers (TWPAs) also show promise for both large bandwidth and unidirectionality but still require additional isolators between the system and first amplifier [Macklin et al. 2015; Vissers et al. 2016].

Finally, we note these requirements are specifically written for a *linear* amplifier whose response amplifies the travelling input signal irrespective of the incident power within the allowed dynamic range. Under these conditions, the amplification process inevitably adds noise with the minimum possible given by Caves' theorem [Caves 1982; Caves et al. 2012]. However, using prior knowledge about the structure of the signal, a *nonlinear* amplifier may actually increase the signal-to-noise ratio by exploiting its nonlinearity to amplify the signal *more* than the noise. This is the basis of readout via bifurcation amplifiers [Vijay, Devoret, and Siddiqi 2009] or more generally those based on multiple instabilities [Wustmann and Shumeiko 2019]. In fact, we can view dispersive readout [Blais et al. 2004] in this light as a nonlinear amplification of one qubit photon into a many-photon flying coherent state. This amplification, like most nonlinear processes, requires fine tuning; there exists an optimal cross-Kerr for a given resonator linewidth as well as an optimal frequency for distinguishing between zero and one photon in the coupled qubit as opposed to between one and two photons. As such, these strategies are amenable to single-qubit measurement, but are difficult to multiplex to many qubits simultaneously.

3.2 Ideal degenerate parametric amplifier (DPA)

In this section, we focus on the model of an ideal degenerate parametric amplifier (DPA): *degenerate* for the ability to have all the response occurring at a single frequency, *parametric* for modulating a parameter in the Hamiltonian. This amplifier will have a single port and

supply amplification in reflection; it will also achieve quantum-limited noise performance.

3.2.1 Input-output theory in the RWA

Before parametric amplifiers in particular, we pause to discuss *input-output* theory, an important tool for quantum optics and cQED alike with a rich history [Gardiner and Zoller 2004; Clerk et al. 2010; Vool and Devoret 2017]. In the context of single oscillator described by bosonic creation $a^\dagger$ and annihilation a operators with a Hamiltonian $\mathcal{H}$, we may write the quantum Langevin equation (QLE) within the rotating wave approximation (RWA) as

$$\dot{a} = \frac{i}{\hbar}\left[\mathcal{H}, a\right] - \frac{\kappa}{2}a + \sqrt{\kappa}a_{\text{in}} \tag{3.1}$$

where κ is both the energy dissipation rate of the mode *and* the coupling to the environment through the incoming transmission line annihilation operator $a_{\text{in}}(t)$, a direct embodiment of the fluctuation dissipation theorem. Note that taking $\kappa \to 0$ recovers the Heisenberg equations of motion.

The transmission line operators associated with the single port have the commutation relation

$$\left[a_{\text{in}}(t), a_{\text{in}}(t')^\dagger\right] = \delta(t - t') \tag{3.2}$$

within the RWA, as well as the associated port boundary condition

$$\sqrt{\kappa}a(t) = a_{\text{in}}(t) + a_{\text{out}}(t) \tag{3.3}$$

also known as the *input-output* relation. This formalism is fundamentally based on a role reversal: instead of considering a circuit that loses and gains energy from the environment, we view the circuit as an elastic scatter of signals coming from the environment. The environment consists of input-output ports, which may be controlled by the experimentalist. Internal losses may be modeled as additional ports in the style of Caldeira and Leggett [Caldeira and Leggett 1983] for which the experimentalist may not measure a_{out}. For a treatment beyond the RWA, please see the Appendix A and [Vool and Devoret 2017], which themselves are based on [Gardiner and Zoller 2004].

3.2.2 Gain of a DPA

Having introduced input-output theory, we may now derive the scattering properties of an ideal degenerate parametric amplifier (DPA). We begin with a simple theoretical model of the minimal quantum-limited DPA introduced by Haus and Mullen [Haus and Mullen 1962]. The detailed explanation of the model is readily available in comprehensive reviews [Clerk et al. 2010; Roy and Devoret 2016] as well as intuitive explanations based on skateboarding in a half-pipe [Aumentado 2020]. We also recommend an analysis of the nonidealities associated with different energy-delivery or "pumping" schemes that con-

tains a pedagogical introduction [Boutin et al. 2017]. Although our treatment here will be written in terms of quantum operators, we emphasize that the fundamental mechanism responsible for amplification comes from classical nonlinear physics; hence analogies to skateboarding in a half-pipe are remarkably accurate. Predication of the amplifier's quantum-limited noise performance requires a quantum treatment only insofar as quantum mechanics lower-bounds the total noise incident on the ports. The amplifier itself simply mixes this incident noise.

Following [Boutin et al. 2017], we start with a phenomenological Hamiltonian in the lab frame that we will later engineer with a desired circuit implementation,

$$\mathcal{H}/\hbar = \omega_a a^\dagger a + \chi(a^{\dagger 2} a_p + a^2 a_p^\dagger) \tag{3.4}$$

where ω_a is the oscillator frequency, χ is the nonlinearity, and $a_p^\dagger$ (a_p) is the creation (annihilation) operator of an excitation in some pump mode intended to deliver the energy necessary for amplification. In three-wave-mixing amplifiers, we deliver that energy with a strong microwave tone incident on the pump mode at frequency $\omega_p \approx 2\omega_a$. In the regime where this pump is strong and stiff, we may treat it classically with the substitution $a_p \approx \alpha_p e^{-i\omega_p t}$ effectively ignoring the fluctuations of the pump mode. This is effectively a mean-field approximation and we are interested in the near-resonance effects about this large pump field.

To eliminate the now explicit time dependence in the Hamiltonian, we apply a time-dependant unitary transformation or equivalently the substitution $a \to a e^{-i\omega_p t/2}$. This generates the prototypical DPA Hamiltonian in the frame rotating at $\omega_p/2$

$$\mathcal{H}_{\text{DPA}}/\hbar = -\Delta_{\text{DPA}} a^\dagger a + \epsilon_2 a^{\dagger 2} + \epsilon_2^* a^2 \tag{3.5}$$

where $\Delta_{\text{DPA}} = \omega_p/2 - \omega_a$ is the pump's detuning from the resonance condition, and ϵ_2 is the squeezing drive strength. When $\epsilon_2 = 0$, this system is a trivial harmonic oscillator that responds to incident signals by simply reflecting them with an additional phase shift depending on the signal's detuning from resonance. For nonzero ϵ_2, the oscillator's ground state is a squeezed state and the response acquires mixing capabilities. We quantitatively investigate this response with the QLE Eq. 3.1 that includes the loss rate κ associated with a single port:

$$\dot{a} = i\left(\Delta_{\text{DPA}} a - 2\epsilon_2 a^\dagger\right) - \frac{\kappa}{2} a + \sqrt{\kappa} a_{\text{in}}$$
$$= i\left(\Delta_{\text{DPA}} + i\frac{\kappa}{2}\right) a - 2i\epsilon_2 a^\dagger + \sqrt{\kappa} a_{\text{in}} \tag{3.6}$$

where we see that a and $a^\dagger$ are now coupled through the squeezing drive. The corresponding QLE for $a^\dagger$ may be similarly derived or equivalently obtained by Hermitian conjugation
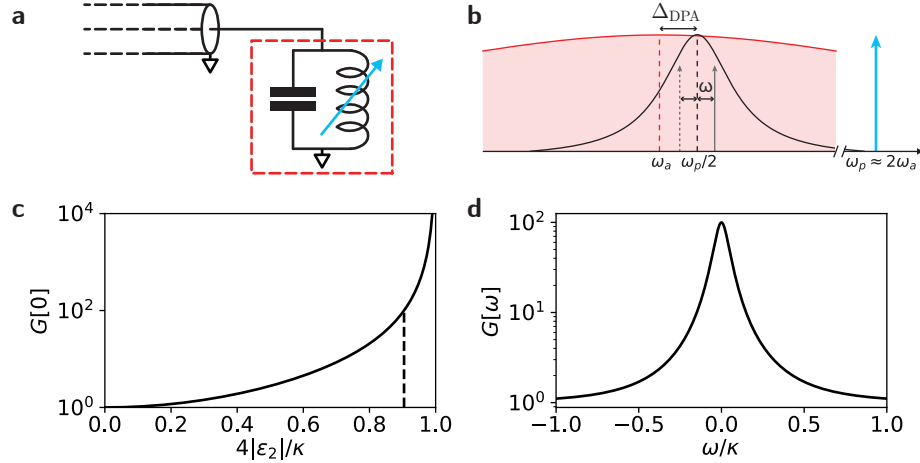
Figure 3.1 | (a) Simple example circuit for a DPA: a single mode coupled to single transmission line. (b) Lab frame frequency landscape to achieve parametric amplification. The bare density of states (red) indicates the mode's linear response centered at frequency ω_a with linewidth κ. When a strong microwave pump tone at frequency ω_p modulates the inductance (blue), the response (black) associated with a monochromatic input signal at frequency $\omega_p/2 + \omega$ (solid gray) is symmetric about $\omega_p/2$ *not* ω_a; the amplification process generates an image tone at the frequency $\omega_p/2 - \omega$ (dashed gray). (c) Dependence of the maximum phase-preserving power gain $G = G[\omega = 0]$ on squeezing drive strength ϵ_2 when $\Delta_{\mathrm{DPA}} = 0$ showing the parametric instability at $|\epsilon_2| = \kappa/4$. Dashed line indicates squeezing strength for (d). (d) Input signal frequency dependence of gain $G[\omega]$ showing near Lorenzian shape.

of the previous, so we have two coupled first-order differential equations of motion.

Taking the Fourier transform and using the boundary condition at the port given by Eq. 3.3 to eliminate a in favor of a_{out}, the scattering or input-output relationship for the output field

$$
\begin{aligned}
\boldsymbol{a}_{\mathrm{out}}[\omega] = & -\frac{(\omega - \Delta_{\mathrm{DPA}} + i\kappa/2)(-\omega - \Delta_{\mathrm{DPA}} + i\kappa/2) + 4|\epsilon_2|^2}{(\omega - \Delta_{\mathrm{DPA}} + i\kappa/2)(-\omega - \Delta_{\mathrm{DPA}} - i\kappa/2) - 4|\epsilon_2|^2} \boldsymbol{a}_{\mathrm{in}}[\omega] \\
& - \frac{i2\epsilon_2\kappa}{(\omega - \Delta_{\mathrm{DPA}} + i\kappa/2)(-\omega - \Delta_{\mathrm{DPA}} - i\kappa/2) - 4|\epsilon_2|^2} \boldsymbol{a}_{\mathrm{in}}[-\omega]^\dagger \quad (3.7) \\
= & \ g_s[\omega]\boldsymbol{a}_{\mathrm{in}}[\omega] + g_i[\omega]\boldsymbol{a}_{\mathrm{in}}[-\omega]^\dagger \quad (3.8)
\end{aligned}
$$

where the frequency ω is defined in the rotating frame and corresponds to the signal frequency $\omega_s = \omega + \omega_p/2$ in the lab frame. Note the notation $\boldsymbol{a}_{\mathrm{in}}[-\omega]^\dagger = (\boldsymbol{a}_{\mathrm{in}}[-\omega])^\dagger$ here corresponds to taking Hermitian conjugation *after* the Fourier transform [Boutin et al. 2017] emphasizing that the response in the lab frame at $\omega_s = \omega_p/2 + \omega$ depends on radiation at the image frequency $\omega_i = \omega_p/2 - \omega$ (see Fig. 3.1b); the opposite convention is often more convenient for dealing with generalized coupling matrices, especially involving multiple modes [Ranzani and Aumentado 2015].

In the last line we defined the signal amplitude gain $g_s[\omega]$ and the image amplitude gain $g_i[\omega]$, which obey the condition $|g_s[\omega]|^2 = |g_i[\omega]|^2 + 1$ enforcing a unitary squeezing transformation between input and output fields [Caves 1982]. The phase of the squeezing tunes with the phase of the squeezing drive ϵ_2. When both the signal and image at $\omega_{s/i} = \omega_p/2 \pm \omega$ are within the measurement bandwidth, $a_{\text{in}}[\omega]$ and $a_{\text{in}}[-\omega]^\dagger$ coherently interfere and the squeezing is evident in the higher moments of the statistics of the output field [Castellanos-Beltran et al. 2008; Boutin et al. 2017]. This regime is often called *phase-sensitive* or *phase-coherent degenerate parametric amplification* [Blackwell and Kotzebue 1961] since the interference manifests as amplifying a single quadrature of the incident signal and deamplifying the other.

In the opposite regime of *phase-preserving* or *phase-incoherent degenerate parametric amplification*, the measurement ignores the information at the image frequency. We may then define the phase-preserving power gain $G[\omega] = |g_s[\omega]|^2$, which can be algebraically transformed to

$$G[\omega] = 1 + \frac{|2\epsilon_2\kappa|^2}{(\kappa^2/4 + \Delta_{\text{DPA}}^2 - \omega^2 - 4|\epsilon_2|^2)^2 + (\kappa\omega)^2} \tag{3.9}$$

which depend on the squeezing drive strength ϵ_2 and the pump frequency through Δ_{DPA}. To achieve large power gain, the denominator of Eq. 3.9 must be close to zero. As seen in Fig. 3.1c, the gain diverges as ϵ_2 approaches $\sqrt{(\Delta_{\text{DPA}}^2 + \kappa^2/4)/4}$, which is the hallmark of parametric instability. For the linear parametric amplifier discussed in this chapter, we restrict $|\epsilon_2|^2 < (\Delta_{\text{DPA}}^2 + \kappa^2/4)/4$ as the model breaks down beyond this value. To properly model the dynamics above this threshold, we must include Kerr nonlinearity, which we save for a detailed discussion in Chapter 4 or Appendix A.

The maximum gain occurs at $\omega = 0$, corresponding to $\omega_p/2$ in the lab frame, and we denote it $G = G[0]$. The profile of $G[\omega]$ is approximately Lorenzian, as shown in Fig. 3.1d for an ϵ_2 such that $G = 100 = 20\,\text{dB}$, and we define the bandwidth B as the full width half maximum or the 3 dB bandwidth. From Eq. 3.9, we verify that this type of resonant amplifier suffers from a gain-bandwidth trade-off

$$B\sqrt{G} = \sqrt{\kappa^2 + 4\Delta_{\text{DPA}}^2}. \tag{3.10}$$

Although arbitrary Δ_{DPA} may be in principle compensated for by increasing $|\epsilon_2|$ in this model, in practice higher order nonlinearities not written in Eq. 3.5 limit the applied pump power. As such, usually we operate with $\Delta_{\text{DPA}} \lesssim \kappa$ and the bandwidth is limited to $B \approx \kappa/\sqrt{G}$.

With an idea of the scattering performance in phase-preserving mode, we may turn to the noise performance[1]. We have already made one crucial assumption necessary to reach quantum-limited noise performance: namely, the DPA has no internal losses or, equivalently, there is only a single port in the QLE Eq. 3.1 as depicted in Fig. 3.1a. A second port

---

[1] Based off a summary in [Aumentado 2020]

will allow signal to leak out, but the quantum-limit for total output noise will be the *same* by unitarity of the scattering matrix, clearly degrading the SNR (see [Boutin et al. 2017] for example calculation). Given the single-port assumption, the total output noise spectrum in the lab frame at $\omega_s = \omega_p + \omega$

$$N_{\text{out}}[\omega_s] = G[\omega]N_{\text{in}}[\omega_s] + (G[\omega] - 1)N_{\text{in}}[-\omega_i] \tag{3.11}$$

which is a combination of the input noise spectrum N_{in} from both the signal and the image frequencies[2]. For standard microwave engineering definitions [Pozar 2012], the noise temperature in the large gain limit for a in-band signal is

$$N_{\text{out}}[\omega_s]/k_B G[\omega] \approx (N_{\text{in}}[\omega_s] + N_{\text{in}}[-\omega_i])/k_B. \tag{3.12}$$

For superconducting parametric amplifiers, we often quote the noise *added* by the amplifier referred to the input $N_{\text{in}}[-\omega_i]$, which is determined at the *image* frequency. To reach the quantum-limit, the input at the image frequency must be sufficiently *idle* [3] and given by a 1D black-body spectrum with temperature T. When $T \ll \hbar\omega_i/k_B$, possible at $\sim$ GHz frequencies with helium dilution refrigeration, the added noise $N_{\text{in}} \approx \hbar\omega_i/2$, corresponding to one-half-photon of added noise per unit bandwidth or the *quantum limit* [Caves 1982].

3.3 The SNAIL parametric amplifier (SPA)

Given we understand how the ideal DPA from Sec. 3.2 realizes the requirement for quantum-limited amplification, we introduce the SNAIL parametric amplifier (SPA) as simple way to implement a DPA with three-wave mixing [Frattini et al. 2018]. We then investigate the trade-offs between the different requirements in Sec. 3.1 and ask the question: is it possible to improve the amplifier dynamic range without sacrificing other desirable characteristics? In this section, which focuses on the work in [Frattini et al. 2018], we answer affirmatively by demonstrating systematic improvement of the SPA's dynamic range. The SPA is based on an array of SNAILs, which provides the flexibility needed to optimize the three-wave mixing amplification process, while simultaneously minimizing the four-wave-mixing Kerr nonlinearity suspected to cause amplifier saturation [Eichler and Wallraff 2014; Liu et al. 2017]. With this flexibility, we have engineered an SPA that achieves a 1-dB compression power ($P_{-1\text{dB}} \in [-102, -112]$ dBm for $G = 20$ dB) on par with the best quantum-limited resonant parametric amplifiers [Mutus et al. 2014; Eichler et al. 2014; Roy et al. 2015], but over the entire tunable bandwidth of 1 GHz without sacrificing any other desirable characteristics. Importantly confirming the noise performance, the SPA improved the readout of a superconducting qubit, where the quantum efficiency of a phase-sensitive

---

[2]Derived by computing $(a_{\text{out}}^\dagger a_{\text{out}})[\omega]$ using Eq. 3.8 and rotating back to the lab frame.
[3]Hence, the term *idler* and *image* are often used interchangeably.

measurement chain involving an SPA was measured to be $\eta = 0.6$ in a self-calibrated manner [Touzard et al. 2019].

This demonstration of dynamic range improvement is crucially accompanied by first-principles theory that elucidates the link between the physical realization of the amplifier and the nonidealities of its response to large input signals. This link is accomplished in two steps. First, we show how to map the physical layout of the SPA to the phenomenological parameters that enter the input-output description of the device. These parameters consist of the three- and four-wave-mixing nonlinear components of the SPA Hamiltonian, which we derived in a lumped-element approximation in Section 2.2, as well as the damping induced through coupling to an input-output port. Second, we describe and validate experimentally how these phenomenological parameters directly determine the nonidealities in the amplifier's response to large input signals. Such a first-principles theoretical description opens the door to further improvements in amplifier dynamic range, which were recently achieved in SPAs [Sivak et al. 2019; Sivak et al. 2020] and further extended to a kinetic-inductance-based implementation of a DPA [Parker et al. 2021]. Furthermore, the optimizations applied here for increased dynamic range may be directly applied to increase the photon number of Schrödinger cat states used to store quantum information, which we will explore in detail starting in Chapter 4. More broadly, many forms of parametrically induced mixing for quantum-information processing may similarly benefit from these optimizations: for instance, frequency conversion for nonreciprocal devices [Sliwa et al. 2015; Lecocq et al. 2017], remote entanglement protocols [Pfaff et al. 2017; Axline et al. 2018; Kurpiers et al. 2018; Campagne-Ibarcq et al. 2018; Burkhart et al. 2021], gates between bosonically encoded qubits [Gao et al. 2018; Gao et al. 2019], and quantum simulation with bosons [Wang et al. 2020] to name a few recent examples.

3.3.1 SPA physical realization

In order to realize the ideal mixing Hamiltonian 3.5 of the DPA, we require nonlinearity and a single degree of freedom coupled to an input-output port. For previous three-wave mixing implementations of degenerate Josephson parametric amplifiers, flux-pumped DC-SQUIDs [Yamamoto et al. 2008; Zhou et al. 2014; Simoen et al. 2015] or RF-SQUIDs [Yurke et al. 1989; Zorin 2016] supply the nonlinearity. As the name implies, SNAILs supply the nonlinearity in the SPA. Depicted in Fig. 3.2a, a prototypical SPA is realized by placing M SNAILs at the center of a $\lambda/2$ section of microstrip transmission line. Fig. 3.2b shows an array of $M = 20$ SNAILs, where each SNAIL consists of an array of three large Josephson junctions (each inductance L_J) in a loop with one smaller junction (inductance L_J/α) as defined in Sec. 2.1. In practice, we chose the smallest L_J that was still larger than the parasitic geometric inductance of the $24\,\mu$m perimeter SNAIL loop such that the geometric inductance may be ignored in the derivation of the SNAIL potential Eq. 2.2. Adding appreciable geometric inductance compared to L_J would interpolate between the SNAIL
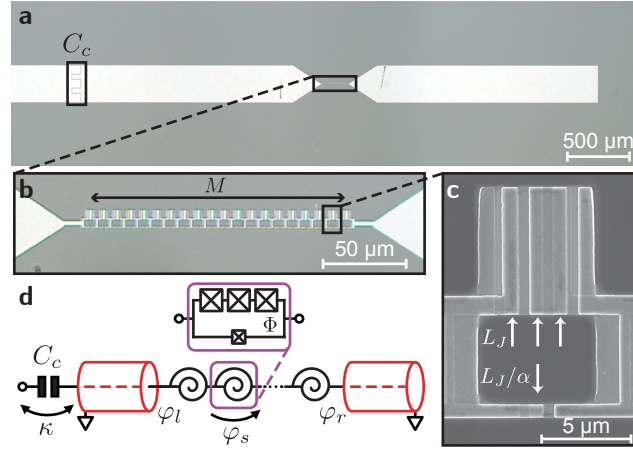
Figure 3.2 | (a) Optical microscope image and (d) corresponding circuit model of a SNAIL parametric amplifier (SPA). An array of M SNAILs is inserted at the center of a $\lambda/2$ section of microstrip transmission line, colored red in (d). (b) Image of an array of $M = 20$ SNAILs. (c) Electron micrograph of a single SNAIL with three larger junctions (each inductance L_J) in a loop with one smaller junctions (inductance L_J/α). Arrows indicate the junctions and the purple inset of (d) gives the SNAIL circuit schematic. In (d), φ_s denotes the phase drop across each SNAIL's small junction. The node phase φ_l (φ_r) denotes the location where the left (right) side of the array of SNAILs connects to the linear embedding structure. The dissipation rate κ is set by the capacitive coupling with cap C_c to the transmission line.

and RF-SQUID potentials, which both implement three-wave-mixing dipoles in their own right, at least assuming we respect the new condition to avoid hysteresis that the L_J/α is larger than the sum of all other inductance in the loop. Experimentally, avoiding this complication is convenient so that room temperature resistance is still a good proxy for total inductance without having to carefully calibrate the geometric inductance. The electron micrograph in Fig. 3.2c shows a representative SNAIL with junctions fabricated via a Dolan bridge process [Dolan 1977] for aluminum (Al) on silicon (Si).

The microstrip transmission-line sections are formed by a 2-μm-thick silver (Ag) layer deposited on the back of a 300-μm-thick high-resistivity Si wafer to act as a ground plane, and by center traces of Al whose length l_{MS} and width w_{MS} adjust the frequency ω_0 and the characteristic impedance Z_c. For all SPA devices presented here, we held the microstrip width constant at $w_{MS} = 300\,\mu$s to set $Z_c = 45\,\Omega$, and adjusted l_{MS} (in conjunction with M, α and L_J) to set the operating frequencies of the devices (see Sec. 3.3.3). The coupling to the $50\,\Omega$ transmission line κ used as the signal input-output port is set by an interdigitated gap capacitor (capacitance C_c) at one end of the SPA resonator. Later devices (E in Table 3.1 and [Sivak et al. 2019]) also have a second weakly capacitively coupled port on the opposite end of the resonator for delivery of the pump (not shown in Fig. 3.2a). Similarly fabricated microstrip resonators, but without any Josephson junctions, were measured to have internal quality factors ≈ 3000, consistent with the limitation imposed by the normal metal Ag

Table 3.1 | Constitutive parameters of 5 devices measured in the experiment: Josephson inductance of largest junction (L_J), number of SNAILs (M), junction inductance ratio (α), coupling capacitance to the $50\,\Omega$ transmission line (C_c), and frequency of the $\lambda/2$ microstrip embedding structure when the array of SNAILs is replaced by a short (ω_0).

Device	L_J (pH)	M	α	C_c (pF)	$\omega_0/2\pi$ (GHz)
A	60	1	0.29	0.048	8.4
B	67	10	0.29	0.039	11.4
C	47	20	0.09	0.068	17.9
D	44	20	0.09	0.075	23.5
E	34	20	0.09	0.088	23.4

backplane. By design, κ is much larger than this internal dissipation rate and the coupling to the pump port: an important requirement for achieving quantum-noise-limited performance.

The experimental characterization of the SPA devices (and all devices in this thesis) was performed in a helium-dilution refrigerator with base temperature of approximately $20\,\text{mK}$ and sufficient attenuation on the input lines from room temperature to ensure the incident radiation noise was quantum-limited at the frequencies within the amplifier's bandwidth [Krinner et al. 2019]. Reflection measurements off of the SPA were performed using a directional coupler to route the output signal to a standard cryogenic amplification setup; a microwave circulator would normally be used instead in future applications (e. g. qubit readout). While cold, a magnet coil mounted beneath the sample applies a magnetic flux Φ to each SNAIL, which we assume to be uniform across the array. All measurements were performed with a PNA-X network analyzer[4], which contains two microwave sources and the capability to quickly perform intermodulation distortion measurements. The strong pump tone needed for amplification was either combined with the signal tone at room temperature or applied on a separate pump line.

3.3.2 SPA model

The device is modeled with the circuit schematic of Fig. 3.2d. As in Sec. 2.1, we treat each SNAIL as a nonlinear inductor that provides an asymmetric potential energy $U_S(\varphi_s)$ Eq. 2.2 and corresponding current-phase relation $I_S(\varphi_s)$ Eq. 2.3, where φ_s is the phase drop across the small junction of the SNAIL. These functions are engineered via the junction inductance ratio α and the externally applied magnetic flux Φ. To include the linear embedding circuit, we enforce current conservation at the left and right boundary nodes of the SNAIL array (phases denoted φ_l and φ_r in Fig. 3.2d), which are connected to the ends of the respective transmission lines. As shown in the lumped element model in Sec. 2.2, properly handling this constraint equation is crucial for the prediction of higher-than-leading

---

[4]PNA-X network analyzer model Keysight N5242A.

order Hamiltonian terms such as Kerr.

While the lumped element model in Sec. 2.2 accurately models devices with either low or high participation ratios p, a distributed element model presented in Sec. A.3 is necessary to accurately capture the flux-dependence of Hamiltonian parameters in devices that cross over from small p at $\Phi/\Phi_0 = 0$ to near-unity p at $\Phi/\Phi_0 = 0.5$. To understand why, we examine the equation that implicitly determines the resonance frequency ω_a for the distributed element model:

$$\omega_a \tan\left(\frac{\pi}{2}\frac{\omega_a}{\omega_0}\right) = \frac{2Z_c}{ML_s(\Phi)} \tag{3.13}$$

where ω_0 is the frequency of the $\lambda/2$ microstrip embedding structure when the SNAIL array is replaced by a short circuit, and Z_c is the microstrip's characteristic impedance. Clearly, this does not match the lumped element frequency prediction $\omega_a = 1/\sqrt{C(ML_s + L)}$ Eq. 2.41 for arbitrary $L_s(\Phi)$. However, in the limit of small p or unity p corresponding to $ML_s \ll Z_c/\omega_a$ and $ML_s \gg Z_c/\omega_a$ respectively, the solution to Eq. 3.13 maybe be approximated by Eq. 2.41 for a suitable choice of L and C.

After quantization of the distributed element model, we express the Hamiltonian of the lowest frequency mode of the SPA up to fourth order as

$$\mathcal{H}_{\mathrm{SPA}}/\hbar = \omega_a \boldsymbol{a}^\dagger \boldsymbol{a} + g_3 \left(\boldsymbol{a} + \boldsymbol{a}^\dagger\right)^3 + g_4 \left(\boldsymbol{a} + \boldsymbol{a}^\dagger\right)^4 \tag{3.14}$$

where $\boldsymbol{a}^\dagger$ ($\boldsymbol{a}$) is the harmonic oscillator creation (annihilation) operator obeying $\left[\boldsymbol{a}, \boldsymbol{a}^\dagger\right] = 1$, ω_a is the resonant frequency of the standing mode, and the third- and fourth-order nonlinearities are denoted g_3 and g_4 respectively. These three Hamiltonian parameters are all tuned *in situ* via the applied magnetic flux Φ through each SNAIL loop. Along with the coupling rate to the transmission line κ, the parameters of $\mathcal{H}_{\mathrm{SPA}}$ determine behavior of the SPA as a degenerate parametric amplifier as we show next.

Pumping an SPA for gain

To operate the SPA as a three-wave-mixing DPA, we apply a strong pump tone at $\omega_p = 2(\omega_a + \Delta) \approx 2\omega_a$ with mean intracavity amplitude α_p. We wish to analyze the response of incident signals so we first seek an effective Hamiltonian of the oscillator in the presence of this strong pump tone. To accomplish this, we displace the oscillator by $\alpha_p e^{-i\omega_p t}$ and with foresight move to a rotating frame at $\omega_p/2$, which, within the rotating wave approximation (RWA), corresponds to the substitution

$$\boldsymbol{a} \to \boldsymbol{a} e^{-i\omega_p t/2} + \alpha_p e^{-i\omega_p t} \tag{3.15}$$

into the SPA Hamiltonian $\mathcal{H}_{\mathrm{SPA}}$ Eq. 3.14. The cubic term in the Hamiltonian responsible for three-wave mixing transforms

$$
\begin{aligned}
g_3 \left(\boldsymbol{a} + \boldsymbol{a}^\dagger \right)^3 &\to g_3 \left(\boldsymbol{a} e^{-i\omega_p t/2} + \alpha_p e^{-i\omega_p t} + \boldsymbol{a}^\dagger e^{+i\omega_p t/2} + \alpha_p^* e^{+i\omega_p t} \right)^3 \\
&= 3g_3 \left(\alpha_p \boldsymbol{a}^{\dagger 2} + \alpha_p^* \boldsymbol{a}^2 \right) + \mathcal{H}_{\mathrm{rotating}}(t)/\hbar \\
&\approx 3g_3 \left(\alpha_p \boldsymbol{a}^{\dagger 2} + \alpha_p^* \boldsymbol{a}^2 \right)
\end{aligned}
\tag{3.16}
$$

where in the second line we grouped the terms into the rotating ones with explicit time dependence, and those resonant terms that are static. Taking the time average over a drive period makes the RWA and results in an effective time-independent Hamiltonian term corresponding to a single-mode squeezing Hamiltonian, the crucial term for parametric amplification in a DPA as in Eq. 3.5.

Continuing this procedure for the remaining terms in $\mathcal{H}_{\mathrm{SPA}}$, we arrive at the effective Hamiltonian in the frame rotating at $\omega_p/2$

$$
\mathcal{H}_{\mathrm{SPA,eff}}/\hbar = -\Delta_{\mathrm{DPA}} \boldsymbol{a}^\dagger \boldsymbol{a} + \epsilon_2 \boldsymbol{a}^{\dagger 2} + \epsilon_2 \boldsymbol{a}^2 + K \boldsymbol{a}^{\dagger 2} \boldsymbol{a}^2
\tag{3.17}
$$

which we identify as the effective DPA Hamiltonian Eq. 3.5 but with the addition of a spurious Kerr nonlinearity[5]. This Kerr term is not innocuous and has serious consequences for the dynamic range of various pumped processes, especially amplifier saturation as we will explore in detail. For further example, the photon-number-dependent rotation of phase space caused by Kerr leads to the distortion of quantum states of light in a microwave cavity at the level of a few photons [Kirchmair et al. 2013; Vlastakis et al. 2013] as well as the "bananization" of squeezing [Boutin et al. 2017; Malnou et al. 2018]. Moreover, the nonlinearity is crucial for regulating the dynamics above the parametric instability threshold by stabilizing Schrödinger cat states, which we examine in detail in Chapter 4.

How do the parameters in the effective Hamiltonian $\mathcal{H}_{\mathrm{SPA,eff}}$ relate to the drive strength α_p and the bare Hamiltonian $\mathcal{H}_{\mathrm{SPA}}$? In principle, the above analysis generates this mapping, but the RWA here is not valid because the pump frequency $\omega_p \approx 2\omega_a$ is detuned from the oscillator frequency by $\approx \omega_a$ itself. There exist many perturbative methods for going beyond the RWA, which have been recently summarized and extended [Venkatraman et al. 2021]. In Appendix A, we use one such semiclassical method based on *harmonic balance*. To

---

[5]In this section, we ignore the small Lamb shift such that $s = -\kappa/2 \pm j\omega_a$ denote the complex pair of poles of the unpumped SPA's small signal response.

second order, it generates the *same* effective Hamiltonian with parameter mapping

$$\Delta_{\text{DPA}}(|\alpha_p|^2) \approx \Delta - \left(\frac{32}{3} g_4 - 28 \frac{g_3^2}{\omega_a} \right) |\alpha_p|^2 \tag{3.18}$$

$$\epsilon_2(\alpha_p) \approx 2 g_3 \alpha_p \tag{3.19}$$

$$K(|\alpha_p|^2) \approx 6 \left(g_4 - 5 \frac{g_3^2}{\omega_a} \right) + \mathcal{O}(|\alpha_p|^2) \tag{3.20}$$

where $\Delta = \frac{\omega_p}{2} - \omega_a$ is the bare pump detuning, Δ_{DPA} now includes the pump-induced Stark shift, the squeezing strength ϵ_2 has a new combinatorial prefactor but is otherwise unchanged from the RWA calculation, and $K(0) = K$ from our second-order perturbation theory calculation Eq. 2.53 in the undriven circuit. Note, these pump-induced Stark shifts are suspected to limit the achievable gain in multipumping schemes for directional amplification [Sliwa et al. 2015; Lecocq et al. 2017] and their corollary in traveling-wave parametric amplifiers (TWPAs) deteriorates phase matching [O'Brien et al. 2014; Macklin et al. 2015; Vissers et al. 2016; Ranzani et al. 2018; Planat et al. 2020].

Given the pumped SPA implements a similar effective Hamiltonian to the DPA, we might expect the SPA to also perform quantum-limited parametric amplification. To analyze the response to an incoming signal at frequency ω_s, in Appendix A we write the QLE without the RWA [Gardiner and Zoller 2004] and utilize the input-output formalism within a semiclassical[6] harmonic balance approximation to derive the phase-preserving power gain of the SPA. Assuming ω_s is near $\omega_p/2$ and that there are $|\alpha_s|^2$ signal and $|\alpha_i|^2$ idler intraresonator average steady-state photons due to the incident signal, we find

$$\begin{aligned} G[\omega] &= 1 + \frac{4|\epsilon_2|^2 \kappa^2}{\left((\Delta_i - \omega)(\Delta_s + \omega) + \kappa^2/4 - 4|\epsilon_2|^2 \right)^2 + (\Delta_i - \Delta_s - 2\omega)^2 \kappa^2/4} \\ &\approx 1 + \frac{4|\epsilon_2|^2 \kappa^2}{\left(\Delta_s^2 - \omega^2 + \kappa^2/4 - 4|\epsilon_2|^2 \right)^2 + \omega^2 \kappa^2} \end{aligned} \tag{3.21}$$

where $\omega = \omega_s - \omega_p/2$, $\Delta_{s/i}(|\alpha_p|^2, |\alpha_s|^2, |\alpha_i|^2) = \Delta_{\text{DPA}}(|\alpha_p|^2) - K(|\alpha_p|^2) \times (|\alpha_{s/i}|^2 + 2|\alpha_{i/s}|^2)$ and in the last line we have used $\Delta_i \approx \Delta_s$ in the large gain limit where $|\alpha_i|^2 \approx |\alpha_s|^2$.

The gain in this limit exactly reproduces the DPA gain Eq. 3.9 but with an effective detuning that includes the Stark shift induced by both the amplification pump and the incident signal. Note that maximum gain G always occurs at $\omega_s = \omega_p/2$, similar to a flux-pumped JPA [Yamamoto et al. 2008; Zhou et al. 2014; Simoen et al. 2015], making the SPA particularly easy to tune up and operate. This property is in contrast with the tuneup procedure for Josephson parametric converters (JPCs) and even four-wave-mixing JPAs, as outlined in Refs. [Liu et al. 2017] and [Hatridge et al. 2011] respectively.

---

[6]Semiclassical refers to the assumption $|\alpha_s|^2 \gg 1$ and $|\alpha_i|^2 \gg 1$, satisfied for any high-gain amplifier even for single-photon level incident signals.
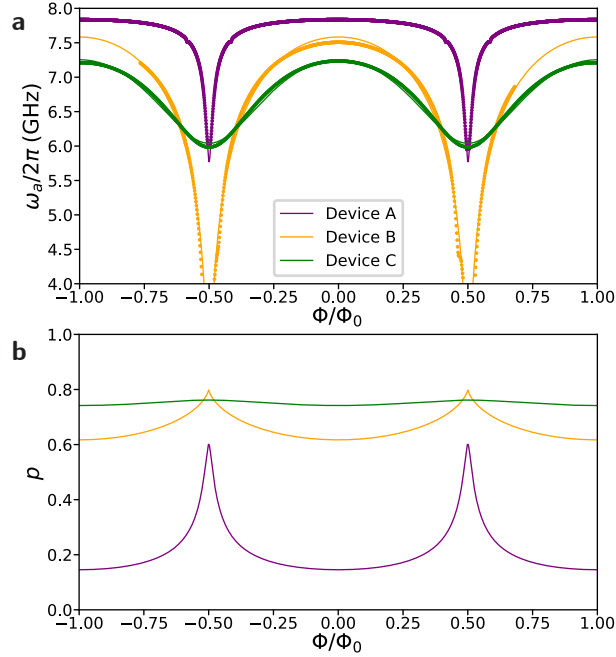
Figure 3.3 | (a) Resonant frequency ω_a as a function of applied magnetic flux Φ for three devices. Solid lines are fits a model based on the schematic in Fig. 3.2d. (b) Inductive participation of the SNAIL array $p = ML_s/(ML_s + L)$ extracted from the model.

As shown by Eq. 3.21, designing an amplifier operating at ω_s reduces to engineering ω_a, g_3, g_4, and κ. This task is accomplished by the appropriate choice of the physical knobs described in Sec. 3.3.1. To illustrate control over these Hamiltonian parameters and provide intuition on this mapping, we compare the set of devices listed in Table 3.1. Throughout this chapter, we will choose $\omega_p = 2\omega_a$ for simplicity, but intentionally detuning the pump can be a useful tool for achieving Kerr-free three-wave mixing [Sivak et al. 2019].

3.3.3 SPA Hamiltonian characteristics

Resonant frequency tunability

We first compare the linear-response characteristics of these devices, specifically the resonant frequency ω_a as a function of applied magnetic flux Φ shown in Fig. 3.3a. The tunability range of ω_a depends on two factors:

1. the flux-tunable SNAIL inductance $L_s(\Phi)$,

2. the participation of the SNAIL array in its embedding structure.

Multiple physical knobs affect both of these factors; here for simplicity we focus on the influence of α and M.

The first factor, the flux dependence of $L_s(\Phi)$, is strongly analogous to that of a DC-SQUID or an RF-SQUID [Clarke and Braginski 2004]: the inductance is tunable between

a minimum at $\Phi/\Phi_0 = 0$ and a maximum at $\Phi/\Phi_0 = 0.5$. The range of this tunability is given by the asymmetry between the inductance in either arm of the superconducting loop which, in the SNAIL, is controlled by the junction inductance ratio α. $\alpha = 1/n$, where n is the number of large junctions as in Sec. 2.1, corresponds to perfect inductive symmetry, resulting in $L_s(0.5\Phi_0) \to \infty$. $\alpha > 1/n$ causes the SNAIL to have multiple inequivalent potential minima and results in hysteretic behavior, which we wish to avoid in a weakly nonlinear oscillator for amplification. $\alpha < 1/n$ gives some asymmetry, where smaller α corresponds to a smaller inductive tunability range.

The second factor influencing the tunable range of ω_a is the fraction of the mode inductance coming from the SNAILs, summarized by the participation ratio, given by $p = ML_s/(L + ML_s)$ in the lumped element model. For a given SNAIL design with an $L_s(\Phi)$, the participation ratio is controlled by the number of SNAILs M in series as well as the length l_{MS} and width w_{MS} of the surrounding microstrip embedding structure. In practice, M provides more control over ω_a due to the practical difficulty in realizing microstrip (or any linear) embedding structures with impedances significantly different from $50\,\Omega$. Thus, M and α are chosen first and then we adjust l_{MS} (while keeping w_{MS} fixed in these devices) to hit our desired operating frequency range.

Focusing on the Φ dependence of ω_a in devices B and C in Fig. 3.3a, we see the ability of α and M to engineer the frequency tunability. For $\alpha = 0.29$ as in device B, the total inductance on either arm of the SNAIL are nearly equal so the SNAIL inductance changes drastically from $\Phi/\Phi_0 = 0$ to $\Phi/\Phi_0 = 0.5$. Conversely, the inductance of each $\alpha = 0.09$ SNAIL in device C changes only a little and the aggregation of these small changes for all 20 SNAILs gives the device its approximately 1 GHz of tunability, nearly a factor of 5 larger than typical values for JPCs [Schackert 2013; Flurin 2015]. This 1 GHz of tunability is achieved while also maintaining a nearly constant participation ratio as shown in Fig. 3.3b, which will have important consequences for the flux dependence of g_3 and g_4 in the next section.

Nonlinear characteristics

Having described the linear response of the SPA resonator, we next demonstrate its operations as a three-wave-mixing DPA. We applied a strong microwave pump tone at $\omega_p = 2\omega_a$ and adjusted the pump power to achieve a maximum of 20 dB of small-signal reflection gain. The near Lorenzian signal frequency dependence is shown for a representative bias point in Fig. 3.4a, conforming to the prediction of Eq. 3.21 at least for the band around the peak gain at $\omega_p/2$. One standard phenomenon that limits amplifier quality is the saturation of the gain with increasing input signal power. As shown in Fig. 3.4b, we measured the input-referred 1-dB compression point $P_{-1\mathrm{dB}}$ as the input signal power where the gain drops by 1 dB. To understand this phenomenon and increase the $P_{-1\mathrm{dB}}$, we perform a systematic study across multiple devices.
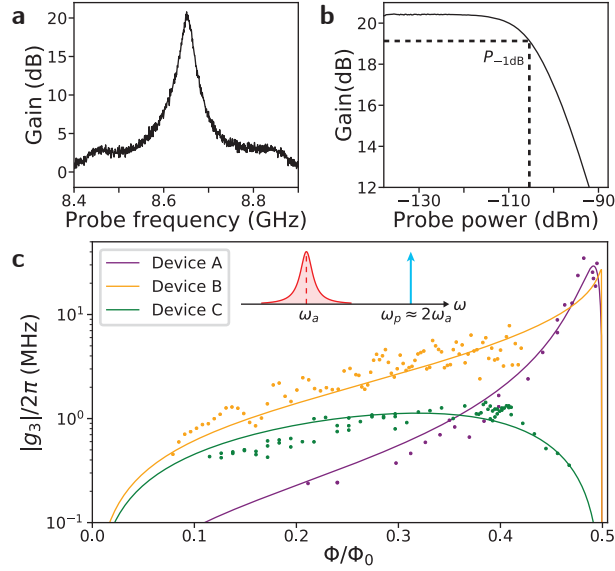
Figure 3.4 | (a) Reflection gain versus input signal frequency when the SPA is biased with a strong tone at $\omega_p \approx 2\omega_a$, frequency landscape inset of (c). (b) Gain G as a function on input signal power shows amplifier saturation. Input power at which the gain reduces by 1 dB is denoted P_{-1dB}. (c) Third-order nonlinearity g_3 versus applied magnetic flux Φ. Solid curves are first-principles theory for g_3.

Toward this goal, we measure the nonlinearity of the SPA Hamiltonian $\mathcal{H}_{SPA}$ Eq. 3.14 as a function of applied flux Φ for all devices in Table 3.1. The dependence of the third order nonlinearity g_3 on Φ is shown in Fig. 3.4c for three representative devices. We extract g_3 by tuning of a $G = 20\,$dB gain point and using the measured values of ω_a and κ as well as a calibration on the applied pump power. Also shown is our first-principles theory calculation, which uses only the linear characteristics fit from Fig. 3.3a and room-temperature measurements of the resistance of the SNAIL array. A global scale factor of ≈ 2 has been applied to the extracted g_3, which could arise from pump-power calibration or the enhanced coupling of the pump to the SNAILs through higher-frequency modes not considered in our simple model.

Comparing devices A and C, we note the relatively constant g_3 for device C ($\alpha = 0.09$) except near $\Phi/\Phi_0 = 0$ and $\Phi/\Phi_0 = 0.5$, where symmetry forbids three-wave mixing terms. In contrast, device A ($\alpha = 0.29$) shows two orders of magnitude variation in g_3 over the same flux range. This comparison highlights the drastic difference in the flux profile of g_3 possible by choices in design parameters. Here, the difference mainly arises from the junction inductance ratio α causing a stark difference in the participation ratio p versus Φ (see Fig. 3.3b), and that g_3 depends strongly on p as in Eq. 2.45.

The fourth-order nonlinearity g_4 is extracted from a Stark shift measurement. In this experiment, we applied a strong approximately 500 MHz detuned drive that populates the resonator with $\bar{n}$ average steady-state photons and shifts its resonant frequency. Here, $\bar{n}$
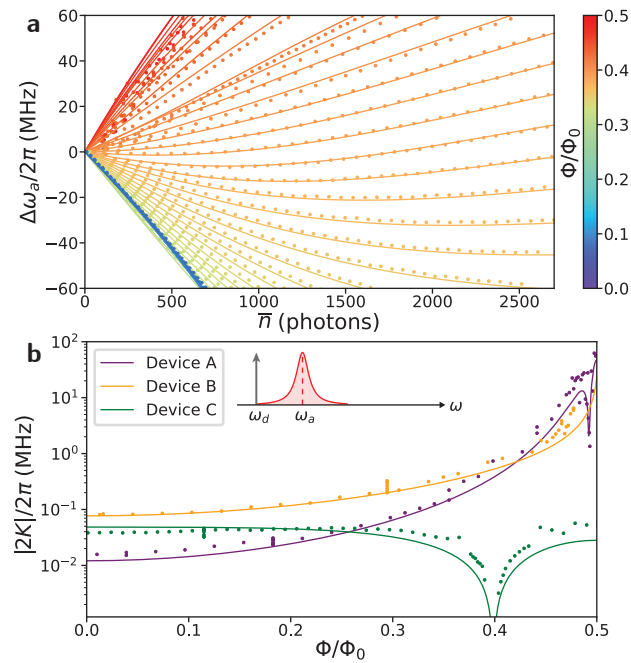
Figure 3.5 | (a) Frequency shift $\Delta\omega_a$ versus the number of steady-state photons populating the resonator $\bar{n}$ induced by a detuned drive tone at ω_d [inset of (b)]. The measured shift is plotted for a few different applied magnetic fluxes Φ (denoted with color). Solid lines are fits to $\Delta\omega_a = 4K\bar{n} + 18K'\bar{n}^2$. (b) Magnitude of the extracted anharmonicity $|2K|$ as a function of applied magnetic flux Φ. Solid lines are first principles theory for the anharmonicity $|2K|$.

Table 3.2 | *In situ* tunable range of phenomenological parameters of five devices measured in the experiment: resonant frequency (ω_a), coupling to the $50\,\Omega$ transmission line (κ), third-order nonlinearity (g_3), and fourth-order nonlinearity (g_4) where we quote the average for devices C, D, and E disregarding the $0.1\,\Phi_0$ region around the Kerr-free point. All parameters given in MHz, except for $\omega_a/2\pi$ in GHz.

Device	$\omega_a/2\pi$ (GHz)	$\kappa/2\pi$ (MHz)	$|g_3|/2\pi$ (MHz)	$|g_4|/2\pi$ (MHz)
A	<6 – 7.84	35 – 55	0.3 – 30	0.001 – 4.9
B	<4 – 7.51	30 – 35	0.5 – 60	0.006 – 0.5
C	5.99 – 7.24	90 – 120	0.4 – 1.5	0.004
D	7.09 – 8.37	180 – 250	0.5 – 1.8	0.003
E	7.76 – 9.24	270 – 440	0.7 – 2.0	0.004

is calibrated using fits of ω_a, κ, and room-temperature line attenuation. In Fig. 3.5a, we plot the measured frequency shift $\Delta\omega_a$ of a typical SPA resonator as a function of $\bar{n}$ and applied magnetic flux Φ (color). The frequency shift changes from negative to positive over half of a flux quantum, indicating a Kerr-free region at some flux. The solid lines are fits to $\Delta\omega_a = 4K\bar{n} + 18K'\bar{n}^2$. From this fit, we extract the Kerr nonlinearity K as defined in Eq. 3.20, which is related to Hamiltonian parameters g_3 and g_4 up to second order in perturbation theory by $K = 6(g_4 - 5g_3^2/\omega_a)$ as derived in Eq. 2.53.

The dependence of K and thus g_4 on Φ is shown in Fig. 3.5b for three representative devices together with our first-principles theory calculation. The contrast between device A and C again highlights the effect of α on the flux profile. Specifically, device A shows a three order of magnitude change in anharmonicity $2K$, while device C's anharmonicity is relatively constant over most of the flux range. Additionally, both devices nominally support a region of suppressed Kerr. However, device A attains this region over a very narrow flux range, making the suppression regime practically useless, while device C shows a robust suppression regime by more than an order of magnitude from its $\Phi/\Phi_0 = 0$ value. The precise flux at which $2K = 0$ depends on α and the series linear inductance through the participation ratio p as seen in Eq. 2.53. this suppression could be useful in application where the circuit design wants some nonlinearity for mixing purpose, but would prefer to suppress spurious Kerr interactions.

Such Kerr suppression at low power is a robust feature of devices based on SNAILs with $\alpha \approx 1/n^2$ [Frattini et al. 2018; Sivak et al. 2019; Sivak et al. 2020] and has also recently been achieved in amplifiers based on shunted-JRMs [Chien et al. 2020]. While devices based on RF-SQUIDs should similarly show a Kerr-free flux-bias point [Zorin 2016], any device based on DC-SQUIDs is incapable of such a suppression point. Additionally, gradiometric SNAILs show promise in extending the Kerr-free point to a continuum of different operating frequencies.

While our previous comparison of devices A–C focused on the flux profile of g_3 and g_4, their overall magnitudes must also be engineered for optimizing amplifier nonideal-

ities, such as saturation power. Besides α and L_J, these magnitudes are also influenced by the number of SNAILs M, on which we focused in Sec. 2.3. To recap, at small values, increasing M strongly affects $|g_3|$ and $|g_4|$, but we note its influence substantially weakens for $M \gtrsim 20$. In fact, decreasing Kerr by more than a factor of 2 requires increasing $M > 200$ when practical design constraints are considered; only at $M \approx 2000$ does the suppression factor become 10 for a mode at the desired operating frequency [Sivak et al. 2020]. As such, subsequent devices (D, E and [Sivak et al. 2019]) have similar magnitudes of nonlinearities and flux profiles to device C, but instead vary the coupling to the transmission line κ. A summary of these phenomenological parameters for all devices is given in Table 3.2. As we show next, these factors affect the gain compression.

3.3.4 SPA dynamic range

Gain compression

Having established the connection between the physical parameters of our device and the properties of $\mathcal{H}_{\mathrm{SPA}}$ Eq. 3.14, we now optimize the nonlinearities (g_3 and g_4) and the coupling to the transmission line (κ) to achieve higher dynamic range. But first, we review the cause of amplifier saturation.

The gain of an ideal DPA Eq. 3.9 shows no dependence on input signal power in accordance with a perfectly linear amplifier, and therefore does not capture the phenomenon of amplifier saturation that is clearly evident in the example Fig. 3.4b. However, the SPA gain Eq. 3.21 that we derived indeed depends on input signal power through the detunings $\Delta_{s/i}(|\alpha_p|^2, |\alpha_s|^2, |\alpha_i|^2)$, which themselves depend in the average number of steady state signal/idler photons $|\alpha_{s/i}|^2$.

Considering the on resonance response $G[\omega = 0]$, we see that we can tune the pump strength α_p and thus ϵ_2 (Eq. 3.19) such that the denominator of Eq. 3.21 goes to 0 and the gain $G = G[0]$ diverges. Resonant parametric amplifiers operate very close to this parametric instability, with ϵ_2 chosen such that the small-signal gain denoted $G_0 = 20\,\mathrm{dB}$ in this work, or sufficiently high for the desired application. As a result, slight changes in this denominator are enough to significantly affect the gain G, altering it from its small-signal value G_0.

Two causes of gain compression can be associated with changes in the denominator of Eq. 3.21:

1. **Kerr-induced Stark shifts**: shifts in $\Delta_{s/i}$ with increasing signal power. More signal power increases α_s and shifts the resonant frequency due to Kerr $K(|\alpha_p|^2)$, defined in Eq. 3.20.

2. **Pump depletion**: the breakdown of the stiff-pump approximation that α_p and thus ϵ_2 and Δ_{DPA} can be considered constant (see Eqs. 3.18–3.19).

Focusing first on Kerr-induced Stark shifts, we now derive a closed form expression for the on-resonance input signal power P_{in} at which the gain changes from G_0 to G. Ignoring pump depletion for now, we work in the approximation that α_p is independent of signal power P_{in}, often termed the *stiff-pump* approximation [Kamal, Marblestone, and Devoret 2009; Roy and Devoret 2018]. Using input-output theory, we can establish the relation between P_{in} and intraresonator populations $|\alpha_{s/i}|^2$. For large gain $G \gg 1$, we obtain $|\alpha_s|^2 \approx |\alpha_i|^2 \approx G P_{\text{in}}/\hbar\omega_a\kappa$ with relative error $\delta(|\alpha_s|^2)/|\alpha_s|^2 \sim 1/\sqrt{G}$. In this approximation, we have

$$G \approx 1 + \frac{4|\epsilon_2|^2\kappa^2}{\left(\Delta_s^2 + \kappa^2/4 - 4|\epsilon_2|^2\right)^2} \tag{3.22}$$

$$G_0 \approx 1 + \frac{4|\epsilon_2|^2\kappa^2}{\left(\Delta_{\text{DPA}}^2 + \kappa^2/4 - 4|\epsilon_2|^2\right)^2} \tag{3.23}$$

where in the second line we have used $\Delta_{s/i}(|\alpha_p|^2, 0, 0) = \Delta_{\text{DPA}}(|\alpha_p|^2)$ for the small-signal gain (see Eq. 3.18) and

$$\Delta_s \approx \Delta_{\text{DPA}} - 6K\frac{G P_{\text{in}}}{\hbar\omega_a\kappa}. \tag{3.24}$$

Plugging in the result for G into Eq. 3.24 and eliminating ϵ_2 in favor of G_0, the input power at which the gain becomes G

$$P_{\text{in}} = \frac{\hbar\omega_a\kappa^2}{6KG}\left(\frac{\Delta_{\text{DPA}}}{\kappa} \pm \sqrt{\frac{\Delta_{\text{DPA}}^2}{\kappa^2} + \frac{\sqrt{G_0} - \sqrt{G}}{\sqrt{G_0 G}}\sqrt{\frac{\Delta_{\text{DPA}}^2}{\kappa^2} + \frac{1}{4}}}\right) \tag{3.25}$$

where $K(|\alpha_p|^2)$ and $\Delta_{\text{DPA}}(|\alpha_p|^2)$ still depend on pump power and thus implicitly on G_0.

Instead of proceeding to eliminate this implicit dependence, for simplicity we consider the case for small negative Kerr and $K(|\alpha_p|^2) \approx K(0) = K$ and $\Delta_{\text{DPA}} \approx \Delta_{\text{DPA}}(0) = \omega_p/2 - \omega_a$. For positive pump detuning $\omega_p > 2\omega_a$, Eq. 3.25 admits one solution for $G < G_0$ and no solutions for $G > G_0$. However for negative detuning, two solutions are possible for $G > G_0$ and one for $G < G_0$: a phenomenon observed and termed *shark fin* shape in JPCs [Liu et al. 2017] and later in SPAs [Sivak et al. 2019].

For the purposes of improving gain compression, we simplify to the case $\omega_p = 2\omega_a$, where

$$P_{\text{in}} = \frac{\kappa}{6|K|} \times \frac{\hbar\omega_a\kappa}{G^{5/4}}\sqrt{\frac{1}{2}\left(1 - \sqrt{\frac{G}{G_0}}\right)} \tag{3.26}$$

may be used to guide our circuit optimization. We see that increasing $P_{-1\text{dB}}$ requires reducing the Kerr-to-dissipation ratio $|K|/\kappa$.

Returning to the second cause of gain compression, *pump depletion* arises from the breakdown of the stiff-pump approximation [Kamal, Marblestone, and Devoret 2009; Roy and

Devoret 2018]. The intrinsic nonlinear coupling required for amplification necessarily couples the source supplying the pump amplitude α_p to the signal amplitude α_s (c. f. Eq. 3.4). Thus, increasing α_s changes α_p and consequently the denominator of Eq. 3.21. Assuming $g_4 = 0$ and considering the derivative of gain with respect to $|\alpha_p|^2$, we can estimate the compression power due to pump depletion as

$$P_{-1\text{dB}}^{\text{pump dep}} \sim \frac{\kappa}{g_3^2/\omega_a} \frac{1}{G_0^{3/2}} \hbar \omega_a \kappa. \tag{3.27}$$

Since this compression mechanism originates directly from the third-order nonlinearity needed for amplification, it is intrinsically unavoidable. Note that, in principle, the limit on fluctuations of $|\alpha_p|^2$ is lower-bounded by quantum fluctuations of the mode supplying the pump; in practice, the semiclassical approximation is often sufficient.

Given these limits on dynamics range, we examine Eqs. 3.26 and 3.27 to formulate a recipe for higher compression powers: decrease nonlinearities g_3 and K, and increase the dissipation κ. Intuitively, this recipe pushes the optimization closer to system that obeys the assumptions underlying Eq. 3.9 for the gain of a DPA, namely a more linear oscillator.

Following this recipe requires more applied pump power to reach the desired gain. However, we must be mindful that the current through the SNAIL does not approach the critical current of its Josephson junctions. In practice, applying pump currents that approach the critical current does not directly cause gain compression, but instead determines whether the amplifier achieves the desired small-signal gain in the first place. To quantitatively understand this limit, we consider the number of pump photons $|\alpha_p|^2$ required to reach the parametric instability or $G \to \infty$ when $\omega_p = 2\omega_a$

$$n_\infty = \left(\frac{\kappa}{8g_3} \right)^2$$

$$= \frac{9}{4} \left(\frac{\kappa}{\omega_a} \frac{c_2}{pc_3} \right)^2 \left(\frac{M}{p\varphi_{\text{zpf}}} \right)^2 \tag{3.28}$$

where in the second line we have written g_3 with Eq. 2.45. Recalling that the critical current limits maximum number of allowed photons in the resonator $n_{\text{crit}} \approx 15(M/p\varphi_{\text{zpf}})^2$ Eq. 2.48, we require $n_\infty < n_{\text{crit}}$ implying

$$1 < \frac{20}{3} \left(pQ \frac{c_3}{c_2} \right)^2 \tag{3.29}$$

where $Q = \omega_a/\kappa$ is the quality factory, c_2 and c_3 are the Taylor coefficients of the SNAIL potential Eq. 2.5, and the prefactor depends on the precise definition of n_{crit}. As such, this limitation translates to the $pQ \gtrsim 1$ constraint in JPAs [Eichler et al. 2014] and JPCs [Abdo, Kamal, and Devoret 2013]. All amplifiers presented here have $pQ > 15$ to ensure that the amplifier produced 20 dB of small-signal gain.
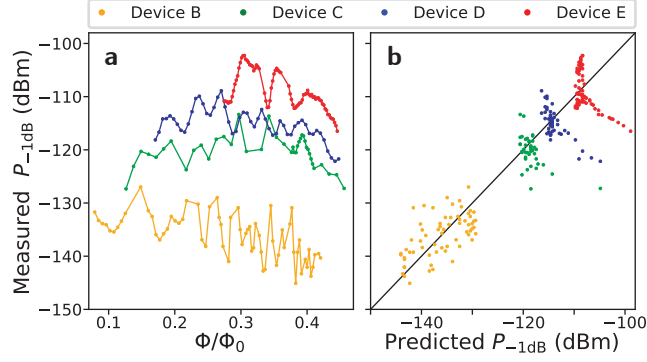
Figure 3.6 | (a) Measured 1-dB compression power $P_{-1\text{dB}}$ as a function of applied magnetic flux Φ for four devices biased at $G = 20\,\text{dB}$ gain. (b) Comparison between measured value and first-principles theory, which semiclassically treats pump depletion and Stark shifts to second order in harmonic balance.

We followed the recipe of reducing nonlinearities and increasing dissipation to design our devices (see Table 3.2) and compared their 1-dB compression powers in Fig. 3.6a as a function of applied flux Φ. For each point, we measured the resonant frequency ω_a, applied a pump at $\omega_p = 2\omega_a$ and adjusted the power to get $G = 20\,\text{dB}$. We then measured the $P_{-1\text{dB}}$ input-referred gain compression power as in Fig. 3.4b. Fig. 3.6b shows the correlations between our first-principles theory prediction of saturation power with the measured $P_{-1\text{dB}}$, where the black line indicates agreement between theory and experiment. This theory self-consistently solves the semiclassical Langevin equations of motion to obtain α_s and α_i for given input pump and signal powers and the gain calculated from there (see Appendix A and [Frattini et al. 2018]). We find that, for our devices, the Stark shift mechanism of gain compression closely approximates the full numerical solutions. In fact, the analytical formula Eq. 3.25 reproduces well the compression power of later devices even for appreciable pump detunings [Sivak et al. 2019].

To confirm the dependence of $P_{-1\text{dB}}$ on K, we focus on device B, which has the largest $|g_4|/2\pi \in [6, 530]\,\text{kHz}$ for different flux bias points. This change in g_4 and thus K results in a systematic 15 dB change in $P_{-1\text{dB}}$ and the theory predicts the trend. Note the scatter in the data of Fig. 3.6 results from ripples in the impedance of the transmission line seen by the SPA, which affects its linewidth κ. The compression power is highly sensitive to this parameter $\propto \kappa^2$ as visible in Eqs. 3.26 and 3.27. In these devices, these ripples predominately originated from the relatively long cable between the sample and the directional coupler used to separate input from output signals. Improvements in device packaging have since enabled shortening the cable and mounting the SPA directly onto a circulator, which drastically reduces this scatter [Sivak et al. 2019].

For device C, we engineered $\kappa/2\pi \in [90, 120]\,\text{MHz}$ and $|g_4|/2\pi \approx 4\,\text{kHz}$ except near its Kerr-free region (see Fig. 3.5b). These changes in κ and K directly result in device C's increased perfomance compared to device B. Devices D and E are similar to device

C but with increasing $\kappa/2\pi$ to [180, 250] MHz and [270, 400] MHz respectively, and again show improved performance. Specifically, the best device, device E, achieves $P_{-1\text{dB}} \in$ [−112, −102] dBm, which is on par with the best known quantum-limited resonant parametric amplifiers [Mutus et al. 2014; Eichler et al. 2014; Roy et al. 2015]. We stress that this performance, achieved with a dynamic bandwidth of 30–40 MHz, is consisted over the entire tunable bandwidth[7] of 1 GHz.

Despite this increase in dynamic range, Fig. 3.6b shows that theory predicted that we should have achieved higher saturation powers at certain applied magnetic fluxes. The flux bias points where theory overpredicts $P_{-1\text{dB}}$ are those where K is suppressed as suggested by Eq. 3.26. Specifically, device C in Fig. 3.5b shows a tenfold reduction in measured $|K|$ at around $\Phi/\Phi_0 = 0.4$. However, the measured $P_{-1\text{dB}}$ did not increase at this flux bias point. Devices D and E show similar Kerr-free regions, but also do not show increased $P_{-1\text{dB}}$.

This puzzle may be resolved by noting that the $P_{-1\text{dB}}$ prediction Eq. 3.26 requires that Kerr $K(|\alpha_p|^2)$ be evaluated at the pump power used to reach 20 dB gain; however, the Kerr extracted from Stark shift measurements in Fig. 3.5b corresponds to the low-power asymptote $K = K(0)$. In fact, we can see from the Stark shift measurements in Fig. 3.5a that the local slope of the Stark shift with respect to drive power is no longer flat at the high powers needed for amplification.

Intermodulation distortion

With this intuition in mind, we turn to a third-order intermodulation distortion (IMD) measurements [Pozar 2012] to extract $K(|\alpha_p|^2)$ while the amplifier is biased at 20 dB gain with the pump on. The standard nomenclature of third-order IMD originates from the fact that four-wave mixing generates third-order terms in the equations of motion. As we will show, this measurement also probes the response of the amplifier to multitone or broadband input signals. Understanding the response to such input signals is particularly important for employing quantum-limited amplifiers in any multiplexed readout scheme of superconducting qubits. In such an application, spurious intermodulation products will directly limit the isolation between readout channels either by directly mixing them or by distorting pulses. Furthermore, such intermodulation products put an upper bound on the quantum efficiency of any practical amplifier since, without careful calibration, distortion of the incident quantum signal is unlikely to be accounted for in the experimentalist's demodulation scheme.

A third-order IMD experiment is performed according to the frequency landscape in Fig. 3.7a. With the pump on and the amplifier biased to $G = 20$ dB, we applied two main signal tones (solid gray arrows) centered at $\omega_p/2 + 2\pi \times 500$ kHz with a relative detuning

---

[7]*Tunable bandwidth* refers to the frequency range over which the center frequency of the gain profile may be tuned and $G = 20$ dB still achieved.
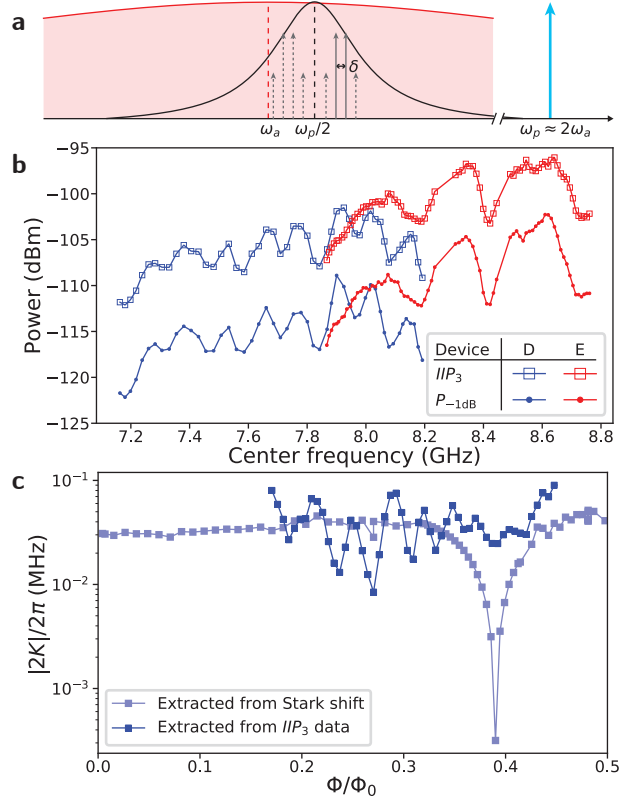
Figure 3.7 | (a) Caricatured (not-to-scale) frequency spectrum in the lab frame for the measurement of third-order intermodulation distortion (IMD) products of an SPA. The red shaded region is the Lorenzian lineshape of the linear mode of width κ. Black is the reflection gain of the amplifier when pumped with a strong microwave tone at $\omega_p \approx 2\omega_a$. Solid arrows show two tones applied above $\omega_p/2$ with a relative detuning δ. Dashed arrows indicate output spectrum which is symmetric about $\omega_p/2$. (b) IIP_3 and $P_{-1\text{dB}}$ as a function of the center frequency ($\omega_p/2$) of the 20-dB gain curve for two devices. (c) Magnitude of Kerr nonlinearity K for device D extracted at high power from IIP_3 (dark blue), and extracted at low power from fits of Stark shift (light blue). Neighboring experimental data points have been joined to emphasize correlations between the two experiments.

$\delta/2\pi = 100\,\text{kHz}$, and measured the power in the resulting sidebands (short dashed gray arrows). Intuitively, two signal photons from one input tone and one from the other combine in a four-wave-mixing process to generate the resulting sideband. Thus, the measured relative power between the main tones and the sidebands indicates the amount of four-wave mixing occurring in the device. Note the entire spectrum is also reflected about $\omega_p/2$ due to the three-wave mixing amplification process; each output tone has its own idler frequency and hence we choose the 500 kHz offset and δ to avoid these.

Sweeping the applied power on the two main signal tones, we extracted the input-referred third-order intercept point IIP_3 at which the measured sideband power should equal the main input signal power. We conform to the usage in standard microwave amplifier data sheets to take IIP_3 as the metric for third-order IMD. To characterize our am-

plifiers, in Fig. 3.7b, we compare the IIP_3 and $P_{-1\text{dB}}$ as a function of the center frequency of the gain curve for two different devices. Each point corresponds to a point tuned up in Fig. 3.6. Strikingly, the features in $P_{-1\text{dB}}$, which we recall are caused by ripples in the line impedance, are exactly reproduced in IIP_3. Such a comparison indicates that the cause of IIP_3, which is four-wave mixing, is most likely responsible for the saturation of the amplifier. This confirms the assertion that Kerr is responsible for the saturation of state-of-the-art amplifiers [Liu et al. 2017; Frattini et al. 2018; Planat et al. 2019].

Quantitatively, by considered the response to two input signals, second-order harmonic balance theory predicts that the measured IIP_3 is related to the Kerr nonlinearity K by the equation

$$IIP_3 = \frac{\kappa}{|2K|} \left(\frac{1}{1 + \sqrt{G}} \right)^3 \hbar\omega_a\kappa, \tag{3.30}$$

which can then be used to *extract* $K(|\alpha_p|^2)$ from IIP_3. In Fig. 3.7c, we compare the extracted $K(|\alpha_p|^2)$ from IIP_3 to $K(0)$ extracted from Stark shift measurements and see the noticeable absence of any suppression of $K(|\alpha_p|^2)$, indicating that appreciable four-wave mixing is still occurring when the amplifier is in operation.

Is it possible to suppress Kerr in the presence of the amplification pump? Indeed, such a suppression can be achieved in SPAs [Sivak et al. 2019]. To understand how, consider the shape of the frequency shift versus drive photons in the Stark shift measurements Fig. 3.5a. There exist fluxes Φ at which $d\Delta\Omega_a/d\bar{n} = 0$ for large $\bar{n}$. Additionally, the number of pump photons needed for formally infinite gain

$$n_\infty = \frac{\Delta_{\text{DPA}}^2 + \kappa^2/4}{4g_3^2} \tag{3.31}$$

is experimentally tunable *in situ* by controlling the pump frequency. These two insights enabled the tuneup of an SPA at a pumped Kerr-free point as confirmed by IMD measurements, and resulted in a $\approx 10\,\text{dB}$ improvement in saturation power to $P_{-1\text{dB}} = -102\,\text{dBm}$ [Sivak et al. 2019].

3.4 Design optimization principles

Based on the developed understanding from the SPA, in this section we summarize the optimization principles for quantum-noise-limited reflection amplifiers. The design procedure is as follows:

1. **Choose inductive nonlinearity**: SNAILs give access to three-wave mixing and a pumped Kerr-free point for increased dynamic range. Kinetic inductive materials are also a good option for reduced Kerr nonlinearity [Parker et al. 2021].

2. **Make all inductance nonlinear**: design a mode centered at or achieving a Kerr-free

point at the desired operating frequency ω_a while ensuring that the inductive partic-
ipation ratio $p \approx 1$.

3. **Choose signal port impedance**: given the mode impedance, the port impedance on
   resonance sets the quality factor Q in a single-mode amplifier. Choose the smallest Q
   such that $pQ \gtrsim 1$.

4. **Reduce Kerr nonlinearity**: for improved dynamic range, reduce the Kerr nonlin-
   earity by increasing the critical current and/or increasing the number of junctions as
   outlined in Sec. 2.3. Ensure after this step that $p \approx 1$.

5. **Signal port matching network**: given a desired port impedance seen at ω_a, match the
   pumped nonlinearity to this impedance and increase bandwidth by adding stages
   to the matching filter [Mutus et al. 2014; Roy et al. 2015], which follow from tech-
   niques for broadband reflection amplifiers [Getsinger 1963; Matthaei, Young, and
   Jones 1980]. Ensure the signal matching network is sufficiently isolating at $2\omega_a$ to
   prevent the amplification pump from leaking out the signal input-output port.

6. **Pump port matching network**: match the pump port to efficiently deliver current
   across the SNAILs at $2\omega_a$, while simultaneously preventing in-band signal leakage
   that otherwise would limit noise performance.

7. **Ensure input line is cold**: quantum-limited noise performance requires cold quan-
   tum noise incident at the idler frequency as well as no attenuation between the signal
   source and the amplifier.

Using these design optimization principles for a SNAIL-based amplifier, we can ideally
achieve a three-wave-mixing reflection amplifier with quantum-limited noise performance,
high gain, power handling on the order of $P_{-1\text{dB}} \approx -100\text{dBm}$, and bandwidth beyond the
gain-bandwidth product. Power handling of kinetic-inductive-based resonant parametric
amplifiers surpasses those based on Josephson junctions at the cost of more applied pump
power [Parker et al. 2021]. The largest outstanding design requirement from Sec. 3.1 is
unidirectionality, but all the above optimizations readily apply to multiparametric schemes
for nonreciprocal device [Abdo et al. 2013a; Sliwa et al. 2015; Lecocq et al. 2017; Lecocq
et al. 2021], including those for increased bandwidth [Naaman et al. 2019].

Before concluding this chapter on amplifiers, we first compare the result of the above
outlined optimization for resonant reflection parametric amplifiers to travelling wave para-
metric amplifiers (TWPAs), which have received attention recently for the promise of wide-
band, directional amplification. Josephson-junction-based TWPAs have similar compres-
sion powers to the SPAs presented here [Macklin et al. 2015]. SNAIL or RF-SQUID based
TWPAs may also increase compression powers via a similar Kerr-free point [Zorin 2016;
Zorin et al. 2017], while kinetic-inductance-based TWPAs surpass them in this metric [Vis-
sers et al. 2016]. The total number of junctions is similar to the most recent SPAs [Sivak et al.

2020] and JPAs [Winkel et al. 2020]. As outlined by a recent review of TWPA progress [Esposito et al. 2021], phase matching [O'Brien et al. 2014] is a difficult technical requirement, even when DC-SQUIDs are flux-tuned *in situ* to minimize ripple [Planat et al. 2020]. Moreover, TWPAs thus far require isolators between the system of interest and the amplifier; and the same level of quantum-noise-limited performance as resonant amplifiers has yet to be achieved in qubit readout. We must ask whether reflection-based parametric amplifiers with increased bandwidth via impedance engineering techniques may be more robust to design and construction tolerances than phase matching in TWPAs.

4

The Kerr-cat qubit

In quantum information processing, quantum error correction (QEC) generally promises to enable the storage and manipulation of quantum information on timescales much longer than the coherence times of the individual faulty parts [Gottesman 2009; Nielsen and Chuang 2010; Devoret and Schoelkopf 2013; Terhal 2015]. The QEC tactic uses larger system size and thus more Hilbert space to choose a clever encoding where the logical information is hidden from the environment, yet still controlled by the experimentalist's protocol. Most noisy environments are only locally correlated and thus cannot decohere quantum information encoded in a non-local manner. Therefore, quantum information can be protected through the use spatial distance in topological proposals [Kitaev 2003; Oreg, Refael, and Oppen 2010; Lutchyn, Sau, and Das Sarma 2010], or entangled qubit states [Shor 1995; Fowler et al. 2012]. Crucially, this concept can be extended to the non-local states in the phase space of a single oscillator [Gottesman, Kitaev, and Preskill 2001; Mirrahimi et al. 2014], with the additional benefit of involving fewer physical components, a property termed *hardware efficiency*. Hardware efficiency is desirable because fully protecting quantum information against all forms of decoherence to the level necessary for useful algorithms is likely to involve several layers of encoding. Thus, it is crucial to introduce efficient error protection into the physical layer while maintaining simplicity [Guillaud and Mirrahimi 2019; Vuillot et al. 2019; Puri et al. 2020].

Within a single oscillator, there exists many encoding options, so-called *bosonic codes* [Albert et al. 2018], including Schrödinger cat codes [Mirrahimi et al. 2014], binomial codes [Michael et al. 2016], and GKP codes [Gottesman, Kitaev, and Preskill 2001] to name a few. In this thesis, we focus on the two-legged Schrödinger cat code, based on superpositions of distinct coherent states—the so-called Schrödinger cat states. While not correcting *all* errors to the level needed in an eventual logical qubit in a quantum algorithm, this code takes the first step: *exponentially* suppressing one error generator rate[1] (for concreteness, the phase-flip rate), while suffering a *linear* increase in the other (bit-flip rate), which generates an effective so-called *noise-biased* qubit.

In this chapter, we focus on the autonomous[2] stabilization of such a noise-biased two-legged cat qubit based on the interplay between Kerr nonlinearity and single-mode squeezing [Cochrane, Milburn, and Munro 1999; Puri, Boutin, and Blais 2017], which we realized experimentally and named the *Kerr-cat qubit* [Grimm et al. 2020]. As we will see, this system corresponds directly to the parametric amplifiers discussed in Chapter 3, except now driven above the parametric instability threshold with a different purpose in mind: to im-

---

[1]For an introduction in the decomposition of environmental noise into strengths of single-qubit errors and an enumeration of all possible single-qubit error channels, see [Nielsen and Chuang 2010].

[2]*Autonomous* here meaning no classical feedforward required: for example, no actions of the room-temperature measurement and control system that depend on measurement results as is common in QEC as canonically discussed.

plement a noise-biased qubit. The Kerr-cat qubit builds directly off of, and can indeed be combined with, the stabilization of two-legged cat qubits based on two-photon dissipation[3] [Leghtas et al. 2013; Mirrahimi et al. 2014], which have also been experimentally realized [Leghtas et al. 2015; Touzard et al. 2018] and recently achieved exponential noise suppression [Lescanne et al. 2020]. We theoretically treat both of these paradigms on the same footing at the level of a single oscillator, and save discussions on implementations with SNAILs and experimental results for Chapter 5.

4.1 Two-legged Schrödinger cat code

The Schrödinger cat code is based on the intuition that coherent states are classically stable states in oscillators so we should make a quantum error correction code out of them. Explicitly coherent states are eigenstates of the annihilation operator $\boldsymbol{a}\,|\alpha\rangle = \alpha\,|\alpha\rangle$ and for this reason superpositions of coherent states were suggested as a code that protects against amplitude damping [Cochrane, Milburn, and Munro 1999]. Since amplitude damping error may be approximated by the jump operator $\sqrt{\kappa_1}\boldsymbol{a}$ corresponding to single-photon loss, coherent states are also the eigenstates dominant jump operator, which in turn leads to their stability in the long time limit. We may further understand coherent states as a translation of the vacuum

$$|\alpha\rangle = \boldsymbol{D}(\alpha)\,|0\rangle$$
$$= e^{-|\alpha|^2/2}\sum_{n=0}^{\infty}\frac{\alpha^n}{\sqrt{n!}}\,|n\rangle \tag{4.1}$$
$$\boldsymbol{D}(\alpha) = e^{\alpha\boldsymbol{a}^\dagger - \alpha^*\boldsymbol{a}} \tag{4.2}$$

where $\boldsymbol{D}(\alpha)$ is the displacement operator and $|n\rangle$ are Fock states with property $\boldsymbol{a}^\dagger\boldsymbol{a}\,|n\rangle = n\,|n\rangle$. Each coherent state has is Poisson-distributed in photon number with an average number of photons $\bar{n} = \langle\alpha|\,\boldsymbol{a}^\dagger\boldsymbol{a}\,|\alpha\rangle = |\alpha|^2$ and a variance $\langle\alpha|\,(\boldsymbol{a}^\dagger\boldsymbol{a} - \bar{n})^2\,|\alpha\rangle = \bar{n}$ [Haroche and Raimond 2006].

One coherent state is not sufficient for storing quantum information; to form a qubit, we will need at least one more coherent state $|\beta\rangle$. The overlap between two coherent states is $\langle\alpha\,|\,\beta\rangle = e^{-\frac{1}{2}|\alpha|^2 - \frac{1}{2}|\beta|^2 + \alpha^*\beta}$ which when squared $|\langle\alpha\,|\,\beta\rangle|^2 = e^{-|\alpha-\beta|^2}$ can be written succinctly in terms of the distance between the two coherent states in phase space. Importantly, this overlap scales exponentially with the distance between the states. For coherent states that are far apart, we hope (and will show formally later for certain errors) that errors that attempt to take one coherent state to the other will be suppressed with this exponential.

However, larger coherent states implies on average more photons in the oscillator and

---

[3]An engineered jump operator of the form $\sqrt{\kappa_2}\boldsymbol{a}^2$, which promises to annihilate two photons at a time but never only one.

many loss mechanisms scale poorly with photon number. For instance, losing a single photon is $\bar{n}$ times more likely for an oscillator with $\bar{n}$ average photons (although note that the energy decay rate to vacuum is κ regardless of the state) [Haroche and Raimond 2006]. We may recognize this linear increase in error probability as the cost associated with performing QEC utilizing a larger Hilbert space. In a standard multi-qubit repetition code, the equivalent cost is the overhead associated with adding more qubits, which scales polynomially with the number of qubits. Crucially, each qubit also adds error channels whereas, in the bosonic case, the number of error channels is the same but we have linearly increased their weight[4]. Hence, this cat code may be hardware efficient if we indeed achieve the same exponential error correcting power as the repetition code.

Given the above, we want a maximal distance between coherent states for a given $\bar{n}$ so we choose the states $|\pm\alpha\rangle$, which both have the same average number of photons $\bar{n} = |\alpha|^2$. However since

$$\langle +\alpha \mid -\alpha \rangle = e^{-2|\alpha|^2} \neq 0, \tag{4.3}$$

the states $|\pm\alpha\rangle$ are not orthogonal (only approximately orthogonal) and we need orthogonal states to define our Bloch sphere. These states are superpositions of $|\pm\alpha\rangle$, the so-called Schrödinger cat states, defined:

$$
\begin{aligned}
|\pm Z\rangle &= \left| \mathcal{C}_\alpha^\pm \right\rangle \\
&= \mathcal{N}_\alpha^\pm \left(|{+}\alpha\rangle \pm |{-}\alpha\rangle \right) \\
&= \mathcal{N}_\alpha^\pm e^{-|\alpha|^2/2} \sum_{n=0}^\infty \left(1 \pm (-1)^n \right) \frac{\alpha^n}{\sqrt{n!}} |n\rangle
\end{aligned}
\tag{4.4}
$$

$$\mathcal{N}_\alpha^\pm = 1/\sqrt{2(1 \pm e^{-2|\alpha|^2})} \tag{4.5}$$

which are orthogonal $\langle \mathcal{C}_\alpha^+ \mid \mathcal{C}_\alpha^- \rangle = 0$ with the appropriately chosen normalization coefficients. By inspection, we notice that $\left| \mathcal{C}_\alpha^\pm \right\rangle$ only have weight on even (odd) Fock states $|n\rangle$ and thus are often referred to as even (odd) Schrödinger cat states.

We define the $\mathbf{Z}$ eigenstates of our Bloch sphere: $\mathbf{Z} |\pm Z\rangle = \pm |\pm Z\rangle$ as depicted in Fig. 4.1a. This is sufficient to define our Pauli operators with standard conventions but for clarity we explicitly write the expressions for Pauli states:

$$|\pm X\rangle = \frac{1}{\sqrt{2}} \left(\left| \mathcal{C}_\alpha^+ \right\rangle \pm \left| \mathcal{C}_\alpha^- \right\rangle \right) \to |\pm\alpha\rangle \tag{4.6}$$

$$|\pm Y\rangle = \frac{1}{\sqrt{2}} \left(\left| \mathcal{C}_\alpha^+ \right\rangle \pm i \left| \mathcal{C}_\alpha^- \right\rangle \right) \to \frac{1}{\sqrt{2}} \left(|{+}\alpha\rangle \mp i |{-}\alpha\rangle \right) \tag{4.7}$$

$$|\pm Z\rangle = \left| \mathcal{C}_\alpha^\pm \right\rangle \to \frac{1}{\sqrt{2}} \left(|{+}\alpha\rangle \pm |{-}\alpha\rangle \right) \tag{4.8}$$

---

[4]Note however that to reach the same total Hilbert space dimensions as q qubits, we need 2^q Fock states [Nielsen and Chuang 2010].
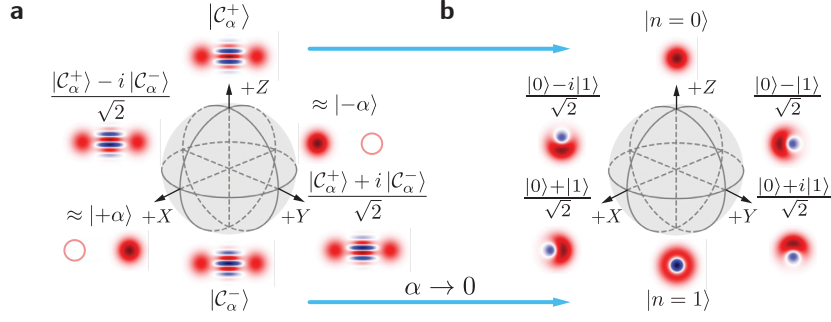
Figure 4.1 | (a) Bloch sphere definition for a two-legged Schrödinger cat qubit spanned by two opposite-phase coherent states $|\pm\alpha\rangle$. We define the $\boldsymbol{Z}$ eigenstates $|\pm Z\rangle = \left|\mathcal{C}_\alpha^\pm\right\rangle$, which define the $|\pm X\rangle$ and $|\pm Y\rangle$ states with standard Pauli matrix conventions (see Eq. 4.6–4.8). The Wigner function of each cardinal state shows its wavefunction in the larger oscillator Hilbert space. (b) Taking the limit $\alpha \to 0$ maps directly to the Fock qubit—the single photon Fock state encoding of an oscillator.

where the limit is taken for moderately large $|\alpha|$.

The corresponding Pauli operators

$$\boldsymbol{X} = \left|\mathcal{C}_\alpha^+\right\rangle\left\langle\mathcal{C}_\alpha^-\right| + \left|\mathcal{C}_\alpha^-\right\rangle\left\langle\mathcal{C}_\alpha^+\right| \tag{4.9}$$

$$\boldsymbol{Y} = -i\left|\mathcal{C}_\alpha^+\right\rangle\left\langle\mathcal{C}_\alpha^-\right| + i\left|\mathcal{C}_\alpha^-\right\rangle\left\langle\mathcal{C}_\alpha^+\right| \tag{4.10}$$

$$\boldsymbol{Z} = \left|\mathcal{C}_\alpha^+\right\rangle\left\langle\mathcal{C}_\alpha^+\right| - \left|\mathcal{C}_\alpha^-\right\rangle\left\langle\mathcal{C}_\alpha^-\right| \tag{4.11}$$

conform to the standard 2×2 matrix definition of Pauli operators within the qubit subspace $\mathcal{C}$. We can additionally define the projector to this cat subspace as

$$\boldsymbol{P}_\mathcal{C} = \left|\mathcal{C}_\alpha^+\right\rangle\left\langle\mathcal{C}_\alpha^+\right| + \left|\mathcal{C}_\alpha^-\right\rangle\left\langle\mathcal{C}_\alpha^-\right| \tag{4.12}$$

which obeys the standard projector identity $\boldsymbol{P}_\mathcal{C}\boldsymbol{P}_\mathcal{C} = \boldsymbol{P}_\mathcal{C}$.

It is also useful to define the ratio of the normalization coefficients

$$r = \frac{\mathcal{N}_\alpha^+}{\mathcal{N}_\alpha^-} = \frac{\sqrt{1 - e^{-2|\alpha|^2}}}{\sqrt{1 + e^{-2|\alpha|^2}}} \to 1 - e^{-2|\alpha|^2} \tag{4.13}$$

solidifying the previous limits as formally the approximation $r \approx 1$, which becomes exponentially accurate and thus reasonable for even a handful of photons $|\alpha|^2$.

With this convenient notation, we see that the action of $\boldsymbol{a}$ causes a bit flip

$$\begin{aligned}
\boldsymbol{a}\,|\pm Z\rangle &= \boldsymbol{a}\left|\mathcal{C}_\alpha^\pm\right\rangle \\
&= \alpha r^{\pm 1}\left|\mathcal{C}_\alpha^\mp\right\rangle \\
&= \alpha r^{\pm 1}\,|\mp Z\rangle
\end{aligned} \tag{4.14}$$

Table 4.1 | Operators O in the harmonic oscillator Hilbert space projected onto the cat qubit subspace $P_{\mathcal{C}} O P_{\mathcal{C}}$ showing their action within the cat subspace. Expressions are shown in various limits: the Fock qubit ($\alpha \to 0$), arbitrary cat size (α), and large cat size with corrections $\mathcal{O}(|\alpha|^k e^{-4|\alpha|^2})$ where $k = 1, 1, 2$ for each row respectively. The ratio of normalization coefficients r is defined in Eq. 4.13.

O	$\alpha \to 0$	α	Large α
a	$\frac{1}{2}(X + iY)$	$\alpha\left(\frac{r+r^{-1}}{2}\right) X - i\alpha\left(\frac{r-r^{-1}}{2}\right) Y$	$\alpha X + i\alpha e^{-2|\alpha|^2} Y$
$a^\dagger$	$\frac{1}{2}(X - iY)$	$\alpha^*\left(\frac{r+r^{-1}}{2}\right) X + i\alpha^*\left(\frac{r-r^{-1}}{2}\right) Y$	$\alpha^* X - i\alpha^* e^{-2|\alpha|^2} Y$
$a^\dagger a$	$\frac{1}{2}(I - Z)$	$|\alpha|^2\left(\frac{r^2+r^{-2}}{2}\right) I + |\alpha|^2\left(\frac{r^2-r^{-2}}{2}\right) Z$	$|\alpha|^2 I - 2|\alpha|^2 e^{-2|\alpha|^2} Z$

with this Bloch sphere definition. In contrast, the action of a^2 leaves the qubit information unchanged

$$a^2 \left|\mathcal{C}_\alpha^\pm\right\rangle = \alpha^2 \left|\mathcal{C}_\alpha^\pm\right\rangle. \tag{4.15}$$

Using this fact, we notice that $\left[a^2, O\right] = 0$ for all $O \in \{X, Y, Z, P_{\mathcal{C}}\}$ which we will leverage for the stabilization of the qubit Bloch sphere throughout the rest of this chapter.

As depicted in Fig. 4.1b, the cat qubit Bloch sphere has a direct mapping, through the limit $\alpha \to 0$, back to the $|n=0\rangle$ and $|n=1\rangle$ Fock-state encoding, which we will refer to as the *Fock qubit* (FQ). The Fock qubit is the bosonic qubit encoding with the smallest possible average photon number of 0.5 photons and corresponds directly to the ground and excited state encoding of a single transmon qubit[5] [Koch et al. 2007]. As such, it is the benchmark encoding to which we often compare our experiments as limit in which no bosonic QEC was performed.

To gain intuition about what common oscillator operators do to within our qubit Bloch sphere, we examine the projections of a few operators in the oscillator Hilbert space onto the cat subspace $\mathcal{C}$ listed in Table 4.1. In the appreciable α limit, actions of either a or $a^\dagger$ will only apply X with all other Pauli operators being exponentially suppressed. Similarly, action of $a^\dagger a$ induces mostly the identity operation with only an exponentially low weight of Z. This mapping of the photon number operator $a^\dagger a$ may also be understood by considering average photon numbers of the even and odd cat states

$$\bar{n}_\pm = \left\langle \mathcal{C}_\alpha^\pm \right| a^\dagger a \left| \mathcal{C}_\alpha^\pm \right\rangle = r^{\pm 2}|\alpha|^2 \tag{4.16}$$

whose difference $\bar{n}_+ - \bar{n}_- = (r^2 - r^{-2})|\alpha|^2 \to -4|\alpha|^2 e^{-2|\alpha|^2}$ is exponentially small in the large $|\alpha|$ limit.

These operators also enumerate the operators through which the environment couples to cause the dominant loss mechanisms in an oscillator: namely single-photon loss (a), single-photon gain ($a^\dagger$), and pure dephasing ($a^\dagger a$). As we see from Table 4.1, the structure

---

[5]At least when a transmon may be approximated as a weakly anharmonic oscillator.

of the cat code exponentially suppresses environmental couplings to both Y and Z, yet enhances couplings to X. So, if we manage to implement a QEC protocol to stabilize the cat qubit subspace, then we have a noise-based qubit: phase flips errors (caused by the environment's application of either Y or Z) are exponentially suppressed, while bit flips (application of X) remain.

Before examining in detail the implementation of such a QEC protocol, we pause here to comment on Bloch sphere definitions. In this thesis, we conform to the Bloch sphere conventions as described in this section and Fig. 4.1 in which $|\pm X\rangle \approx |\pm\alpha\rangle$ and $|\pm Z\rangle = |\mathcal{C}_\alpha^\pm\rangle$. As we saw, this basis choice conveniently maps to the Fock qubit and leaves pure dephasing or phase flips of an oscillator (via $a^\dagger a$) to cause phase flips on the encoded cat qubit (via Z). Similarly, this leads to a noise-biased qubit with suppressed phase-flips and increased bit-flips: the equivalent of a phase-flip repetition code [Shor 1995]. However, in some contexts and references, the conventions are inverted via a Hadamard transform to implement a bit-flip repetition code. Explicitly, this definition gives $|\pm X\rangle = |\mathcal{C}_\alpha^\pm\rangle$ and $|\pm Z\rangle \approx |\pm\alpha\rangle$ with a mapping of Pauli operators

$$X \to Z \tag{4.17}$$

$$Y \to -Y \tag{4.18}$$

$$Z \to X \tag{4.19}$$

in all of previous expressions. Such Hadamard-rotated conventions are particularly convenient when considering higher levels of encoding with multiple cat qubits [Guillaud and Mirrahimi 2019; Puri et al. 2020], for instance in a surface code [Bonilla Ataides et al. 2021; Darmawan et al. 2021; Singh et al. 2021]. Given two such conventions, we will attempt to use the language of *coherent states* versus *cat states* where possible to delineate the different Bloch sphere axes; however, all mathematical expressions with Pauli operators and Bloch sphere axes use the convention $|\pm Z\rangle = |\mathcal{C}_\alpha^\pm\rangle$.

4.2 The need for stabilization

As described in the previous section, in order to take advantage of the structure of the cat code, we must implement a QEC protocol to stabilize the cat qubit Bloch sphere so that our error properties are determined by the mapping of oscillator operators in Table 4.1. In an undriven harmonic oscillator, dissipation will tend to push the states outside the cat qubit Bloch sphere causing a *leakage* error. For instance, given an oscillator with frequency ω_a and single-photon loss rate κ_1, if we prepare the initial state $|\alpha\rangle$, the state after time t will deterministically evolve to $|\alpha(t)\rangle = |\alpha e^{-i\omega_a t - \kappa_1 t/2}\rangle$. Despite the presence of loss, the quantum state remains pure since state at all points of the evolution is an eigenstate of the jump operator $\sqrt{\kappa_1}a$. The deterministic evolution results from the near-identity Kraus

operator governing the density matrix evolution, or the *no-jump* evolution [Haroche and Raimond 2006].

This no-jump evolution must be corrected or the coherent states will inevitably decay to vacuum $|0\rangle$. At the very least, additional energy must be supplied. In bosonic codes implemented with superconducting circuits thus far, this no jump evolution has either been ignored [Ofek et al. 2016], corrected by periodically applied unitary evolutions conditioned on prior measurement results [Hu et al. 2019; Campagne-Ibarcq et al. 2020], or corrected autonomously via Hamiltonian engineering [Grimm et al. 2020] or engineered dissipation [Leghtas et al. 2015; Touzard et al. 2018; Lescanne et al. 2020; Gertler et al. 2021]. In multi-qubit stabilizer codes based on transmon qubits like the repetition code [Kelly et al. 2015; Chen et al. 2021] or the surface code [Andersen et al. 2020], the equivalent no-jump evolution is correctable by incorporating dynamical decoupling [Viola, Knill, and Lloyd 1999] into the stabilizer measurement circuits that attempts to symmetrize the noise channels into only depolarizing noise and leakage errors. Ultimately, for QEC to succeed, the protocol must correct for the no-jump evolution, not just the jumps, and ensure that it acts as the identity within the code space without causing leakage.

In this thesis, we focus on autonomous stabilization of the two-legged cat code. As illustrated above, the no-jump evolution predominantly causes leakage errors, the common case for undriven bosonic code implementations. We further take the continuous limit of autonomous stabilization to engineer a Hamiltonian and dissipation that continuously and autonomously prevents and corrects leakage errors by resupplying energy to the system and evacuating entropy from the system in a way that is completely agnostic to the qubit state.

4.3 Stabilizing 1 coherent state

Before we tackle the stabilization of the entire cat qubit Bloch sphere, we first answer the question: how do you stabilize a single coherent state in an oscillator? The answer is rather straight forward: apply a linear single-photon drive. Although simple, treating this case explicitly will lead to intuition when we move on to stabilizing the entire cat qubit Bloch sphere. Additionally, we aggressively invoke the rotating wave approximation (RWA) to simplify the discussion and the analytical form of the equations. However, as we mentioned when treating the SPA in Chapter 3, the RWA is often not valid in three-wave-mixing applications and a myriad of methods may be employed to make more controllable approximations [Venkatraman et al. 2021].

Consider a harmonic oscillator with frequency ω_a that is driven coherently with a linear single-photon drive at frequency ω_p and drive strength ϵ_1. In the frame rotating at ω_p to make the drive term time independent, we have the Hamiltonian

$$\mathcal{H}_1/\hbar = -\Delta a^\dagger a + \epsilon_1 a^\dagger + \epsilon_1^* a \tag{4.20}$$

where $\Delta = \omega_p - \omega_a$. We expect such a linear drive to displace the oscillator, so we make a displacement transformation by α_0:

$$\begin{aligned} \boldsymbol{\mathcal{H}}_1'/\hbar &= \boldsymbol{D}^\dagger(\alpha_0)\boldsymbol{\mathcal{H}}_1\boldsymbol{D}(\alpha_0)/\hbar \\ &= -\Delta \boldsymbol{a}^\dagger \boldsymbol{a} + (-\Delta\alpha_0 + \epsilon_1)\,\boldsymbol{a}^\dagger + \text{H.c.} \end{aligned} \tag{4.21}$$

where H.c. stands for Hermitian conjugate of the second term. We then solve for $\alpha_0 = \epsilon_1/\Delta$ to cancel the second term, leaving us with a Hamiltonian in the displaced frame that is just the original harmonic oscillator. The ground state of the undriven harmonic oscillator is the vacuum or 0-photon Fock state $|0\rangle$ and so the ground state of our original Hamiltonian (4.20) is $\boldsymbol{D}(\alpha_0)|0\rangle = |\alpha_0\rangle$ or a coherent state as promised. The excited states are the higher n-photon Fock states $|n\rangle$, so similarly for Eq. 4.20 the higher excited states are displaced Fock states $\boldsymbol{D}(\alpha_0)|n\rangle$.

The above was a full quantum treatment for a detuned drive in the limit of no dissipation. Physically however, we know that driving an oscillator on resonance $\Delta \to 0$ does not inject infinite energy, so we need dissipation to regulate the drive. To include dissipation, we often use the quantum Langevin equation (as in Ch. 3):

$$\dot{\boldsymbol{a}} = \frac{i}{\hbar}[\boldsymbol{\mathcal{H}}_1, \boldsymbol{a}] - \frac{\kappa_1}{2}\boldsymbol{a} + \sqrt{\kappa_1}\,\boldsymbol{a}_{\text{in}} \tag{4.22}$$

$$= i(\Delta + i\kappa_1/2)\boldsymbol{a} - i\epsilon_1 + \sqrt{\kappa_1}\,\boldsymbol{a}_{\text{in}} \tag{4.23}$$

where we have already subsumed the drive into the Hamiltonian so that $\boldsymbol{a}_{\text{in}}$ is only the standard delta-time-correlated Gaussian quantum fluctuations with zero mean. Solving for the steady state average amplitude $\alpha_0 = \langle \boldsymbol{a}\rangle$, we find $\alpha_0 = \epsilon_1/(\Delta + i\kappa_1/2)$ which agrees with are previous result in the limit $\kappa_1 \to 0$.

In the context of storing and manipulating quantum information, we would often like to work in the regime of small yet nonzero dissipation and separate how the dissipation alters the quantum states from how it may cause errors in a chosen encoding. Moreover, we hope to perform quantum gates much faster than the error rates so we will not be interested only in the steady states. In this vain, it can be helpful both for intuition and computation to cast the QLE above into the form

$$\dot{\boldsymbol{a}} = \frac{i}{\hbar}\left[\boldsymbol{\mathcal{H}}_{1c}\boldsymbol{a} - \boldsymbol{a}\boldsymbol{\mathcal{H}}_{1c}^\dagger\right] + \sqrt{\kappa_1}\,\boldsymbol{a}_{\text{in}} \tag{4.24}$$

$$\boldsymbol{\mathcal{H}}_{1c} = -\tilde{\Delta}\boldsymbol{a}^\dagger\boldsymbol{a} + \epsilon_1\boldsymbol{a}^\dagger + \epsilon_1^*\boldsymbol{a} \tag{4.25}$$

$$\tilde{\Delta} = \Delta + i\kappa_1/2 \tag{4.26}$$

allowing us to identify $\boldsymbol{\mathcal{H}}_{1c}$ as a non-Hermitian Hamiltonian with complex eigenvalues, where importantly the quantum noise to satisfy all commutation relations is maintained by $\boldsymbol{a}_{\text{in}}$. In the language of master equations, $\boldsymbol{\mathcal{H}}_{1c}$ generates the no-jump evolution.

To see why this is useful, we may start from the Langevin equations, do a displacement transformation by α_0, and extract the Hamiltonian in the displaced frame

$$\mathcal{H}'_{1c} = -\tilde{\Delta} a^\dagger a + \left(-\tilde{\Delta}\alpha_0 + \epsilon_1\right) a^\dagger + \text{H.c.} \tag{4.27}$$

where again $\tilde{\Delta}$ is the complex detuning from Eq. 4.26. We again solve for $\alpha_0 = \epsilon_1/\tilde{\Delta}$ to cancel the last term, which is the same answer as from the QLE. After substitution, we are left with a Hamiltonian of a harmonic oscillator with complex frequency $\tilde{\Delta}$ whose eigenstates are again $|n\rangle$ in this displaced frame, thus $D(\alpha_0)|n\rangle$ in the original frame. Note, the sign of Δ determines whether $|0\rangle$ (and thus also $|\alpha_0\rangle$) is the highest or lowest energy state; however, the term "ground state" is justified insofar as dissipation (here photon loss) leaves the system in $|0\rangle$ ($|\alpha_0\rangle$ in the original frame) in the long-time limit.

Non-Hermitian Hamiltonians are a valuable tool for analyzing the eigenstates and eigenenergies of the no-jump evolution. They do not however contain the stochastic evolution from the jump part of the master equation, nor equivalently the noise supplied by a_{in} in the QLE. Coherent states though are eigenstates of the jump operator a, and so the single-photon jumps do not affect them. We may also consider the action of single photon loss on the excited states

$$\begin{aligned} a D(\alpha_0)|n\rangle &= D(\alpha_0)\left(a + \alpha_0\right)|n\rangle \\ &= \sqrt{n}D(\alpha_0)|n-1\rangle + \alpha_0 D(\alpha_0)|n\rangle \end{aligned} \tag{4.28}$$

where we notice that repeated application of a would bring the system to $D(\alpha_0)|0\rangle$. This justifies the name "ground state" for this state as steady state solution even though it is either the highest or lowest energy eigenstate of $\mathcal{H}_{1c}$ (Eq. 4.25) depending on the sign of Δ.

A similar analysis may be performed for other jump operators and their matrix elements between the eigenstates of the complex Hamiltonian. For instance, consider the action of the single-photon gain operator $a^\dagger$ on a displaced n-photon Fock state

$$\begin{aligned} a^\dagger D(\alpha_0)|n\rangle &= D(\alpha_0)\left(a^\dagger + \alpha_0^*\right)|n\rangle \\ &= \sqrt{n+1}D(\alpha_0)|n+1\rangle + \alpha_0^* D(\alpha_0)|n\rangle \end{aligned} \tag{4.29}$$

We again see that $a^\dagger$ acting on a displaced Fock, like a, leaves a superposition of displaced Fock states with the *same* displacement amplitude α_0. Also similarly, the action of pure

dephasing $a^\dagger a$ on a displaced n-photon Fock state

$$
\begin{aligned}
a^\dagger a D(\alpha_0) \ket{n} &= D(\alpha_0) \left(a^\dagger + \alpha_0^* \right) (a + \alpha_0) \ket{n} \\
&= \alpha_0 \sqrt{n+1} D(\alpha_0) \ket{n+1} \\
&\quad + \left(|\alpha|^2 + n \right) D(\alpha_0) \ket{n} \\
&\quad + \alpha_0^* \sqrt{n} D(\alpha_0) \ket{n-1}
\end{aligned}
\tag{4.30}
$$

also leaves a superposition of displaced Fock states with the same displacement amplitude. As we will see, this has consequences for the success of QEC. The Wigner functions of these error states remain relatively *close* to the original state $D(\alpha_0) \ket{n}$, where closeness will be defined relative to other phase space location that we also wish to stabilize to form our Schrödinger cat qubit.

4.4 Stabilizing 2 coherent states: the Kerr cat

Seeking the stabilization of the entire cat Bloch sphere to make a nonlocal encoding, we wish to extend our stabilization protocol to make both $\ket{\pm\alpha}$ ground states. Importantly, we also want to stabilize the manifold of their superpositions so as to stabilize the entire Bloch sphere of Section 4.1 spanned by the cat states $\ket{\mathcal{C}_\alpha^\pm}$. As noted in Eq. 4.15, these cat states are eigenstates of a^2. Given we know how to stabilize one coherent state with Eq. 4.25, we can try making the substitution $a \to a^2$ to get

$$
\mathcal{H}_{2c} = -\tilde{K} a^{\dagger 2} a^2 + \epsilon_2 a^{\dagger 2} + \epsilon_2^* a^2
\tag{4.31}
$$

$$
\tilde{K} = K + i\kappa_2/2
\tag{4.32}
$$

where ϵ_2 is the squeezing strength or two-photon drive that we will generate through three-wave mixing as we did in the SPA Chapter 3, K is the self-Kerr nonlinearity defined to be half of the transmon anharmonicity[6], and κ_2 is a two-photon engineered dissipation rate generated by a jump operator $\sqrt{\kappa_2} a^2$.

   To see that the cat states $\ket{\mathcal{C}_\alpha^\pm}$ are indeed eigenstates of Eq. 4.31, it is helpful to factor as

$$
\begin{aligned}
\mathcal{H}_{2c} &= -\tilde{K} \left[a^{\dagger 2} - \epsilon_2^*/\tilde{K} \right] \left[a^2 - \epsilon_2/\tilde{K} \right] + |\epsilon_2|^2/\tilde{K} \\
&= -\tilde{K} \left[a^{\dagger 2} - \alpha^{*2} \tilde{K}^*/\tilde{K} \right] \left[a^2 - \alpha^2 \right] + |\epsilon_2|^2/\tilde{K}
\end{aligned}
\tag{4.33}
$$

where in the second line we have suggestively made the substitution $\alpha = \sqrt{\epsilon_2/\tilde{K}}$. With this substitution and the eigenvalue equation $a^2 \ket{\mathcal{C}_\alpha^\pm} = \alpha^2 \ket{\mathcal{C}_\alpha^\pm}$, it is easy to see that $\ket{\mathcal{C}_\alpha^\pm}$

---

[6]As in Eq. 2.53 but with a sign convention change since we focus here to negative anharmonicity and further math is convenient with $K > 0$.

are degenerate eigenstates. Therefore, all superpositions of $|\mathcal{C}_\alpha^\pm\rangle$ are also degenerate eigenstates, which is precisely the cat qubit Bloch sphere we want to stabilize.

To get a feeling for the rest of the eigenstates and whether $|\mathcal{C}_\alpha^\pm\rangle$ are stable solutions in the long time limit, we use the displacement transformation by α_0 as we did previously to generate the Hamiltonian in the displaced frame:

$$\begin{aligned}
\mathcal{H}'_{2c} = {}& \left[-2\tilde{K}\alpha_0^2\alpha_0^* + 2\epsilon_2\alpha_0^*\right]\boldsymbol{a}^\dagger + \text{H.c.} \\
& + \left(-\tilde{K}\alpha_0^2 + \epsilon_2\right)\boldsymbol{a}^{\dagger 2} + \text{H.c.} \\
& - 4\tilde{K}|\alpha_0|^2\boldsymbol{a}^\dagger\boldsymbol{a} - \tilde{K}\boldsymbol{a}^{\dagger 2}\boldsymbol{a}^2 \\
& - 2\tilde{K}\alpha_0\boldsymbol{a}^{\dagger 2}\boldsymbol{a} + \text{H.c.}.
\end{aligned} \tag{4.34}$$

To find α_0, we must solve to null the linear displacement term. There are three solutions: $\alpha_0 = 0$, and $\alpha_0 = \pm\alpha$ with $\alpha = \sqrt{\epsilon_2/\tilde{K}}$. These respectively correspond to a saddle point and two stable points in phase space of a classical oscillator with Hamiltonian Eq. 4.31.

Dealing with each solution in turn, we expect the $\alpha_0 = 0$ solution to be unstable in the long-time limit. Classically, looking a flow in phase space, we indeed find that $\alpha_0 = 0$ is not an attractor and that dissipation (both one- and two-photon) tends to take the system toward the other solutions $\alpha_0 = \pm\alpha$ [Dykman et al. 1998; Zorin and Makhlin 2011; Wustmann and Shumeiko 2013]. Quantum mechanically, numerically diagonalizing the Hamiltonian finds the eigenstates. As we will see in the next section, evaluating the matrix elements of $\boldsymbol{a}$ between eigenstates, we notice that repeatedly applying $\boldsymbol{a}$ leaves the system in a mixture of the states $|\mathcal{C}_\alpha^\pm\rangle$. Thus, $|\mathcal{C}_\alpha^\pm\rangle$ are the degenerate ground states, which have maximum (minimum) energy depending on the sign of K. Eigenstates with weight near the origin of phase space are excited states and are not stationary under repeated application of $\boldsymbol{a}$. As such, both quantum mechanically and classically, the $\alpha_0 = 0$ solution will not be that interesting for us.

Next, we examine the Hamiltonian in the frame displaced by $\alpha_0 = \pm\alpha$:

$$\left.\mathcal{H}'_{2c}\right|_{\alpha_0=\pm\alpha} = -4\tilde{K}|\alpha|^2\boldsymbol{a}^\dagger\boldsymbol{a} - \tilde{K}\boldsymbol{a}^{\dagger 2}\boldsymbol{a}^2 \mp 2\tilde{K}\alpha\boldsymbol{a}^{\dagger 2}\boldsymbol{a} + \text{H.c.} \tag{4.35}$$

which looks like a Kerr nonlinear oscillator with an extra cubic distortion term or photon-number-dependent displacement. In the large α limit, this last term will give no correction at first order perturbation theory and will cause a second order correction to the self-Kerr term in this displaced frame. As such, we can view our phase space as now containing two identical anharmonic oscillators, each centered at $\pm\alpha$ respectively. We give the frequency of these oscillators a name

$$\begin{aligned}
\tilde{\omega}_{\text{gap}} = \omega_{\text{gap}} - i\kappa_{\text{gap}}/2 &= -4\tilde{K}|\alpha|^2 \\
&= -4K|\alpha|^2 - i2\kappa_2|\alpha|^2
\end{aligned} \tag{4.36}$$

whose real part ω_{gap} and imaginary part $\kappa_{\text{gap}}/2$ will play an important role in the mitigation of error processes. Eigenstates of these oscillators are Fock states, which are $D(\pm\alpha)\,|n\rangle$ in the original frame of equation 4.31. We expect then, in the large α limit, for the eigenspectrum to split into pairs of degenerate levels until the energy of those levels reaches near the top of the barrier in phase space, which leaves $\sim |\alpha|^2/4$ pairs of degenerate levels. We confirm this conclusion numerically in the following section.

Furthermore, we can already see here the protection against leakage errors that we get from this stabilization. The frequency of each oscillator is $\omega_{\text{gap}} = -4K|\alpha|^2$, which signifies the detuning of a drive from ω_a needed to cause a transition to a higher excited state. This is the same sort of protection that a transmon qubit (which can be approximated as an anharmonic oscillator) has against leakage errors to the f-state during gates: the anharmonicity prevents it. In the Kerr-cat qubit, the small oscillation frequency ω_{gap} around each of the individual wells at $\pm\alpha$ plays the role of anharmonicity in the transmon: it is the energy separation from the unwanted Hilbert space. Additionally, the associated dissipation in these displaced oscillators is half the imaginary part of the frequency $\kappa_{\text{gap}} = 4\kappa_2|\alpha|^2$. As such, any error mechanism that manages despite the anharmonicity to cause a small displacement in phase space away from our code states $|\pm\alpha\rangle$ will decay back to $|\pm\alpha\rangle$ exponentially with amplitude decay rate $2\kappa_2|\alpha|^2$ [Mirrahimi et al. 2014; Puri et al. 2019; Lescanne et al. 2019].

4.5 The quantum solution

To confirm our analytical calculations in the previous section and gain intuition about the phase-space structure of our stabilization Hamiltonian, we specify in this section the purely dispersive Kerr-cat Hamiltonian

$$
\begin{aligned}
\mathcal{H}_{2\text{c}}|_{\tilde{K}=K} &= -K a^{\dagger 2} a^2 + \epsilon_2 a^{\dagger 2} + \epsilon_2^* a^2 \\
&= -K \left(a^{\dagger 2} - \alpha^{*2} \right) \left(a^2 - \alpha^2 \right) + |\epsilon_2|^2/\tilde{K}
\end{aligned}
\tag{4.37}
$$

corresponding to Eq. 4.31 with $\kappa_2 = 0$ implying $\tilde{K} = K$. In order to visualize the structure of this Hamiltonian in phase space, we plot in Fig. 4.2a the energy as a function of classical phase space coordinates by performing the substitution $a, a^\dagger \to a, a^*$ in Eq. 4.37. Such a substitution is justified given our Hamiltonian is normal-ordered. We notice that constant energy contours through phase space form a double-well structure with a separatrix passing through the origin that divides the classical closed orbits into two categories: those closed around one extremum $\pm\alpha$, or those closed around all three extrema $0, \pm\alpha$. We numerically diagonalize Eq. 4.37 in the photon number basis and find the ground states are indeed the even and odd Schrödinger cat states [Puri, Boutin, and Blais 2017]. We mark the $\pm$ superpositions of the cat states (or $|\pm X\rangle$ states) by the green (orange) markers respec-
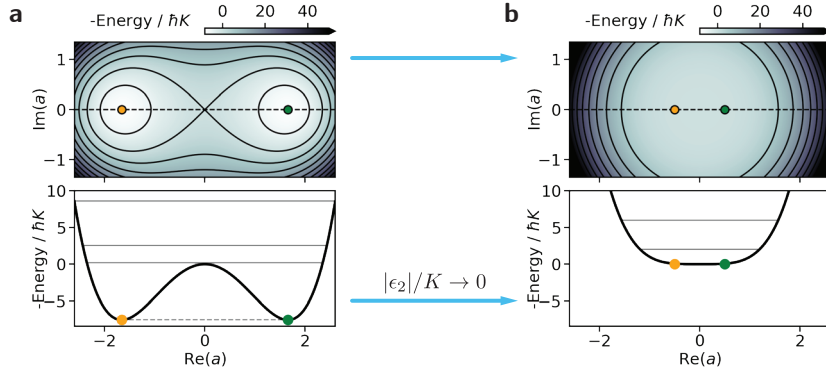
Figure 4.2 | (a),(b) Energy dependence of Hamiltonian Eq. 4.37 as a function of classical phase space coordinates a, $a^\dagger \rightarrow a$, a^* for purely Hamiltonian Kerr-cat qubit with $\bar{n} = 2.75$ and a transmon-based Fock qubit ($\epsilon_2 = 0$) respectively. Top panels contain contours of constant energy (solid black) with full energy dependence in color. Black dashed line indicates the line cut plotted in bottom panels. Green (orange) markers indicate quadrature expectation values of $|\pm X\rangle$, as well as their degenerate eigenenergies in the bottom panel (dashed gray line). Solid gray lines indicate eigenenergies of the first few excited states.

tively. The location of these markers denotes the pair of quadrature expectation values of operators $(a + a^\dagger)/2$ and $(a - a^\dagger)/2i$, which indeed are located at the extremum $\pm\alpha$ respectively. These two states $|\pm X\rangle \approx |\pm\alpha\rangle$ are separated in phase space by an energy barrier, and yet are also eigenstates.

Standard quantum mechanical intuition might lead us to believe that the local states $|\pm X\rangle \approx |\pm\alpha\rangle$ acquire a finite energy splitting due to quantum tunnelling to the opposite well; however, this is strictly *incorrect*. As we already saw, $\left|\mathcal{C}_\alpha^\pm\right\rangle$ and thus $|\pm\alpha\rangle$ are *exactly degenerate* eigenstates of Eq. 4.37. The breakdown of this intuition comes from a symmetry of the Hamiltonian that forbids this tunnel splitting for the ground states; the symmetry namely is that the Hamiltonian may be written strictly as a function of a^2 and $a^{\dagger 2}$, and therefore there is no quadratic-in-momentum term in the kinetic energy. A Hamiltonian term of the form $a^\dagger a$ breaks this symmetry and results in an exponentially small tunnel splitting as we will explore in the following sections (see also Table 4.1). Adding dissipation (in either single- or two-photon form) opens the closed orbits to trajectories that spiral toward the steady-state attractors at $\pm\alpha$, as analytically predicted via semiclassical methods [Dykman et al. 1998; Wustmann and Shumeiko 2013; Zorin and Makhlin 2011] or even via fully quantum mechanical steady state solutions [Bartolo et al. 2016; Roberts and Clerk 2020].

In Fig. 4.2b, we compare to the case where $\epsilon_2 = 0$ corresponding to an undriven Kerr-nonlinear oscillator, whose lowest two eigenstates implement the Fock qubit. In this case, there is no energy barrier between the states $|\pm X\rangle = (|0\rangle + |1\rangle)/\sqrt{2}$. The Hamiltonian has actually increased its symmetry—a discrete two-fold rotational symmetry is now continuous—and therefore these states are also exactly degenerate. In the Fock qubit case,
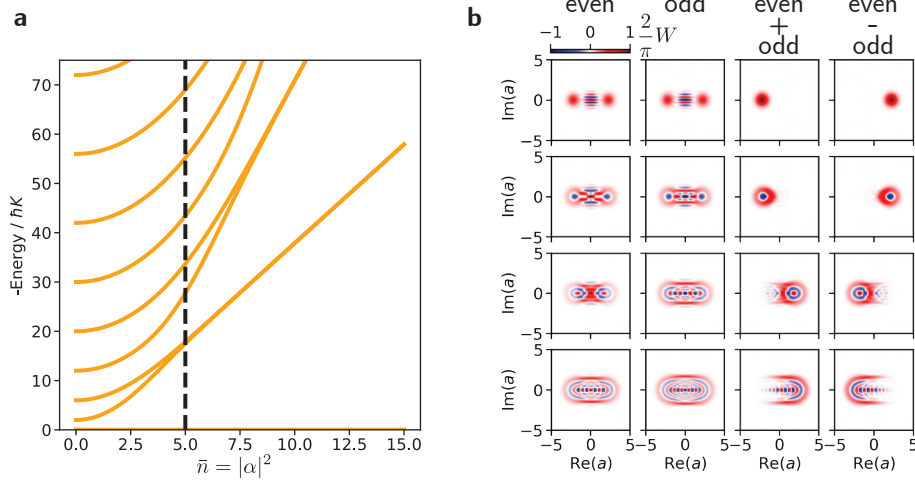
Figure 4.3 | (a) Eigenstate energy (relative to the degenerate ground states' energies) dependence of Hamiltonian Eq. 4.37 on the average number of photons $\bar{n} = |\alpha|^2 = |\epsilon_2/K|$. Black dashed line denotes $\bar{n} = 5$ used in (b). (b) Left two columns: Wigner functions of the first 8 eigenstates separated by their even or odd photon-number-parity eigenvalue. Right two columns: the $\pm$ superstitions of the even and odd parity eigenstates that become degenerate at large $\bar{n}$. The top row, from left to right, are the $|-Z\rangle$, $|+Z\rangle$, $|-X\rangle$, and $|+X\rangle$ states of the cat qubit Bloch sphere.

there is no drive present to privilege a frame, so this degeneracy is a direct consequence of working in the frame rotating at ω_a. The difference then between the Kerr-cat qubit and the Fock qubit is not so much the existence of the eigenstate degeneracy, but the *robustness* of that degeneracy to perturbations (again, see Table 4.1).

To further understand the robustness of the Kerr-cat Hamiltonian, we turn to the structure of the excited states of Eq. 4.37. In Fig. 4.3a, we plot the numerically calculated eigenenergies (relative to the degenerate ground state energies) as function of $\bar{n} = |\alpha|^2 = |\epsilon_2/K|$. Again, at $\epsilon_2 = 0$, we see the expected spectrum of a Kerr-nonlinear resonator with anharmonicity $2K$. As $\bar{n}$ increases, the eigenspectrum begins to show additional degeneracies. Specifically, at the black dashed line $\bar{n} = 5$, the second and third excited states—mapping back to $|n = 2\rangle$ and $|n = 3\rangle$ respectively when $\epsilon_2 = 0$—pair up and becomes degenerate[7]. Such a pairing of the eigenspectrum is signature of *period-doubling* phenomena [Dykman et al. 2018] and justifies the use of phase diagrams to delineate the different regimes [Dykman et al. 1998; Wustmann and Shumeiko 2013] as we will pursue shortly.

Before this, consider the Wigner functions of the lowest eight eigenstates plotted in Fig. 4.3b for $\bar{n} = 5$. The first row denotes the cat-qubit Bloch sphere with degenerate ground states $|\mathcal{C}_\alpha^\pm\rangle$ as well as their symmetric and antisymmetric superpositions $|\pm X\rangle \approx |\pm\alpha\rangle$, which are clearly localized to $\pm\alpha$ respectively. The next two excited states are already sufficiently degenerate so that their symmetric and antisymmetric superpositions

---

[7]Degenerate here means sufficiently close in energy to be considered degenerate in experiment—or degenerate to within the linewidth induced by dissipation.

may also be considered eigenstates. We see in Fig. 4.3b that these states are also well lo-
calized to $\pm\alpha$ and look approximately like $\boldsymbol{D}(\pm\alpha)\,|n=1\rangle$. In energy, they also live below
the top of the energy barrier, although less so than the ground states. The next two excited
states—numbers 4 and 5—are energetically above the energy barrier, outside the classical
separatrix. As such, they are not yet degenerate, implying their symmetric and antisym-
metric superpositions are not eigenstates. If an environmental fluctuation were to drive a
transition from say one of the lower local symmetric states to these eigenstates, the previous
locality would be washed away at rate of order the energy splitting. To counteract these
leakage-inducing transitions, the addition of two-photon [Puri et al. 2019] and colored-
single-photon [Putterman et al. 2021] dissipation have been suggested. Heuristically, as
long as dissipation keeps the quantum state in the $\approx |\alpha|^2/4$ pairs of degenerate levels be-
low the energy barrier, the induced cat-qubit phase-flip rate will be exponentially small
because the state will remain local. Finally, higher and higher excited states should again
converge to those of an undriven anharmonic oscillator, before that resembling squeezed
Fock states centered at the origin.

4.6 Including detuning and single-photon loss

The previous two sections gave a model for the stabilization of a Kerr-cat qubit in the ideal
case. However, experimentally applied drives will never be perfectly on resonance and
single-photon loss will never be truly absent. This section will add these terms back to the
model and show that the entire cat Bloch sphere may be stabilized and protected even in
their presence. The treatment will result in conditions on the magnitude of the detuning
and single-photon loss to remain in the protected cat regime. We also saw when discussing
SPAs in Chapter 3 that two-photon drives give rise to squeezing and amplification, thus far
absent in this chapter. Including both of these effects requires introducing a phase diagram,
previously developed [Dykman et al. 1998; Wustmann and Shumeiko 2013] and semiclas-
sically adapted to SPAs specifically in Appendix A [Sivak et al. 2019].

Let us begin with the general non-Hermitian Hamiltonian in the frame rotating to make
the two-photon drive static (so half of the squeezing drive frequency ω_p in a three-wave
mixing implementation)

$$\boldsymbol{\mathcal{H}}_{\text{KC}} = -\tilde{\Delta}\boldsymbol{a}^\dagger\boldsymbol{a} - \tilde{K}\boldsymbol{a}^{\dagger 2}\boldsymbol{a}^2 + \epsilon_2\boldsymbol{a}^{\dagger 2} + \epsilon_2^*\boldsymbol{a}^2 \tag{4.38}$$

where as before

$$\tilde{\Delta} = \Delta + i\kappa_1/2 \tag{4.39}$$

$$\tilde{K} = K + i\kappa_2/2 \tag{4.40}$$

are the complex detuning and complex Kerr nonlinearities respectively. Going into the

displaced frame with test amplitude α_0,

$$\begin{aligned}
\mathcal{H}'_{\text{KC}} = {} & \left[-2\tilde{K}\alpha_0^2\alpha_0^* + 2\epsilon_2\alpha_0^* - \tilde{\Delta}\alpha_0 \right] \boldsymbol{a}^\dagger + \text{H.c.} \\
& + \left(-\tilde{K}\alpha_0^2 + \epsilon_2 \right) \boldsymbol{a}^{\dagger 2} + \text{H.c.} \\
& + \left(-4\tilde{K}|\alpha_0|^2 - \tilde{\Delta} \right) \boldsymbol{a}^\dagger \boldsymbol{a} - \tilde{K}\boldsymbol{a}^{\dagger 2}\boldsymbol{a}^2 \\
& - 2\tilde{K}\alpha_0 \boldsymbol{a}^{\dagger 2}\boldsymbol{a} + \text{H.c.}
\end{aligned} \tag{4.41}$$

is the transformed Hamiltonian. To null the linear displacement terms, we solve the polynomial equation

$$2\tilde{K}\alpha_0^2\alpha_0^* = 2\epsilon_2\alpha_0^* - \tilde{\Delta}\alpha_0 \tag{4.42}$$

We can see immediately that $\alpha_0 = 0$ is a solution and then we are free to divide by $2\tilde{K}\alpha_0$ and rearrange to solve for the remaining solutions:

$$\frac{\epsilon_2}{\tilde{K}}\frac{\alpha_0^*}{\alpha_0} = |\alpha_0|^2 + \frac{\tilde{\Delta}}{2\tilde{K}} \tag{4.43}$$

This rearrangement is convenient for solving the magnitude $|\alpha_0|$ first and then the phase later. Multiplying both sides by their complex conjugates, we have

$$\left|\frac{\epsilon_2}{\tilde{K}}\right|^2 = |\alpha_0|^4 + 2\,\text{Re}\left\{\frac{\tilde{\Delta}}{2\tilde{K}}\right\}|\alpha_0|^2 + \left|\frac{\tilde{\Delta}}{2\tilde{K}}\right|^2 \tag{4.44}$$

which is a quadratic equation for $|\alpha_0|^2$ with solutions

$$|\alpha_0|^2 = -\text{Re}\left\{\frac{\tilde{\Delta}}{2\tilde{K}}\right\} \pm \sqrt{\left|\frac{\epsilon_2}{\tilde{K}}\right|^2 - \left(\text{Im}\left\{\frac{\tilde{\Delta}}{2\tilde{K}}\right\}\right)^2} \tag{4.45}$$

$$= \frac{1}{2|\tilde{K}|^2}\left(-\Delta K + \frac{\kappa_1\kappa_2}{4}\right) \pm \sqrt{\left|\frac{\epsilon_2}{\tilde{K}}\right|^2 - \left(\frac{K\kappa_1 - \Delta\kappa_2}{4|\tilde{K}|^2}\right)^2} \tag{4.46}$$

where this expression gives all possible solutions (stable and unstable) as long as we require the discriminant ≥ 0 and $|\alpha_0|^2 \geq 0$.

We will examine these regimes in the next section, but first for completeness we want to solve for the phase ϕ_0 as well. Parameterizing as $\alpha_0 = |\alpha_0|e^{-i\phi_0}$, we choose to take the

imaginary part of Eq. 4.43 which leaves

$$\text{Im}\left\{\frac{\epsilon_2}{\tilde{K}}e^{+i2\phi_0}\right\} = \text{Im}\left\{\frac{\tilde{\Delta}}{2\tilde{K}}\right\} \tag{4.47}$$

$$\sin\left(2\phi_0 - \arg\left(\epsilon_2/\tilde{K}\right)\right) = \frac{K\kappa_1 - \Delta\kappa_2}{4|\epsilon_2||\tilde{K}|} \tag{4.48}$$

Importantly, there are always 2 valid phases ϕ_0 within one drive period—a defining feature of period doubling. Defining $\tilde{\phi}_0 = \phi_0 - \arg(\epsilon_2/\tilde{K})/2$, the equation for the valid phases reduces to

$$\sin\left(2\tilde{\phi}_0\right) = \frac{K\kappa_1 - \Delta\kappa_2}{4|\epsilon_2||\tilde{K}|} \tag{4.49}$$

where it is clear there exist π-periodic solutions for $\tilde{\varphi}_0$, which implies two coherent states that are always 180 degrees out of phase or symmetric about the origin of phase space. This 180 degrees out of phase is a robust consequence of period doubling; if solutions $|\alpha_0| \neq 0$ are stable, there will always be two that are 180 degrees out of phase.

4.7 Multi-stability regions

The goal of this section is to find the regions of parameter space where the five possible solutions of Eq. 4.42 are actually stable solutions. Our five possible solutions are: $\alpha_0 = 0$, and two-oppositely phased solutions for each the $+$ and $-$ solution in Eq. 4.45. As depicted in Figure 4.4, we will find three regions in parameter space that will host one, two, or three stable solutions of α_0 respectively. To delineate these regions, we will use the conditions on the solutions to Eq. 4.45 that $|\alpha_0| \geq 0$ and that $|\alpha_0| \in \mathbb{R}$, which translates to the discriminant from the quadratic formula being positive.

For clarity, we briefly summarize what these conditions enforce are the stable solutions before explicitly deriving the boundaries.

1. **Region I**: Only $\alpha_0 = 0$ is stable and so this is the trivial solution corresponding to a single stable point.

2. **Region II**: Two states with opposite phases are stable, both with amplitudes given by the $+$ solution of Eq. 4.45. This is the desired regime for Schrödinger cat state stabilization.

3. **Region III**: This tri-stable regime has three steady states with $\alpha_0 = 0$ and $|\alpha_0|$ given by the $-$ solution of Eq. 4.45.

These regions in parameter space are plotted for three different regimes of κ_2 and K in Figure 4.4, from the purely dispersive Kerr-cat regime where $\kappa_2 = 0$ on the left to the driven-dissipative case where $\kappa_2 \gg K$ on the right.
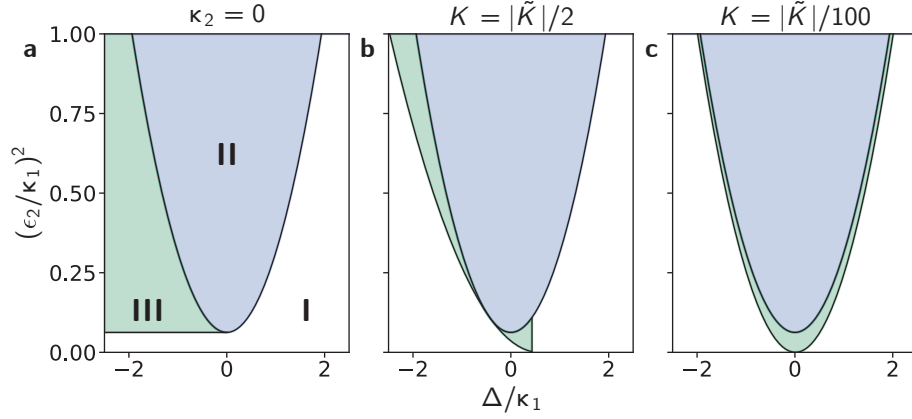
Figure 4.4 | Stability diagrams for $|\tilde{K}| = 10\kappa_1$ with (a) $\kappa_2 = 0$, (b) $K = |\tilde{K}|/2$ and (c) $K = |\tilde{K}|/100$, which span from a pure Kerr cat to a purely driven-dissipative stabilization. There exist three distinct regions in parameter space delineated by the number of stable solutions to equation (4.43). Region I (white), II (blue), and III (green) have one, two, or three stable solutions respectively. For cat qubits, we intentionally bias deep inside region II where quantum information is well-protected in the form of the two-legged Schrödinger cat code defined in Sec. 4.1.

Now we explicitly derive the boundaries between these regions. In order for any $\alpha_0 \neq 0$ solutions to exist, we require $|\alpha_0| \in \mathbb{R}$ or

$$\left| \frac{\epsilon_2}{\tilde{K}} \right|^2 \geq \left(\mathrm{Im} \left\{ \frac{\tilde{\Delta}}{2\tilde{K}} \right\} \right)^2$$

$$\implies |\epsilon_2|^2 \geq \frac{(K\kappa_1 - \Delta\kappa_2)^2}{16|\tilde{K}|^2} \tag{4.50}$$

Saturating this constraint to equality defines the parabolic boundary between regions I and III, which flattens into a horizontal line in the limit $\kappa_2 \to 0$. Interestingly, for $\kappa_2 \neq 0$, we can find a $\Delta = K\kappa_1/\kappa_2$ at which applying vanishing two-photon drive ($\epsilon_2 \to 0$) still satisfies this condition and results in tri-stability, as can be seen by region III touching the horizontal axis in Fig. 4.4b–4.4c.

In order for the $-$ solution to exist, along with the condition Eq. 4.50, we require $|\alpha_0| \geq 0$ by first insisting

$$-\mathrm{Re} \left\{ \tilde{\Delta}/2\tilde{K} \right\} \geq 0$$

$$\implies K\Delta \leq \kappa_1\kappa_2/4 \tag{4.51}$$

whose boundary is independent of ϵ_2 and thus a vertical line delineating region I from region III as evident in Figure 4.4b. Note that the sign of K, in the plots assumed to be positive to conform the usual case of negative anharmonicity, will determine the direction

of the inequality. In general, flipping the sign of K will invert the Δ axis.

Finally, for existence of the $+$ solution, we require condition Eq. 4.50 and enforce $|\alpha| \geq 0$ by requiring

$$
\left| \frac{\epsilon_2}{\tilde{K}} \right|^2 - \left(\mathrm{Im} \left\{ \frac{\tilde{\Delta}}{2\tilde{K}} \right\} \right)^2 \geq \left(\mathrm{Re} \left\{ \frac{\tilde{\Delta}}{2\tilde{K}} \right\} \right)^2
$$

$$
\implies \left| \frac{\epsilon_2}{\tilde{K}} \right|^2 \geq \left| \frac{\tilde{\Delta}}{2\tilde{K}} \right|^2
$$

$$
\implies |\epsilon_2|^2 \geq \frac{\Delta^2 + \kappa_1^2/4}{4} \tag{4.52}
$$

which importantly is completely independent of $\tilde{K}$.

Given the three conditions Eqs. 4.50, 4.51, 4.52 and excluding saddle points of the Hamiltonian Eq. 4.38 as unstable, we delineate parameter space into the three regions with one, two, and three stable solutions for α_0 as promised[8]. Cuts of this parameter space are plotted on the $|\epsilon_2|^2$ and Δ plane in Fig. 4.4. Note, for a two-photon drive that results from a three-wave-mixing process, $|\epsilon_2|^2$ is proportional to the drive power, and $\Delta = \omega_p/2 - \omega_a$ is the detuning of half the pump frequency ω_p from resonance. For all three cuts, we use the condition $|\tilde{K}| = 10\kappa_1$ and vary the phase of $\tilde{K}$ or equivalently the ratio of κ_2 to K.

Starting with Fig. 4.4a, we have the purely dispersive Kerr-cat regime where $\kappa_2 = 0$ and therefore $\tilde{K} = K$. There exists a single triple point at $\Delta = 0$ and $|\epsilon_2|^2 = \kappa_1^2/16$ at which all three solution regimes coexist. This triple point also coincides with the minimum of the parabola from condition Eq. 4.52. As such, increasing $|\epsilon_2|^2$ beyond the threshold $(\Delta^2 + \kappa_1^2/4)/4$, which precisely corresponds to the parametric instability in parametric amplifiers (see Eq. 3.21), the oscillator enters the bi-stable regime of region II that we discuss in detail in the next section. For the remaining boundary between regions I and III, condition Eq. 4.50 reduces to a horizontal line which requires $|\epsilon_2| \geq \kappa_1/4$ in order to have any solutions with $|\alpha_0| \neq 0$.

Moving to Fig. 4.4b, Kerr and two-photon dissipation contribute equally with $K = |\tilde{K}|/2$. The boundary to enter region II is unchanged compared to the previously purely dispersive case because condition Eq. 4.52 is independent of $\tilde{K}$. However, condition Eq. 4.50 is now a parabola with a minimum at $\Delta/\kappa_1 = K/\kappa_2$. Instead of intersecting the region II boundary at one location, there are now two intersections resulting in two separate triple points. In general, as κ_2/K is increased these two triple points separate staying constrained to the boundary of region II.

Increasing κ_2 so that $K = |\tilde{K}|/100$ leads to Fig. 4.4c where the two triple points have moved outside the plotted window. Region III now nearly completely encases region II

---

[8]Proving stability requires examining attractors in phase space [Dykman et al. 1998; Zorin and Makhlin 2011; Wustmann and Shumeiko 2013], or solving the steady state exactly [Bartolo et al. 2016; Roberts and Clerk 2020].

such that moving from region I to region II requires passage through region III. Specifically, in the limit $K \to 0$, the intersection between regions I and III is defined by condition Eq. 4.50 as $|\epsilon_2|^2 \geq \Delta^2/4$, which mimics condition Eq. 4.52 without the offset by $\kappa_1^2/16$.

Before continuing, we should also note a few comments about Stark shifts. So far, Hamiltonian Eq. (4.38) has been written in the frame that makes the two-photon-drive resonant (so $\omega_p/2$ for three-wave mixing) and the Kerr term has been normal-ordered. Experimentally, there will always be a Stark-shift (or more generally a renormalization) of the oscillator frequency due to the application of the drive. This can be included in the above discussion by making the substitution $\Delta \to \Delta + f(|\epsilon_2|^2)$ since the oscillator frequency now depends on the drive power, for example see Eq. 3.18. For the standard AC Stark shift, $f(|\epsilon_2|^2) \propto |\epsilon_2|^2$ which will warp the regions of stability in Fig. 4.4 by bending them to the left [Wustmann and Shumeiko 2013; Sivak et al. 2019]. The foremost qualitative feature added by considering the AC Stark shift is the existence of a critical detuning (> 0 for $K > 0$ as plotted) above which increasing the drive power will no longer bring the system into region II, but instead remains in the trivial region I. In parametric amplifiers, this qualitative feature explains the inability to tune up large gain for large blue-detuned squeezing drives, as derived by Eq. 3.25.

Now that we understand how the stable solutions for α_0 depend on experimental parameters, we can ask what quantum fluctuations will do in the full quantum-mechanical problem. In general, fluctuations will smear the boundaries between the different regions as well as couple states localized at each of the stable α_0 solutions. However, as long as the stable α_0 solutions are far apart in phase space, coherent states centered at each α_0 (and/or their superpositions) will be a good basis for describing dynamics. Moreover, in this limit the density matrix of the oscillator in the long time limit will be a mixture of these coherent states which is precisely why they are the classically steady states to begin with.

4.8 Robustness of the bi-stable regime: home for cats

Having understood the boundaries in parameter space between different regions of stability, we focus now on the home for the Schrödinger cat code outlined at the beginning of this chapter in Sec. 4.1: region II. In this region it is useful to rewrite the solutions for α_0 in terms of deviations from the solutions $\pm\sqrt{\epsilon_2/\tilde{K}}$. To this end, we rewrite the $+$ solution of Eq. 4.45 for the magnitude and the phase Eq. 4.49 as

$$|\alpha_0|^2 = \left|\frac{\epsilon_2}{\tilde{K}}\right| \left[-\text{Re}\left\{\tilde{\delta}\right\} + \sqrt{1 - \left(\text{Im}\left\{\tilde{\delta}\right\}\right)^2} \right] \tag{4.53}$$

$$\sin\left(2\tilde{\varphi}_0\right) = \text{Im}\left\{\tilde{\delta}\right\} \tag{4.54}$$

where $\tilde{\varphi}_0$ is the phase referenced to the case $\tilde{\Delta} = 0$ and

$$
\begin{aligned}
\tilde{\delta} &= \frac{\tilde{\Delta}}{2\tilde{K}} \left| \frac{\tilde{K}}{\epsilon_2} \right| = \frac{\tilde{\Delta}\tilde{K}^*}{2|\epsilon_2||\tilde{K}|} \\
&= \frac{(\Delta K + \kappa_1\kappa_2/4)}{2|\epsilon_2||\tilde{K}|} + i\frac{K\kappa_1 - \Delta\kappa_2}{4|\epsilon_2||\tilde{K}|}
\end{aligned}
\tag{4.55}
$$

is a dimensionless detuning. When $\tilde{\delta} = 0$, the problem reduces to the one from Section 4.4 where the solutions are $\alpha_0 = \pm\sqrt{\epsilon_2/\tilde{K}}$. The reduced detuning encodes the discrepancy from this case caused by finite detuning Δ or single-photon loss κ_1. The magnitude

$$
|\tilde{\delta}| = \frac{|\tilde{\Delta}|}{2|\epsilon_2|} = \frac{\sqrt{\Delta^2 + \kappa_1^2/4}}{2|\epsilon_2|}
\tag{4.56}
$$

also conveniently encapsulates the condition Eq. 4.52 to be inside region II as $|\tilde{\delta}|^2 < 1$.

To analyze the steady state deep inside region II, we consider the limit $|\tilde{\delta}|^2 \ll 1$. We then Taylor expand

$$
\begin{aligned}
|\alpha_0|^2 &\to \left| \frac{\epsilon_2}{\tilde{K}} \right| \left[1 - \text{Re}\left\{\tilde{\delta}\right\} - \frac{1}{2}\left(\text{Im}\left\{\tilde{\delta}\right\}\right)^2 + \mathcal{O}(|\tilde{\delta}|^3) \right] \\
&= \left| \frac{\epsilon_2}{\tilde{K}} \right| \left[1 - \frac{\Delta K + \kappa_1\kappa_2/4}{2|\epsilon_2||\tilde{K}|} - \frac{(K\kappa_1 - \Delta\kappa_2)^2}{32|\epsilon_2|^2|\tilde{K}|^2} + \mathcal{O}(|\tilde{\delta}|^3) \right]
\end{aligned}
\tag{4.57}
$$

to see that the photon number deviates linearly in $\text{Re}\left\{\tilde{\delta}\right\}$ from the unperturbed solution. Similarly the phase $\tilde{\varphi}_0$ deviates linearly with $\text{Im}\left\{\tilde{\delta}\right\}/2$ in the small angle expansion.

Truncating more aggressively to ignore terms $\mathcal{O}(|\tilde{\delta}|^2)$ and combining the amplitude and phase information, we have

$$
\alpha_0 \to \pm\sqrt{\frac{\epsilon_2}{\tilde{K}}} \left[1 - \frac{\tilde{\delta}}{2} + \mathcal{O}(|\tilde{\delta}|^2) \right]
\tag{4.58}
$$

which readily lends the interpretation that $\tilde{\delta}/2$ is simply an additional displacement. This reveals a robustness to noise processes that can be written in the Hamiltonian form $-(\Delta + i\kappa_1/2)a^\dagger a$—which includes single-photon loss, single-photon gain, low-frequency detuning noise originating from flux charge noise, and some part of pure dephasing noise (see Appendix B). Such noise processes may be mapped to small displacements insofar as $|\tilde{\delta}|/2 \ll |2\alpha|^2$, meaning they are small compared to the distance between our two stable qubit ground states. The induced leakage errors are then *local* in phase space, and jumps associated with single- or two-photon loss may correct them before they develop into a full logical phase flip between coherent states.

4.8.1 Eigenstate perturbations

To inspect the changes detuning and single-photon loss induce on the eigensates, we turn to the displaced frame Hamiltonian Eq. 4.41

$$\mathcal{H}'_{\text{KC}} = \frac{\tilde{\Delta}}{2} e^{-i2\varphi_0} a^{\dagger 2} + \text{H.c.}$$
$$+ \left(-4\tilde{K}|\alpha_0|^2 - \tilde{\Delta} \right) a^{\dagger} a - \tilde{K} a^{\dagger 2} a^2$$
$$- 2\tilde{K}\alpha_0 a^{\dagger 2} a + \text{H.c.} \tag{4.59}$$

assuming α_0 solves Eq. 4.43 under the conditions of region II. We see a slightly squeezed, anharmonic oscillator with an additional distortion term (last line). Comparing with the same Hamiltonian setting $\tilde{\Delta} = 0$ in Eq. (4.35), the only differences are an offset of the frequency and a two-photon drive both of strength $\tilde{\Delta}$. The relative frequency offset is small insofar as $|\tilde{\delta}|/2 \ll 1$. Looking at this displaced oscillator frequency more carefully, we find

$$\tilde{\omega}_{\text{gap}} = \left(-4\tilde{K}|\alpha_0|^2 - \tilde{\Delta} \right) \tag{4.60}$$

$$= -4\tilde{K} \left| \frac{\epsilon_2}{\tilde{K}} \right| \left[\sqrt{1 - \left(\text{Im}\left\{ \tilde{\delta} \right\} \right)^2} - \frac{\tilde{\delta}^*}{2} \right] \tag{4.61}$$

$$= \left(-4K|\alpha_0|^2 - \Delta \right) - i \left(2\kappa_2|\alpha_0|^2 + \frac{\kappa_1}{2} \right) \tag{4.62}$$

whose real and imaginary parts increase with $|\alpha_0|^2$; both the frequency and the amplitude decay rate back to the $|n = 0\rangle$ state increase with $|\alpha_0|^2$ in this displaced frame.

Upon further inspection of the displaced Hamiltonian Eq. 4.59, we might be concerned that this Hamiltonian mirrors the form of our original Hamiltonian Eq. 4.38 but with an extra term. Ignoring the extra term first since it annihilates the lowest Fock state $|n = 0\rangle$, we need to be sure that states around the center of this displaced phase space will be stable or else we will again have multiple solutions. However, so long as $|\tilde{\Delta}| < |\tilde{\omega}_{\text{gap}}|$, we should only have a single stable solution in phase space. The ground state in this case is a squeezed state, where $|\tilde{\Delta}|/|\tilde{\omega}_{\text{gap}}|$ is a small parameter that sets the amount of squeezing. The axis of the squeezing in the displaced frame relative to the direction of the opposite solution is given by the phase of $\tilde{\Delta}$. In the case $\Delta = 0$, the ground state of this displaced oscillator is slightly elongated in the direction of the opposite stable solution; for nonzero Δ and $\kappa_1 = 0$, the elongation of the ground state is orthogonal to the prior case. Although small in magnitude, this squeezing is important for the structure of the ground state manifold and also for evaluating the jump rate between the two stable α_0 solutions. While we often use stochastic master equations with phenomenological noise strengths to numerically simulate these rates, analytical calculations often reduce the dynamics via an instanton approximation that latches to the most-probable tunnelling path through phase space between the two

steady state solutions [Marthaler and Dykman 2007]. The phase of $\tilde{\Delta}$ heavily influences this as can be visualized by the squeezing term in the displaced frame Hamiltonian. In general this path makes an S-shape connecting the two-wells that snaps to a straight line when $\Delta = 0$ [Dykman et al. 1998; Marthaler and Dykman 2007; Zorin and Makhlin 2011; Zhang and Dykman 2017].

Returning to the last term in Eq. 4.59, perturbatively it connects higher level local states, which are approximately displaced Fock states, across the energy barrier to other such states centered at the opposite extrema in phase space. We may visualize this effect by considering the Wigner functions in Fig. 4.3 of the superpositions of higher eigenstates that are still below the top of the energy barrier; they appear to be leaking toward the opposite well. As such, the nonlocal encoding of local states necessary for the exponential suppression of phase flip errors gets polynomially worse for higher excited states. Hence, dissipation is necessary to cool back down to the ground states and maintain protection.

To summarize this chapter, we introduced the two-legged Schrödinger cat qubit as a noise-biased qubit defined by the Bloch sphere in Sec. 4.1 and analyzed its coupling to the environment through low-weight operators $\boldsymbol{a}$, $\boldsymbol{a}^\dagger$, and $\boldsymbol{a}^\dagger\boldsymbol{a}$ summarize by Table 4.1. We introduced a fully autonomous stabilization and QEC protocol via the Hamiltonian 4.38 that ideally achieves exponential phase-flip suppression with a linear increase in bit-flip rate [Cochrane, Milburn, and Munro 1999; Mirrahimi et al. 2014; Puri, Boutin, and Blais 2017; Puri et al. 2019]. This corresponds to the implementation of a canonical multi-qubit phase-flip repetition code, but implemented only with an average of $\bar{n}$ photons within a single oscillator. It also simultaneously and autonomously corrects leakage errors. Finally, we derived a phase diagram in terms of experimental parameters and found three regions of stability with one, two and three steady states respectively. The bi-stable regime corresponds to the safe haven for the Schrödinger cat qubit, and the robustness to noise of the Hamiltonian form $-(\Delta + i\kappa_1/2)\boldsymbol{a}^\dagger\boldsymbol{a}$ comes directly from the long-time stability of the period-doubling in this bifurcated system.

5

Realization of a Kerr-cat qubit

As we investigated theoretically in the previous chapter, a combination of a single-mode squeezing drive and Kerr nonlinearity stabilizes a two-legged Schrödinger cat qubit. In this section, we focus on the experimental realization of such an autonomous stabilization scheme [Grimm et al. 2020]. We will show an increase in the transverse relaxation time of more than one order of magnitude compared to the single-photon Fock-state encoding. Crucially, we also perform a complete set of single-qubit gates on timescales more than sixty times faster than the shortest coherence time. Finally, we also demonstrate single-shot readout of the noise-biased qubit in a quantum nondemolition (QND) way while under stabilization. Further extensions of these results will be presented in Chapter 6. Overall, our results showcase the combination of fast quantum control and robustness against errors, which is intrinsic to stabilized nonlocal encodings, as well as the potential to be used in quantum information processing [Puri et al. 2019; Puri et al. 2020; Guillaud and Mirrahimi 2019; Goto 2016b].

Our single-mode bosonic implementation should be directly compared to repetition codes of transmon qubits [Kelly et al. 2015]. Recent results from Google Quantum AI harness 21 transmons qubits (not counting the tunable-coupler qubits between them) in a repetition code to achieve a 100-fold error suppression [Chen et al. 2021]: a feat possible only with many input-output lines and carefully crafted protocols to periodically extract leakage [McEwen et al. 2021]. Our results [Grimm et al. 2020] and those based on purely dissipative cats [Lescanne et al. 2020] achieve similar levels of suppression, with only linear increase of errors in the orthogonal direction, all while utilizing significantly fewer degrees of freedom, input-output ports, and room-temperature electronics.

5.1 Single qubit implementation

Our implementation is simple and versatile: a superconducting SNAIL-based transmon under parametric driving. Unlike other hardware-efficient encodings with bosonic qubits [Ofek et al. 2016; Hu et al. 2019; Campagne-Ibarcq et al. 2020], the most nonlinear mode of our system encodes and stabilizes the qubit without requiring auxiliary nonlinear modes that often introduce additional uncorrectable errors. As we saw in Chapter 4, the purely dispersive Kerr-cat qubit is governed by the Hamiltonian 4.37, which consists of a single-mode squeezing drive and Kerr nonlinearity that we must now engineer.

For this goal, our experimental implementation consists of a superconducting nonlinear resonator placed inside a 3D microwave cavity (Fig. 5.1a). This is a standard setup in 3D transmon qubits with a few key modifications. The foremost modification, employing a SNAIL (see Chapter 2) as the nonlinear inductor, allows us to create single-mode squeezing through three-wave mixing by applying a strong microwave pump tone at fre-
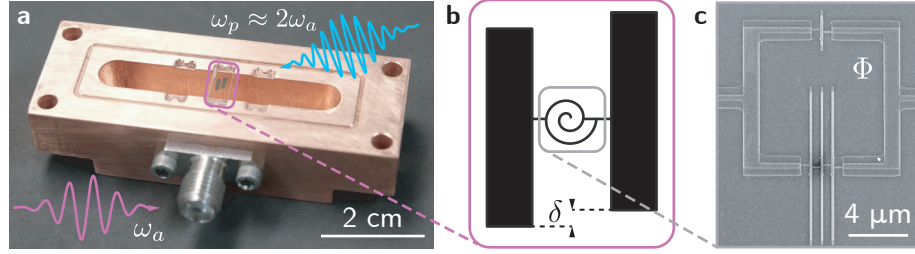
Figure 5.1 | (a) Photograph of the nonlinear resonator (purple frame) inside the copper section of the readout cavity. The second half of the cavity, machined from 6061 Al (not shown), is aperture-coupled to a section of Al WR-90 waveguide (not shown), which acts as a high-pass Purcell filter with a cutoff frequency $\approx 8.2\,\text{GHz}$ and assists in delivering the strong squeezing pump tone at $\omega_p \approx 2\omega_a$. (b) Schematic of the nonlinear resonator hosting the Schrödinger cat states. The large pads (black) set the nonlinear resonator's dipole capacitance to $E_C/h \approx 65\,\text{MHz}$, and the pad offset δ sets the dispersive coupling to the readout cavity. Biased with an external magnetic flux Φ, A SNAIL, electron micrograph in (c), provides the nonlinearity necessary for both the Kerr and the squeezing drive through three-wave mixing.

quency ω_p near twice the resonator frequency ω_a. Fabricated this time with a bridge-free technique [Lecocq et al. 2011] of aluminum on sapphire (see Fig. 5.1c), the SNAIL makes the resonator flux tunable. Here, we flux-tune the resonant frequency of the device to $\omega_a/2\pi = 6\,\text{GHz}$ by flowing DC-current through a coil mounted beneath the copper section of the readout cavity. The SNAIL also supplies four-wave mixing capabilities and thus the desired Kerr nonlinearity, see Sec. 2.2 and Eq. 2.53. Large capacitor pads, depicted in Fig. 5.1b, with dipole charging energy $E_C/h \approx 65\,\text{MHz}$ help reduce the Kerr nonlinearity to a measured anharmonicity $2K/2\pi = 13.4\,\text{MHz}$. In summary, we have a low-anharmonicity capacitively-shunted flux qubit [Yan et al. 2016], biased away from a flux sweetspot at $\Phi = 0.26\,\Phi_0$ to maintain appreciable three-wave-mixing nonlinearity $g_3/2\pi \approx 20\text{MHz}$ that may otherwise be approximated as a Fock qubit (FQ). At this frequency, the Fock qubit has an amplitude damping time $T_1 = 15.5\,\mu\text{s}$, and a transverse relaxation time $T_2 = 3.4\,\mu\text{s}$.

The Fock qubit is employed for initialization and measurement of the Kerr-cat qubit during most experiments in this work. This is possible because, as discussed in Sec. 4.1 and Fig. 4.1, the states share a common Bloch sphere definition $|\pm Z\rangle = |\mathcal{C}_\alpha^\pm\rangle$ with the appropriately chosen values of α for the Kerr-cat qubit and $\alpha \to 0$ for the Fock qubit. Intuitively, photon number parity is conserved by the Hamiltonian 4.37 regardless of the value of ϵ_2. Consequently, ramping the squeezing drive on and off slowly with respect to $1/2K$ adiabatically maps between the Fock qubit and Kerr-cat qubit [Puri, Boutin, and Blais 2017], an operation we will refer to as *mapping*.

5.2 Proof of cat by Rabi oscillations

We now show that we indeed implement the Hamiltonian 4.37, and thus stabilize a Kerr-cat qubit, by demonstrating the unique features of Rabi oscillations around the X axis of its Bloch sphere. To this end, we apply an additional coherent drive with amplitude ϵ_x and frequency $\omega_p/2 = \omega_a$. Within the RWA, this adds the Hamiltonian term $\epsilon_x \boldsymbol{a}^\dagger + \epsilon_x^* \boldsymbol{a}$. We may project onto the Kerr-cat Bloch sphere using Table 4.1 in the appreciable $|\alpha|^2$ limit

$$\boldsymbol{P}_\mathcal{C} \left(\epsilon_x \boldsymbol{a}^\dagger + \epsilon_x^* \boldsymbol{a} \right) \boldsymbol{P}_\mathcal{C} \approx (\epsilon_x \alpha^* + \epsilon_x^* \alpha)\boldsymbol{X} + i(\epsilon_x \alpha^* - \epsilon_x^* \alpha)e^{-2|\alpha|^2}\boldsymbol{Y} \tag{5.1}$$

where we see Rabi oscillations predominantly around the X axis with the Rabi rate

$$\Omega_x = \mathrm{Re}\left\{ 4\epsilon_x \alpha^* \right\} \tag{5.2}$$

and an exponentially small Rabi rate around the Y axis. Intuitively, the drive lifts the degeneracy between $|\pm X\rangle \approx |\pm \alpha\rangle$ by linearly tilting the Hamiltonian's action in phase space, causing a relative energy difference between the two extrema in Fig. 4.2a. The change however is *only* relative; one well moves up in energy and the other down by the same amount. Thus, all the cat states even/odd $|\pm Z\rangle = \left| \mathcal{C}_\alpha^\pm \right\rangle$ and parityless $|\pm Y\rangle$ remain degenerate. This simple argument already hints at the robustness of the cat-state degeneracy to Hamiltonian terms of the form $\boldsymbol{a}$ or $\boldsymbol{a}^\dagger$.

Another equivalent picture considers the action of the Hamiltonian in phase space. Assuming the stabilization drive ϵ_2 is strong enough to fix the locations $\pm\alpha$ in phase space, then the action of the drive makes an infinitesimal displacement before it is stabilized back, a form of Zeno dynamics in the two-photon dissipation case [Touzard et al. 2018]. When the displacement pushes the fringes of the cat states vertically, then a small phase within the Bloch sphere is accumulated to which the stabilization is agnostic by construction. When the displacement pushes the fringes in the orthogonal direction, the cat-state fringes do not roll and the action is identity within the cat-code space. No matter the picture though, cat states become other cat states with different or undefined parity, but the coherent states are approximately eigenstates of the added drive Hamiltonian and thus are not affected by it.

These pictures are only valid for large enough α and so long as the population stays within the Kerr-cat Bloch sphere (i.e. no leakage errors). In order for the on-resonance drive at $\omega_p/2$ to cause leakage to higher excited states, the drive strength ϵ_x would need to overcome the detuning by $\omega_{\mathrm{gap}} \approx -4K|\alpha|^2$ (Eq. 4.36 or reading off Fig. 4.2a). The adiabaticity condition to prevent leakage then restricts $\epsilon_x \ll \omega_{\mathrm{gap}}$, which in turn restricts the maximum Rabi rate to

$$|\Omega_x| \ll 4|\omega_{\mathrm{gap}}\alpha| \approx 16|K\alpha|^3 \tag{5.3}$$
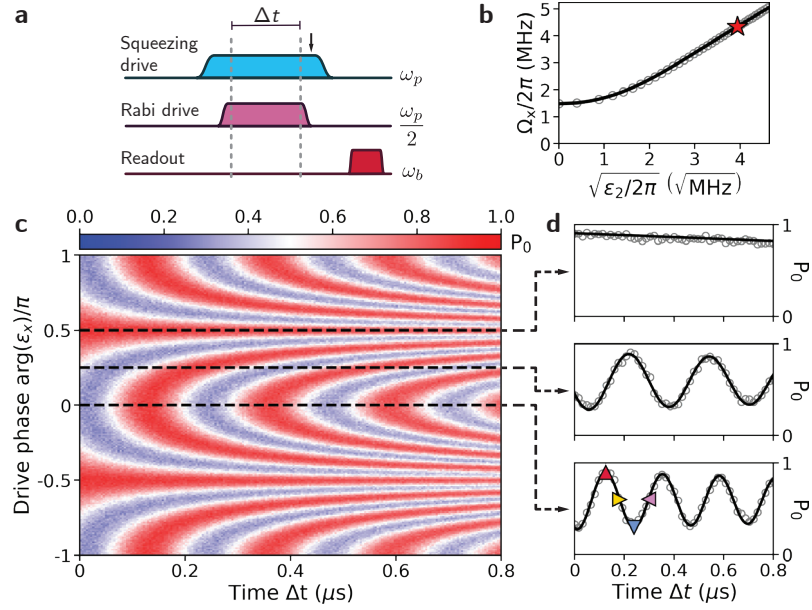
Figure 5.2 | (a) Pulse sequence to perform the following functions: (1) initialize the Kerr-cat qubit ($|0\rangle \to |\mathcal{C}_\alpha^+\rangle$), (2) drive Rabi oscillations for a varying time Δt, and (3) map onto the Fock qubit and perform dispersive readout. ω_p, $\omega_p/2$, and ω_b are the frequencies of the respective drives. Black arrow indicates the endpoint of numerical simulations for (b) and (d). (b) Dependence of the Rabi frequency Ω_x on $\sqrt{\epsilon_2}$ when $\arg(\epsilon_x) = 0$ as calibrated in (c). Open gray circles are experimental data; black solid line is a one-parameter fit used to calibrate ϵ_2. The red star marker indicates the condition $\epsilon_2/2\pi == 15.5$ MHz used for (c) and (d). (c) Dependence of the experimentally measured Rabi oscillations on time Δt and on the phase of the Rabi drive $\arg(\epsilon_x)$ with respect to $\arg(\epsilon_2)/2$, set to 0 for convenience. The color gives the ground state population of the Fock qubit (P_0) at the end of the experiment. (d) Cuts of (c) for three Rabi-drive phases indicated by dashed lines. Open gray circles are experimental data and black lines are simulation. Symbols indicate the times at which the simulated density matrix approximates the cardinal states $|+Z\rangle$, $|+Y\rangle$, $|-Z\rangle$, and $|-Y\rangle$ of the Kerr-cat qubit (increasing time order).

using Eq. 5.2. Note this is a factor of $|\alpha|$ enhancement of the Rabi rate over the naïve limit provided by interpreting ω_{gap} as a sort of anharmonicity of the Kerr-cat qubit [Puri, Boutin, and Blais 2017]. In practice this constraint may be further relaxed considerably with pulse engineering techniques [Chow et al. 2010; Chen et al. 2016].

Note also that the Rabi rate Eq. 5.2 differs from the Rabi rate of a Fock qubit in two ways. First, it depends on the amplitude of the squeezing drive through $\alpha = \sqrt{\epsilon_2/K}$. Second, it varies with the phase of the applied Rabi drive phase $\arg(\epsilon_x)$ relative to $\arg(\alpha) = \arg(\epsilon_2/K)/2$. These two features of the Rabi oscillations are important signatures of stabilizing a Kerr-cat qubit.

We first focus on the effect of the squeezing drive on the Rabi frequency. As depicted by the pulse sequence in Fig. 5.2a, we initialize in $|+Z\rangle = \left|\mathcal{C}_\alpha^+\right\rangle$ and apply a Rabi drive constant $|\epsilon_x|$ and correctly calibrated phase $\arg(\epsilon_x) = \arg(\alpha)$ for a variable time Δt and a variable amplitude $|\epsilon_2|$, extracted from the oscillation in the measured Fock-qubit $|n = 0\rangle$ state population fraction at the end of the experiment. For $\epsilon_2 = 0$, we are simply driving Fock qubit Rabi oscillations giving a direct calibration of $|\epsilon_x|/2\pi = 740\,\text{kHz}$. For large values of $|\epsilon_2|$, the Rabi frequency becomes a linear function of $\sqrt{\epsilon_2}$, confirming the theoretical prediction of Eq. 5.2. The solid black line shows a one-parameter fit to a numerical master equation simulation, which includes single-photon loss at rate $\kappa_1 = 1/T_1$ as the only dissipation [Grimm et al. 2020].

We now turn to another unique feature of these Rabi oscillations by setting $|\epsilon_2|/2\pi = 15.5\,\text{MHz}$ and varying both Δt and $\arg(\epsilon_x)$. As expected, the measured oscillations shown in Fig. 5.2c are π-periodic[1] in $\arg(\epsilon_x)$. Three cuts through this data (dashed lines) are shown in Fig. 5.2d. The top panel corresponds to a phase difference of $\pi/2$ between the coherent state amplitude and the Rabi drive, meaning that oscillations are suppressed. The slow decay in probability follows from the expected influence of single-photon loss on the cat-states, which we will examine in more detail with coherence measurements in Sec. 5.5. The middle and bottom panels use the same scaling factor and are thus parameter-free predictions in good agreement with the measured data. Having benchmarked our simulation in this way, we may use it to compute the full density matrix. We find good agreement with the four cardinal cat states on the Kerr-cat Bloch sphere at the four marker-indicated time points, apart from a small distortion due to the finite ramp time of the initial mapping.

5.3 Single qubit gate fidelities

Having benchmarked our system and shown that we indeed control a Kerr-cat qubit, we pursue a fast set of high-fidelity single qubit gates. The number of gates per coherence time is an important qubit performance metric and, similar to any physically implemented

---

[1]Eq. 5.2 might imply they should be 2π-periodic, but the experimental protocol involves population measurements of $|\pm Z\rangle$, making the measured data agnostic to the sign of the Rabi rate Ω_x.

qubit, the effective anharmonicity sets speed limit in absence of other technical considerations. For stabilized cat qubits, this is given by the generalized complex energy gap $\tilde{\omega}_{\mathrm{gap}} = \omega_{\mathrm{gap}} - i\kappa_{\mathrm{gap}}/2$ (Eqs. 4.36 and 4.62), where $\omega_{\mathrm{gap}} \approx -4K|\alpha|^2$ is the Hamiltonian gap that prevents leakage and $\kappa_{\mathrm{gap}} \approx 4\kappa_2|\alpha|^2 + \kappa_1$ is the dissipative gap that autonomously corrects for leakage.

With these limits in mind, we characterize the mapping operation and a complete set of single-qubit gates on the Kerr-cat qubit by performing process tomography. In the remaining experiments of this chapter corresponding to this work [Grimm et al. 2020], the average photon number of the cat states is set to $\bar{n} = 2.6$ and frequency shifts induced by the squeezing drive are taken into account by setting $\omega_p/2$ to the Stark-shifted resonator frequency. While we have an analytical formula for this Stark-shift Eq. 3.18, in practice we choose the squeezing drive frequency that minimizes spurious Z rotations induced by a Hamiltonian term of the form $-\Delta a^\dagger a$. As may be seen from Table 4.1, within the cat qubit Bloch sphere this spurious Rabi rate

$$\Omega_z = 4\Delta|\alpha|^2 e^{-2|\alpha|^2} \tag{5.4}$$

is exponentially small with increasing average photon number. Despite this, $\bar{n} = 2.6$ in this experiment was not large enough to ignore this effect, in contrast to the later experiments we will consider in Chapter 6.

The pulse sequence for tomography of the adiabatic mapping between the Fock qubit and the Kerr-cat qubit is shown in Fig. 5.3a. The Fock qubit is initialized on each of the six cardinal points of the Bloch sphere: $|\pm X\rangle$, $|\pm Y\rangle$, and $|\pm Z\rangle$ respectively. The respective operation is then performed, in this case just the mapping from Fock qubit to Kerr-cat qubit and back, and the expectation values $\langle X \rangle$, $\langle Y \rangle$, and $\langle Z \rangle$ are measured by a combination of Fock qubit pulses and dispersive readout (gray box). The expectation values are normalized by the bare Fock qubit Rabi contrast to focus on the gates in the Kerr-cat qubit as opposed to those on the Fock qubit. We plot the measured state vectors on a Bloch sphere in Fig. 5.3b. An estimate of the fidelity $\mathcal{F}_{\mathrm{map}} \approx 0.855 \pm 0.002$ ($\pm$ one standard deviation) is obtained by the Pauli transfer matrix approach [Chow et al. 2012]. This number reflects both the fidelity of the tomography Fock qubit pulses, which are not short compared to $T_2 = 3.4\,\mu\mathrm{s}$ due to the speed limit set by the anharmonicity $2K/2\pi = 13.4\,\mathrm{MHz}$, as well as the mapping itself. As such, apart from normalization by the Fock qubit Rabi contrast, the presented fidelities include state-preparation-and-measurement (SPAM) errors. We expect these errors to be dominated by decoherence during the comparatively slow adiabatic ramps. This could be remedied in future experiments by using optimal faster-than-adiabatic pulse shapes, which can reduce the duration of the mapping by a factor of more than 40 with respect to its current value of $320\,\mathrm{ns}$ with the tanh profile used here [Puri, Boutin, and Blais 2017].
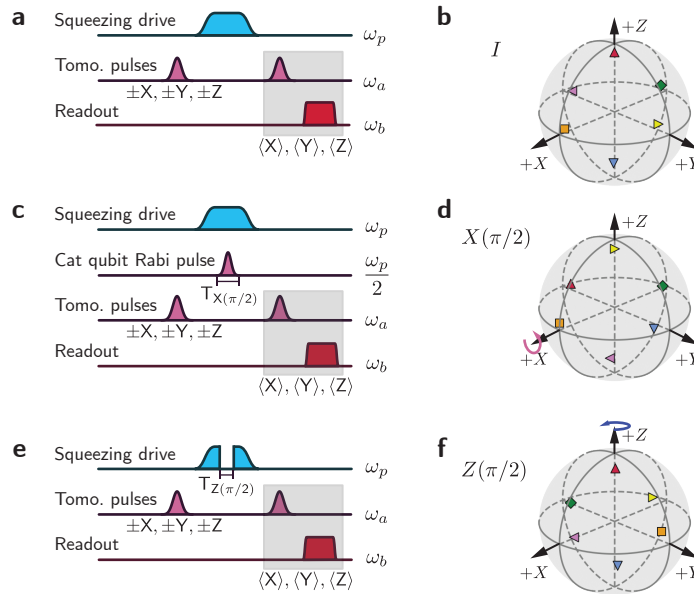
Figure 5.3 | (a), (c), (e), Pulse sequences for process tomography of mapping between Fock qubit and Kerr-cat qubit, which is ideally the identity operation I (a), mapping and $X(\pi/2)$ gate (c), as well as mapping and the $Z(\pi/2)$ gate (e). In each sequence, the Fock qubit is initialized on the $|\pm X\rangle$, $|\pm Y\rangle$, and $|\pm Z\rangle$ cardinal points of the Bloch sphere, the respective operation is performed, and the expectation values $\langle X \rangle$, $\langle Y \rangle$ and $\langle Z \rangle$ are measured by a combination of Fock qubit pulses and dispersive readout (gray box). In (c), $T_{X(\pi/2)} = 24$ ns is the total duration of the Gaussian Rabi pulse applied to the Kerr-cat qubit. In (e), $T_{Z(\pi/2)} = 38$ ns is the duration for which the squeezing drive is abruptly switched off to perform the gate. (b), (d), (f), Process tomography for the operations respectively. The expectation-value vector after the operation for initialization in each cardinal point is given by each marker, where color and shape denote initial state. The fidelities are 0.855 ± 0.002, 0.857 ± 0.001, and 0.811 ± 0.001, respectively.

5.3.1 Continuous gate between cats

We now turn to the pulse sequence shown in Fig. 5.3c, which additionally performs and $X(\pi/2)$ gate on the Kerr-cat qubit[2]. The pulse shape is chosen to be approximately Gaussian with a standard deviation of $6\,$ns truncated to a total pulse duration of $T_{X(\pi/2)} = 24\,$ns. The energy gap that sets the speed limit via Eq. 5.3 for these pulses was measured with spectroscopy experiments to be $\omega_{\mathrm{gap}}/2\pi \approx 50\,$MHz for the presented sample when biased at $\bar{n} = 2.6$ in agreement with numerical diagonalization of the effective Hamiltonian Eq. 4.37. The pulse amplitude is scaled to realize the desired $\pi/2$ rotation angle, but we emphasize that the amplitude may be chosen to implement an arbitrary angle of rotation $X(\theta)$ in direct analogy to microwave-activated gates on Fock qubits[3]. Different from the Fock qubit however, only the $X(\theta)$ gate may be applied to the Kerr cat qubit via single photon drive, not $Y(\theta)$ nor $Z(\theta)$. This is a direct consequence of the protection of our Kerr-cat qubit. Neither we nor the environment may apply gates $\propto \boldsymbol{Y}$ or $\propto \boldsymbol{Z}$ while the stabilization is active, as was evident in the $\arg(\epsilon_x)$ phase dependence of the Rabi oscillations in Fig. 5.2c.

The process tomography data for the $X(\pi/2)$ gate (Fig. 5.3d) shows the desired rotation around the X-axis with a fidelity $\mathcal{F}_{X(\pi/2)} = 0.857 \pm 0.001$. Comparing this value to $\mathcal{F}_{\mathrm{map}}$ indicates that $\mathcal{F}_{X(\pi/2)}$ is mostly limited by SPAM errors. In fact, complementary measurements based on modified randomized benchmarking estimate the infidelity due to over-rotation and decoherence during the gate operation to be about 0.01, which is approximately the decoherence limit given the gate time [Grimm et al. 2020].

5.3.2 Discrete gate by free Kerr evolution

As the previous operation is compatible with an arbitrary angle of rotation $X(\theta)$, only an additional $\pi/2$ rotation around the Z axis is needed to reach any point on the Kerr-cat Bloch sphere. Nominally, such a gate is incompatible with the stabilization as it could be used to go between $|+X\rangle \approx |+\alpha\rangle$ and $|+Y\rangle$. Moreover, this gate by construction explicitly unbiases the qubit noise channel: it maps coherent states to cat states. As such, applications that hope to leverage this noise bias may only use the $Z(\pi/2)$ gate as part of the preparation or measurement portion of a desired algorithm [Puri et al. 2019; Guillaud and Mirrahimi 2019; Puri et al. 2020].

To implement such a $Z(\pi/2)$ gate, consider the free evolution of a Kerr Hamiltonian

---

[2]We use the notational convention that $X(\theta)$ corresponds to a unitary rotation by angle θ around the X axis, such that $X(\pi)$ is a "π-pulse" give by the unitary $\boldsymbol{X}$.

[3]In transmon implementations of Fock qubits, the equivalent speed limit is given by the anharmonicity $2K$. The pulse amplitude and phase tune the rotation angle θ and the axis of rotation axis respectively, as can be seen by the drive Hamiltonian projected onto the Fock qubit $\mathrm{Re}\,\{\epsilon_x\}\,\boldsymbol{X} - i\mathrm{Im}\,\{\epsilon_x\}\,\boldsymbol{Y}$ (see Table 4.1).

($\epsilon_2 = 0$) starting from a coherent state

$$e^{+iKt\boldsymbol{a}^{\dagger 2}\boldsymbol{a}^2} \left|+\alpha\right\rangle = e^{-|\alpha|^2/2} \sum_{n=0}^{\infty} \frac{\alpha^n}{\sqrt{n!}} e^{+iKt\boldsymbol{a}^{\dagger 2}\boldsymbol{a}^2} \left|n\right\rangle$$

$$= e^{-|\alpha|^2/2} \sum_{n=0}^{\infty} \frac{\alpha^n}{\sqrt{n!}} e^{+iKtn(n-1)} \left|n\right\rangle$$

$$\propto \begin{cases} \left|+\alpha\right\rangle & \text{if } t = \pi/K; \\ \left|+i\alpha\right\rangle - i\left|-i\alpha\right\rangle & \text{if } t = \pi/2K. \end{cases} \tag{5.5}$$

which refocuses[4] back to $\left|+\alpha\right\rangle$ every Kerr revival time π/K [Yurke and Stoler 1988; Kirchmair et al. 2013]. At half of the revival time $\pi/2K \approx 37.3$ ns, the coherent state refocuses back to a parityless cat state, which is our $\left|+Y\right\rangle$ state but with an overall $\pi/2$ phase shift in phase space. Thus free Kerr evolution implements the desired gate[5].

With the squeezing drive on $\epsilon_2 \neq 0$, the stabilization fixes the Kerr-cat Bloch sphere states in place in phase space. Quickly and diabatically turning the squeezing drive off ($\epsilon_2 = 0$), waiting $T_{Z(\pi/2)} = 38$ ns $\approx \pi/2K$ to perform a controlled amount of free Kerr evolution, and quickly ramping the squeezing ϵ_2 back on with a π phase shift therefore implements the desired gate. Recall a π phase shift on ϵ_2 via the drive at frequency ω_p corresponds to a $\pi/2$ shift in the frame of the Kerr-cat qubit at frequency $\omega_p/2$. Thus, the π phase shift of ϵ_2 effectively redefines the Bloch sphere from $\alpha \to i\alpha$: specifically, $\left|\pm Z\right\rangle = \left|\mathcal{C}_\alpha^\pm\right\rangle$ before the gate to $\left|\pm Z\right\rangle = \left|\mathcal{C}_{i\alpha}^\pm\right\rangle$ after the gate[6]. Note the symmetry provided by the period-doubling implies that we made a choice to associate a π phase shift of ϵ_2 with $+\pi/2$ phase shift of the code states. The opposite convention is equally valid, implying $\alpha \to -i\alpha$ and consequently from $\left|\pm Z\right\rangle = \left|\mathcal{C}_\alpha^\pm\right\rangle$ before, to $\left|\mp Z\right\rangle = \left|\mathcal{C}_{-i\alpha}^\mp\right\rangle$ after, which, together with the identity $\left|\mathcal{C}_{-i\alpha}^\mp\right\rangle = \left|\mathcal{C}_{i\alpha}^\pm\right\rangle$, makes it clear that physically the resultant state is no different, just the Bloch sphere convention and hence the interpretation of the resultant gate as $Z(\pm\pi/2)$ respectively.

Sticking with the convention to implement $Z(+\pi/2)$, we now measure the performance of this gate with full process tomography. The data are shown in Fig. 5.3f with an extracted fidelity of $\mathcal{F}_{Z(\pi/2)} = 0.811 \pm 0.001$. We attribute the reduction of this fidelity with respect to $\mathcal{F}_{\text{map}}$ to the difference between the gate time $T_{Z(\pi/2)}$ and $\pi/2K$, and to the finite rise time of the step function in ϵ_2 of about 4 ns; both of which are not limitations of our device but of our room-temperature electronics.

We have now demonstrated a complete set of single qubit gates on the Kerr cat qubit, consisting of an $X(\theta)$ gate in 24 ns and a $Z(\pi/2)$ gate in 38 ns. In two-legged Schrödinger

---

[4]Note $n(n-1)$ is an even number for all integers n.

[5]Our nonlinear oscillator in principle has both g_3 and g_4 terms (Eq. 2.40), but for the dynamics near ω_a these may be approximated by free Kerr evolution (c.f. Eq. 2.49).

[6]In practice, the chosen phase of ϵ_2 must also account for pump detuning and so the new frame change is given by $\pi/2 + (\omega_p/2 - \omega_a)T_{Z(\pi/2)}$.

cat qubits autonomously stabilized with two-photon dissipation rate κ_2, the equivalent $X(\theta)$ gate has previously been achieved [Touzard et al. 2018]. In such experiments, $\kappa_{\text{gap}} \approx 4\kappa_2|\alpha|^2 + \kappa_1$ (see Eq. 4.62) limits the achievable gate speeds based on calculations similar to those generating Eq. 5.3 [Mirrahimi et al. 2014]. Since two-photon dissipation has thus far been engineered via auxiliary nonlinear modes, experimental realizations have thus far been limited to $\kappa_2/2\pi = 0.18\,\text{MHz}$ [Touzard et al. 2018], which, assuming similar $|\alpha|^2$, should be compared to $|2K|/2\pi = 13.4\,\text{MHz}$ in our work [Grimm et al. 2020]. This comparison makes evident the advantage of storing the cat-states in the most nonlinear mode, where the Kerr nonlinearity assists in the stabilization and allows faster gate times in state-of-the-art implementation. The gate speeds in both stabilization methods, however, benefit linearly from larger average photon number $\bar{n} = |\alpha|^2$. The important consideration then for the comparison of gate time to coherence times is the achievable $\bar{n}$-dependence of coherence times, a discussion we postpone for Sec. 5.5 and later Chapter 6.

5.4 Cat-quadrature readout

Before measuring the coherence times of our Kerr-cat qubit, we wish to further reduce the experimental dependence on the quality of the Fock qubit. So far, we have characterized the basic properties and gate operations of the Kerr-cat qubit by mapping back onto the Fock qubit and using the well-understood dispersive readout [Blais et al. 2004] to extract information. This readout, however, explicitly turns off the stabilization and any error-protection we have, which is undesirable. We now demonstrate an entirely new way to perform a quantum non-demolition (QND) measurement of the X component of the stabilized Kerr-cat qubit, which we call *cat-quadrature readout* (CQR) [Puri et al. 2019].

As an overview, we apply an additional strong microwave drive at $\omega_{\text{cqr}} = \omega_b - \omega_p/2$, which generates a bilinear frequency-converting interaction between the nonlinear resonator hosting the Kerr-cat qubit, and the readout cavity at frequency ω_b. The stabilization provided by the squeezing drive projects this bilinear interaction within the Kerr-cat qubit subspace to a conditional displacement on the readout cavity whose direction depends on the Kerr-cat qubit state $|\pm X\rangle \approx |\pm\alpha\rangle$. This displaced field then leaks out of the readout cavity at ω_b and the output field is collected and demodulated by a precision microwave measurement setup including a quantum-limited amplifier to infer the qubit state $|\pm X\rangle \approx |\pm\alpha\rangle$.

5.4.1 CQR model as conditional displacement

Mathematically now, and in more detail, we derive the above qualitative description of CQR. Consider the addition of a strong microwave drive tone at frequency $\omega_{\text{cqr}} = \omega_b - \omega_p/2$ and assume it couples to the most nonlinear mode a with an amplitude α_{cqr}. The nonlinearity necessary to generate the frequency conversion process originates from the

SNAIL mixing element and comes from the Hamiltonian term

$$g_3 \left(\boldsymbol{a} + \frac{g_{ba}}{\Delta_{ba}} \boldsymbol{b} + \text{H.c.} \right)^3 \rightarrow g_3 \left(\boldsymbol{a} e^{-i\omega_p t/2} + \alpha_{\text{cqr}} e^{-i\omega_{\text{cqr}} t} + \frac{g_{ba}}{\Delta_{ba}} \boldsymbol{b} e^{-i\omega_b t} + \text{H.c.} \right)^3$$

$$= 6g_3 \frac{g_{ba}}{\Delta_{ba}} \left(\alpha_{\text{cqr}} \boldsymbol{a} \boldsymbol{b}^\dagger + \alpha_{\text{cqr}}^* \boldsymbol{a}^\dagger \boldsymbol{b} \right) + \mathcal{H}_{\text{rotating}}(t)/\hbar$$

$$\approx 6g_3 \frac{g_{ba}}{\Delta_{ba}} \left(\alpha_{\text{cqr}} \boldsymbol{a} \boldsymbol{b}^\dagger + \alpha_{\text{cqr}}^* \boldsymbol{a}^\dagger \boldsymbol{b} \right) \tag{5.6}$$

where g_{ba} is the bare capacitive coupling rate, $\Delta_{ba} = \omega_b - \omega_a$ so that the hybridization may be simply written in the dispersive approximation[7]. In the first line, we have transformed to the displaced and co-rotating frame of Kerr-cat mode $\boldsymbol{a}$ at $\omega_p/2$ and readout cavity $\boldsymbol{b}$ at ω_b and invoked the RWA explicitly in the final line but also throughout[8].

From this, we see that the addition of this strong drive at ω_{cqr} implements an effective interaction Hamiltonian of the form

$$\mathcal{H}_{\text{cqr}}/\hbar = g_{\text{cqr}} \boldsymbol{a} \boldsymbol{b}^\dagger + g_{\text{cqr}}^* \boldsymbol{a}^\dagger \boldsymbol{b} \tag{5.7}$$

where $g_{\text{cqr}} = 6g_3\alpha_{\text{cqr}}(g_{ba}/\Delta_{ba})$ within both the dispersive and RWA approximations. This frequency-converting beamsplitter interaction has been generated by three-wave mixing in other contexts: through flux-pumped RF-SQUIDs [Allman et al. 2014], flux-pumped DC-SQUIDS [Lecocq et al. 2017], and JRMs [Abdo et al. 2013b; Abdo, Kamal, and Devoret 2013; Flurin et al. 2015; Sliwa et al. 2015]. Four-wave-mixing implementations have been used to controllably release quantum states of light [Pfaff et al. 2017], especially for remote entanglement protocols [Axline et al. 2018; Kurpiers et al. 2018; Campagne-Ibarcq et al. 2018; Burkhart et al. 2021], as well as for gates between harmonic oscillators used as quantum memories [Gao et al. 2018; Gao et al. 2019] and quantum simulators [Wang et al. 2020]. When implemented without the squeezing drive $\epsilon_2 = 0$, this interaction implements a *fluorescence* readout of the Fock qubit [Campagne-Ibarcq et al. 2016], which we may use in lieu of dispersive readout as in Chapter 6 or simply to calibrate the interaction strength in the current discussion to be $|g_{\text{cqr}}|/2\pi = 1.7\,\text{MHz}$ for the chosen drive power.

To see how this frequency converting process acts within the Kerr-cat qubit subspace,

---

[7]The dispersive approximation is not necessary. The relevant quantity is the undriven cross-cubic nonlinearity $\propto c_3 E_J \varphi_{a,\text{zpf}}^2 \varphi_{b,\text{zpf}}$ where the zero-point fluctuations are those for the eigenmodes as seen by the SNAIL nonlinearity (c. f. Sec. 2.5). For simplicity this term is approximated $g_3 g_{ba}/\Delta_{ba}$ here.

[8]As before, the RWA is strictly not valid, but a leading order non-RWA treatment simply renormalizes g_{cqr}.

with with squeezing drive on $|\epsilon_2| \neq 0$ we may project using Table 4.1

$$\boldsymbol{P_C}\mathcal{H}_{\mathrm{cqr}}\boldsymbol{P_C} = \left(g_{\mathrm{cqr}}\alpha\boldsymbol{b}^\dagger + g_{\mathrm{cqr}}^*\alpha^*\boldsymbol{b}\right)\left(\frac{r+r^{-1}}{2}\right)\boldsymbol{X}$$

$$- i\left(g_{\mathrm{cqr}}\alpha\boldsymbol{b}^\dagger - g_{\mathrm{cqr}}^*\alpha^*\boldsymbol{b}\right)\left(\frac{r-r^{-1}}{2}\right)\boldsymbol{Y} \tag{5.8}$$

$$\approx \left(g_{\mathrm{cqr}}\alpha\boldsymbol{b}^\dagger + g_{\mathrm{cqr}}^*\alpha^*\boldsymbol{b}\right)\boldsymbol{X}$$

$$+ i\left(g_{\mathrm{cqr}}\alpha\boldsymbol{b}^\dagger - g_{\mathrm{cqr}}^*\alpha^*\boldsymbol{b}\right)e^{-2|\alpha|^2}\boldsymbol{Y} \tag{5.9}$$

where r is the ratio of cat state normalization coefficients (Eq. 4.13), and for appreciable photon number $|\alpha|^2$ the readout cavity $\boldsymbol{b}$ is predominantly coupled to $\boldsymbol{X}$ with an exponentially small coupling to $\boldsymbol{Y}$. The Hamiltonian Eq. 5.9 implements a displacement of cavity b conditioned predominantly on $\boldsymbol{X}$ or on which coherent state $|\pm\alpha\rangle$.

This conditional displacement Hamiltonian is interesting in its own right in the context of controlling harmonic oscillators with ancillary qubits. Engineering such a Hamiltonian was central to the recent stabilization of GKP states [Campagne-Ibarcq et al. 2020], although it that case through an echoed stroboscopic interaction with transmon qubits [Eddins et al. 2018; Touzard et al. 2019]. With a Kerr-cat qubit, such an interaction comes with the added benefit that the $\boldsymbol{b}$ cavity only couples to the qubit through the $\boldsymbol{X}$ operator, which commutes with the predominant qubit error—bit-flips in this encoding, which are applications of the jump operator $\boldsymbol{X}$. This property is a crucial ingredient for fault-tolerant control and error syndrome extraction in GKP codes, other bosonic codes, and QEC schemes generally [Puri et al. 2019].

Returning to the context of CQR considering the oscillator $\boldsymbol{b}$ as a readout cavity, the conditional displacement Hamiltonian Eq. 5.9 for readout in superconducting circuits dates back to the *quantronium* [Vion et al. 2002] and is also associated with radiation pressure coupling in optomechanics [Aspelmeyer, Kippenberg, and Marquardt 2014]. For efficient readout as with CQR, the interaction must be parametrically modulated [Didier, Bourassa, and Blais 2015], as was implemented recently in superconducting circuits [Touzard et al. 2019; Ikonen et al. 2019; Dassonneville et al. 2020] and shown to have advantages over dispersive readout for fast readout pulses. Furthermore, this readout mechanism is compatible with using input-squeezed light for increased sensitivity in a way that dispersive readout is not [Didier, Bourassa, and Blais 2015; Eddins et al. 2018].

To see how this conditional displacement interaction indeed performs readout of $|\pm X\rangle \approx |\pm\alpha\rangle$, consider the dynamics of the readout cavity $\boldsymbol{b}$ described by the QLE in the same ro-

tating frame and within the RWA

$$\dot{\boldsymbol{b}} = \frac{i}{\hbar}\left[\mathcal{H}_{\text{cqr}}, \boldsymbol{b}\right] - \frac{\kappa_b}{2}\boldsymbol{b} + \sqrt{\kappa_b}\boldsymbol{b}_{\text{in}}$$

$$\approx -ig_{\text{cqr}}\alpha\left(\boldsymbol{X} + ie^{-2|\alpha|^2}\boldsymbol{Y}\right) - \frac{\kappa_b}{2}\boldsymbol{b} + \sqrt{\kappa_b}\boldsymbol{b}_{\text{in}} \tag{5.10}$$

where $\kappa_b/2\pi = 1.9\,\text{MHz}$ is the total single-photon-loss rate of the readout cavity, and $\boldsymbol{b}_{\text{in}}$ is the standard delta-time-correlated input field with the property $\langle\boldsymbol{b}_{\text{in}}\rangle = 0$ for this protocol. Ignoring the exponentially small term, we then solve for the coherent-state amplitude $\beta = \langle\boldsymbol{b}\rangle$ in response to turning on the drive at frequency ω_{cqr} at $t = 0$

$$\beta(t, X) = \frac{-i2g_{\text{cqr}}\alpha}{\kappa_b}X\left(1 - e^{-\kappa t/2}\right) \tag{5.11}$$

where we have assumed the qubit started at $t = 0$ in an eigenstate $|{\pm}X\rangle$ denoted via the eigenvalue $X = \pm 1$. The steady state value is therefore $|\beta\rangle$ with $\beta = \mp i2\alpha g_{\text{cqr}}/\kappa_b$.

As derived [Didier, Bourassa, and Blais 2015] and verified [Touzard et al. 2018], the voltage signal-to-noise ratio, which is square-root of the usual power-defined SNR,

$$\sqrt{\text{SNR}(\tau)} = \sqrt{32\eta}\frac{|g_{\text{cqr}}\alpha|}{\kappa_b}\left[\kappa_b\tau - 4\left(1 - e^{-\kappa_b\tau/2}\right) + \left(1 - e^{-\kappa_b\tau}\right)\right]^{1/2} \tag{5.12}$$

where τ is measurement pulse time and η is the quantum efficiency of the entire measurement, itself defined as the ratio of the measurement rate and the total dephasing rate. This expression is for the optimal demodulation envelope [Gambetta et al. 2007; Ryan et al. 2015; Bultink et al. 2018], as derived in [Touzard et al. 2019] for conditional displacement readout. At long times, the scaling of the $\sqrt{\text{SNR}(\kappa_b\tau \gg 1)} \propto (\kappa_b\tau)^{1/2}$ matches dispersive readout; however, at short times $\sqrt{\text{SNR}(\kappa_b\tau \ll 1)} \propto (\kappa_b\tau)^{3/2}$ outpaces dispersive readout which itself remains $\propto (\kappa_b\tau)^{1/2}$. Furthermore, the entire SNR $\propto |\alpha|^2$ implying that qubit readout should improve for larger photon-number cats without any other subsequent changes to readout power or efficiency. Such SNR scalings lend an advantage to CQR in terms of optimizing qubit readout for faster and/or higher fidelity measurements.

We may now use the steady state β (Eq. 5.11) to estimate the validity of our projection into the Kerr-cat qubit manifold in Eq. 5.9. In a mean-field treatment, we take $\boldsymbol{b} \to \beta$ in Eq. 5.7 resulting in Hamiltonian

$$\mathcal{H}_{\text{cqr}}/\hbar\Big|_{\boldsymbol{b}\to\beta} \approx g_{\text{cqr}}^*\beta\boldsymbol{a}^\dagger + g_{\text{cqr}}\beta^*\boldsymbol{a}$$

$$= \mp i2\frac{|g_{\text{cqr}}|^2}{\kappa_b}(\alpha\boldsymbol{a}^\dagger - \alpha^*\boldsymbol{a}) \tag{5.13}$$

that implements a single-photon drive on the Kerr-cat qubit. According to Eq. 5.2, the induced Rabi rate from such a drive is identically zero because $\text{Re}\left\{\mp i\alpha\alpha^*\right\} = 0$, indicating

there are no spurious in-manifold rotations during the readout. In a weak measurement sense, this implies trajectories within the Kerr-cat qubit Bloch sphere will only be stochastically kicked toward $\pm X$ with no diffusion in the YZ plane; this is the same result[9] as observed with dispersive readout of transmon qubits under near-unity-efficiency homodyne detection [Murch et al. 2013].

Additionally, the readout process could cause leakage out of the Kerr-cat qubit Bloch sphere, which in turn would limit both readout fidelity and QNDness. This leakage however is suppressed so long as $|g_{\mathrm{cqr}}\beta| \ll \omega_{\mathrm{gap}}$ via that same mechanism for suppressed leakage in the $X(\theta)$ gate in Sec. 5.2. Rewriting this bound with an eye toward the SNR in Eq. 5.12

$$\mathrm{SNR} \propto |g_{\mathrm{cqr}}\alpha|^2 \ll |\omega_{\mathrm{gap}}\kappa_b\alpha|/2$$
$$\approx 2K\kappa_b|\alpha|^3, \tag{5.14}$$

we notice that the SNR may be efficiently increased by $|\alpha|^2$ and the limit imposed by leakage is simultaneously increased. Given this, the optimization to increase noise bias, gate speed, and readout SNR all converge toward making cats with larger average photon number. The remaining important factor is the scaling of coherence, which promises an exponential gain on one axis with a linear degradation of the other as we will investigate shortly.

5.4.2 CQR experimental verification

We now characterize the fidelity of this readout by first initializing the Kerr-cat qubit along its X axis and then applying a CQR pulse at $\omega_{\mathrm{cqr}} = \omega_b - \omega_p/2$ for a time $T_{\mathrm{cqr}} = 3.6\,\mu s$ as shown in Fig. 5.4a. Two histograms of the measured cavity field are shown in the top two panels of Fig. 5.4b after amplification with a near-quantum-limited measurement chain and subsequent demodulation with the optimal envelope. The phase of conditional displacement $\arg(g_{\mathrm{cqr}}) = +\pi/2$ is chosen make the signal appear in the in-phase quadrature I of the demodulation. With this choice, the top (middle) panel corresponds to a positively (negatively) displaced output field when the qubit was prepared in $|\pm X\rangle \approx |\pm\alpha\rangle$.

The separation is large enough to implement a single-shot readout by setting a threshold at $I/\sigma = 0$ (dashed line), where I/σ is a dimensionless quantity corresponding to the I-quadrature signal divided by the standard deviation σ of the histograms. This convention allows the experimental SNR to be visually read to be ≈ 4.3 from the figure with the definition

$$\mathrm{SNR} = \frac{|I_{+X} - I_{-X}|^2}{2\sigma^2} \tag{5.15}$$

where $I_{\pm X}$ corresponds to the center of the blob $\langle I \rangle$ for each preparation $|\pm X\rangle$.

---

[9] With Hadamard-rotated Bloch sphere convention so that stochastic kicks were toward $\pm Z$.
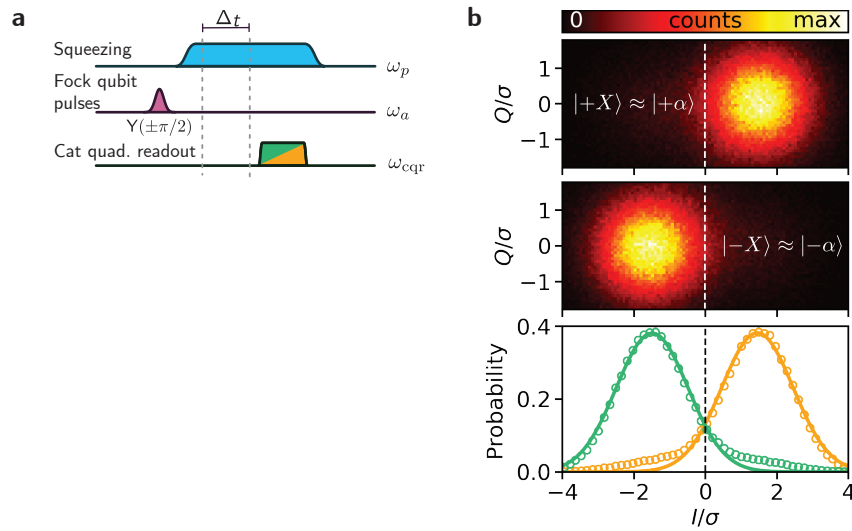
Figure 5.4 | (a) Pulse sequence for (b). After initialization in $|{\pm}X\rangle \approx |{\pm}\alpha\rangle$ ($Y(\pm\pi/2)$ on the Fock qubit and mapping) and minimal wait time $\Delta t = 24$ns, a pulse at frequency $\omega_{\mathrm{cqr}} = \omega_b - \omega_p/2$ is applied for $T_{\mathrm{cqr}} = 3.6\,\mu$s converting the quadrature amplitude of the Kerr-cat qubit to a drive on the readout cavity at ω_b. (b) Top and middle: histogram of the integrated and demodulated cavity output field when performing CQR after preparation in $|{\pm}X\rangle \approx |{\pm}\alpha\rangle$ respectively. Bottom: corresponding probability distribution along the I quadrature. Open orange (green) circles show measured data for each preparation and solid lines are Gaussian fits of width σ used to scale the quadrature axes, I and Q. Setting threshold at $I/\sigma = 0$ (dashed line) implements a direct single-shot readout of the Kerr-cat qubit along its X-axis.

We may further quantify the total readout fidelity with the conservative definition

$$\mathcal{F} = 1 - p(-X|+X) - p(+X|-X) \tag{5.16}$$

where $p(\pm X|\mp X)$ is the probability of assigning the readout state $\pm X$ differently from the initialized state $|\mp X\rangle$. These probabilities may be directly and experimentally determined by integrating the probability on the wrong side of the threshold line in Fig. 5.4. With this method, the readout fidelity for this experiment is $\mathcal{F} = 0.74$. This is a lower bound including errors in state preparation caused by thermal population in the Fock qubit $|n = 1\rangle$ state, which contributes an infidelity of about 8%. Similarly, imperfections during the initial Fock qubit pulse and mapping both reduce $\mathcal{F}$.

Finally, we characterize the quantum-non-demolition (QND) aspect of the CQR via an experiment that performs two successive measurements. The QNDness may be quantified by the metric

$$\mathcal{Q} = \frac{1}{2}\left(P(+X|+X) + P(-X|-X)\right) \tag{5.17}$$

where $P(\pm X|\pm X)$ is the probability of obtaining measurement outcome $\pm X$ in two successive measurements. The experimentally extracted QNDness for this system was $\mathcal{Q} = 0.85$, which we improve upon in the experiments to be discussed in Chapter 6.

5.5 Kerr-cat coherences

Given that we have both a complete set of single qubit gates and QND readout of a Kerr-cat qubit, we proceed to measure the coherences on the different cardinal points of the Bloch sphere. We begin with the phase-flip rate of the Kerr-cat qubit. Fig. 5.5a depicts the pulse sequence to measure the decay of the $\langle X \rangle$ component of the coherence. To prepare the Kerr-cat qubit in $|\pm X\rangle \approx |\pm\alpha\rangle$, as we did to characterize CQR we start in the Fock-qubit $|n = 0\rangle$ and perform the rotation $Y(\pm\pi/2)$ to prepare $|\pm X\rangle$ of the Fock qubit. After the adiabatic mapping sequence, we have prepared $|\pm X\rangle \approx |\pm\alpha\rangle$ of the Kerr-cat qubit. We then wait a variable amount of time Δt with the squeezing drive on and then perform CQR to measure the Kerr-cat qubit state along the X axis.

With this pulse sequence, we measure the decay of the $\langle X \rangle$ coherence in Fig. 5.5b (blue data points) for our Kerr-cat qubit with $\bar{n} = 2.6$ average photons. We fit the data to a single-exponential decay with characteristic times $\tau_{+X} = 105\,\mu s \pm 1\,\mu s$ and $\tau_{-X} = 106\,\mu s \pm 1\,\mu s$ for the respective initial states. Additional measurements with dispersive readout confirm this result [Grimm et al. 2020].

Similarly, the coherence times of both the $\langle Y \rangle$ and $\langle Z \rangle$ components are measured using CQR, but employing only operations on the Kerr-cat qubit after the initial mapping from $|n = 0\rangle \rightarrow |\mathcal{C}_\alpha^+\rangle$ (see Fig. 5.5c,e). Most notably, a single $Z(\pi/2)$ gate based on free Kerr
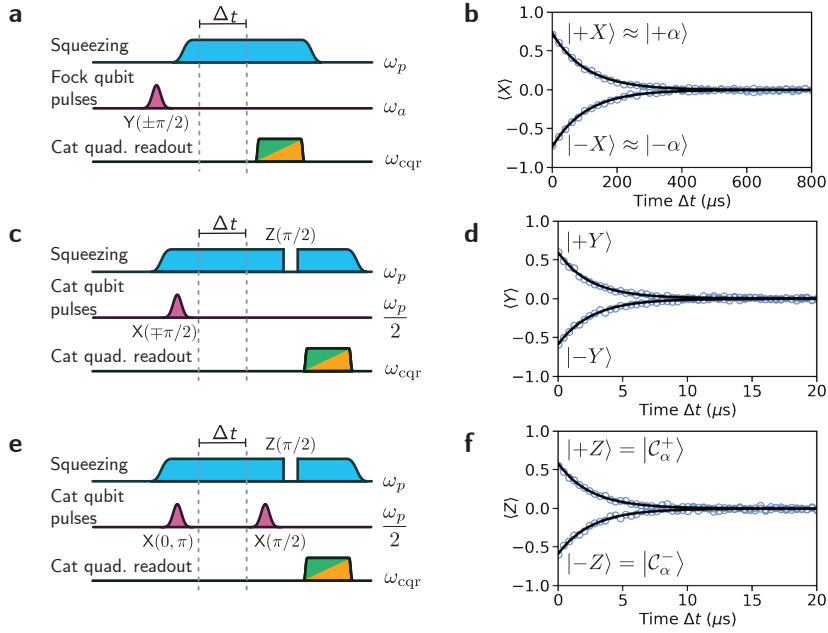
Figure 5.5 | (a) Pulse sequence for (b). After initialization in $|\pm X\rangle \approx |\pm\alpha\rangle$ ($Y(\pm\pi/2)$ on the Fock qubit and mapping) and variable wait time Δt, a pulse at frequency $\omega_{\text{cqr}} = \omega_b - \omega_p/2$ implements cat-quadrature readout (CQR). (b) Kerr-cat qubit $\langle \boldsymbol{X}\rangle$-component coherence: open blue circles are data and solid black lines are single-exponential fits with decay times $\tau_{+X} = 105\,\mu\text{s} \pm 1\mu\text{s}$ and $\tau_{+X} = 106\,\mu\text{s} \pm 1\mu\text{s}$. (c) Pulse sequence for (d). After initialization in $|\pm Y\rangle$ (mapping $|0\rangle \to |\mathcal{C}_\alpha^+\rangle$ and $X(\mp\pi/2)$ gate) and variable wait time Δt, a $Z(\pi/2)$ gate is preformed followed by CQR. (d) Kerr-cat qubit $\langle \boldsymbol{Y}\rangle$-component coherence with decay times $\tau_{+Y} = 2.51\,\mu\text{s} \pm 0.06\mu\text{s}$ and $\tau_{-Y} = 2.60\,\mu\text{s} \pm 0.05\mu\text{s}$. (e) Pulse sequence for (f). After initialization in $|\pm Z\rangle = |\mathcal{C}_\alpha^\pm\rangle$ (mapping $|0\rangle \to |\mathcal{C}_\alpha^+\rangle$ and either $X(0)$ or $X(\pi)$ gate) and variable wait time Δt, an $X(\pi/2)$ and a $Z(\pi/2)$ gate are preformed followed by CQR. (f) Kerr-cat qubit $\langle \boldsymbol{Z}\rangle$-component coherence with decay times $\tau_{+Z} = 2.60\,\mu\text{s} \pm 0.07\mu\text{s}$ and $\tau_{-Z} = 2.56\,\mu\text{s} \pm 0.07\mu\text{s}$.

evolution is necessary to map the desired coherence to the X axis for CQR. The resulting decay curves are displayed in Fig. 5.5d,f. Single-exponential fits of the data yield the decay times $\tau_{+Y} = 2.51\,\mu s \pm 0.06\,\mu s$, $\tau_{-Y} = 2.60\,\mu s \pm 0.05\,\mu s$, $\tau_{+Z} = 2.60\,\mu s \pm 0.07\,\mu s$, and $\tau_{-Z} = 2.56\,\mu s \pm 0.07\,\mu s$. These values are slightly smaller than the predicted bit-flip time due to single-photon loss $T_1/2\bar{n} = 2.98\,\mu s$ [Haroche and Raimond 2006]. Through numerical simulations of the stochastic master equation, we find that introducing a single-photon gain process through a jump operator $\sqrt{n_{\text{th}}\kappa_1}a^\dagger$ (where $\kappa_1 = 1/T_1$) may account for this discrepancy. With this additional noise term, the prediction for the bit-flip rate becomes $2\bar{n}(1 + 2n_{\text{th}})\kappa_1$. Using the thermal population $n_{\text{th}} = 0.04$ measured in the Fock qubit with $|\epsilon_2| = 0$ with a protocol involving pulses to higher excited states [Geerlings et al. 2013], we would expect a bit-flip time of $\approx 2.8\,\mu s$, which is still slightly larger than the experimentally measured values. Heating to a value of $n_{\text{th}} = 0.08$ (yielding $\approx 2.6\,\mu s$) could account for this difference. Having increased heating in the presence of strong microwave drives may result from the bounded nature of the cosine potential [Lescanne et al. 2019]. Thus, engineering Josephson junction circuits that can accommodate larger drive powers may be key to further increasing coherence.

Our results demonstrate a 30-fold increase in the phase-flip time of the protected Kerr-cat qubit with respect to the Fock qubit. As a biased-noise qubit, we achieve a noise bias of ≈ 40. This bias and 30-fold increase comes at the expense of a linear degradation in the shortest coherence time, here the bit-flip time. Crucially, we perform a full set of single-qubit gates on the Kerr-cat qubit on timescales that are $\approx 1\%$ of its bit-flip time, with quoted fidelities currently limited by SPAM errors. Moreover, we demonstrate a new form of QND readout of the Kerr-cat qubit without turning off the stabilization. The combination of error protection, fast gates and single-shot readout opens the door to using stabilized Schrödinger cat states as physical qubits in a future quantum computer. The simplicity of our implementation, which is moreover compatible with quasi-2D on-chip architectures, provides a straightforward path to coupling several Kerr-cat qubits and demonstrating operations between them. In particular, as we will discuss on more detail in the following Chapter 6, our qubit permits a noise-bias-preserving controlled-NOT gate [Puri et al. 2020], which would be impossible with standard two-level systems [Guillaud and Mirrahimi 2019]. Moreover, Kerr-cat qubits could be applied as auxiliary systems for fault-tolerant error detection on other logical qubits [Puri et al. 2019]. These applications will require further improvements in device performance such as the bit-flip time, currently limited by losses due to hybridization to the copper readout cavity.

The limitation of the phase-flip time also requires further investigation. Measurements performed at other flux points with less third-order nonlinearity indicate that coherence decreases when stronger drives have to be applied to the system to reach similar photons numbers $\bar{n} = |\alpha|^2$. Similarly, an increase in photon number beyond the $\bar{n} = 2.6$ operating point discussed in this chapter decreases coherence. This is probably related to heating

effects associated with the strong driving of Josephson junctions [Slichter et al. 2012; Sank et al. 2016; Lescanne et al. 2019] causing leakage to higher excited states outside of the Kerr-cat qubit Bloch sphere. Such leakage can be counteracted through controlled two-photon dissipation back towards the states of the Kerr-cat qubit [Puri et al. 2019], or similarly by a colored spectrum of single-photon dissipation that ideally corrects the leakage without further reducing the bit-flip time [Putterman et al. 2021].

Two-photon dissipation has previously been utilized to autonomously stabilize Schrödinger cat states [Leghtas et al. 2015; Touzard et al. 2018], but only recently has an exponential increase in the coherent state lifetime been achieved [Lescanne et al. 2020]. The crucial insight was that coherence was previously limited by heating events in auxiliary degrees of freedom with cross-Kerr to the mode hosting the Schrödinger cat qubit. These auxiliary modes were necessary to provide the four-wave mixing needed to generate two-photon dissipation, but heating events caused dephasing noise with weight larger than $\kappa_{\text{gap}} \approx \kappa_2 |\alpha|^2 + \kappa_1$, which were uncorrectable errors. By engineering a nonlinear element that supported the necessary four-wave mixing to generate $\kappa_2/2\pi = 40\,\text{kHz}$ but with suppressed cross-Kerr nonlinearity, the exponential increase in coherent state lifetime was achieved until saturating at $\approx 1\,\text{ms}$ likely due to residual cross-Kerr coupling to another auxiliary qubit used for measurement and tomography [Lescanne et al. 2020]. However, quantum operations with these dissipation-only stabilized cats remain difficult to achieve due to the relatively low value of κ_2 [Touzard et al. 2018]. In the following chapter, we will explore how to further extend the lifetime of Kerr-cat qubits by designing systems that can host larger cats; but the optimal solution may be to rely mostly on the squeezing and Kerr nonlinearity for high gate speeds, while correcting residual leakage with two-photon dissipation for longer coherent state lifetimes.

6

Future directions for Kerr-cat qubits

In this chapter, we look toward future applications of the Kerr-cat as a noise-biased qubit for quantum information processing. Namely, the Kerr-cat may implement an ancillary qubit for the *fault-tolerant* error syndrome detection of other logical qubits [Puri et al. 2019], as well as a logical qubit component in a larger code that promises to reduce the total of number of physical qubits required to reach a sufficiently low logical error rate [Guillaud and Mirrahimi 2019; Puri et al. 2020].

To see the need for fault-tolerant ancillary qubit interactions, many recent experiments on bosonic codes are indeed limited by the quality of the ancillary transmon qubit [Leghtas et al. 2015; Ofek et al. 2016; Touzard et al. 2018; Hu et al. 2019; Lescanne et al. 2020; Campagne-Ibarcq et al. 2020]. The nearly harmonic bosonic mode of interest must be entangled with an the ancillary transmon for both gate operations and QEC. Transmon errors that occur while entangled often produce errors on the bosonic mode that are *uncorrectable* within the original QEC protocol. A first step toward fault-tolerance involves noise-biasing the transmon by instead using the $|n = 0\rangle$ and $|n = 2\rangle$ as the computational states and arranging the interaction with the bosonic mode of interest to be *transparent* to transmon decay events $|n = 2\rangle \rightarrow |n = 1\rangle$ that must be subsequently detected before further decay $|n = 1\rangle \rightarrow |n = 0\rangle$ [Rosenblum et al. 2018; Reinhold et al. 2020]. An alternative strategy might be to utilize undriven protected qubits [Gyenis et al. 2021a], for instance the fluxonium [Manucharyan et al. 2009; Nguyen et al. 2019], the heavy fluxonium [Earnest et al. 2018; Zhang et al. 2021] or the 0-π qubit [Gyenis et al. 2021b] that have successfully increased at least a single coherence time beyond transmons. These qubits however are designed to operate at sweet spots in parameter space. To increase coherence, these sweet spots are chosen to protect against the lab-frame environmental spectra of charge and flux noise. As such, once drives are applied, the qubit will become sensitive to environmental noise at different frequencies [Yan et al. 2013; Yan et al. 2016], not necessarily suppressed by the previous parameter choices. This suggests the need for the additional complication of dynamical sweet spots [Didier et al. 2019; Huang et al. 2021] to maintain the same level of coherence *during* the gates, which is the most crucial time in regards to the fault-tolerance of ancillary qubits.

Conversely, the Kerr-cat qubit is continuously driven and so all subsequent operations will appear as perturbations on top of the autonomous stabilization in much the same way as cat-quadrature readout (CQR) appeared as a perturbation (see Sec. 5.4). We may therefore expect any protection resulting in noise-bias to persist during entanglement interactions. To improve Kerr-cat qubits for this application, further improvements in both the gate fidelities and the coherent state lifetime are necessary. In the next section, we begin to tackle both of these questions by optimizing for larger photon number cat states and

explore the results on CQR and coherent state lifetimes.

For the longer term goals of quantum computation, autonomously stabilized two-legged Schrödinger cat qubits have also been suggested as a means to reduce the overhead of QEC to reach a sufficiently low fidelity for useful algorithms [Guillaud and Mirrahimi 2019; Puri et al. 2020]. These proposals build off the realization that *noise-bias* may be exploited to achieve higher error thresholds in certain QEC codes [Aliferis and Preskill 2008], which were later extended to surface codes [Tuckett, Bartlett, and Flammia 2018; Bonilla Ataides et al. 2021]. Although these techniques increase error thresholds for general noise-biased qubits, they suffer from the no-go theorem that any Hamiltonian that implements a controlled-not (CNOT) operation between two standard two-level system qubits *must unbias* the noise channels of the respective qubits. Intuitively, this means the short-lived coherence axis of one qubit must reduce the lifetime of the long-lived axis of the other, since they must be coupled *during* the Hamiltonian evolution; there is not enough Hilbert space to avoid this coupling.

Crucially, this no-go theorem, which was suggested [Aliferis and Preskill 2008] and later proven [Guillaud and Mirrahimi 2019], has a work around through the use of Schrödinger cat qubits [Puri et al. 2020]. By utilizing the Hilbert space already available within a single oscillator, a noise-bias-preserving CNOT gate may be performed by exploiting the symmetry and topology of the two-legged-cat code in phase space. By continuously deforming the code space via the phase of the squeezing drive, the proposed implementation may be understood as a conditional exchange operation of the two coherent state $|\pm\alpha\rangle$ in phase space. We will explore this topological CNOT gate in detail and a potential realization with two Kerr-cat qubits in Sec. 6.2. If such a CNOT may indeed be implemented with sufficiently high fidelities, the overhead associated with quantum computation may be significantly reduced with Schrödinger cat qubits [Guillaud and Mirrahimi 2019; Puri et al. 2020], especially in surface codes [Darmawan et al. 2021] where magic-state preparation may also similarly benefit [Singh et al. 2021].

6.1 Less Kerr for larger cats

With these applications in mind, we focus on improving the performance of the Kerr-cat qubit. Although adding two-photon dissipation is a possibility [Puri et al. 2019], we would like to extend the exponential suppression of phase-flips that saturated at $\bar{n} = 2.6$ in the previous sample of Chapter 5 [Grimm et al. 2020]. In the purely two-photon dissipative case [Lescanne et al. 2020], the coherent state lifetime saturated to $\approx 1\,\mathrm{ms}$ for $\bar{n} \geq 5$. Here, we explore the photon-number dependence of the properties of the Kerr-cat qubit and show that such lifetimes are not limited to the purely dissipative case. The structure of the Kerr-cat Hamiltonian contains the salient properties for protection, namely the robustness to perturbations by the most common environmental noises.

In this section, we show coherent state lifetime improvements to $\approx 1\,\text{ms}$, a factor of 380 improvement over the transverse relaxation rate of the Fock qubit in this sample, $T_2 = 2.8\,\mu\text{s}$. The noise bias for this point reaches $\approx 10^3$, yet crucially with cat state lifetimes $\approx 1\,\mu\text{s}$ that falls linearly in $\bar{n}$ from the Fock qubit life time of $T_1 = 23.5\,\mu\text{s}$, which itself may be straightforwardly improved with state-of-the-art fabrication techniques. Moreover, these lifetimes are compatible with the same fast gates shown in Chapter 5, whose speed limit $\omega_{\text{gap}} \approx -4K|\alpha|^2$—while starting smaller than the previous sample—also scales linearly with $\bar{n}$. Finally, the same increase in $\bar{n}$ that increases coherence also improves the quality of cat-quadrature readout (CQR), bringing it toward—although not yet surpassing in speed—the best dispersive readout of transmon qubits [Johnson et al. 2012; Risté et al. 2012; Hatridge et al. 2013; Jeffrey et al. 2014; Walter et al. 2017].

The most salient design change leading to these results is the reduction of Kerr nonlinearity by an order of magnitude to the Fock qubit anharmonicity $2K/2\pi = 0.98\,\text{MHz}$ as measured by the Kerr-refocusing time [Yurke and Stoler 1988; Kirchmair et al. 2013]. We actuated this reduction by increasing the number of SNAILs to an array of $M = 2$, increasing the critical current of all junctions by the same factor (c. f. Fig. 2.3b), and reducing the SNAIL's junction inductance ratio α. Borrowing intuition from our results on improved power handling of SPAs in Chapter 3, we may separate the nonlinearity into two categories: the nonlinearity we need to generate the Kerr cat Hamiltonian, and the rest of the nonlinearity. Our design change reduces the three-wave mixing nonlinearity g_3 (Eq. 2.45) and the Kerr nonlinearity K (Eq. 2.53) that we require for stabilization; but it also reduces the rest of the nonlinearity suspected to cause heating in response to strong drives [Slichter et al. 2012; Sank et al. 2016; Lescanne et al. 2019]. Equivalently, we have increased the maximum number of allowed photons in the nonlinear resonator $n_{\text{crit}} \propto M^2$ (Eq. 2.48). Our previous experiments indicated that drive-induced heating becomes problematic at some fraction of n_{crit}. Given this assumption, we may derive an expected increase in Kerr-cat size using Eq. 3.19 at which drive induced heating becomes problematic

$$
\begin{aligned}
|\alpha|^2 &= |\epsilon_2/K| \\
&= |2g_3\alpha_p/K| \\
&\propto M|\alpha_p| \\
&\propto M^2
\end{aligned}
\tag{6.1}
$$

where in the third line we invoke $|g_3/K| \propto M$ (Eqs. 2.45–2.53), and in the last line that the allowed n_{crit} scales the limit on $|\alpha_p| \propto M$. Following this logic, we conclude that increasing the number of SNAILs to decrease the Kerr nonlinearity effectively increases the experimentally achievable cat size.

We may also ask what we give up under such a optimization to reduce Kerr nonlinearity for larger photon numbers. To list them succinctly in order of importance, the possible

drawbacks are

1. Slower, and thus lower fidelity, $Z(\pi/2)$ Kerr gate which takes $T_{Z(\pi/2)} = \pi/2K$ irrespective of $\bar{n}$.

2. Reduction of the energy gap $\omega_{\text{gap}} \approx -4K|\alpha|^2$ might be expected, although if we achieve the expected cat size increase in Eq. 6.1 and remember $K \propto 1/M^2$ (Eq. 2.53) then ω_{gap} is actually independent of M.

3. Slower, and thus lower fidelity, mapping gate; although, this may be sped up via pulse engineering techniques [Puri, Boutin, and Blais 2017] and is not strictly necessary if all preparation and measurement are done within the Kerr-cat qubit Bloch sphere.

4. Slower, and thus lower fidelity, Fock qubit operations—gates and dispersive readout— although again we do not intend to use them.

With these considerations in mind, we explore in the rest of this section an experimental realization of $M = 2$ SNAILs and Fock-qubit anharmonicity $2K/2\pi = 0.98$ MHz intended to create a larger and longer-lived Kerr-cat qubit.

6.1.1 Eigenstate pairing in Kerr-cats

To verify that we indeed may make a Kerr-cat qubit with larger average photon number, we seek to validate our Hamiltonian. Specifically, consider Eq. 4.38 without two-photon dissipation $\kappa_2 = 0$

$$\mathcal{H}_{\text{KC}} = -\Delta a^\dagger a - K a^{\dagger 2} a^2 + \epsilon_2 a^{\dagger 2} + \epsilon_2^* a^2 \tag{6.2}$$

where $\Delta = \omega_p/2 - \omega_a$ (or Eq. 3.18 if pump-induced Stark shift is included) and we have ignored κ_1 assuming it has minimal effect on the no-jump evolution in the regime $|\text{Im}\,\tilde{\delta}| \ll 1$ (see Eq. 4.55). The predicted eigenspectrum for this Hamiltonian with $\Delta = 0$ was plotted in Fig. 4.3a.

In order to measure this eigenspectrum, we perform the experiment indicated in the pulse sequence in Fig. 6.1a. We adiabatically ramp on the squeezing drive with no detuning $\Delta = 0$ and an ϵ_2 to achieve a known $\bar{n} = |\epsilon_2/K|$ that was calibrated via Rabi oscillations in a similar manner to Fig. 5.2. A cat-quadrature readout (CQR) is performed to prepare $|\pm X\rangle \approx |\pm\alpha\rangle$ based on the measurement outcome. We then apply a weak saturation spectroscopy tone at frequency ω_{spec} and perform a second CQR to see if the spectroscopy tone causes a transition.

The measured data of the second CQR measurement postselected on the first are plotted in Fig. 6.1b as a function of the swept spectroscopy tone detuning $\omega_p/2 - \omega_{\text{spec}}$ and the swept photon number $\bar{n} = |\epsilon_2/K|$ of the Kerr-cat qubit that was independently calibrated.
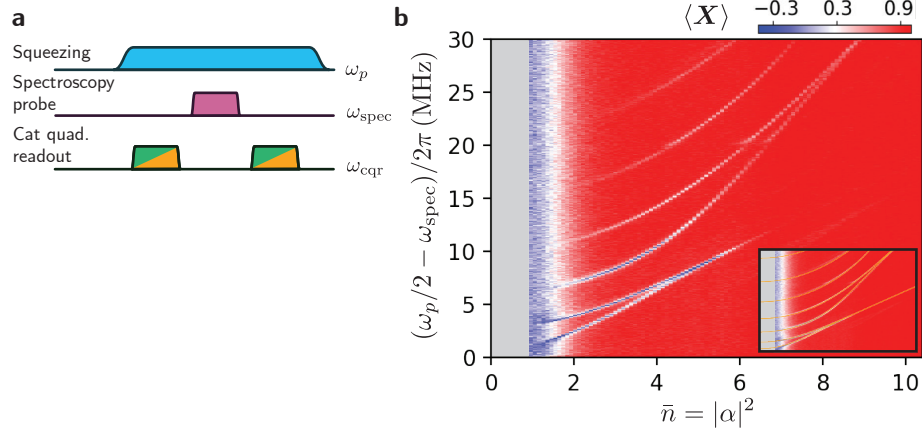
Figure 6.1 | (a) Pulse sequence for the spectroscopy in (b). The squeezing drive is ramped on with strength ϵ_2 adiabatically and an initial CQR measurement is performed to prepare $|\pm X\rangle \approx |\pm\alpha\rangle$. A weak saturation spectroscopy probe tone with frequency ω_{spec} is applied and a a second CQR measurement performed. (b) The results of the second CQR measurement conditioned on the first as a function of average photon number $\bar{n} = |\epsilon_2/K|$ (swept via ϵ_2) and detuning of the spectroscopy probe tone from the Kerr-cat frequency $\omega_p/2 - \omega_{\text{spec}}$. Gray box denotes excluded region where CQR is not a high-fidelity preparation. The inset overlays predictions of Eq. 6.2 (orange) with no free parameters.

As $\epsilon_2 \rightarrow 0$, the eigenspectrum clearly resembles that of a Kerr nonlinear oscillator where the transition from $|n = 0\rangle$ to $|n\rangle$ is given by $Kn(n-1)$. The gray region corresponds to photon numbers where the first CQR measurement is no longer a reliable QND preparation nor calibrated correctly to be a high-fidelity measurement. As the squeezing drive strength increases, we notice that the transition frequencies pair together as pairs of excited states become degenerate. For instance, at $\bar{n} = 5$, the first two excited states are nearly degenerate and the transition disappears for $\bar{n} > 6$. At this point, the eigenstates are degenerate to within the bandwidth of the second CQR measurement and the measurement—now truly a *quadrature* measurement for these two states as well—outcome is indistinguishable from $|\pm X\rangle \approx |\pm\alpha\rangle$ where the population started. Explicitly, if the first measurement prepares $|\pm X\rangle \approx |\pm\alpha\rangle$, a resonant transition would drive the state to $\approx \boldsymbol{D}(\pm\alpha)|n = 1\rangle$, which are themselves eigenstates once the true eigenstates of definite photon-number-parity become degenerate. As $\bar{n}$ approaches 8, the second set of excited states begin to pair together and themselves become degenerate.

The inset depicts a no-free-parameter prediction of the transitions (orange lines) based on Eq. 6.2 with $\Delta = 0$, $2K/2\pi = 0.98$ MHz and ϵ_2 calibrated as mentioned previously. The remarkable agreement shows the true power of effective Hamiltonians like Eq. 6.2 to capture the relevant dynamics in periodically driven systems. Furthermore, despite the fact that the RWA approximation is not valid in this system, the spectroscopic agreement gives us confidence that we are not missing important contributions to the effective Hamiltonian

dynamics. In the current system, the effective of any rotating terms, which may be explicitly cataloged and calculated order by order [Venkatraman et al. 2021], is to renormalize the parameters in the effective Hamiltonian without adding distinct ones.

Finally, the degeneracy of the excited states depicted here will have a direct consequence on the observed lifetime of the coherent states. In the previous sample of Chapter 5 where $\bar{n} = 2.6$, the first two excited states were outside of the double-well and not yet degenerate. Therefore, any excitation event resulting from environmental applications of $a^\dagger$ or $a^\dagger a$ would result in a phase-flip event. Once $\bar{n} > 6$ however, the excited state degeneracy means that an excitation even transferring population to them would not cause an immediate dephasing event. There is a chance for single-photon loss κ_1—or two-photon loss but we assume $\kappa_2 = 0$ here—to autonomously correct the leakage event before it causes a logical phase-flip in the Kerr-cat qubit [Puri et al. 2019].

6.1.2 Longer coherence with larger cats

Given that we have spectroscopic evidence and Rabi oscillations between cat states (not shown) to confirm that we can stabilize a Kerr-cat qubit with at least $\bar{n} = 10$ photons, we pursue coherence measurements of the cat state and coherent state lifetimes respectively as a function of $\bar{n}$. Importantly, we use only CQR and gates within the Kerr-cat Bloch sphere to perform these measurements. This has the advantage of being less reliant on the quality of the Fock qubit, as well as the experimental advantage of a reduced number of calibration experiments. For these experiments, we again set $\Delta = 0$. The squeezing drive induces a negligible Stark shift for the range of $\bar{n}$ considered, which cannot be detected via spurious Z rotation (c. f. Eq. 5.4) given our coherence times.

The pulse sequence to measure the Schrödinger cat state lifetime, depicted in Fig.6.2a, resembles a modified Ramsey sequence on the Kerr-cat qubit. We perform CQR and then a $Z(\pi/2)$ gate via free Kerr evolution for $T_{Z(\pi/2)} = 508\,\text{ns}$ to prepare the parityless cat $|\pm Y\rangle$. We then wait a variable delay time Δt, and perform a second $Z(\pi/2)$ gate followed by CQR. Single-exponential fits give the decay timescale for the cat state lifetime plotted as a function of $\bar{n} = |\alpha|^2$ in Fig.6.2c. Importantly, the cat state lifetime decreases as expected $\propto T_1/2\bar{n}$ and is reduced to around $1\,\mu\text{s}$ at $\bar{n} = 10$, implying we pay linearly in photon number with our Kerr-cat qubit stabilization as an autonomous QEC protocol.

To measure the coherent state lifetime, we utilize the pulse sequence depicted in Fig. 6.2b. CQR prepares $|\pm X\rangle \approx |\pm\alpha\rangle$ based on the measured outcome, and a second CQR measures the coherent state population after a variable wait time Δt. Single exponential fits to the decay of the coherence give the characteristic decay timescales plotted in orange as a function of $\bar{n}$ in Fig. 6.2b.

In contrast to the purely two-photon dissipative cats where coherent state lifetime increases exponentially and then saturates [Lescanne et al. 2020], the measured coherent state lifetime here displaces distinct features as a function of photon number. At low $\bar{n}$, we ob-
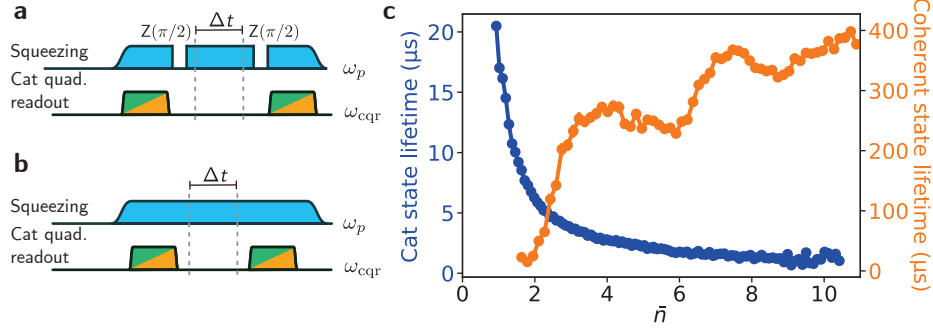
Figure 6.2 | (a) Pulse sequence for measuring cat state lifetime is a modified Ramsey sequence: adiabatic mapping, CQR readout and $Z(\pi/2)$ gate to prepare $|\pm Y\rangle$, wait a variable delay time Δt, then $Z(\pi/2)$ and CQR readout. (b) Pulse sequence for measuring coherent state lifetime. Both experiments are fit to single exponentials and decay timescales are reported in (c). (c) Cat (blue) and coherent (orange) state lifetimes as a function of $\bar{n} = |\epsilon_2/K|$ with no explicit pump detuning $\Delta = 0$. Cat lifetimes follow expected dependence $\propto 1/\bar{n}$. Coherent state lifetime changes between regimes of exponential increase and nearly flat plateau regions.

serve an exponential increase in lifetime until an apparent plateau at $\tau_{\pm X} \approx 250\,\mu$s for $\bar{n} \approx 3$. The plateau continues, with a slight downward trend, until another sharp uptick in lifetime around $\bar{n} \approx 6$. This uptick itself saturates at $\approx 350\,\mu$s with another downward trend until $\bar{n} \approx 9$ where the lifetime increases yet again until finally saturating at $400\,\mu$s. After the plotted $\bar{n}$, the lifetime monotonically decreases.

To understand the emergence of these apparent steps in coherent state lifetime, consider again the eigenspectrum as measured by the spectroscopy in Fig. 6.1b. The upticks in lifetime occur at photon numbers $\bar{n} \approx 6$ and $\bar{n} \approx 9$ where the first pair and second pair of excited states respectively become indistinguishably degenerate. From this observation, we may associate an explanation for each region of the coherent state lifetime. At low $\bar{n}$, the exponential lifetime increase originates from the exponential protection of the degeneracy of the ground states. However, once the lifetime reaches a certain value it is no longer limited by this error. Instead, in the first plateau, leakage events to the first excited states, which are still above the double well barrier and at distinct energies, cause instant dephasing events. When $\bar{n} \approx 6$, the first excited states are now below the barrier and their degeneracy becomes exponentially protected. A similar story occurs for the second plateau and corresponding uptick; leakage to the second pair of excited states is the limiting factor on coherence until their degeneracy becomes exponentially protected. As such, we see that the structure of the Kerr-cat Hamiltonian affords continued error protection even against leakage to higher excited states.

The goal then for further increased coherence may be achieved by increasing $\bar{n}$ for the same values of phenomenological noise (i. e. heating events). Experimentally, we tend to see that increasing drive power increases the phenomenological heating that we earlier as-
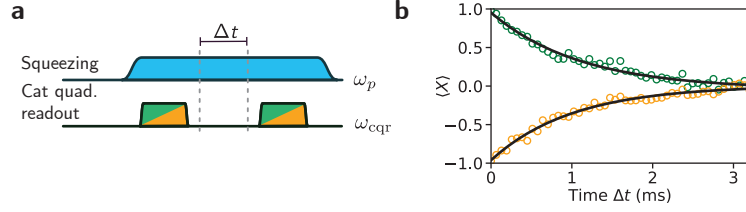
Figure 6.3 | (a) Pulse sequence for measuring coherent state lifetime (b). The squeezing drive has strength $|\epsilon_2/K| = 3.89$ and explicit red-detuning $\Delta/2\pi = -5.5\,\mathrm{MHz}$. (c) Green (orange) data points are measured $\langle X \rangle$ coherence conditioned on initial state $|\pm X\rangle \approx |\pm\alpha\rangle$. Black are single exponential fits constrained to have the same decay timescale $\tau_{\pm X} = 1.06\,\mathrm{ms} \pm 0.047\,\mathrm{ms}$.

sociated with applying drive powers that approach the critical number of photons, which is itself defined by the photon number that applies the critical current across the respective Josephson junctions in the system. We may then ask if it is possible to increase the photon number without increasing the phenomenological heating. One way that we already accomplished this was through reducing the Kerr nonlinearity and increasing n_{crit}. However, within the same device, we may also utilize the pump detuning to accomplish the same goal.

To see this, consider the expression for photon number Eq. 4.53 in the bistable regime with $\mathrm{Im}\,\tilde{\delta} \to 0$ and $\kappa_2 = 0$

$$|\alpha|^2 = \left|\frac{\epsilon_2}{K}\right| \left(1 - \mathrm{Re}\left\{\tilde{\delta}\right\}\right) \tag{6.3}$$

where $\mathrm{Re}\,\tilde{\delta} = \Delta/2|\epsilon_2|$ in this case. We see that choosing a red-detuned squeezing drive $\Delta = \omega_p/2 - \omega_a < 0$ will increase the photon number. The limit on red-detuning however is provided by the tristable regime. In the tristable regime, additional tunneling paths between wells become available that are expected to degrade coherence [Dykman et al. 1998; Marthaler and Dykman 2007]. To avoid the tristable regime, the condition then to remain in the bistable regime is $|\tilde{\delta}| < 1$, which in the case of $\kappa_1/\Delta \to 0$ implies $|\Delta| < 2|\epsilon_2|$.

We experimentally investigate this property by explicitly detuning the squeezing drive by $\Delta/2\pi = -5.5\,\mathrm{MHz}$ and measuring the coherent state lifetime with the pulse sequence in Fig. 6.2a. We choose $|\epsilon_2/K| = 3.89$, which achieves the maximum coherence for this detuning. The measured data are displayed in Fig. 6.3b. Black lines are single exponential fits, constrained to have the same fit parameters, which results in a decay timescale for the coherent state lifetime of $\tau_{\pm X} = 1.06\,\mathrm{ms} \pm 0.047\,\mathrm{ms}$.

6.1.3 Quantum jumps with CQR

To finish this section on improvements to the Kerr-cat qubit, we characterize the quality of the cat-quadrature readout (CQR). As we saw in Sec. 5.4, the signal-to-noise ratio (SNR)
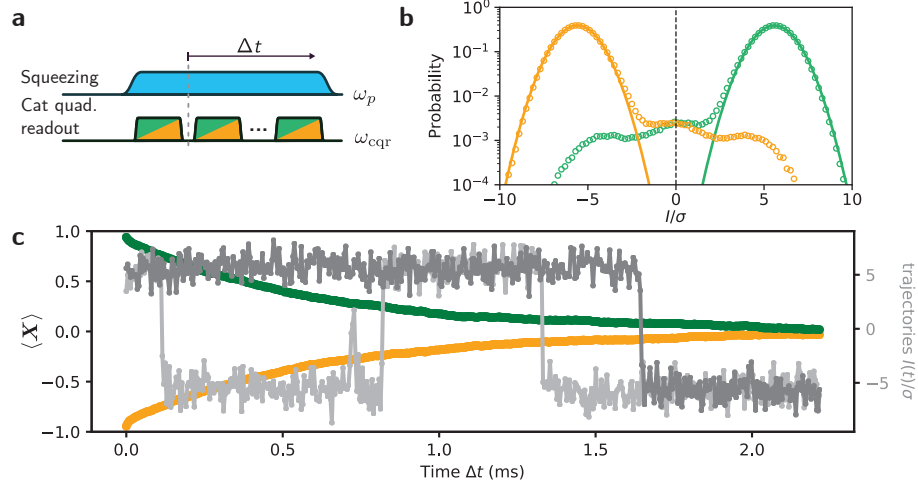
Figure 6.4 | (a) Pulse sequence for (b) and (c). Squeezing drive is adiabatically ramped on with strength $|\epsilon_2/K| = 7.85$ and an explicit red-detuning $\Delta/2\pi = -4.0\,\mathrm{MHz}$. CQR measurements are repeatedly performed, each with total duration $T_\mathrm{cqr} = 4.44\,\mu\mathrm{s}$ that includes ring up, ring down and full integration time. (b) Histogram of all CQR measurements conditioned on its preceding measurement with I-quadrature axis scaled by the standard deviation σ of Gaussian fits (black). Counts centered at $I/\sigma = 0$ correspond to excited states. Extracted QNDness $\mathcal{Q} = 0.992$. (c) Two examples of single trajectories (gray), where each point corresponds to a single CQR measurement, show quantum jumps between $|\pm X\rangle \approx |\pm\alpha\rangle$. Green (orange) is average over many trajectories postselected on the first measurement giving $|\pm X\rangle$. Single exponential fits give time constant $\tau_\mathrm{cqr} = 594\,\mu\mathrm{s} \pm 19\,\mu\mathrm{s}$.

scales proportionally to the photon number $\bar{n} = |\alpha|^2$ of the Kerr-cat qubit (Eq. 5.12). Given this, we might expect that increasing the photon number also improves CQR, and that is indeed the case.

To experimentally investigate the CQR quality, we perform the pulse sequence depicted in Fig. 6.4a. With an explicit detuning of $\Delta/2\pi = -4.0\,\mathrm{MHz}$, we ramp on a squeezing drive with strength $|\epsilon_2/K| = 7.85$. We then repeatedly perform CQR measurements in a pulsed fashion with a total pulse duration including ring up and ring down of $T_\mathrm{cqr} = 4.44\,\mu\mathrm{s}$. In this sample, the linewidth of the readout resonator was $\kappa_b/2\pi = 0.4\,\mathrm{MHz}$, which could be increased in future devices for faster readout. However, as noted in Sec. 5.4, conditional displacement readout schemes like CQR are particularly good at short times and are also amenable to fast reset protocols [Didier, Bourassa, and Blais 2015; Touzard et al. 2019].

A histogram of all measurements, conditioned on the preceding measurement and projected along the in-phase I quadrature, is shown in Fig. 6.4b. The axis is scaled by the standard deviation σ of the Gaussian fit to the histogram (black). The spurious counts near $I/\sigma = 0$ result from population in higher excited states due to the imperfect adiabatic mapping with finite detuning Δ. As defined Eq. 5.15, the bare signal-to-noise ration SNR $= 125$. We find experimentally that waiting for the system to thermalize with the squeezing drive on before the first CQR measurement drastically reduces the excited state

population (not shown). Despite this, we may also extract the QNDness (defined Eq. 5.17) $\mathcal{Q} = 0.992$ by experimentally calculating the probability that two successive measurements have the same outcome, which is less than the decoherence-limited bound of 0.995. Using a stringent threshold for preparation, we may extract the uncorrected readout fidelity, defined in Eq. 5.16, as $\mathcal{F} = 0.996$.

The quality of the readout may be further examined by considering the quantum jump trajectories, of which two examples are plotted (gray) in Fig. 6.4c. Each time point in the trajectory corresponds to the measurement decision associated with a single CQR pulse. Averaging many trajectories together recovers the decay green (orange) when the entire trajectory average is postselected conditional on the initial state determined by the first measurement. A single exponential fit extracts the timescale $\tau_{\text{cqr}} = 594\,\mu s \pm 19\,\mu s$, which should be compared to the coherent state lifetime $\tau_{\pm X} = 712\,\mu s$ when no CQR pulses—other than an initial and final—are applied.

Quantum jumps, long since measured in macroscopically coherent superconducting circuits [Vijay, Slichter, and Siddiqi 2011], are an excellent characterization of the health of a measurement apparatus and are fundamentally important for investigating measurement backaction and weak measurement [Murch et al. 2013; Hatridge et al. 2013]. Importantly, we note that these results are not quantum jumps of parity [Sun et al. 2014] in undriven harmonic oscillators that were later used for error-tracking and QEC [Ofek et al. 2016]. Instead, they are quantum jumps between the macroscopically distinct period-doubled coherent states $|\pm\alpha\rangle$, which in turn are ground states of the periodically driven system. As such, cat-quadrature readout of a Kerr-cat qubit implements a high fidelity measurement as well as high quality state preparation. Additionally, with a $\approx 1\,$ms lifetime and fast single qubit gates, the Kerr-cat qubit is a promising tool for future applications, such as fault-tolerant error syndrome detection [Puri et al. 2019; Grimsmo and Puri 2021].

6.2 Topological CNOT between two Kerr-cat qubits

In this section, we consider the implementation of the topological CNOT gate that preserves the noise bias and how it may be implemented with two Kerr-cat qubits [Puri et al. 2020]. If high fidelity, the overhead associated with quantum computations may be significantly reduced [Guillaud and Mirrahimi 2019; Puri et al. 2020], especially if cat-qubits form the physical qubits for surface codes [Darmawan et al. 2021] that exploit the intrinsic noise bias.

6.2.1 Topological coherent state exchange

Before discussing the full CNOT, we focus on a single qubit gate—a discrete $Z(\pi) = Z$ gate—that contains the necessary features of topology and noise-bias-preservation that underlie the CNOT. This gate is based on the exchange of the coherent states $|\pm\alpha\rangle$ in phase space. The exchange operation will not depend on the path or speed, only the underly-

ing topology associated with encircling the origin of phase space. To begin, consider the definition of a Z gate, which can simply be defined by the eigenvalue equation

$$
\begin{aligned}
\boldsymbol{Z} \left| \pm Z \right\rangle &= \boldsymbol{Z} \left| \mathcal{C}_\alpha^\pm \right\rangle \\
&= \pm \left| \mathcal{C}_\alpha^\pm \right\rangle \\
&= \pm \left| \pm Z \right\rangle
\end{aligned}
\tag{6.4}
$$

just as we defined in Sec. 4.1. Next, note the symmetry of phase space of the two-legged cat code is a two-fold discrete rotational symmetry. Thus there are two indistinguishable codes in the same oscillator defined by the two definitions

$$
\left| \pm Z \right\rangle = \left| \mathcal{C}_\alpha^\pm \right\rangle ,
\tag{6.5}
$$

$$
\left| \pm Z' \right\rangle = \left| \mathcal{C}_{-\alpha}^\pm \right\rangle
\tag{6.6}
$$

respectively. These two codes have the important relationship between them that

$$
\left| \mathcal{C}_{-\alpha}^\pm \right\rangle = \pm \left| \mathcal{C}_\alpha^\pm \right\rangle
\tag{6.7}
$$

which again results from the rotational symmetry of the code. As such, if we loosely consider the coherent states as indistinguishable particles, then an exchange operation of $\alpha \to -\alpha$ between these two codes is equivalent to remaining within the same code but with an additional Z gate. Explicitly, the exchange $\alpha \to -\alpha$ gives:

$$
\left| \pm Z \right\rangle = \left| \mathcal{C}_\alpha^\pm \right\rangle \to \left| \mathcal{C}_{-\alpha}^\pm \right\rangle = \pm \left| \mathcal{C}_\alpha^\pm \right\rangle = \pm \left| \pm Z \right\rangle
\tag{6.8}
$$

which is identically the definition Eq. 6.4. This exchange operation may be experimentally applied by rotating cat states by π in phase space, which itself comes from a full 2π rotation of the squeezing drive ϵ_2. This underlying symmetry results directly from the period-doubling phenomena intrinsic to the Kerr-cat qubit. The exchange operation is entirely topological in origin; it depends neither on the path taken through phase space nor the speed as long as the origin is encircled.

6.2.2 Exchange conditioned on a second cat: the CNOT

The preceding topological Z gate now must be conditioned on the state of a second Kerr-cat qubit to implement the CNOT gate. To exactly accomplish this, the derived Hamilto-

nian [Puri et al. 2020] has the form

$$\mathcal{H}_{\text{CNOT}}/\hbar = -K_b\left(\boldsymbol{b}^{\dagger 2} - \beta^2\right)\left(\boldsymbol{b}^2 - \beta^2\right)$$
$$-K_a\left[\boldsymbol{a}^{\dagger 2} - \alpha^2 e^{-i2\phi}\left(\frac{\beta - \boldsymbol{b}^\dagger}{2\beta}\right) - \alpha^2\left(\frac{\beta + \boldsymbol{b}^\dagger}{2\beta}\right)\right]$$
$$\times\left[\boldsymbol{a}^2 - \alpha^2 e^{+i2\phi}\left(\frac{\beta - \boldsymbol{b}}{2\beta}\right) - \alpha^2\left(\frac{\beta + \boldsymbol{b}}{2\beta}\right)\right]$$
$$+\dot{\phi}\left(\frac{\boldsymbol{b} + \boldsymbol{b}^\dagger - 2\beta}{4\beta}\right)\boldsymbol{a}^\dagger\boldsymbol{a} \tag{6.9}$$

where $\boldsymbol{a}$ and $\boldsymbol{b}$ each represent Kerr-cat qubits with self-Kerr nonlinearities K_a and K_b respectively, stabilized at coherent state amplitudes $\pm\alpha$ and $\pm\beta$ respectively. For simplicity, in this section we take α and β to be real numbers. To implement the gate, we control the phase ϕ and roll its from $\phi(t=0)=0 \to \phi(t=T)=\pi$, which must be adiabatic compared to ω_{gap}.

Considering $\mathcal{H}_{\text{CNOT}}$ line by line, the first line stabilizes cat $\boldsymbol{b}$ at coherent state amplitude $\pm\beta$. The next two lines implement a rotation of cat $\boldsymbol{a}$ conditioned on $\boldsymbol{b}$ in $|\pm\beta\rangle$. The final line corresponds to a dynamic phase needed to perfectly cancel a small geometric phase; for reasonably sized cats $\bar{n} \gtrsim 3$, this effect is negligible [Puri et al. 2020].

Consider Eq. 6.9 the ideal Hamiltonian to be implemented, we expand to write all the terms in a more familiar form

$$\mathcal{H}_{\text{CNOT}}/\hbar = -K_b\left(\boldsymbol{b}^{\dagger 2} - \beta^2\right)\left(\boldsymbol{b}^2 - \beta^2\right) \tag{6.10}$$
$$-K_a\boldsymbol{a}^{\dagger 2}\boldsymbol{a}^2 \tag{6.11}$$
$$+K_a\alpha^2\cos(\phi)\left(\boldsymbol{a}^{\dagger 2}e^{+i\phi} + \text{h.c.}\right) \tag{6.12}$$
$$-iK_a\frac{\alpha^2}{\beta}\sin(\phi)\left(\boldsymbol{a}^{\dagger 2}\boldsymbol{b}e^{+i\phi} + \text{h.c.}\right) \tag{6.13}$$
$$-K_a\frac{\alpha^4}{2\beta}\sin(2\phi)\left(i\boldsymbol{b}^\dagger + \text{h.c.}\right) \tag{6.14}$$
$$-K_a\frac{\alpha^4}{\beta^2}\sin^2(\phi)\boldsymbol{b}^\dagger\boldsymbol{b} \tag{6.15}$$
$$-\dot{\phi}\boldsymbol{a}^\dagger\boldsymbol{a}/2 \tag{6.16}$$
$$+\dot{\phi}\boldsymbol{a}^\dagger\boldsymbol{a}\left(\boldsymbol{b}^\dagger + \text{h.c.}\right)/4\beta \tag{6.17}$$

where again $\phi(t=0)=0 \to \phi(t=T)=\pi$. Breaking down these terms individually from top to bottom, we require

1. Stabilization of cat $\boldsymbol{b}$ via Kerr and squeezing drive.

2. Self-Kerr of cat a.

3. Squeezing drive on cat a with amplitude $K_a \alpha^2 \cos(\phi) e^{+i\phi}$.

4. Squeezing drive on cat a that depends on b—this is the most important interaction term.

5. Linear drive on b that only corrects leakage and causes no Rabi oscillations within the Kerr-cat qubit (see Eq. 5.2).

6. Detuning on cat b.

7. Detuning on cat a.

8. Conditional displacement of cat b dependent on the photon number $a^\dagger a$.

While this list of terms may appear experimentally intimidating, numerical simulations confirm that for cat sizes $\alpha^2 = \beta^2 > 4$, only the first four lines are necessary for fidelities better than 0.99.

As such, there is only one new term that would not otherwise be present in a system of two uncoupled Kerr-cat qubits: namely, Eq. 6.13. To see that this interaction term indeed implements the required operation, we project Eq. 6.12–6.13 on the Kerr-cat Bloch sphere of qubit b

$$
\begin{aligned}
&\boldsymbol{P}_{\mathcal{C}_b} \left(K_a \alpha^2 e^{+i\phi} \left[\cos(\phi) - i \sin(\phi) \boldsymbol{b}/\beta \right] \boldsymbol{a}^{\dagger 2} + \text{h.c.} \right) \boldsymbol{P}_{\mathcal{C}_b} \\
&= K_a \alpha^2 e^{+i\phi} \left[\cos(\phi) - i \sin(\phi) \left(\boldsymbol{X_b} + i e^{-2\beta^2} \boldsymbol{Y_b} \right) \right] \boldsymbol{a}^{\dagger 2} + \text{h.c.} \\
&= K_a \alpha^2 e^{+i\phi} \left[\cos(\phi) - i \sin(\phi) \boldsymbol{X_b} + \sin(\phi) e^{-2\beta^2} \boldsymbol{Y_b} \right] \boldsymbol{a}^{\dagger 2} + \text{h.c.} \\
&= K_a \alpha^2 e^{+i\phi} \left[e^{-i\phi \boldsymbol{X_b}} + \sin(\phi) e^{-2\beta^2} \boldsymbol{Y_b} \right] \boldsymbol{a}^{\dagger 2} + \text{h.c.} \\
&\approx K_a \alpha^2 e^{i\phi(1-\boldsymbol{X_b})} \boldsymbol{a}^{\dagger 2} + \mathcal{O}\left(K_a \alpha^2 e^{-2\beta^2} \right) \boldsymbol{Y_b} \boldsymbol{a}^{\dagger 2} + \text{h.c.}
\end{aligned}
\tag{6.18}
$$

from which it is clear that the $\boldsymbol{X_b}$ eigenvalue determines whether the squeezing drive phase on a acquires the phase factor $e^{i2\phi}$ or 1.

Finally, we discuss how to implement the desired interaction term, which is a controllable third order coupling $g_{\text{int}} \boldsymbol{a}^{\dagger 2} \boldsymbol{b} + \text{H.c.}$. As long as both modes participate in a four-wave-mixing nonlinearity, a microwave drive at $2\omega_a - \omega_b$ implements the desired interaction, which is a similar process to the pumping scheme used from two-photon-dissipation-based Schrödinger cat state stabilization [Leghtas et al. 2015]. Therefore, any architecture that supports capacitively coupled SNAIL-based qubits may implement this topological CNOT between two Kerr-cat qubits. We have implemented one such architecture based on striplines in 3D [Axline et al. 2016] in which all the experimental results in Sec. 6.1 were obtained, but quasi-2D implementations are equally viable. At the time of writing, we have

realized two coupled SNAIL-based nonlinear oscillators in this architecture that each individually support Kerr-cat qubits, and we are excited to experimentally investigate this topological CNOT.

7

Conclusions

The experiments in this thesis have answered affirmatively that three-wave mixing is a powerful tool for both quantum-noise-limited amplification and the protection of quantum information via the autonomous stabilization of a Schrödinger cat qubit. The third-order nonlinearity necessary for three-wave mixing may be added to a Josephson circuit by replacing a single Josephson junction with a SNAIL and a DC-flux bias. This simplicity opens up a host of opportunities to introduce three-wave mixing in quantum information applications.

One exciting direction could be the application of Kerr-free three-wave mixing to activate quantum operations between otherwise uncoupled quantum systems. Often residual cross-Kerr interactions limit the fidelity of operations and accumulate entanglement during idle times of a quantum processor. The prospect of cross-Kerr-free systems that maintain the minimal necessary nonlinear coupling to perform operations may be key to further improvement, as was recently the case in for autonomous stabilization of a cat qubit via two-photon dissipation [Lescanne et al. 2020].

Generally, both presented applications of single-mode squeezing—for amplification of small signals with SPAs and stabilization of a Kerr-cat qubit—were shown to benefit from systems with less bare nonlinearity: less third-order g_3, less Kerr K, and less higher-order nonlinearities. This reduction seems to push the design toward a purely linear system, yet a purely linear system cannot perform three-wave mixing. Crucially however, the reduction of nonlinearity was achieved without the addition of linear inductance; the nonlinearity's inductive participation ratio remained close to unity. Perhaps counterintuitively, lowering nonlinearity in this fashion actually *enhanced* the achievable single-mode squeezing strength $\epsilon_2 = 2g_3\alpha_p$ in these devices because more pump photons $|\alpha_p|^2$ could be applied. To make the point numerically, the best presented SPA reached $|\epsilon_2|/2\pi \approx 110\,\text{MHz}$ despite $g_3/\pi \approx 2\,\text{MHz}$ and Kerr nonlinearity $2K/2\pi \approx 50\,\text{kHz}$. As such, for applications where the rate of the *driven* interaction—here, single-mode squeezing but it could be for tunable coupling or control—that results from three-wave mixing is the important parameter, less nonlinearity with large participation in the modes of interest is the recommended path forward. In these instances, as is the case for room-temperature electronics, the ultimate performance limits will result from parasitic inductance or technical restrictions on applied pump power.

The further reduction of nonlinearity for increased performance of Schrödinger cat qubits requires a more careful consideration. In qubit implementations generally, gate and readout speed compared to decoherence rate is a key metric, and a large enough anharmonicity to prevent leakage errors during these operations is important. The success of the transmon thus far is in part due to its simplicity in achieving coherence while maintaining enough anharmonicity to allow for control speeds nearly limited by control elec-

tronics. Meanwhile, protected qubits based on novel superconducting circuits promise larger anharmonicity and increased coherence at the expensive of more complicated control schemes [Gyenis et al. 2021a]. Both transmons and other protected circuits require appreciable bare nonlinearity to realize their respective Hamiltonians, and thus driven interactions break down at smaller drive powers.

Kerr-cat qubits represent a different approach. As discussed in Chapter 6, Kerr-cat qubits benefit—except for the fidelity of the free-Kerr-evolution gate—from reduced bare nonlinearity that enable the creation of cat states with larger photon number and longer coherent state lifetime. We expect this trend of less Kerr for larger cats and longer coherent state lifetimes to continue; however, this is not the whole story. For quantum information processing, the achievable gate fidelities involving Schrödinger cat states are also crucial. The quality of these gates may be loosely determined by the gate speed limit to decoherence rate ratio, $\omega_{\text{gap}}T_1/2\bar{n} \approx 2KT_1$, which is independent of photon number and clearly improves for larger K. As such, we expect there to be an optimum Kerr for a given application depending on the tradeoff between achievable gate speed and noise-bias. Improvements in gate design and control techniques will help by increasing the gate speed for a given ω_{gap}, and thereby allowing a design with less nonlinearity to further increase the coherent state lifetime and noise bias.

Focusing on future applications of autonomously stabilized two-legged cat qubits, the Kerr-cat qubit shows promise for implementing a fault-tolerant error syndrome detector for other QEC codes [Puri et al. 2019]. Preventing uncorrectable errors from propagating to other qubits is crucial for the suppressing logical errors a the level necessary for useful computations [Grimsmo and Puri 2021]. Additionally, Kerr-cat qubits may themselves shed light on the quantum-classical transition [Zurek 2003] and may be useful in weak force measurements [Munro et al. 2002]. Networks of coupled bistable oscillators can be mapped onto Ising spins and used to investigate non-equilibrium quantum phase transitions [Dykman et al. 2018] or to solve combinatorial optimization problems [Marandi et al. 2014; Goto 2016a; Puri et al. 2017].

Perhaps on a grander scale, Schrödinger cat qubits promise to reduce the overhead associated with quantum error correction when compared to standard qubits made from isolated two-level systems [Guillaud and Mirrahimi 2019; Puri et al. 2020]. Crucially, such applications will require coupling multiple such qubits together with high fidelity operations. At the time of writing, the first two qubit gate between stabilized cats—the topological CNOT discussed in the previous chapter—is already under way. On top of this however, there is still much more one can imagine—perhaps a bias-preserving Toffoli gate between three cat qubits [Guillaud and Mirrahimi 2019]. Regardless, we believe the future is bright for cats and SNAILs and the further inclusion of three-wave mixing in superconducting circuits. I look forward to seeing what will come.

A

The SPA beyond the RWA

In three-wave mixing, the strong microwave pump tone that supplies the energy for the mixing process is often detuned from the modes of interest by a frequency of order the oscillator frequency. As such, the rotating wave approximation (RWA) is not valid in its most simple form and higher order approximations are necessary [Gardiner and Zoller 2004; Vool and Devoret 2017; Venkatraman et al. 2021]. This appendix more carefully considers the SPA beyond the first-order RWA. Remarkably, the dynamics are often mappable back to original effective Hamiltonians derived in Chapter 3 but with renormalized parameters.

A.1 Quantum Langevin equation (QLE) beyond the RWA

Beyond the RWA, we want equations of motion of the circuit degrees of freedom in which the evolution of the bath is already integrated out. Separating out the circuit from its environment, modelled as a transmission line with characteristic impedance Z_c, the equation of motion for any system operator Y with system Hamiltonian $\mathcal{H}_{\text{sys}}$ is

$$\dot{Y} = \frac{i}{\hbar} \left[\mathcal{H}_{\text{sys}}, Y \right] + \frac{i}{Z_c} \left\{ \dot{\Phi} - V_{\text{in}}, [\Phi, Y] \right\} \tag{A.1}$$

where Φ, the system's flux at the location of coupling to the environment, appears because we have chosen to express the environment in terms of the input voltage V_{in} from the environment. The derivation of Eq. A.1 assumes an arbitrary system coupled to a bath with a constant density of states [Gardiner and Zoller 2004]. The corresponding input-output relation is

$$2\dot{\Phi} = V_{\text{in}} + V_{\text{out}}. \tag{A.2}$$

A.1.1 Linear oscillator

To emphasize the utility of Eq. A.1, consider the case of a transmission line coupled to a linear LC oscillator. In this case, $\mathcal{H}_{\text{sys}} = Q^2/2C + \Phi^2/2L$, and taking $Y = \Phi$ and $Y = Q$ respectively yield

$$\dot{\Phi} = Q/C \tag{A.3}$$

$$\dot{Q} = -\Phi/L - \frac{1}{Z_c}(\dot{\Phi} - V_{\text{in}}) \tag{A.4}$$

which are the standard classical equations now written for operators.

A.1.2 Weakly nonlinear oscillator

For $\mathcal{H}_{\text{sys}}$ consisting of a single degree of freedom, we can introduce bosonic creation and annihilation operators according to $\boldsymbol{\Phi} = \Phi_{\text{zpf}}(\boldsymbol{a} + \boldsymbol{a}^{\dagger})$ where $\Phi_{\text{zpf}} = \sqrt{\hbar Z_a / 2}$ with Z_a the impedance. The equations of motion for the annihilation operator are

$$\dot{\boldsymbol{a}} = \frac{i}{\hbar}\left[\mathcal{H}_{\text{sys}}, \boldsymbol{a}\right] + \frac{Z_a}{2Z_c}\left[\mathcal{H}_{\text{sys}}, \boldsymbol{a} + \boldsymbol{a}^{\dagger}\right] + i\sqrt{\frac{Z_a}{2Z_C^2}}\boldsymbol{V}_{\text{in}} \tag{A.5}$$

which thus far has not made the RWA.

In the common cQED case where the transmission line is coupled to a weakly nonlinear resonator as in $\mathcal{H}_{\text{sys}}/\hbar = \omega_a \boldsymbol{a}^{\dagger}\boldsymbol{a} + \cdots$, the second commutator of the loss term may be approximated to first order as $\left[\omega_a \boldsymbol{a}^{\dagger}\boldsymbol{a}, \boldsymbol{a} + \boldsymbol{a}^{\dagger}\right] = \omega_a(-\boldsymbol{a} + \boldsymbol{a}^{\dagger})$. The counter-rotating term may be dropped within the RWA and the equation simplifies to

$$\dot{\boldsymbol{a}} = \frac{i}{\hbar}\left[\mathcal{H}_{\text{sys}}, \boldsymbol{a}\right] - \frac{Z_a}{2Z_c}\omega_a \boldsymbol{a} + i\sqrt{\frac{Z_a}{2Z_C^2}}\boldsymbol{V}_{\text{in}} \tag{A.6}$$

Remembering that the energy decay rate of a classical damped harmonic oscillator $\kappa = \omega_a Z_a / Z_c$ and ignoring the counter-rotating part of $\boldsymbol{V}_{\text{in}}$ under the RWA, we arrive at the famous QLE under both the RWA and Markov approximation:

$$\dot{\boldsymbol{a}} = \frac{i}{\hbar}\left[\mathcal{H}_{\text{sys}}, \boldsymbol{a}\right] - \frac{\kappa}{2}\boldsymbol{a} + \sqrt{\kappa}\boldsymbol{a}_{\text{in}} \tag{A.7}$$

where $\boldsymbol{a}_{\text{in}} = i\boldsymbol{V}_{\text{in}}/\sqrt{2\omega_a Z_c}$ has the interpretation of "square root of photon flux" in the standard quantum optics notation [Clerk et al. 2010; Vool and Devoret 2017].

A.2 QLE including arbitrary coupling circuit

We can also extend the above treatment generating the QLE A.1 to include a frequency dependent environment, similar to the treatment for extended bandwidth in amplifiers [Roy et al. 2015]. The resulting QLE for single oscillator with canonical flux $\boldsymbol{\Phi}$ and charge $\boldsymbol{Q}$ coupled to an environment characterized by admittance $Y_{\text{env}}[\omega]$ is

$$\dot{\boldsymbol{Q}} = \frac{i}{\hbar}\left[U_{\text{sys}}(\boldsymbol{\Phi}), \boldsymbol{Q}\right] - \boldsymbol{I}_{\text{env}} \tag{A.8}$$

$$\dot{\boldsymbol{\Phi}} = \frac{\boldsymbol{Q}}{C} \tag{A.9}$$

$$\boldsymbol{I}_{\text{env}}[\omega] = \left(j\omega\boldsymbol{\Phi}[\omega] - \boldsymbol{V}_{\text{in}}[\omega]\right)Y_{\text{env}}[\omega] \tag{A.10}$$

where $U_{\text{sys}}(\boldsymbol{\Phi})$ is the arbitrary inductive potential of the oscillator in parallel with the kinetic energy given by a single capacitor C. The first equation expresses Kirchhoff's current

conservation law between the inductive and capacitive branches of the resonator and the leakage current I_{env} into the environment. The second equation is essentially Kirchoff's voltage law for the resonator. The last equation specifies how leakage current is related to the system and transmission line degrees of freedom. We have written it in the Fourier domain, because in general the coupling is nonlocal in time and therefore not Markovian. The input voltage operator $V_{\text{in}}[\omega]$ contains the ω component of any incident signals as well as the noise from the transmission line.

We again introduce bosonic raising and lowering operators use them to rewrite Eq. A.9

$$\dot{a} + \dot{a^\dagger} = \frac{Q_{\text{zpf}}}{\Phi_{\text{zpf}}C}i(a^\dagger - a) \tag{A.11}$$

$$= \omega_a i(a^\dagger - a) \tag{A.12}$$

while remembering that all operators including $a(t)$ and $a^\dagger(t)$ in the Heisenberg picture are time dependent. We are free to take the Fourier transform with respect to this time dependance to get the exceedingly convenient relation

$$a[-\omega]^\dagger = -\frac{\omega - \omega_a}{\omega + \omega_a}a[\omega] \tag{A.13}$$

between the Fourier components of the creation and annihilation operators for excitations inside an oscillator with frequency ω_a.

This relation summarizes the RWA in the Fourier domain. It implies that for nearly resonant signals and responses the $a[-\omega]^\dagger$ term can be dropped from equations for $a[\omega]$, because it is suppressed by the fractional detuning of the signal. However, for off-resonant signals like those often used as pumps for 3-wave mixing processes, there is no suppression; the system of Eqs. A.8-A.9 cannot be reduced to a single first order differential equation as in the standard RWA QLE (Eq. 3.1).

A.3 Distributed-element model of the SPA

While the lumped-element model in Sec. 2.2 elucidates the important details in the theoretical treatment of the SPA and provides physical intuition, it cannot strictly be applied to the SPA devices presented in this thesis. In the SPA, the SNAIL array is embedded in a transmission line resonator, which is a distributed element. Later versions of SPAs actually consider the SNAIL array itself as a nonlinear transmission line [Sivak et al. 2020], but here we focus on the regime where the SNAIL array may be considered lumped.

The Lagrangian of such a system can be written as

$$
\mathcal{L} = \left(\int_{-l_{\mathrm{MS}}/2}^{-0} + \int_{+0}^{l_{\mathrm{MS}}/2} \right) \left[\frac{c}{2} (\partial_t \phi) - \frac{1}{2\ell} (\partial_x \phi)^2 \right] dx
$$
$$
- M U_S \left(\frac{\varphi_r - \varphi_l}{M} \right), \tag{A.14}
$$

where c is the capacitance per unit length and ℓ is the inductance per unit length. The generalized flux $\phi(x,t)$ on the transmission line is a one-dimensional massless Klein-Gordon field which has a discontinuity at $x = 0$, where the transmission line is interrupted by the lumped-element SNAIL array. For convenience, we have introduced $\varphi_l = \phi(-0,t)/\varphi_0$ and $\varphi_r = \phi(0+,t)/\varphi_0$ to denote the superconducting phase on both sides of the array.

Using zero current boundary conditions at $x = \pm l_{\mathrm{MS}}/2$ and linearizing the Lagrange equation of motion for this system, we can perform an eigenmode decomposition and find the resonant frequency ω_a of the structure as the smallest nontrivial solution of the equation

$$
\omega_a \tan \left(\frac{\pi}{2} \frac{\omega_a}{\omega_0} \right) = \frac{2 Z_c}{M L_s} \tag{A.15}
$$

where $Z_c = \sqrt{\ell/c}$ is the characteristic impedance of the transmission line, and $\omega_0 = \pi/l_{\mathrm{MS}} \sqrt{lc}$ is the resonant frequency when the array of SNAILs is replaced with a short.

Following Refs. [Wallquist, Shumeiko, and Wendin 2006; Nigg et al. 2012], we calculate the nonlinearities of the SPA as

$$
g_3 = \frac{4 Z_c c_3}{3 M^2 L_J} \sqrt{\frac{Z_c}{R_Q}} \left[\frac{\cos^2 \left(\frac{\pi}{2} \frac{\omega_a}{\omega_0} \right)}{\pi \frac{\omega_a}{\omega_0} + \sin \left(\pi \frac{\omega_a}{\omega_0} \right)} \right]^{3/2}, \tag{A.16}
$$

$$
2K = \frac{\omega_a \sin^2 \left(\pi \frac{\omega_a}{\omega_0} \right) \cot \left(\frac{\pi}{2} \frac{\omega_a}{\omega_0} \right)}{c_2 M^2 \left[\pi \frac{\omega_a}{\omega_0} + \sin \left(\pi \frac{\omega_a}{\omega_0} \right) \right]^2} \frac{Z_c}{R_Q}
$$

$$
\times \left[c_4 - \frac{c_3^2}{c_2} \frac{3 + 5 \left(\frac{\omega_a M L_s}{2 Z_c} \right)^2}{1 + 3 \left(\frac{\omega_a M L_s}{2 Z_c} \right)^2} \right], \tag{A.17}
$$

where $R_Q = \hbar/(2e)^2$ is the reduced resistance quantum. More complete derivations available in Ref. [Sivak et al. 2019; Sivak et al. 2020].

The limits of small and unity participation ratio correspond in this model to $M L_s \ll Z_c/\omega_a$ and $M L_s \gg Z_c/\omega_a$, respectively. In these limits, the corrections to Kerr due to c_3 coincide in both the distributed- (Eq. A.17) and lumped-element (Eq. 2.53) models.

A.4 Harmonic balance including period-doubling

Although used for the original study of SPA dynamic range [Frattini et al. 2018], itself based on previous works [Kamal, Marblestone, and Devoret 2009; Zhou et al. 2014; Sundqvist and Delsing 2014], this section follows the notation of later work that self-consistently includes the period-doubling effect [Sivak et al. 2019].

We wish to analyze the response of the SPA system using standard input-output theory together with the QLE for mode a. First, recall that a linear harmonic oscillator pumped at ω_p and probed at ω_s responds independently to each of these frequency components of the incoming field. In contrast, a nonlinear oscillator like the SPA will produce a response at all harmonics $\omega_{mn} = m\omega_p + n\omega_s$. The conventional DPA theory in Sec. 3.2 only takes into account one additional harmonic (the idler) at $\omega_i = \omega_p - \omega_s$, although in practice all higher intermodulation products (IMDs) will be created. Their magnitudes are often small and therefore neglecting these harmonics is a reasonable starting point.

To go beyond these treatment, we must account for further harmonics generated by through mixing to other frequencies. Up to second order in harmonic balance, we consider the following harmonics:

1. Pump ω_p, signal ω_s, and idler $\omega_i = \omega_p - \omega_s$ comprise the minimal set need for the DPA model of Sec. 3.2.

2. $2\omega_p$, $2\omega_s$, $2\omega_i$, $\omega_p + \omega_s$, $\omega_p + \omega_i$, $\omega_s - \omega_i$, and DC are required in the consistent calculation that takes into account Stark shift that is linear in photon number. These harmonics lead to g_3^2/ω_a corrections to K and the pump-induced Stark shift $\left(\frac{32}{3}g_4 - 28\frac{g_3^2}{\omega_a}\right) n_p$

3. $\omega_p/2$, $\omega_p/2 - \omega_s$, $\omega_p/2 - \omega_i$ account for the possible period-doubling effect examined within the RWA in Chapter 4.

Given this list of harmonics and considering the relation Eq. A.13, we make the ansatz for the intracavity amplitude according to a semiclassical harmonic balance solution to the QLE in the form

$$\alpha(t) = \sum_x \left(\alpha_x e^{-i\omega_x t} + \frac{\omega_a - \omega_x}{\omega_a + \omega_x} \alpha_x^* e^{+i\omega_x t} \right) \tag{A.18}$$

where x runs over all harmonics described previously. We then plug this ansatz into the QLE Eq. A.8 with Hamiltonian $\mathcal{H}_{\text{SPA}}$ Eq. 3.14 to generate a self-consistent set of equations that links the amplitudes of all chosen harmonics. Importantly, we *never* invoke the RWA, because all out-of-band harmonics do not satisfy it. This importantly relies on the relation Eq. A.13. Instead of the RWA, the approximation made here is encoded in the number of harmonics included; the amplitudes at other harmonics are assumed small and inconsequential to the dynamics at the considered frequencies.

Equations for the out-of-band harmonics can be partially solved and the system further reduced to three complex equations for the amplitudes at frequencies ω_s, ω_i, and $\omega_p/2$ de-

noted α_s, α_i, and α_h for the *signal, idler,* and *half*-frequency or period-doubled portions of the intracavity state. The three equations are:

$$\left(\omega + \Delta_{\mathrm{DPA}} + i\kappa/2\right)\alpha_s = u_s + \left(4g_3\alpha_p + 12g_4^*\alpha_h^2\right)\alpha_i^* + 12g_4^*\left(|\alpha_s|^2 + 2|\alpha_i|^2 + 2|\alpha_h|^2\right)\alpha_s$$
(A.19)

$$\left(-\omega + \Delta_{\mathrm{DPA}} + i\kappa/2\right)\alpha_i = u_i + \left(4g_3\alpha_p + 12g_4^*\alpha_h^2\right)\alpha_s^* + 12g_4^*\left(|\alpha_i|^2 + 2|\alpha_s|^2 + 2|\alpha_h|^2\right)\alpha_i$$
(A.20)

$$\left(\Delta_{\mathrm{DPA}} + i\kappa/2\right)\alpha_h = u_h + 4g_3\alpha_p\alpha_h^* + 12g_4^*\left(|\alpha_h|^2 + 2|\alpha_s|^2 + 2|\alpha_i|^2\right)\alpha_h \qquad \text{(A.21)}$$

where $\omega = \omega_s - \omega_p/2$ is the signal detuning; $\Delta_{\mathrm{DPA}} = \omega_p/2 - \omega_a - \left(\frac{32}{3}g_4 - 28\frac{g_3^2}{\omega_a}\right)n_p$; and u_s, u_i, and u_p denote the drive strengths at the corresponding frequencies. Note that the pump amplitude $\alpha_p = u_p/\omega_a$ here does not include any corrections due to α_s, α_i, and α_h—they have been reabsorbed into the above equations. Strictly, α_p is not on the same footing as the other amplitudes and is more like a drive amplitude boundary condition.

A.4.1 Gain of the SPA

Given the set of harmonic balance equations A.19- A.21, we examine the response at the signal frequency ω_s by rewriting the first two equations as

$$\left(\omega + \Delta_s + i\kappa/2\right)\alpha_s - \left(4g_3\alpha_p + 12g_4^*\alpha_h^2\right)\alpha_i^* = u_s \qquad \text{(A.22)}$$

$$\left(-\omega + \Delta_i - i\kappa/2\right)\alpha_i^* - \left(4g_3\alpha_p^* + 12g_4^*\alpha_h^{*2}\right)\alpha_s = u_i^* \qquad \text{(A.23)}$$

where

$$\Delta_s = \Delta_{\mathrm{DPA}} - 12g_4^*\left(|\alpha_s|^2 + 2|\alpha_i|^2 + 2|\alpha_h|^2\right) \qquad \text{(A.24)}$$

$$\Delta_i = \Delta_{\mathrm{DPA}} - 12g_4^*\left(|\alpha_i|^2 + 2|\alpha_s|^2 + 2|\alpha_h|^2\right) \qquad \text{(A.25)}$$

are the Stark-shift-adjusted signal and idler detunings respectively. Using the parameter mapping to the DPA model of $\epsilon_2 = 2g_3\alpha_p$ and for simplicity assuming we are in the single minimum regime such that $\alpha_h = 0$, the system reduces to

$$\begin{pmatrix} \omega + \Delta_s + i\kappa/2 & -2\epsilon_2 \\ -2\epsilon_2^* & -\omega + \Delta_i - i\kappa/2 \end{pmatrix} \begin{pmatrix} \alpha_s \\ \alpha_i^* \end{pmatrix} = \begin{pmatrix} u_s \\ u_i^* \end{pmatrix} \qquad \text{(A.26)}$$

Inverting the susceptibility matrix, we arrive at

$$\begin{pmatrix} \alpha_s \\ \alpha_i^* \end{pmatrix} = \frac{1}{D[\omega]} \begin{pmatrix} -\omega + \Delta_i - i\kappa/2 & 2\epsilon_2 \\ 2\epsilon_2^* & \omega + \Delta_s + i\kappa/2 \end{pmatrix} \begin{pmatrix} u_s \\ u_i^* \end{pmatrix} \tag{A.27}$$

$$D[\omega] = \left(\omega + \Delta_s + i\kappa/2\right)\left(-\omega + \Delta_i - i\kappa/2\right) - 4|\epsilon_2|^2 \tag{A.28}$$

which directly maps to the DPA model of Sec. 3.2 but with slightly different Stark-shift-renormalized detunings for the signal and idler amplitudes. Using the input-output relation, we then find the signal amplitude gain

$$\begin{aligned} g_s[\omega] = u_{s,\text{out}}/u_s &= i\kappa\alpha_s - 1 \\ &= \frac{i\kappa\left(-\omega + \Delta_i - i\kappa/2\right)}{D[\omega]} - 1 \\ &= \frac{\left(-\omega + \Delta_i - i\kappa/2\right)\left(-\omega - \Delta_s + i\kappa/2\right) + 4|\epsilon_2|^2}{\left(\omega + \Delta_s + i\kappa/2\right)\left(-\omega + \Delta_i - i\kappa/2\right) - 4|\epsilon_2|^2} \end{aligned} \tag{A.29}$$

and the corresponding phase-preserving power gain $G[\omega] = |g_s[\omega]|^2$

$$G[\omega] = 1 + \frac{4|\epsilon_2|^2\kappa^2}{\left((\Delta_i - \omega)(\Delta_s + \omega) + \kappa^2/4 - 4|\epsilon_2|^2\right)^2 + (\Delta_i - \Delta_s - 2\omega)^2\kappa^2/4} \tag{A.30}$$

$$\approx 1 + \frac{4|\epsilon_2|^2\kappa^2}{\left(\Delta_s^2 - \omega^2 + \kappa^2/4 - 4|\epsilon_2|^2\right)^2 + \omega^2\kappa^2} \tag{A.31}$$

where is last line we have used $\Delta_i \approx \Delta_s$ in the large gain limit where $|\alpha_i|^2 \approx |\alpha_s|^2$. This result is now matches the gain of an ideal DPA Eq. 3.9 with a detuning renormalized by the Stark shift of the incident signal.

A.4.2 Period doubling multi·stability

We can now rederive the multi-stability regions from Sec. 4.7 but without invoking the RWA. Up to second order in harmonic balance, we have the equation of motion for the amplitude α_h oscillating at $\omega_p/2$ in the lab frame Eq. A.21. To find ground state multi-stable solutions, we suppose there are no drives applied other than the squeezing drive at $\omega_p/2$. Thus, we set $u_s = 0$, $u_i = 0$, $u_h = 0$; this immediately implies $\alpha_s = 0$ and $\alpha_i = 0$. The remaining Eq. A.21 reduces to

$$\left(\Delta_{\text{DPA}} - 12g_4^*|\alpha_h|^2 + i\kappa/2\right)\alpha_h = 4g_3\alpha_p\alpha_h^* \tag{A.32}$$

which is exactly Eq. 4.43 from the RWA case of Sec. 4.7 if we make the parameter mapping

$$\epsilon_2 = 2g_3\alpha_p \tag{A.33}$$

$$\kappa_1 = \kappa \tag{A.34}$$

$$\tilde{\Delta} = \Delta_{\text{DPA}} + i\kappa_1/2$$

$$= \omega_p/2 - \omega_a - \left(\frac{32}{3}g_4 - 28\frac{g_3^2}{\omega_a} \right) n_p + i\kappa_1/2 \tag{A.35}$$

$$\tilde{K} = -6g_4^* \tag{A.36}$$

Thus, the solution to second order on harmonic balance can be mapped *exactly* to the RWA solution, but with a renormalized parameters. Specifically, the squeezing strength ϵ_2 is renormalized; the prefactor is now 2 instead of 3 from naïve combinatorics within the RWA. And the detuning Δ_{DPA} is now parametrically dependent on the pump power and thus Δ depends linearly on $|\epsilon_2|^2$ and the multi-stability diagram of Fig. 4.4 bends quadratically to the left (assuming the standard case of negative anharmonicity) [Wustmann and Shumeiko 2013; Sivak et al. 2019].

Two photon loss from pump depletion

Although two-photon loss does not appear (i. e. $\tilde{K}$ is found to be real and thus $\kappa_2 = 0$), there is a straightforward way to alter the SPA model to find an emergent two-photon loss. In fact, the necessary addition is none other that the standard model for *pump depletion* [Roy and Devoret 2018].

To see this, consider the way two-photon loss κ_2 has thus far been engineered [Mirrahimi et al. 2014; Leghtas et al. 2015; Touzard et al. 2018; Lescanne et al. 2020]. A nonlinear auxiliary mode with annihilation operator $\boldsymbol{b}$ at frequency ω_b and single-photon loss κ_b is driven at frequency $\omega_p - \omega_b \approx 2\omega_a - \omega_b$ to generate the effective interaction Hamiltonian

$$\mathcal{H}_{\text{int}}/\hbar = g\boldsymbol{a}^2\boldsymbol{b}^\dagger + \text{H.c.} \tag{A.37}$$

where g is proportional to the drive amplitude and the effective cross-four-wave-mixing nonlinearity. Within the RWA and assuming $g \ll \kappa_b$ so that the b mode may be adiabatically eliminated, we write the QLE for $\boldsymbol{b}$ and find the steady state amplitude as $\beta = -i2g\alpha_h^2/\kappa_b$. The new harmonic balance equation for α_h is

$$\left(\Delta_{\text{DPA}} - (12g_4^* - i4|g|^2/\kappa_b)|\alpha_h|^2 + i\kappa/2 \right) \alpha_h = 4g_3\alpha_p\alpha_h^* \tag{A.38}$$

which affords the same parameter mapping except with $\tilde{K} = -6g_4^* + i\kappa_2/2$ and $\kappa_2 = 4|g|^2/\kappa_b$. Thus, this induces an effective two–photon dissipation of with strength κ_2 in accordance with the RWA model of stabilized cat qubits in Chapter 4.

To connect with the study of pump depletion in linear parametric amplifies, we notice the same interaction Eq. A.37 may be generated without an additional drive if cross-three-wave couplings are available. Indeed, designing the auxiliary mode's frequency $\omega_b = \omega_p$ causes the interaction to be resonant and the resultant interaction strength $g \propto \varphi_{a,\text{zpf}}^2 \varphi_{b,\text{zpf}}$. This corresponds to the worst-case scenario for pump depletion in parametric amplifiers; the pump tone is resonant with the mode delivering the current to the inductive nonlinearity causing ϵ_2 and thus the gain to be more sensitive to incident signal photons. Interestingly, when $|\epsilon_2|^2 > |\tilde{\Delta}|^2$ in the bi-stable regime, this pump depletion mechanism actually further stabilizes the resultant cat-qubit. Contrary to below threshold for parametric amplification, intentionally increasing the pump depletion effect may be desirable in future implementations of Kerr-cat qubits to increase κ_2 with no added microwave drive tones.

B
Master equations and effective Hamiltonians

This chapter will explore the relationship between the stochastic master equations, Langevin equations and the quantum jump interpretation of evolution under an effective no-jump Hamiltonian that is interrupted by jumps. Rather than a complete description of each, we will simply define each case and point out salient references. The details given are intended not to be complete (since quantum optics textbooks [Gardiner and Zoller 2004; Haroche and Raimond 2006] are dedicated to this) but to aid our discussions in future sections of this this thesis. We will specify exclusively to single-oscillator systems. Each of these descriptions of open quantum systems has their merit and often different descriptions provide different intuition so it useful to understand common loss mechanisms from each of these perspectives.

B.1 Master equations in Lindblad form

The master equation describes the reduce density matrix of the system after tracing out the environment [Haroche and Raimond 2006]. Based on a Kraus sum formulation and the Markov approximation that the environment is memory-less—correlation time shorter than any relevant dynamics—the master equation in Lindblad form for the density matrix $\rho(t)$ of the system of interest is

$$\frac{d\boldsymbol{\rho}(t)}{dt} = -\frac{i}{\hbar}\left[\boldsymbol{\mathcal{H}}, \boldsymbol{\rho}(t)\right] + \sum_\mu \boldsymbol{\mathcal{D}}\left[\boldsymbol{L}_\mu\right]\boldsymbol{\rho}(t) \tag{B.1}$$

where the summation is over all jump operators $\boldsymbol{L}_\mu$ and the Lindblad superoperator $\boldsymbol{\mathcal{D}}\left[\boldsymbol{O}\right]$ for and arbitrary operator $\boldsymbol{O}$ is defined

$$\boldsymbol{\mathcal{D}}\left[\boldsymbol{O}\right]\boldsymbol{\rho} = \boldsymbol{O}\boldsymbol{\rho}\boldsymbol{O}^\dagger - \frac{1}{2}\left(\boldsymbol{O}^\dagger\boldsymbol{O}\boldsymbol{\rho} + \boldsymbol{\rho}\boldsymbol{O}^\dagger\boldsymbol{O}\right) \tag{B.2}$$

which has two types of terms: The first term is the jump term responsible for evolution under application of the jump operator $\boldsymbol{O}$. The second set of terms is the no-jump evolution that originates from the environment witnessing no jumps; this information that no jumps have occurred necessarily updates the density matrix through renormalization insisting that the density matrix has $\operatorname{Tr}\boldsymbol{\rho} = 1$.

To cast this more explicitly, we can write the master equation (B.1) in the form

$$\frac{d\boldsymbol{\rho}}{dt} = -\frac{i}{\hbar}\left(\boldsymbol{\mathcal{H}}_{\text{eff}}\boldsymbol{\rho} - \boldsymbol{\rho}\boldsymbol{\mathcal{H}}_{\text{eff}}^\dagger\right) + \sum_\mu \boldsymbol{L}_\mu\boldsymbol{\rho}\boldsymbol{L}_\mu^\dagger \tag{B.3}$$

where we have defined an effective non-Hermitian Hamiltonian

$$\boldsymbol{\mathcal{H}}_{\text{eff}} = \boldsymbol{\mathcal{H}} - i\frac{\hbar}{2}\sum_\mu \boldsymbol{L}_\mu^\dagger \boldsymbol{L}_\mu \tag{B.4}$$

that generates the no-jump evolution of the density matrix. $\boldsymbol{\mathcal{H}}_{\text{eff}}$ is diagonalizable, which follows from $\left[\boldsymbol{\mathcal{H}}_{\text{eff}}, \boldsymbol{\mathcal{H}}_{\text{eff}}^\dagger\right] = 0$, but the eigenvalues are in general complex in contrast to its Hermitian counterpart $\boldsymbol{\mathcal{H}}$. In the context of storing and manipulating quantum information, it is often convenient to analyze the jump-evolution separately as these jumps could, for instance, correspond to errors. The eigenstates of $\boldsymbol{\mathcal{H}}_{\text{eff}}$ are a convenient basis for this analysis. Specifically, we will often design an $\boldsymbol{\mathcal{H}}_{\text{eff}}$ to accomplish a specific task (e.g. stabilize a Bloch sphere or enact a desired operation) and then subsequently ask how jumps will change the outcome or cause errors.

B.2 Wigner function evolution

Density matrices of an oscillator can always be mapped to Wigner functions or characteristic functions; so density matrix evolution can also be similarly mapped. These phase-space representations of density matrices preserve the natural locality that is often lost when looking at a general density matrix. Moreover, evolution is phase space is particularly convenient when comparing evolution to the classical behavior of a similar system and isolating the salient features of the dynamics that rely on quantum-beyond-classical mechanics [Zurek 2003].

B.2.1 Definitions

Following [Haroche and Raimond 2006], we define the symmetric order characteristic function

$$C_{\text{s}}^{[\rho]}(\lambda) = \left\langle \boldsymbol{D}(\lambda)\right\rangle = \text{Tr}\left[\boldsymbol{\rho}e^{\lambda a^\dagger - \lambda^* a}\right] \tag{B.5}$$

where the superscript allows for the generalization to $C_{\text{s}}^{[O]}(\lambda)$ for an general operator $\boldsymbol{O}$ by replacing $\boldsymbol{O}$ on the right hand side. We will often suppress the superscript when using the density matrix such that $C_{\text{s}}(\lambda) = C_{\text{s}}^{[\rho]}(\lambda)$.

The Wigner function is the 2D Fourier transform of $C_{\text{s}}(\lambda)$ defined

$$W(\alpha) = \frac{1}{\pi^2}\int d^2\lambda\, C_{\text{s}}(\lambda)e^{\alpha\lambda^* - \alpha^*\lambda} \tag{B.6}$$

$$= \frac{2}{\pi}\text{Tr}\left[\boldsymbol{D}(-\alpha)\boldsymbol{\rho}\boldsymbol{D}(\alpha)\boldsymbol{\mathcal{P}}\right] \tag{B.7}$$

where the second line we have used the equivalent representation as the average value of parity $\boldsymbol{\mathcal{P}} = e^{i\pi a^\dagger a}$ of the displaced density matrix. A similar generalization via a Fourier transform of the above defines $W^{[O]}(\alpha)$ with $W(\alpha) = W^{[\rho]}(\alpha)$. Both the Wigner function

and the symmetric order characteristic function are complete representations of the density matrix $\rho(t)$ and so we are free to translate between them at will. Visualizing dynamics in the space of Wigner functions will be a particularly useful tool.

For completeness and ease of some calculations, we also define the normal- and anti-normal-order characteristic functions

$$C_n^{[\rho]}(\lambda) = \text{Tr}\left[\rho e^{\lambda a^\dagger} e^{-\lambda^* a}\right] \tag{B.8}$$

$$C_{an}^{[\rho]}(\lambda) = \text{Tr}\left[\rho e^{-\lambda^* a} e^{\lambda a^\dagger}\right] \tag{B.9}$$

which are related to the symmetric order characteristic function via

$$C_n^{[\rho]}(\lambda) = e^{|\lambda|^2/2} C_s^{[\rho]}(\lambda) \tag{B.10}$$

$$C_{an}^{[\rho]}(\lambda) = e^{-|\lambda|^2/2} C_s^{[\rho]}(\lambda) \tag{B.11}$$

The Husimi-Q distribution is similarly defined as the Fourier transform of the anti-normal-order characteristic function

$$Q^{[\rho]}(\alpha) = \frac{1}{\pi^2} \int d^2\lambda\, C_{an}(\lambda) e^{\alpha\lambda^* - \alpha^*\lambda} \tag{B.12}$$

$$= \frac{1}{\pi} \langle 0| \, D(-\alpha)\rho D(\alpha) \, |0\rangle \tag{B.13}$$

which, in the second line, we express as the overlap with the vacuum, commonly experimentally reconstructed through histograms of heterodyne-detected signals.

B.2.2 Fokker-Planck equations

In general can view loss as a diffusive process in phase space [Zurek 2003]. To see this, we will focus on the evolution of the Wigner function. If we have the general master equation (B.1), we can derive a differential equation for the dynamics of the Wigner function

$$\frac{dW^{[\rho]}}{dt} = -\frac{i}{\hbar}\left(W^{[\mathcal{H}\rho]} - W^{[\rho\mathcal{H}]}\right) + \frac{1}{2}\sum_\mu\left(2W^{[L_\mu\rho L_\mu^\dagger]} - W^{[L_\mu^\dagger L_\mu\rho]} - W^{[\rho L_\mu^\dagger L_\mu]}\right) \tag{B.14}$$

$$= -\frac{i}{\hbar}\left(W^{[\mathcal{H}_{\text{eff}}\rho]} - W^{[\rho\mathcal{H}_{\text{eff}}^\dagger]}\right) + \sum_\mu W^{[L_\mu\rho L_\mu^\dagger]} \tag{B.15}$$

which is still has a quite general form. To reduce the right hand side to only a function of $W^{[\rho]}$, we need the correspondence rules

$$W^{[Oa^\dagger]} = \left(\alpha^* + \frac{1}{2} \frac{\partial}{\partial \alpha} \right) W^{[O]} \tag{B.16}$$

$$W^{[a^\dagger O]} = \left(\alpha^* - \frac{1}{2} \frac{\partial}{\partial \alpha} \right) W^{[O]} \tag{B.17}$$

$$W^{[Oa]} = \left(\alpha - \frac{1}{2} \frac{\partial}{\partial \alpha^*} \right) W^{[O]} \tag{B.18}$$

$$W^{[aO]} = \left(\alpha + \frac{1}{2} \frac{\partial}{\partial \alpha^*} \right) W^{[O]} \tag{B.19}$$

where α and α^* are treated as independent variables for differentiation. Given that any operator in the Hilbert space of a single oscillator can always be expressed as a function of a and $a^\dagger$, the above relations are sufficient to reduce the dynamics to a differential equation for $W^{[\rho]}(\alpha, \alpha^*, t)$.

B.3 Some common dissipators

Here, we list some common dissipators of oscillators in superconducting circuits. We will derive the effective no-jump Hamiltonian for each example, and show that the no-jump evolution from all of these jump operators was indeed included in the model of two-legged cat state stabilization in Chapter 4.

B.3.1 One-photon loss

Single-photon loss comes from the environment coupling to the photon annihilation operator operator a with a given weight. This can be expressed succinctly with a single jump operator $L = \sqrt{\kappa_1} a$, leaving the master equation

$$\frac{d\rho}{dt} = \kappa_1 \mathcal{D}[a] \rho \tag{B.20}$$

which can be expressed via the effective Hamiltonian term $-i\frac{\kappa_1}{2} a^\dagger a$.

The differential equation of the Fokker-Plank type for the Wigner function is

$$\frac{d}{dt} W^{[\rho]}(\alpha, \alpha^*, t) = \frac{\kappa_1}{2} \left(\frac{\partial^2}{\partial \alpha \partial \alpha^*} + \frac{\partial}{\partial \alpha} \alpha + \frac{\partial}{\partial \alpha^*} \alpha^* \right) W^{[\rho]}(\alpha, \alpha^*, t) \tag{B.21}$$

where the second two terms represent a drift toward the origin $\alpha = \alpha^* = 0$ at rate $\kappa_1/2$ and the first term maintains the quantum fluctuations, preventing the Wigner function from collapsing to delta function. Instead, the steady state can be shown to be the vacuum $W^{[|0\rangle\langle 0|]}(\alpha) = \frac{2}{\pi} e^{-2|\alpha|^2}$.

B.3.2 One-photon gain and loss

Environments are not always cold and may be characterized as a black-body with a given temperature that sets a certain thermal population n_{th} equilibrium. To model this, we include single photon gain as well as loss to get the master equation

$$\frac{d\boldsymbol{\rho}}{dt} = (n_{\text{th}} + 1)\kappa_1 \boldsymbol{\mathcal{D}}\left[\boldsymbol{a}\right]\boldsymbol{\rho} + n_{\text{th}}\kappa_1 \boldsymbol{\mathcal{D}}\left[\boldsymbol{a}^\dagger\right]\boldsymbol{\rho} \tag{B.22}$$

which leads to the effective Hamiltonian term

$$-i(2n_{\text{th}} + 1)\kappa_1 \boldsymbol{a}^\dagger \boldsymbol{a}/2. \tag{B.23}$$

B.3.3 Two-photon loss

A two-photon loss corresponds to the Jump operator $\boldsymbol{L} = \sqrt{\kappa_2}\boldsymbol{a}^2$ that promises to take away two photons at a time, never one. The master equation with just this dissipation takes the form

$$\frac{d\boldsymbol{\rho}}{dt} = \kappa_2 \boldsymbol{\mathcal{D}}\left[\boldsymbol{a}^2\right]\boldsymbol{\rho} \tag{B.24}$$

which can be expressed via the effective Hamiltonian term

$$-i\frac{\kappa_2}{2}\boldsymbol{a}^{\dagger 2}\boldsymbol{a}^2 \tag{B.25}$$

or an imaginary Kerr nonlinearity.

B.3.4 Dephasing

Oscillators do not always keep the same frequency. Frequencies can drift slowly over time, and jumps in other coupled-modes can also cause jumps in oscillator frequency. Slow drifts over time—such as due to flux noise that whose spectrum is peaked at low frequencies—may be modelled as Hamiltonian evolution under Hamiltonian term $\delta \boldsymbol{a}^\dagger a h$ where delta is sampled every experimental shot from a distribution.

Heating events in other coupled modes with a cross-Kerr to the oscillator of interest, as well as the higher frequency components of flux noise, may be modeled by the effective white-noise-dephasing model with the jump operator $\boldsymbol{L} = \sqrt{\kappa_\phi}\boldsymbol{a}^\dagger \boldsymbol{a}$. The effective no-jump Hamiltonian due to this jump operator would be

$$-i\frac{\kappa_\phi}{2}(\boldsymbol{a}^\dagger \boldsymbol{a})^2 = -i\frac{\kappa_\phi}{2}(\boldsymbol{a}^\dagger \boldsymbol{a} + \boldsymbol{a}^{\dagger 2}\boldsymbol{a}^2) \tag{B.26}$$

which is an imaginary detuning term and Kerr term once normal ordered.

References

Abdo, B., A. Kamal, and M. Devoret, "Nondegenerate three-wave mixing with the Josephson ring modulator", Physical Review B **87**, 014508 (2013).

Abdo, B., K. Sliwa, L. Frunzio, and M. Devoret, "Directional Amplification with a Josephson Circuit", Physical Review X **3**, 031001 (2013).

Abdo, B., K. Sliwa, F. Schackert, N. Bergeal, M. Hatridge, L. Frunzio, A. D. Stone, and M. Devoret, "Full Coherent Frequency Conversion between Two Propagating Microwave Modes", Physical Review Letters **110**, 173902 (2013).

Albert, V. V., K. Noh, K. Duivenvoorden, D. J. Young, R. T. Brierley, P. Reinhold, C. Vuillot, L. Li, C. Shen, S. M. Girvin, B. M. Terhal, and L. Jiang, "Performance and structure of single-mode bosonic codes", Physical Review A **97**, Publisher: American Physical Society, 032346 (2018).

Aliferis, P. and J. Preskill, "Fault-tolerant quantum computation against biased noise", Physical Review A **78**, 052331 (2008).

Allman, M. S., J. D. Whittaker, M. Castellanos-Beltran, K. Cicak, F. da Silva, M. P. DeFeo, F. Lecocq, A. Sirois, J. D. Teufel, J. Aumentado, and R. W. Simmonds, "Tunable Resonant and Nonresonant Interactions between a Phase Qubit and LC Resonator", Physical Review Letters **112**, 123601 (2014).

Altland, A. and B. D. Simons, *Condensed Matter Field Theory* (Cambridge University Press, Cambridge, 2010).

Andersen, C. K., A. Remm, S. Lazar, S. Krinner, N. Lacroix, G. J. Norris, M. Gabureac, C. Eichler, and A. Wallraff, "Repeated quantum error detection in a surface code", en, Nature Physics **16**, Bandiera_abtest: a Cg_type: Nature Research Journals Number: 8 Primary_atype: Research Publisher: Nature Publishing Group Subject_term: Quantum information;Qubits Subject_term_id: quantum-information;qubits, 875–880 (2020).

Aspelmeyer, M., T. J. Kippenberg, and F. Marquardt, "Cavity optomechanics", Reviews of Modern Physics **86**, Publisher: American Physical Society, 1391–1452 (2014).

Aumentado, J., "Superconducting Parametric Amplifiers: The State of the Art in Josephson Parametric Amplifiers", IEEE Microwave Magazine **21**, Conference Name: IEEE Microwave Magazine, 45–59 (2020).

Axline, C., M. Reagor, R. Heeres, P. Reinhold, C. Wang, K. Shain, W. Pfaff, Y. Chu, L. Frunzio, and R. J. Schoelkopf, "An architecture for integrating planar and 3D cQED devices", Applied Physics Letters **109**, 042601 (2016).

Axline, C. J., L. D. Burkhart, W. Pfaff, M. Zhang, K. Chou, P. Campagne-Ibarcq, P. Reinhold, L. Frunzio, S. M. Girvin, L. Jiang, M. H. Devoret, and R. J. Schoelkopf, "On-demand quantum state transfer and entanglement between remote microwave cavity memories", en, Nature Physics, 1 (2018).

Backes, K. M., D. A. Palken, S. A. Kenany, B. M. Brubaker, S. B. Cahn, A. Droster, G. C. Hilton, S. Ghosh, H. Jackson, S. K. Lamoreaux, A. F. Leder, K. W. Lehnert, S. M. Lewis, M. Malnou, R. H. Maruyama, N. M. Rapidis, M. Simanovskaia, S. Singh, D. H. Speller, I. Urdinaran, L. R. Vale, E. C. van Assendelft, K. van Bibber, and H. Wang, "A quantum enhanced search for dark matter axions", en, Nature **590**, Bandiera_abtest: a Cg_type: Nature Research Journals Number: 7845 Primary_atype: Research Publisher: Nature Publishing Group Subject_term: Dark energy and dark matter;Experimental particle physics;Quantum metrology Subject_term_id: dark-energy-and-dark-matter;experimental-particle-physics;quantum-metrology, 238–242 (2021).

Bartolo, N., F. Minganti, W. Casteels, and C. Ciuti, "Exact steady state of a Kerr resonator with one- and two-photon driving and dissipation: Controllable Wigner-function multimodality and dissipative phase transitions", Physical Review A **94**, 033841 (2016).

Bergeal, N., F. Schackert, M. Metcalfe, R. Vijay, V. E. Manucharyan, L. Frunzio, D. E. Prober, R. J. Schoelkopf, S. M. Girvin, and M. H. Devoret, "Phase-preserving amplification near the quantum limit with a Josephson ring modulator", en, Nature **465**, 64–68 (2010).

Bergeal, N., R. Vijay, V. E. Manucharyan, I. Siddiqi, R. J. Schoelkopf, S. M. Girvin, and M. H. Devoret, "Analog information processing at the quantum limit with a Josephson ring modulator", en, Nature Physics **6**, 296–302 (2010).

Bienfait, A., P. Campagne-Ibarcq, A. H. Kiilerich, X. Zhou, S. Probst, J. J. Pla, T. Schenkel, D. Vion, D. Esteve, J. J. L. Morton, K. Moelmer, and P. Bertet, "Magnetic Resonance with Squeezed Microwaves", Physical Review X **7**, 041011 (2017).

Bienfait, A., J. J. Pla, Y. Kubo, M. Stern, X. Zhou, C. C. Lo, C. D. Weis, T. Schenkel, M. L. W. Thewalt, D. Vion, D. Esteve, B. Julsgaard, K. Mølmer, J. J. L. Morton, and P. Bertet, "Reaching the quantum limit of sensitivity in electron spin resonance", en, Nature Nanotechnology **11**, 253–257 (2016).

Blackwell, L. A. and K. L. Kotzebue, *Semicondcuctor-Diode Parametric Amplifiers* (Prentice Hall, Englewood Cliffs, NJ, 1961).

Blais, A., A. L. Grimsmo, S. M. Girvin, and A. Wallraff, "Circuit quantum electrodynamics", Reviews of Modern Physics **93**, Publisher: American Physical Society, 025005 (2021).

Blais, A., R.-S. Huang, A. Wallraff, S. M. Girvin, and R. J. Schoelkopf, "Cavity quantum electrodynamics for superconducting electrical circuits: An architecture for quantum computation", Physical Review A **69**, Publisher: American Physical Society, 062320 (2004).

Bonilla Ataides, J. P., D. K. Tuckett, S. D. Bartlett, S. T. Flammia, and B. J. Brown, "The XZZX surface code", en, Nature Communications **12**, 2172 (2021).

Bourassa, J., F. Beaudoin, J. M. Gambetta, and A. Blais, "Josephson-junction-embedded transmission-line resonators: From Kerr medium to in-line transmon", Physical Review A **86**, Publisher: American Physical Society, 013814 (2012).

Boutin, S., D. M. Toyli, A. V. Venkatramani, A. W. Eddins, I. Siddiqi, and A. Blais, "Effect of Higher-Order Nonlinearities on Amplification and Squeezing in Josephson Parametric Amplifiers", Physical Review Applied **8**, 054030 (2017).

Boyd, R. W., *Nonlinear Optics*, 3rd ed. (Elsevier Inc., 2008).

Brubaker, B. M., L. Zhong, Y. V. Gurevich, S. B. Cahn, S. K. Lamoreaux, M. Simanovskaia, J. R. Root, S. M. Lewis, S. Al Kenany, K. M. Backes, I. Urdinaran, N. M. Rapidis, T. M. Shokair, K. A. van Bibber, D. A. Palken, M. Malnou, W. F. Kindel, M. A. Anil, K. W. Lehnert, and G. Carosi, "First Results from a Microwave Cavity Axion Search at $24\text{ }\text{ }\ensuremath{\mu}\mathrm{eV}$", Physical Review Letters **118**, 061302 (2017).

Bultink, C. C., B. Tarasinski, N. Haandbæk, S. Poletto, N. Haider, D. J. Michalak, A. Bruno, and L. DiCarlo, "General method for extracting the quantum efficiency of dispersive qubit readout in circuit QED", Applied Physics Letters **112**, 092601 (2018).

Burkhart, L. D., J. D. Teoh, Y. Zhang, C. J. Axline, L. Frunzio, M. Devoret, L. Jiang, S. Girvin, and R. Schoelkopf, "Error-Detected State Transfer and Entanglement in a Superconducting Quantum Network", PRX Quantum **2**, Publisher: American Physical Society, 030321 (2021).

Caldeira, A. O. and A. J. Leggett, "Quantum tunnelling in a dissipative system", en, Annals of Physics **149**, 374–456 (1983).

Campagne-Ibarcq, P., A. Eickbusch, S. Touzard, E. Zalys-Geller, N. E. Frattini, V. V. Sivak, P. Reinhold, S. Puri, S. Shankar, R. J. Schoelkopf, L. Frunzio, M. Mirrahimi, and M. H. Devoret, "Quantum error correction of a qubit encoded in grid states of an oscillator", en, Nature **584**, Number: 7821 Publisher: Nature Publishing Group, 368–372 (2020).

Campagne-Ibarcq, P., P. Six, L. Bretheau, A. Sarlette, M. Mirrahimi, P. Rouchon, and B. Huard, "Observing Quantum State Diffusion by Heterodyne Detection of Fluorescence", Physical Review X **6**, 011002 (2016).

Campagne-Ibarcq, P., E. Zalys-Geller, A. Narla, S. Shankar, P. Reinhold, L. Burkhart, C. Axline, W. Pfaff, L. Frunzio, R. J. Schoelkopf, and M. H. Devoret, "Deterministic Remote Entanglement of Superconducting Circuits through Microwave Two-Photon Transitions", Physical Review Letters **120**, 200501 (2018).

Castellanos-Beltran, M. A., K. D. Irwin, G. C. Hilton, L. R. Vale, and K. W. Lehnert, "Amplification and squeezing of quantum noise with a tunable Josephson metamaterial", en, Nature Physics **4**, 929–931 (2008).

Caves, C. M., "Quantum limits on noise in linear amplifiers", Physical Review D **26**, Publisher: American Physical Society, 1817–1839 (1982).

Caves, C. M., J. Combes, Z. Jiang, and S. Pandey, "Quantum limits on phase-preserving linear amplifiers", Physical Review A **86**, Publisher: American Physical Society, 063802 (2012).

Chapman, B. J., E. I. Rosenthal, J. Kerckhoff, B. A. Moores, L. R. Vale, J. A. B. Mates, G. C. Hilton, K. Lalumière, A. Blais, and K. W. Lehnert, "Widely Tunable On-Chip Microwave Circulator for Superconducting Quantum Circuits", Physical Review X **7**, 041043 (2017).

Chen, Z., J. Kelly, C. Quintana, R. Barends, B. Campbell, Y. Chen, B. Chiaro, A. Dunsworth, A. G. Fowler, E. Lucero, E. Jeffrey, A. Megrant, J. Mutus, M. Neeley, C. Neill, P. J. J. O'Malley, P. Roushan, D. Sank, A. Vainsencher, J. Wenner, T. C. White, A. N. Korotkov, and J. M. Martinis, "Measuring and Suppressing Quantum State Leakage in a Super-conducting Qubit", Physical Review Letters **116**, Publisher: American Physical Society, 020501 (2016).

Chen, Z., K. J. Satzinger, J. Atalaya, A. N. Korotkov, A. Dunsworth, D. Sank, C. Quintana, M. McEwen, R. Barends, P. V. Klimov, S. Hong, C. Jones, A. Petukhov, D. Kafri, S. Demura, B. Burkett, C. Gidney, A. G. Fowler, A. Paler, H. Putterman, I. Aleiner, F. Arute, K. Arya, R. Babbush, J. C. Bardin, A. Bengtsson, A. Bourassa, M. Broughton, B. B. Buckley, D. A. Buell, N. Bushnell, B. Chiaro, R. Collins, W. Courtney, A. R. Derk, D. Eppens, C. Erickson, E. Farhi, B. Foxen, M. Giustina, A. Greene, J. A. Gross, M. P. Harrigan, S. D. Harrington, J. Hilton, A. Ho, T. Huang, W. J. Huggins, L. B. Ioffe, S. V. Isakov, E. Jeffrey, Z. Jiang, K. Kechedzhi, S. Kim, A. Kitaev, F. Kostritsa, D. Landhuis, P. Laptev, E. Lucero, O. Martin, J. R. McClean, T. McCourt, X. Mi, K. C. Miao, M. Mohseni, S. Montazeri, W. Mruczkiewicz, J. Mutus, O. Naaman, M. Neeley, C. Neill, M. Newman, M. Y. Niu, T. E. O'Brien, A. Opremcak, E. Ostby, B. Pató, N. Redd, P. Roushan, N. C. Rubin, V. Shvarts, D. Strain, M. Szalay, M. D. Trevithick, B. Villalonga, T. White, Z. J. Yao, P. Yeh, J. Yoo, A. Zalcman, H. Neven, S. Boixo, V. Smelyanskiy, Y. Chen, A. Megrant, J. Kelly, and Google Quantum AI, "Exponential suppression of bit or phase errors with cyclic error correction", en, Nature **595**, 383–387 (2021).

Chien, T.-C., O. Lanes, C. Liu, X. Cao, P. Lu, S. Motz, G. Liu, D. Pekker, and M. Hatridge, "Multiparametric amplification and qubit measurement with a Kerr-free Josephson ring modulator", Physical Review A **101**, Publisher: American Physical Society, 042336 (2020).

Chow, J. M., L. DiCarlo, J. M. Gambetta, F. Motzoi, L. Frunzio, S. M. Girvin, and R. J. Schoelkopf, "Optimized driving of superconducting artificial atoms for improved single-qubit gates", Physical Review A **82**, Publisher: American Physical Society, 040305 (2010).

Chow, J. M., J. M. Gambetta, A. D. Córcoles, S. T. Merkel, J. A. Smolin, C. Rigetti, S. Poletto, G. A. Keefe, M. B. Rothwell, J. R. Rozen, M. B. Ketchen, and M. Steffen, "Universal Quan-

tum Gate Set Approaching Fault-Tolerant Thresholds with Superconducting Qubits", Physical Review Letters **109**, 060501 (2012).

Clarke, J., "A superconducting galvanometer employing Josephson tunnelling", Philosophical Magazine **13**, 115–127 (1966).

J. Clarke and A. I. Braginski, eds., *The SQUID Handbook*, Vol. 1 (Wiley, Weinheim, 2004).

Clerk, A. A., M. H. Devoret, S. M. Girvin, F. Marquardt, and R. J. Schoelkopf, "Introduction to Quantum Noise, Measurement and Amplification", Reviews of Modern Physics **82**, arXiv: 0810.4729, 1155–1208 (2010).

Cochrane, P. T., G. J. Milburn, and W. J. Munro, "Macroscopically distinct quantumsuperposition states as a bosonic code for amplitude damping", Physical Review A **59**, 2631–2634 (1999).

Cottet, A., Z. Leghtas, and T. Kontos, "Theory of interactions between cavity photons induced by a mesoscopic circuit", Physical Review B **102**, Publisher: American Physical Society, 155105 (2020).

Darmawan, A. S., B. J. Brown, A. L. Grimsmo, D. K. Tuckett, and S. Puri, "Practical quantum error correction with the XZZX code and Kerr-cat qubits", arXiv:2104.09539 [quant-ph], arXiv: 2104.09539 (2021).

Dassonneville, R., T. Ramos, V. Milchakov, L. Planat, É. Dumur, F. Foroughi, J. Puertas, S. Leger, K. Bharadwaj, J. Delaforce, C. Naud, W. Hasch-Guichard, J. J. García-Ripoll, N. Roch, and O. Buisson, "Fast High-Fidelity Quantum Nondemolition Qubit Readout via a Nonperturbative Cross-Kerr Coupling", Physical Review X **10**, Publisher: American Physical Society, 011045 (2020).

Devoret, M. H. and R. J. Schoelkopf, "Superconducting Circuits for Quantum Information: An Outlook", EN, Science, Publisher: American Association for the Advancement of Science (2013).

Devoret, M. H., "Does Brian Josephson's Gauge-Invariant Phase Difference Live on a Line or a Circle?", en, Journal of Superconductivity and Novel Magnetism (2021).

Didier, N., J. Bourassa, and A. Blais, "Fast Quantum Nondemolition Readout by Parametric Modulation of Longitudinal Qubit-Oscillator Interaction", Physical Review Letters **115**, Publisher: American Physical Society, 203601 (2015).

Didier, N., E. A. Sete, J. Combes, and M. P. da Silva, "Ac Flux Sweet Spots in Parametrically Modulated Superconducting Qubits", Physical Review Applied **12**, Publisher: American Physical Society, 054015 (2019).

Dolan, G. J., "Offset masks for lift-off photoprocessing", Applied Physics Letters **31**, Publisher: American Institute of Physics, 337–339 (1977).

Dykman, M. I., C. Bruder, N. Lörch, and Y. Zhang, "Interaction-induced time-symmetry breaking in driven quantum oscillators", Physical Review B **98**, Publisher: American Physical Society, 195444 (2018).

Dykman, M. I., C. M. Maloney, V. N. Smelyanskiy, and M. Silverstein, "Fluctuational phase-flip transitions in parametrically driven oscillators", Physical Review E **57**, 5202–5212 (1998).

Earnest, N., S. Chakram, Y. Lu, N. Irons, R. K. Naik, N. Leung, L. Ocola, D. A. Czaplewski, B. Baker, J. Lawrence, J. Koch, and D. I. Schuster, "Realization of a $\mathrm{\ensuremath{\Lambda}}$ System with Metastable States of a Capacitively Shunted Fluxonium", Physical Review Letters **120**, Publisher: American Physical Society, 150504 (2018).

Eddins, A., S. Schreppler, D. M. Toyli, L. S. Martin, S. Hacohen-Gourgy, L. C. G. Govia, H. Ribeiro, A. A. Clerk, and I. Siddiqi, "Stroboscopic Qubit Measurement with Squeezed Illumination", Physical Review Letters **120**, Publisher: American Physical Society, 040505 (2018).

Eichler, C., Y. Salathe, J. Mlynek, S. Schmidt, and A. Wallraff, "Quantum-Limited Amplification and Entanglement in Coupled Nonlinear Resonators", Physical Review Letters **113**, 110502 (2014).

Eichler, C. and A. Wallraff, "Controlling the dynamic range of a Josephson parametric amplifier", En, EPJ Quantum Technology **1**, 2 (2014).

Esposito, M., A. Ranadive, L. Planat, and N. Roch, "Perspective on traveling wave microwave parametric amplifiers", arXiv:2107.13033 [cond-mat, physics:quant-ph], arXiv: 2107.13033 (2021).

Flurin, E., N. Roch, J. D. Pillet, F. Mallet, and B. Huard, "Superconducting Quantum Node for Entanglement and Storage of Microwave Radiation", Physical Review Letters **114**, 090503 (2015).

Flurin, E., "The Josephson Mixer: A swiss army knife for microwave quantum optics", PhD thesis (École Normale Supérieure, 2015).

Fowler, A. G., M. Mariantoni, J. M. Martinis, and A. N. Cleland, "Surface codes: Towards practical large-scale quantum computation", Physical Review A **86**, 032324 (2012).

Frattini, N. E., V. V. Sivak, A. Lingenfelter, S. Shankar, and M. H. Devoret, "Optimizing the Nonlinearity and Dissipation of a SNAIL Parametric Amplifier for Dynamic Range", Physical Review Applied **10**, 054020 (2018).

Frattini, N. E., U. Vool, S. Shankar, A. Narla, K. M. Sliwa, and M. H. Devoret, "3-wave mixing Josephson dipole element", Applied Physics Letters **110**, 222603 (2017).

Gambetta, J., W. A. Braff, A. Wallraff, S. M. Girvin, and R. J. Schoelkopf, "Protocols for optimal readout of qubits using a continuous quantum nondemolition measurement", Physical Review A **76**, 012325 (2007).

Gao, Y. Y., B. J. Lester, K. S. Chou, L. Frunzio, M. H. Devoret, L. Jiang, S. M. Girvin, and R. J. Schoelkopf, "Entanglement of bosonic modes through an engineered exchange interaction", en, Nature **566**, 509–512 (2019).

Gao, Y. Y., B. J. Lester, Y. Zhang, C. Wang, S. Rosenblum, L. Frunzio, L. Jiang, S. M. Girvin, and R. J. Schoelkopf, "Programmable Interference between Two Microwave Quantum Memories", Physical Review X **8**, Publisher: American Physical Society, 021073 (2018).

Gardiner, C. and P. Zoller, *Quantum Noise*, 3rd ed. (Springer-Verlag Berlin Heidelberg, 2004).

Geerlings, K., Z. Leghtas, I. M. Pop, S. Shankar, L. Frunzio, R. J. Schoelkopf, M. Mirrahimi, and M. H. Devoret, "Demonstrating a Driven Reset Protocol for a Superconducting Qubit", Physical Review Letters **110**, 120501 (2013).

Gertler, J. M., B. Baker, J. Li, S. Shirol, J. Koch, and C. Wang, "Protecting a bosonic qubit with autonomous quantum error correction", en, Nature **590**, 243–248 (2021).

Getsinger, W., "Prototypes for Use in Broadbanding Reflection Amplifiers", IEEE Transactions on Microwave Theory and Techniques **11**, Conference Name: IEEE Transactions on Microwave Theory and Techniques, 486–497 (1963).

Goto, H., "Bifurcation-based adiabatic quantum computation with a nonlinear oscillator network", en, Scientific Reports **6**, Bandiera_abtest: a Cc_license_type: cc_by Cg_type: Nature Research Journals Number: 1 Primary_atype: Research Publisher: Nature Publishing Group Subject_term: Computer science;Nonlinear phenomena;Quantum information;Superconducting devices Subject_term_id: computer-science;nonlinear-phenomena;quantum-information;superconducting-devices, 21686 (2016).

Goto, H., "Universal quantum computation with a nonlinear oscillator network", Physical Review A **93**, Publisher: American Physical Society, 050301 (2016).

Gottesman, D., "An Introduction to Quantum Error Correction and Fault-Tolerant Quantum Computation", arXiv:0904.2557 [quant-ph], arXiv: 0904.2557 (2009).

Gottesman, D., A. Kitaev, and J. Preskill, "Encoding a qubit in an oscillator", Physical Review A **64**, 012310 (2001).

Grimm, A., N. E. Frattini, S. Puri, S. O. Mundhada, S. Touzard, M. Mirrahimi, S. M. Girvin, S. Shankar, and M. H. Devoret, "Stabilization and operation of a Kerr-cat qubit", en, Nature **584**, Number: 7820 Publisher: Nature Publishing Group, 205–209 (2020).

Grimsmo, A. L. and S. Puri, "Quantum Error Correction with the Gottesman-Kitaev-Preskill Code", PRX Quantum **2**, Publisher: American Physical Society, 020101 (2021).

Guillaud, J. and M. Mirrahimi, "Repetition Cat Qubits for Fault-Tolerant Quantum Computation", Physical Review X **9**, 041053 (2019).

Gyenis, A., A. Di Paolo, J. Koch, A. Blais, A. A. Houck, and D. I. Schuster, "Moving beyond the Transmon: Noise-Protected Superconducting Quantum Circuits", PRX Quantum **2**, Publisher: American Physical Society, 030101 (2021).

Gyenis, A., P. S. Mundada, A. Di Paolo, T. M. Hazard, X. You, D. I. Schuster, J. Koch, A. Blais, and A. A. Houck, "Experimental Realization of a Protected Superconducting Circuit Derived from the 0–$\ensuremath{\pi}$ Qubit", PRX Quantum **2**, Publisher: American Physical Society, 010339 (2021).

Haroche, S. and J.-M. Raimond, *Exploring the Quntum: Atoms, Cavities, and Photons* (Oxford University Press, 2006).

Hatridge, M., S. Shankar, M. Mirrahimi, F. Schackert, K. Geerlings, T. Brecht, K. M. Sliwa, B. Abdo, L. Frunzio, S. M. Girvin, R. J. Schoelkopf, and M. H. Devoret, "Quantum Back-Action of an Individual Variable-Strength Measurement", en, Science **339**, 178–181 (2013).

Hatridge, M., R. Vijay, D. H. Slichter, J. Clarke, and I. Siddiqi, "Dispersive magnetometry with a quantum limited SQUID parametric amplifier", Physical Review B **83**, 134501 (2011).

Haus, H. A. and J. A. Mullen, "Quantum Noise in Linear Amplifiers", Physical Review **128**, Publisher: American Physical Society, 2407–2413 (1962).

Hover, D., Y.-F. Chen, G. J. Ribeill, S. Zhu, S. Sendelbach, and R. McDermott, "Superconducting low-inductance undulatory galvanometer microwave amplifier", Applied Physics Letters **100**, 063503 (2012).

Hu, L., Y. Ma, W. Cai, X. Mu, Y. Xu, W. Wang, Y. Wu, H. Wang, Y. P. Song, C.-L. Zou, S. M. Girvin, L.-M. Duan, and L. Sun, "Quantum error correction and universal gate set operation on a binomial bosonic logical qubit", en, Nature Physics **15**, 503–508 (2019).

Huang, Z., P. S. Mundada, A. Gyenis, D. I. Schuster, A. A. Houck, and J. Koch, "Engineering Dynamical Sweet Spots to Protect Qubits from $1/f$ Noise", Physical Review Applied **15**, Publisher: American Physical Society, 034065 (2021).

Ikonen, J., J. Goetz, J. Ilves, A. Keränen, A. M. Gunyho, M. Partanen, K. Y. Tan, D. Hazra, L. Grönberg, V. Vesterinen, S. Simbierowicz, J. Hassel, and M. Möttönen, "Qubit Measurement by Multichannel Driving", Physical Review Letters **122**, Publisher: American Physical Society, 080503 (2019).

Jeffrey, E., D. Sank, J. Y. Mutus, T. C. White, J. Kelly, R. Barends, Y. Chen, Z. Chen, B. Chiaro, A. Dunsworth, A. Megrant, P. J. J. O'Malley, C. Neill, P. Roushan, A. Vainsencher, J. Wenner, A. N. Cleland, and J. M. Martinis, "Fast Accurate State Measurement with Superconducting Qubits", Physical Review Letters **112**, 190504 (2014).

Johnson, J. E., C. Macklin, D. H. Slichter, R. Vijay, E. B. Weingarten, J. Clarke, and I. Siddiqi, "Heralded State Preparation in a Superconducting Qubit", Physical Review Letters **109**, 050506 (2012).

Kamal, A., A. Marblestone, and M. Devoret, "Signal-to-pump back action and self-oscillation in double-pump Josephson parametric amplifier", Physical Review B **79**, 184301 (2009).

Kelly, J., R. Barends, A. G. Fowler, A. Megrant, E. Jeffrey, T. C. White, D. Sank, J. Y. Mutus, B. Campbell, Y. Chen, Z. Chen, B. Chiaro, A. Dunsworth, I.-C. Hoi, C. Neill, P. J. J. O'Malley, C. Quintana, P. Roushan, A. Vainsencher, J. Wenner, A. N. Cleland, and J. M. Martinis, "State preservation by repetitive error detection in a superconducting quantum circuit", en, Nature **519**, 66–69 (2015).

Kirchmair, G., B. Vlastakis, Z. Leghtas, S. E. Nigg, H. Paik, E. Ginossar, M. Mirrahimi, L. Frunzio, S. M. Girvin, and R. J. Schoelkopf, "Observation of quantum state collapse and revival due to the single-photon Kerr effect", en, Nature **495**, 205–209 (2013).

Kitaev, A. Y., "Fault-tolerant quantum computation by anyons", en, Annals of Physics **303**, 2–30 (2003).

Koch, J., V. Manucharyan, M. H. Devoret, and L. I. Glazman, "Charging Effects in the Inductively Shunted Josephson Junction", Physical Review Letters **103**, 217004 (2009).

Koch, J., T. M. Yu, J. Gambetta, A. A. Houck, D. I. Schuster, J. Majer, A. Blais, M. H. Devoret, S. M. Girvin, and R. J. Schoelkopf, "Charge-insensitive qubit design derived from the Cooper pair box", Physical Review A **76**, 042319 (2007).

Krinner, S., S. Storz, P. Kurpiers, P. Magnard, J. Heinsoo, R. Keller, J. Lütolf, C. Eichler, and A. Wallraff, "Engineering cryogenic setups for 100-qubit scale superconducting circuit systems", en, EPJ Quantum Technology **6**, Number: 1 Publisher: SpringerOpen, 1–29 (2019).

Kurilovich, P. D., V. D. Kurilovich, V. Fatemi, M. H. Devoret, and L. I. Glazman, "Microwave response of an Andreev bound state", arXiv:2106.00028 [cond-mat], arXiv: 2106.00028 (2021).

Kurpiers, P., P. Magnard, T. Walter, B. Royer, M. Pechal, J. Heinsoo, Y. Salathé, A. Akin, S. Storz, J.-C. Besse, S. Gasparinetti, A. Blais, and A. Wallraff, "Deterministic quantum state transfer and remote entanglement using microwave photons", en, Nature **558**, 264–267 (2018).

Lecocq, F., L. Ranzani, G. A. Peterson, K. Cicak, X. Y. Jin, R. W. Simmonds, J. D. Teufel, and J. Aumentado, "Efficient Qubit Measurement with a Nonreciprocal Microwave Amplifier", Physical Review Letters **126**, Publisher: American Physical Society, 020502 (2021).

Lecocq, F., L. Ranzani, G. A. Peterson, K. Cicak, R. W. Simmonds, J. D. Teufel, and J. Aumentado, "Nonreciprocal Microwave Signal Processing with a Field-Programmable Josephson Amplifier", Physical Review Applied **7**, 024028 (2017).

Lecocq, F., I. M. Pop, Z. Peng, I. Matei, T. Crozes, T. Fournier, C. Naud, W. Guichard, and O. Buisson, "Junction fabrication by shadow evaporation without a suspended bridge", en, Nanotechnology **22**, Publisher: IOP Publishing, 315302 (2011).

Leghtas, Z., S. Touzard, I. M. Pop, A. Kou, B. Vlastakis, A. Petrenko, K. M. Sliwa, A. Narla, S. Shankar, M. J. Hatridge, M. Reagor, L. Frunzio, R. J. Schoelkopf, M. Mirrahimi, and M. H. Devoret, "Confining the state of light to a quantum manifold by engineered two-photon loss", en, Science **347**, 853–857 (2015).

Leghtas, Z., G. Kirchmair, B. Vlastakis, R. J. Schoelkopf, M. H. Devoret, and M. Mirrahimi, "Hardware-Efficient Autonomous Quantum Memory Protection", Physical Review Letters **111**, 120501 (2013).

Lescanne, R., L. Verney, Q. Ficheux, M. H. Devoret, B. Huard, M. Mirrahimi, and Z. Leghtas, "Escape of a Driven Quantum Josephson Circuit into Unconfined States", Physical Review Applied **11**, Publisher: American Physical Society, 014030 (2019).

Lescanne, R., M. Villiers, T. Peronnin, A. Sarlette, M. Delbecq, B. Huard, T. Kontos, M. Mirrahimi, and Z. Leghtas, "Exponential suppression of bit-flips in a qubit encoded in an oscillator", en, Nature Physics, Publisher: Nature Publishing Group, 1–5 (2020).

Liu, G., T.-C. Chien, X. Cao, O. Lanes, E. Alpern, D. Pekker, and M. Hatridge, "Josephson parametric converter saturation and higher order effects", Applied Physics Letters **111**, 202603 (2017).

Lutchyn, R. M., J. D. Sau, and S. Das Sarma, "Majorana Fermions and a Topological Phase Transition in Semiconductor-Superconductor Heterostructures", Physical Review Letters **105**, Publisher: American Physical Society, 077001 (2010).

Macklin, C., K. O'Brien, D. Hover, M. E. Schwartz, V. Bolkhovsky, X. Zhang, W. D. Oliver, and I. Siddiqi, "A near–quantum-limited Josephson traveling-wave parametric amplifier", en, Science **350**, 307–310 (2015).

Maleeva, N., L. Grünhaupt, T. Klein, F. Levy-Bertrand, O. Dupre, M. Calvo, F. Valenti, P. Winkel, F. Friedrich, W. Wernsdorfer, A. V. Ustinov, H. Rotzinger, A. Monfardini, M. V. Fistul, and I. M. Pop, "Circuit quantum electrodynamics of granular aluminum resonators", en, Nature Communications **9**, 3889 (2018).

Malnou, M., D. A. Palken, L. R. Vale, G. C. Hilton, and K. W. Lehnert, "Optimal Operation of a Josephson Parametric Amplifier for Vacuum Squeezing", Physical Review Applied **9**, Publisher: American Physical Society, 044023 (2018).

Manucharyan, V. E., "Superinductance", Ph.D. (Yale University, 2012).

Manucharyan, V. E., J. Koch, L. I. Glazman, and M. H. Devoret, "Fluxonium: Single Cooper-Pair Circuit Free of Charge Offsets", en, Science **326**, 113–116 (2009).

Marandi, A., Z. Wang, K. Takata, R. L. Byer, and Y. Yamamoto, "Network of time-multiplexed optical parametric oscillators as a coherent Ising machine", en, Nature Photonics **8**, Number: 12 Publisher: Nature Publishing Group, 937–942 (2014).

Marthaler, M. and M. I. Dykman, "Quantum interference in the classically forbidden region: A parametric oscillator", Physical Review A **76**, Publisher: American Physical Society, 010102 (2007).

Masluk, N. A., "Reducing the losses of the fluxonium artificial atom", Ph.D. (Yale University, 2012).

Masluk, N. A., I. M. Pop, A. Kamal, Z. K. Minev, and M. H. Devoret, "Microwave Characterization of Josephson Junction Arrays: Implementing a Low Loss Superinductance", Physical Review Letters **109**, 137002 (2012).

Matthaei, G. L., L. Young, and E. M. T. Jones, *Microwave Filters, Impedance-matching Networks, and Coupling Structures*, en (Artech House Books, 1980).

Matveev, K. A., A. I. Larkin, and L. I. Glazman, "Persistent Current in Superconducting Nanorings", Physical Review Letters **89**, 096802 (2002).

McEwen, M., D. Kafri, Z. Chen, J. Atalaya, K. J. Satzinger, C. Quintana, P. V. Klimov, D. Sank, C. Gidney, A. G. Fowler, F. Arute, K. Arya, B. Buckley, B. Burkett, N. Bushnell, B. Chiaro, R. Collins, S. Demura, A. Dunsworth, C. Erickson, B. Foxen, M. Giustina, T. Huang, S. Hong, E. Jeffrey, S. Kim, K. Kechedzhi, F. Kostritsa, P. Laptev, A. Megrant, X. Mi, J. Mutus, O. Naaman, M. Neeley, C. Neill, M. Niu, A. Paler, N. Redd, P. Roushan, T. C. White, J. Yao, P. Yeh, A. Zalcman, Y. Chen, V. N. Smelyanskiy, J. M. Martinis, H. Neven, J. Kelly, A. N. Korotkov, A. G. Petukhov, and R. Barends, "Removing leakage-induced correlated errors in superconducting quantum error correction", en, Nature Communications **12**, 1761 (2021).

Metelmann, A. and A. A. Clerk, "Nonreciprocal Photon Transmission and Amplification via Reservoir Engineering", Physical Review X **5**, 021025 (2015).

Metelmann, A. and A. A. Clerk, "Quantum-Limited Amplification via Reservoir Engineering", Physical Review Letters **112**, 133904 (2014).

Michael, M. H., M. Silveri, R. T. Brierley, V. V. Albert, J. Salmilehto, L. Jiang, and S. M. Girvin, "New Class of Quantum Error-Correcting Codes for a Bosonic Mode", Physical Review X **6**, Publisher: American Physical Society, 031006 (2016).

Minev, Z. K., Z. Leghtas, S. O. Mundhada, L. Christakis, I. M. Pop, and M. H. Devoret, "Energy-participation quantization of Josephson circuits", arXiv:2010.00620 [cond-mat, physics:quant-ph], arXiv: 2010.00620 (2021).

Mirrahimi, M., Z. Leghtas, V. V. Albert, S. Touzard, R. J. Schoelkopf, L. Jiang, and M. H. Devoret, "Dynamically protected cat-qubits: a new paradigm for universal quantum computation", en, New Journal of Physics **16**, 045014 (2014).

Mooij, J. E., T. P. Orlando, L. Levitov, L. Tian, C. H. v. d. Wal, and S. Lloyd, "Josephson Persistent-Current Qubit", en, Science **285**, 1036–1039 (1999).

Mundhada, S. O., A. Grimm, S. Touzard, U. Vool, S. Shankar, M. H. Devoret, and M. Mirrahimi, "Generating higher-order quantum dissipation from lower-order parametric processes", en, Quantum Science and Technology **2**, 024005 (2017).

Mundhada, S., A. Grimm, J. Venkatraman, Z. Minev, S. Touzard, N. Frattini, V. Sivak, K. Sliwa, P. Reinhold, S. Shankar, M. Mirrahimi, and M. Devoret, "Experimental Implementation of a Raman-Assisted Eight-Wave Mixing Process", Physical Review Applied **12**, 054051 (2019).

Munro, W. J., K. Nemoto, G. J. Milburn, and S. L. Braunstein, "Weak-force detection with superposed coherent states", Physical Review A **66**, Publisher: American Physical Society, 023819 (2002).

Murch, K. W., S. J. Weber, C. Macklin, and I. Siddiqi, "Observing single quantum trajectories of a superconducting quantum bit", en, Nature **502**, 211–214 (2013).

Mutus, J. Y., T. C. White, R. Barends, Y. Chen, Z. Chen, B. Chiaro, A. Dunsworth, E. Jeffrey, J. Kelly, A. Megrant, C. Neill, P. J. J. O'Malley, P. Roushan, D. Sank, A. Vainsencher, J. Wenner, K. M. Sundqvist, A. N. Cleland, and J. M. Martinis, "Strong environmental coupling in a Josephson parametric amplifier", Applied Physics Letters **104**, 263513 (2014).

Naaman, O., M. O. Abutaleb, C. Kirby, and M. Rennie, "On-chip Josephson junction microwave switch", Applied Physics Letters **108**, 112601 (2016).

Naaman, O., D. G. Ferguson, A. Marakov, M. Khalil, W. F. Koehl, and R. J. Epstein, "High Saturation Power Josephson Parametric Amplifier with GHz Bandwidth", in 2019 IEEE MTT-S International Microwave Symposium (IMS), ISSN: 2576-7216 (June 2019), pp. 259–262.

Nguyen, L. B., Y.-H. Lin, A. Somoroff, R. Mencia, N. Grabon, and V. E. Manucharyan, "High-Coherence Fluxonium Qubit", Physical Review X **9**, Publisher: American Physical Society, 041041 (2019).

Nielsen, M. A. and I. L. Chuang, *Quantum computation and quantum information*, en, 10th anniversary ed (Cambridge University Press, Cambridge ; New York, 2010).

Nigg, S. E., H. Paik, B. Vlastakis, G. Kirchmair, S. Shankar, L. Frunzio, M. H. Devoret, R. J. Schoelkopf, and S. M. Girvin, "Black-Box Superconducting Circuit Quantization", Physical Review Letters **108**, 240502 (2012).

O'Brien, K., C. Macklin, I. Siddiqi, and X. Zhang, "Resonant Phase Matching of Joseph-son Junction Traveling Wave Parametric Amplifiers", Physical Review Letters **113**, Publisher: American Physical Society, 157001 (2014).

Ofek, N., A. Petrenko, R. Heeres, P. Reinhold, Z. Leghtas, B. Vlastakis, Y. Liu, L. Frunzio, S. M. Girvin, L. Jiang, M. Mirrahimi, M. H. Devoret, and R. J. Schoelkopf, "Extending the lifetime of a quantum bit with error correction in superconducting circuits", en, Nature **536**, Number: 7617 Publisher: Nature Publishing Group, 441–445 (2016).

Oreg, Y., G. Refael, and F. von Oppen, "Helical Liquids and Majorana Bound States in Quantum Wires", Physical Review Letters **105**, Publisher: American Physical Society, 177002 (2010).

Parker, D. J., M. Savytskyi, W. Vine, A. Laucht, T. Duty, A. Morello, A. L. Grimsmo, and J. J. Pla, "A near-ideal degenerate parametric amplifier", arXiv:2108.10471 [cond-mat, physics:quant-ph], arXiv: 2108.10471 (2021).

Pfaff, W., C. J. Axline, L. D. Burkhart, U. Vool, P. Reinhold, L. Frunzio, L. Jiang, M. H. Devoret, and R. J. Schoelkopf, "Controlled release of multiphoton quantum states from a microwave cavity memory", en, Nature Physics **13**, 882–887 (2017).

Planat, L., R. Dassonneville, J. P. Martínez, F. Foroughi, O. Buisson, W. Hasch-Guichard, C. Naud, R. Vijay, K. Murch, and N. Roch, "Understanding the Saturation Power of Josephson Parametric Amplifiers Made from SQUID Arrays", Physical Review Applied **11**, Publisher: American Physical Society, 034014 (2019).

Planat, L., A. Ranadive, R. Dassonneville, J. Puertas Martínez, S. Léger, C. Naud, O. Buisson, W. Hasch-Guichard, D. M. Basko, and N. Roch, "Photonic-Crystal Josephson Traveling-Wave Parametric Amplifier", Physical Review X **10**, Publisher: American Physical Society, 021021 (2020).

Pop, I. M., I. Protopopov, F. Lecocq, Z. Peng, B. Pannetier, O. Buisson, and W. Guichard, "Measurement of the effect of quantum phase slips in a Josephson junction chain", en, Nature Physics **6**, 589–592 (2010).

Pozar, D. M., *Microwave Engineering*, 4th ed. (John Wiley & Sons, Inc., 2012).

Puri, S., C. K. Andersen, A. L. Grimsmo, and A. Blais, "Quantum annealing with all-to-all connected nonlinear oscillators", en, Nature Communications **8**, Bandiera_abtest: a Cc_license_type: cc_by Cg_type: Nature Research Journals Number: 1 Primary_atype: Research Publisher: Nature Publishing Group Subject_term: Quantum information;Quantum simulation Subject_term_id: quantum-information;quantum-simulation, 15785 (2017).

Puri, S., S. Boutin, and A. Blais, "Engineering the quantum states of light in a Kerr-nonlinear resonator by two-photon driving", en, npj Quantum Information **3**, 18 (2017).

Puri, S., A. Grimm, P. Campagne-Ibarcq, A. Eickbusch, K. Noh, G. Roberts, L. Jiang, M. Mirrahimi, M. H. Devoret, and S. M. Girvin, "Stabilized Cat in a Driven Nonlinear Cavity: A Fault-Tolerant Error Syndrome Detector", Physical Review X **9**, 041009 (2019).

Puri, S., L. St-Jean, J. A. Gross, A. Grimm, N. E. Frattini, P. S. Iyer, A. Krishna, S. Touzard, L. Jiang, A. Blais, S. T. Flammia, and S. M. Girvin, "Bias-preserving gates with stabilized cat qubits", en, Science Advances **6**, Publisher: American Association for the Advancement of Science Section: Research Article, eaay5901 (2020).

Putterman, H., J. Iverson, Q. Xu, L. Jiang, O. Painter, F. G. S. L. Brandão, and K. Noh, "Colored Kerr cat qubits", arXiv:2107.09198 [quant-ph], arXiv: 2107.09198 (2021).

Ranzani, L., M. Bal, K. C. Fong, G. Ribeill, X. Wu, J. Long, H.-S. Ku, R. P. Erickson, D. Pappas, and T. A. Ohki, "Kinetic inductance traveling-wave amplifiers for multiplexed qubit readout", Applied Physics Letters **113**, Publisher: American Institute of Physics, 242602 (2018).

Ranzani, L. and J. Aumentado, "Graph-based analysis of nonreciprocity in coupled-mode systems", en, New Journal of Physics **17**, 023024 (2015).

Reinhold, P., S. Rosenblum, W.-L. Ma, L. Frunzio, L. Jiang, and R. J. Schoelkopf, "Error-corrected gates on an encoded qubit", en, Nature Physics **16**, 822–826 (2020).

Risté, D., J. G. van Leeuwen, H.-S. Ku, K. W. Lehnert, and L. DiCarlo, "Initialization by Measurement of a Superconducting Quantum Bit Circuit", Physical Review Letters **109**, 050507 (2012).

Roberts, D. and A. A. Clerk, "Driven-Dissipative Quantum Kerr Resonators: New Exact Solutions, Photon Blockade and Quantum Bistability", Physical Review X **10**, Publisher: American Physical Society, 021022 (2020).

Rosenblum, S., P. Reinhold, M. Mirrahimi, L. Jiang, L. Frunzio, and R. J. Schoelkopf, "Fault-tolerant detection of a quantum error", en, Science **361**, 266–270 (2018).

Roy, A. and M. Devoret, "Introduction to parametric amplification of quantum signals with Josephson circuits", Comptes Rendus Physique, Quantum microwaves / Micro-ondes quantiques **17**, 740–755 (2016).

Roy, A. and M. Devoret, "Quantum-limited parametric amplification with Josephson circuits in the regime of pump depletion", Physical Review B **98**, 045405 (2018).

Roy, T., S. Kundu, M. Chand, A. M. Vadiraj, A. Ranadive, N. Nehra, M. P. Patankar, J. Aumentado, A. A. Clerk, and R. Vijay, "Broadband parametric amplification with impedance engineering: Beyond the gain-bandwidth product", Applied Physics Letters **107**, 262601 (2015).

Ryan, C. A., B. R. Johnson, J. M. Gambetta, J. M. Chow, M. P. da Silva, O. E. Dial, and T. A. Ohki, "Tomography via correlation of noisy measurement records", Physical Review A **91**, 022118 (2015).

Sank, D., Z. Chen, M. Khezri, J. Kelly, R. Barends, B. Campbell, Y. Chen, B. Chiaro, A. Dunsworth, A. Fowler, E. Jeffrey, E. Lucero, A. Megrant, J. Mutus, M. Neeley, C. Neill, P. J. J. O'Malley, C. Quintana, P. Roushan, A. Vainsencher, T. White, J. Wenner, A. N. Korotkov, and J. M. Martinis, "Measurement-Induced State Transitions in a Superconducting Qubit: Beyond the Rotating Wave Approximation", Physical Review Letters **117**, 190503 (2016).

Schackert, F., "A Practical Quantum-Limited Parametric Amplifier Based on the Josephson Ring Modulator", Ph.D. (Yale University, 2013).

Shor, P. W., "Scheme for reducing decoherence in quantum computer memory", Physical Review A **52**, R2493–R2496 (1995).

Simoen, M., C. W. S. Chang, P. Krantz, J. Bylander, W. Wustmann, V. Shumeiko, P. Delsing, and C. M. Wilson, "Characterization of a multimode coplanar waveguide parametric amplifier", Journal of Applied Physics **118**, Publisher: American Institute of Physics, 154501 (2015).

Singh, S., A. S. Darmawan, B. J. Brown, and S. Puri, "High-Fidelity Magic-State Preparation with a Biased-Noise Architecture", arXiv:2109.02677 [quant-ph], arXiv: 2109.02677 (2021).

Sivak, V. V., S. Shankar, G. Liu, J. Aumentado, and M. H. Devoret, "Josephson Array-Mode Parametric Amplifier", Physical Review Applied **13**, Publisher: American Physical Society, 024014 (2020).

Sivak, V., N. Frattini, V. Joshi, A. Lingenfelter, S. Shankar, and M. Devoret, "Kerr-Free Three-Wave Mixing in Superconducting Quantum Circuits", Physical Review Applied **11**, 054060 (2019).

Slichter, D. H., R. Vijay, S. J. Weber, S. Boutin, M. Boissonneault, J. M. Gambetta, A. Blais, and I. Siddiqi, "Measurement-Induced Qubit State Mixing in Circuit QED from Up-Converted Dephasing Noise", Physical Review Letters **109**, Publisher: American Physical Society, 153601 (2012).

Sliwa, K. M., M. Hatridge, A. Narla, S. Shankar, L. Frunzio, R. J. Schoelkopf, and M. H. Devoret, "Reconfigurable Josephson Circulator/Directional Amplifier", Physical Review X **5**, 041020 (2015).

Smith, W. C., A. Kou, U. Vool, I. M. Pop, L. Frunzio, R. J. Schoelkopf, and M. H. Devoret, "Quantization of inductively shunted superconducting circuits", Physical Review B **94**, 144507 (2016).

Smith, W. C., M. Villiers, A. Marquet, J. Palomo, M. R. Delbecq, T. Kontos, P. Campagne-Ibarcq, B. Douçot, and Z. Leghtas, "Magnifying quantum phase fluctuations with Cooper-pair pairing", arXiv:2010.15488 [cond-mat, physics:quant-ph], arXiv: 2010.15488 (2020).

Sterck, A., R. Kleiner, and D. Koelle, "Three-Junction SQUID Rocking Ratchet", Physical Review Letters **95**, Publisher: American Physical Society, 177006 (2005).

Sun, L., A. Petrenko, Z. Leghtas, B. Vlastakis, G. Kirchmair, K. M. Sliwa, A. Narla, M. Hatridge, S. Shankar, J. Blumoff, L. Frunzio, M. Mirrahimi, M. H. Devoret, and R. J. Schoelkopf, "Tracking photon jumps with repeated quantum non-demolition parity measurements", en, Nature **511**, 444–448 (2014).

Sundqvist, K. M. and P. Delsing, "Negative-resistance models for parametrically flux-pumped superconducting quantum interference devices", En, EPJ Quantum Technology **1**, 6 (2014).

Terhal, B. M., "Quantum error correction for quantum memories", Reviews of Modern Physics **87**, Publisher: American Physical Society, 307–346 (2015).

Touzard, S., A. Grimm, Z. Leghtas, S. O. Mundhada, P. Reinhold, C. Axline, M. Reagor, K. Chou, J. Blumoff, K. M. Sliwa, S. Shankar, L. Frunzio, R. J. Schoelkopf, M. Mirrahimi, and M. H. Devoret, "Coherent Oscillations inside a Quantum Manifold Stabilized by Dissipation", Physical Review X **8**, 021005 (2018).

Touzard, S., A. Kou, N. E. Frattini, V. V. Sivak, S. Puri, A. Grimm, L. Frunzio, S. Shankar, and M. H. Devoret, "Gated Conditional Displacement Readout of Superconducting Qubits", Physical Review Letters **122**, 080502 (2019).

Tuckett, D. K., S. D. Bartlett, and S. T. Flammia, "Ultrahigh Error Threshold for Surface Codes with Biased Noise", Physical Review Letters **120**, 050505 (2018).

Venkatraman, J., X. Xiao, R. G. Cortiñas, and M. H. Devoret, "On the static effective Hamiltonian of a rapidly driven nonlinear system", arXiv:2108.02861 [cond-mat, physics:math-ph, physics:physics, physics:quant-ph], arXiv: 2108.02861 (2021).

Vijay, R., M. H. Devoret, and I. Siddiqi, "Invited Review Article: The Josephson bifurcation amplifier", Review of Scientific Instruments **80**, 111101 (2009).

Vijay, R., D. H. Slichter, and I. Siddiqi, "Observation of Quantum Jumps in a Superconducting Artificial Atom", Physical Review Letters **106**, Publisher: American Physical Society, 110502 (2011).

Viola, L., E. Knill, and S. Lloyd, "Dynamical Decoupling of Open Quantum Systems", Physical Review Letters **82**, 2417–2421 (1999).

Vion, D., A. Aassime, A. Cottet, P. Joyez, H. Pothier, C. Urbina, D. Esteve, and M. H. Devoret, "Manipulating the Quantum State of an Electrical Circuit", Science **296**, Publisher: American Association for the Advancement of Science, 886–889 (2002).

Vissers, M. R., R. P. Erickson, H.-S. Ku, L. Vale, X. Wu, G. C. Hilton, and D. P. Pappas, "Low-noise kinetic inductance traveling-wave amplifier using three-wave mixing", Applied Physics Letters **108**, 012601 (2016).

Vlastakis, B., G. Kirchmair, Z. Leghtas, S. E. Nigg, L. Frunzio, S. M. Girvin, M. Mirrahimi, M. H. Devoret, and R. J. Schoelkopf, "Deterministically Encoding Quantum Information Using 100-Photon Schrödinger Cat States", en, Science **342**, 607–610 (2013).

Vool, U., A. Kou, W. C. Smith, N. E. Frattini, K. Serniak, P. Reinhold, I. M. Pop, S. Shankar, L. Frunzio, S. M. Girvin, and M. H. Devoret, "Driving Forbidden Transitions in the Fluxonium Artificial Atom", Physical Review Applied **9**, 054046 (2018).

Vool, U. and M. Devoret, "Introduction to quantum electromagnetic circuits", en, International Journal of Circuit Theory and Applications **45**, _eprint: https://onlinelibrary.wiley.com/doi/pdf/10.1002/cta.2359, 897–934 (2017).

Vuillot, C., H. Asasi, Y. Wang, L. P. Pryadko, and B. M. Terhal, "Quantum error correction with the toric Gottesman-Kitaev-Preskill code", Physical Review A **99**, 032344 (2019).

Wal, C. H. v. d., A. C. J. t. Haar, F. K. Wilhelm, R. N. Schouten, C. J. P. M. Harmans, T. P. Orlando, S. Lloyd, and J. E. Mooij, "Quantum Superposition of Macroscopic Persistent-Current States", en, Science **290**, 773–777 (2000).

Wallquist, M., V. S. Shumeiko, and G. Wendin, "Selective coupling of superconducting charge qubits mediated by a tunable stripline cavity", Physical Review B **74**, 224506 (2006).

Wallraff, A., D. I. Schuster, A. Blais, L. Frunzio, R.-S. Huang, J. Majer, S. Kumar, S. M. Girvin, and R. J. Schoelkopf, "Strong coupling of a single photon to a superconducting qubit using circuit quantum electrodynamics", en, Nature **431**, Bandiera_abtest: a Cg_type: Nature Research Journals Number: 7005 Primary_atype: Research Publisher: Nature Publishing Group, 162–167 (2004).

Walter, T., P. Kurpiers, S. Gasparinetti, P. Magnard, A. Potočnik, Y. Salathé, M. Pechal, M. Mondal, M. Oppliger, C. Eichler, and A. Wallraff, "Rapid High-Fidelity Single-Shot Dispersive Readout of Superconducting Qubits", Physical Review Applied **7**, 054020 (2017).

Wang, C. S., J. C. Curtis, B. J. Lester, Y. Zhang, Y. Y. Gao, J. Freeze, V. S. Batista, P. H. Vaccaro, I. L. Chuang, L. Frunzio, L. Jiang, S. M. Girvin, and R. J. Schoelkopf, "Efficient Multiphoton Sampling of Molecular Vibronic Spectra on a Superconducting Bosonic Processor", Physical Review X **10**, Publisher: American Physical Society, 021060 (2020).

Winkel, P., I. Takmakov, D. Rieger, L. Planat, W. Hasch-Guichard, L. Grünhaupt, N. Maleeva, F. Foroughi, F. Henriques, K. Borisov, J. Ferrero, A. V. Ustinov, W. Wernsdorfer, N. Roch, and I. M. Pop, "Nondegenerate Parametric Amplifiers Based on Dispersion-Engineered Josephson-Junction Arrays", Physical Review Applied **13**, Publisher: American Physical Society, 024015 (2020).

Wustmann, W. and V. Shumeiko, "Parametric effects in circuit quantum electrodynamics", Low Temperature Physics **45**, Publisher: American Institute of Physics, 848–869 (2019).

Wustmann, W. and V. Shumeiko, "Parametric resonance in tunable superconducting cavities", Physical Review B **87**, 184501 (2013).

Yamamoto, T., K. Inomata, M. Watanabe, K. Matsuba, T. Miyazaki, W. D. Oliver, Y. Nakamura, and J. S. Tsai, "Flux-driven Josephson parametric amplifier", Applied Physics Letters **93**, 042510 (2008).

Yan, F., S. Gustavsson, J. Bylander, X. Jin, F. Yoshihara, D. G. Cory, Y. Nakamura, T. P. Orlando, and W. D. Oliver, "Rotating-frame relaxation as a noise spectrum analyser of a superconducting qubit undergoing driven evolution", en, Nature Communications **4**, 2337 (2013).

Yan, F., S. Gustavsson, A. Kamal, J. Birenbaum, A. P. Sears, D. Hover, T. J. Gudmundsen, D. Rosenberg, G. Samach, S. Weber, J. L. Yoder, T. P. Orlando, J. Clarke, A. J. Kerman, and W. D. Oliver, "The flux qubit revisited to enhance coherence and reproducibility", en, Nature Communications **7**, ncomms12964 (2016).

You, J. Q., X. Hu, S. Ashhab, and F. Nori, "Low-decoherence flux qubit", Physical Review B **75**, 140515 (2007).

Yurke, B., L. R. Corruccini, P. G. Kaminsky, L. W. Rupp, A. D. Smith, A. H. Silver, R. W. Simon, and E. A. Whittaker, "Observation of parametric amplification and deamplification in a Josephson parametric amplifier", Physical Review A **39**, Publisher: American Physical Society, 2519–2533 (1989).

Yurke, B. and D. Stoler, "The dynamic generation of Schrödinger cats and their detection", en, Physica B+C **151**, 298–301 (1988).

Zapata, I., R. Bartussek, F. Sols, and P. Hänggi, "Voltage Rectification by a SQUID Ratchet", Physical Review Letters **77**, Publisher: American Physical Society, 2292–2295 (1996).

Zhang, H., S. Chakram, T. Roy, N. Earnest, Y. Lu, Z. Huang, D. K. Weiss, J. Koch, and D. I. Schuster, "Universal Fast-Flux Control of a Coherent, Low-Frequency Qubit", Physical Review X **11**, Publisher: American Physical Society, 011010 (2021).

Zhang, Y. and M. I. Dykman, "Preparing quasienergy states on demand: A parametric oscillator", Physical Review A **95**, Publisher: American Physical Society, 053841 (2017).

Zhou, X., V. Schmitt, P. Bertet, D. Vion, W. Wustmann, V. Shumeiko, and D. Esteve, "High-gain weakly nonlinear flux-modulated Josephson parametric amplifier using a SQUID array", Physical Review B **89**, 214517 (2014).

Zimmerman, J. E. and A. H. Silver, "Macroscopic Quantum Interference Effects through Superconducting Point Contacts", Physical Review **141**, 367–375 (1966).

Zorin, A. B., "Josephson Traveling-Wave Parametric Amplifier with Three-Wave Mixing", Physical Review Applied **6**, 034006 (2016).

Zorin, A. B., M. Khabipov, J. Dietel, and R. Dolata, "Traveling-wave parametric amplifier based on three-wave mixing in a Josephson metamaterial", arXiv:1705.02859 [cond-mat, physics:quant-ph], arXiv: 1705.02859 (2017).

Zorin, A. B. and Y. Makhlin, "Period-doubling bifurcation readout for a Josephson qubit", Physical Review B **83**, 224506 (2011).

Zurek, W. H., "Decoherence, einselection, and the quantum origins of the classical", Reviews of Modern Physics **75**, Publisher: American Physical Society, 715–775 (2003).